CHEMICAL REVIEWS

pubs.acs.org/CR

Review

Review of Multifunctional Separators: Stabilizing the Cathode and the Anode for Alkali (Li, Na, and K) Metal–Sulfur and Selenium Batteries

Hongchang Hao,* Tanya Hutter, Brad L. Boyce, John Watt, Pengcheng Liu, and David Mitlin*

Cite This: *Chem. Rev.* 2022, 122, 8053–8125

Read Online

ACCESS | Metrics & More | Article Recommendations

ABSTRACT: Alkali metal batteries based on lithium, sodium, and potassium anodes and sulfur-based cathodes are regarded as key for next-generation energy storage due to their high theoretical energy and potential cost effectiveness. However, metal–sulfur batteries remain challenged by several factors, including polysulfides' (PSs) dissolution, sluggish sulfur redox kinetics at the cathode, and metallic dendrite growth at the anode. Functional separators and interlayers are an innovative approach to remedying these drawbacks. Here we critically review the state-of-the-art in separators/interlayers for cathode and anode protection, covering the Li–S and the emerging Na–S and K–S systems. The approaches for improving electrochemical performance may be categorized as one or a combination of the following: Immobilization of polysulfides (cathode); catalyzing sulfur redox kinetics (cathode); introduction of protective layers to serve as an artificial solid electrolyte interphase (SEI) (anode); and combined improvement in electrolyte wetting and homogenization of ion flux (anode and cathode). It is demonstrated that while the advances in Li–S are relatively mature, less progress has been made with Na–S and K–S due to the more challenging redox chemistry at the cathode and increased electrochemical instability at the anode. Throughout these sections there is a complementary discussion of functional separators for emerging alkali metal systems based on metal–selenium and the metal–selenium sulfide. The focus then shifts to interlayers and artificial SEI/cathode electrolyte interphase (CEI) layers employed to stabilize solid-state electrolytes (SSEs) in metal–sulfur solid-state batteries (SSBs). The discussion of SSEs focuses on inorganic electrolytes based on Li- and Na-based oxides and sulfides but also touches on some hybrid systems with an inorganic matrix and a minority polymer phase. The review then moves to practical considerations for functional separators, including scaleup issues and Li–S technoeconomics. The review concludes with an outlook section, where we discuss emerging mechanics, spectroscopy, and advanced electron microscopy (*e.g.* cryo-transmission electron microscopy (cryo-TEM) and cryo-focused ion beam (cryo-FIB))-based approaches for analysis of functional separator structure–battery electrochemical performance interrelations. Throughout the review we identify the outstanding open scientific and technological questions while providing recommendations for future research topics.

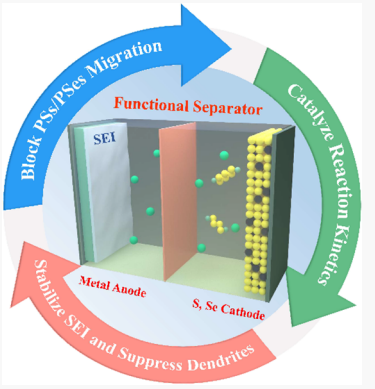

CONTENTS

Received: September 28, 2021
Published: March 29, 2022

https://doi.org/10.1021/acs.chemrev.1c00838
Chem. Rev. 2022, 122, 8053–8125

1. INTRODUCTION: BACKGROUND OF METAL−SULFUR BATTERIES AND BEYOND

Over the past few decades, rechargeable batteries have been widely applied in a broad range of applications ranging from portable electronics to electric vehicles. Commercial lithium ion batteries (LIBs) rely on the reversible insertion−extraction of Li ions in the oxide cathodes (layered, spinel, and polyanion families) and graphite anodes.[1,2] This generation of LIBs is limited to a specific energy of around 225 Wh kg^{-1}, with incremental energy improvements being made with increased cathode voltage, anode capacity, cell form factors, *etc.* To expand the use of LIBs into heavy trucking and other long-range automotive applications, there is a strong incentive to develop batteries with energies over 400 Wh kg^{-1}.[3,4] Lithium metal batteries (LMBs), sodium metal batteries (SMBs), and potassium metal batteries (KMBs) are attracting wide scientific attention, with the Li−S system being the most commercially mature. Lithium−sulfur batteries (LSBs) are highly promising due to the theoretical specific capacities of S (1673 mAh g^{-1}) and Li (3860 mA h g^{-1}), as well the favorable technoeconomics and earth abundance of S. Alkali metal batteries based on Na metal and K metal offer the possibility of even lower cost and greater availability of precursors, but at the expense of specific energy and overall battery performance.

While Li−S has been studied for several decades prior, the work by Nazar et al. in 2009 set off a flurry of the most recent research activity.[5] The two-electron-transfer cathodic discharge process involves the phase transitions from elemental sulfur to lithium sulfide ($S_8 + 16\ e^- + 16\ Li^+ \rightarrow 8\ Li_2S$), theoretically delivering a remarkable specific energy density of 2600 Wh kg^{-1}. In practical terms, the specific energy of Li−S can reach 400−600 Wh kg^{-1}.[6] The difference between the practical and theoretical values arises from several factors including the need to employ around 50 wt % inactive carbon host for the S, as well as the practical need to employ an oversized metal anode foil. Despite the inability to achieve even one-fourth of the anticipated specific energy in practical cells, Li−S batteries remain promising. It is expected that with the advent of sub-50-μm Li foils and of "Li-free anode" cell architectures (where the capacity-balanced Li is stored in the cathode), substantially higher cell energies will be possible.[7,8]

The Na−S and K−S systems undergo somewhat analogous electrochemical storage mechanisms as Li−S, although with a different intermediate phase transition sequence.[9−12] Based on the two-electron reaction of sulfur, the Na−S and K−S batteries can deliver theoretical energies of 1273 Wh kg^{-1} and 1023 Wh kg^{-1}, respectively. If one-third of that energy is ultimately achievable in practical cells, this makes the energies of Na−S and K−S batteries competitive with existing LIBs. There are several electrochemical disparities between Na−S and K−S versus the Li−S system. Issues with Na−S and K−S include less distinct two-phase voltage plateaus, larger polarization voltages, different intermediate phases, and potentially a lower capacity terminal phase for the case of K−S. Table 1 shows the physical properties of the three alkali metals and the corresponding theoretical and measured electrochemical properties.

Table 1. Physical and Electrochemical Properties of Li, Na, and K

Property	Lithium (Li)	Sodium (Na)	Potassium (K)
Atomic mass	6.94	23.00	39.10
Abundance (%)	0.0017	2.8	2.6
Cost of carbonate ($ ton^{-1})	17000	200	1000
Melting point (°C)	180.5	97.7	63.5
Density (g/cm^3)	0.534	0.968	0.862
Shear modulus (GPa)	4.2	3.3	1.3
Brinell hardness (MPa)	5	0.69	0.36
Shannon ionic radius (Å)	0.76	1.02	1.38
$E°$ (M^+/M) *vs* SHE in aqueous (V)	−3.040	−2.713	−2.924
Gravimetric capacity (mA h g^{-1})	3860	1166	687
Volumetric capacity (mA h cm^{-3})	2062	1131	589
Ionic diffusivity in hard carbon ($\times 10^{-9}$ cm^2 s^{-1})	2.1[21]	1[22]	1.2[22]
Ionic diffusivity in tellurene and alloy (cm^2 s^{-1})[23]	10^{-14} – 10^{-15}	10^{-15} – 10^{-16}	10^{-16} – 10^{-17}
Ionic diffusivity in black phosphorus/graphite composite (cm^2 s^{-1})[24]	10^{-12} – 10^{-10}	10^{-13} – 10^{-11}	10^{-14} – 10^{-12}
Ionic conductivity of 1 M MFSI in DME (mS cm^{-1})	16.9[25]	16[26]	13.1[27]
Ionic conductivity of 1 M MFSI in EC:DMC (mS cm^{-1})[28]	9.3	9.7	10.7
Ionic conductivity of 1 M MPF_6 in EC:DMC (mS cm^{-1})[29]	9.8	10	11.5
Desolvation energy in EC (kJ mol^{-1})[28]	208.9	152.8	114.6

With analogous chemical properties to sulfur, selenium (Se) represents another promising cathode material with a theoretical specific capacity of 675 mA g^{-1}, being widely paired with Li, Na, and K metal anodes for high-energy metal batteries' construction.[13−15] Compared to sulfur, Se possesses much higher electrical conductivity (1×10^{-11} *vs* 0.5×10^{-27} S m^{-1}) and, thus, improved reaction kinetics with alkali metals. Polyselenide dissolution, crossover, and shuttle are issues for Se-based cathodes. However, they appear to be substantially less severe than the polysulfide shuttle in terms of causing poor Coulombic efficiency (CE) and capacity decay.[16,17] Selenium−sulfur Se_xS_y alloys (*e.g.*, SeS_2 and SeS) made in carbon or other hosts represent another emerging cathode system, combining the fast rate capability of Se with the higher capacity of S.[18−20]

To date, there have been extensive research efforts to understand the intrinsic electrochemistry mechanisms of alkali metal−sulfur batteries and beyond. Optimizing performance has been approached from broad perspectives. This includes

https://doi.org/10.1021/acs.chemrev.1c00838
Chem. Rev. 2022, 122, 8053−8125

Table 2. Thermal and Electrochemical Properties of the Li−S, Na−S, and K−S Systems

Property	Li−S	Na−S	K−S
$\Delta_r G°$ (kJ mol^{-1})	−432.57	−357.77	−362.73
Theoretical gravimetric energy of the M−S system (Wh kg^{-1})	2571	1273	917
Theoretical volumetric energy of the M−S system (Wh L^{-1})[3,11]	2955	1545	952
Volume change from S_8 to M_2S	80%	171%	296%
Stable binary phases at RT in the phase diagram	Li_2S[36]	Na_2S, Na_2S_2, Na_2S_4, Na_2S_5[37]	K_2S, K_2S_2, K_2S_3, K_2S_4, K_2S_5, K_2S_6[38]
Diffusion coefficient of polysulfide in DMSO (10^{-6} cm^2/s)[39]	4.889 ± 0.054	5.157 ± 0.051	5.774 ± 0.053
M_2S_8 solubility in TEGDME (M)	0.18[40]	1.32[41]	NA

engineering of the electrode materials and binders, designing improved liquid or solid-state electrolytes, and creating functional separators with tuned properties; the last aspect is the focus of this review. While the primary function of a battery separator is to prevent electrical shorting, the modern metal−sulfur separator is endowed with a range of additional functional properties.[30−32] The concept of a functional separator is traceable to a "functional interlayer", which is defined as a secondary film present between the separator and the active cathode and/or anode.[32,33] The film may be freestanding, or it may remain bound to the separator surface chemically and/or mechanically. In 2012, Manthiram's group demonstrated the application of a functional interlayer for a Li−S cell.[34] The authors inserted a free-standing multiwalled carbon nanotube (MWCNT) interlayer between the separator and cathode, which mitigated the crossover of the lithium polysulfides (LiPSs) to the anode. Later, the same group designed a functional separator based on a lightweight carbon coating, which improved the electrochemical performance of the Li−S cell as well.[35] This review begins with the electrochemistry and the associated challenges of alkali metal−sulfur batteries and Se-based analogs, discussing and contrasting mechanisms for the Li−S, Na−S, and K−S systems. Functional separators/interlayers are then detailed in terms of the key mechanisms for improving the performance of the cathode (S, Se, and SeS) and of the anode. This review then provides a critical discussion regarding future research directions, focusing on the most promising emerging approaches for extending the performance of Li−S, Na−S, and K−S cells and of Se-based analogs. Throughout the discussions, we emphasize the outstanding basic science questions in addition to the technological issues. The Future Outlook section also provides a complementary discussion of the state-of-the-art analytical tools that are most relevant for bringing new insight to these questions, including *in situ* and *operando* techniques.

2. BASIC ELECTROCHEMISTRY OF THE LI−S, NA−S, AND K−S SYSTEMS

A comparison of the relative properties for different S-based alkali metal batteries is summarized in Table 2. These numbers include the capacities, energy densities, and calculated volume expansion for the reactions of S to Li_2S, Na_2S, and K_2S. The table also shows thermodynamically stable phases within the binary systems of Li−S, Na−S, and K−S at room temperature (RT). The differences between various polysulfides (LiPSs, NaPSs, and KPSs) are also summarized, in terms of solubility and diffusion coefficient. Table 3 lists the representative Li−S, Na−S, and K−S batteries, with various host structures, sulfur allotropes, electrolyte systems, cell configurations, and so on. Accordingly, sulfur may undergo various redox pathways, as those parameters change.

It should be noted that compared with Li−S and Na−S, the emerging K−S architectures suffer from greater problems with metal anode instability with a range of ether and carbonate electrolytes, in part due to a K-based solid electrolyte interphase that does not fully passivate the metal.[12,42] The ongoing growth of a K-based SEI during cycling or static aging results in accelerated electrolyte consumption and cell drying, leading to button cells being tested in the flooded configuration so to achieve satisfactory performance. This is also generally true for the Na−S system as compared with Li−S, with an unstable (not self-terminating) Na-based SEI being a concern in both ether and carbonate electrolytes.[43] Hence, the amount of electrolyte added to laboratory K−S and Na−S button cells is often unrealistically large. Considering that electrolyte takes up most of the weight of the cell, applying lean electrolytes while maintaining rate capability and cyclability is a key research target with these two emerging systems, similarly to the current aims for Li−S.[44]

Extensive SEI growth leads to interrelated electrochemical performance deterioration (decreased cycling life and rate capability; electrical shorting due to dendrites) and safety concerns (cell swelling and bursting; fires due to electrical shorts). In laboratory stainless steel button cells, the excessive electrolyte ensures that the cell does not dry out, while gas generation is masked by the rigid can that does not swell or burst under most conditions. In flexible pouch cells, which much better represent the near-commercial Li−S architectures, gas generation leads to rapid cell swelling and potentially to it bursting, releasing gas (mostly CO_2) and remnant electrolyte. Hence, there is an onus to transition from button cell data to pouch cell data for any metal−sulfur system that is being seriously considered for commercial viability. For the Na−S and K−S systems, this represents a largely unexplored direction. It also represents another key future research direction for functional separators, be it for Li, Na, or K.

Could the functional separator-enhanced performance achieved with rigid button cell architectures be transitioned to soft pouch cells with lean-electrolyte configurations? Could functional separators be sufficiently effective in minimizing unstable SEI growth as to prevent cell drying and gas generation over thousands of cycles? Another key difference of pouch cells versus button cells concerns the pressure that is employed to hold the battery together. While usually being ignored in discussing mechanisms, assembled button cells will naturally exert above 10 MPa to the anode−separator−cathode stack. Conversely, a flexible pouch cell will not exert any pressure, unless it is externally applied, often being 1 MPa or less. Without a significant stress to press a functional separator against both electrodes, will the functionality be maintained? In more broad terms, what is the role of pressure in the efficacy of functional separators in stabilizing the SEI and preventing dendrites at the anode, in aiding targeted redox reactions at the

https://doi.org/10.1021/acs.chemrev.1c00838
Chem. Rev. 2022, 122, 8053−8125

Table 3. Electrochemical Performance of Representative Li−S, Na−S, and K−S Systems

Cathode structure	S content (wt %) [Mass loading (mg cm^{-2})]	Voltage window (V)	Electrolyte [Electrolyte-to-sulfur (E/S) ratio]	Sulfur reox pathway	Cyclability (mAh g^{-1}) after n^{th} cycles [CE range upon cycling]	Ref
			Li−S System			
S-Co/N-codoped carbon	92 [9.7]	1.8−2.7	1 M LiTFSI in DOL/DME + $LiNO_3$ [15]	$S_8 \leftrightarrow Li_2S_4 \leftrightarrow Li_2S$	620 (100th) at 0.05C [NA]	53
S-C@MoS_2	80 [4]	1.8−2.7	1 M LiTFSI in DOL/DME + $LiNO_3$ [5]	$S_8 \leftrightarrow Li_2S_4 \leftrightarrow Li_2S$	≈700 (120th) at 0.1C [NA]	54
Li_2S_6 + WS_2-rGO-CNT	[7.68]	1.7−2.8	1 M LiTFSI in DOL/DME + $LiNO_3$ [NA]	$S_8 \leftrightarrow Li_2S_4 \leftrightarrow Li_2S$	860 (100th) at 0.5C [NA]	55
(Li_2S+Te)/Carbon paper	4 mg cm^{-2} of Li_2S	1.8−2.8	1 M LiTFSI in DOL/DME + $LiNO_3$ [NA]	Li-anode-free (Ni foil as anode) $Te+Li_2S_n \rightarrow Li_2Te_xS_y \rightarrow Li_2TeS_3$ (Stabilizing Li deposition)	>310 (240th) at 0.2C [≈99.72%]	8
S@PAN/S_7Se	68 [1−1.5]	1−3	1 M $LiPF_6$ in EC/DMC + FEC [10−20]	$S_8 \leftrightarrow Li_2S_2/Li_2S$	648 (500th) at 5C [≈100%]	56
Microporous carbon/S	37.7 [1]	1−3	1 M $LiPF_6$ in EC/DEC [30]	$S_{1-4} \leftrightarrow Li_2S$	510 (1000th) at 1C [≈100%]	57
$Se_{0.06}$SPAN	47.25 [1]	1−3	1 M LiTFSI in DOL/DME + $LiNO_3$ [5]	$S_n \leftrightarrow Li_2S_n \leftrightarrow Li_2S$ ($n \leq 4$)	1130 (500th) at 0.13C [≈100%]	58
			Na−S System			
S@CB@AlOOH	[3.2]	1.2−2.6	1.5 M $NaClO_4$ in TEGDME + $NaNO_3$ [12.5]	$S_8 \leftrightarrow Na_2S_{8-6} \leftrightarrow Na_2S_{2-1}$	378 (500th) at 1C [95−105%]	59
CoS_2/C@S	70 [9.1]	0.8−2.8	1 M $NaClO_4$ in TEGDME [NA]	$S_8 \rightarrow Na_2S_x \rightarrow Na_2S_{6,5} \rightarrow Na_2S_{4,3} \rightarrow Na_2S_2 \rightarrow Na_2S$	≈540 (70th) at 0.5C [≈100%]	60
Activated carbon cloth/Na_2S_6	[3.4]	1.2−2.45	1.5 M $NaClO_4$ in TEGDME + $NaNO_3$ [10.4]	$S_8 \rightarrow Na_2S_8 \rightarrow Na_2S_6 \rightarrow Na_2S_3^{\bullet -} \rightarrow Na_2S_2 \rightarrow Na_2S$	678 (700th) at 0.5C [≈100%]	61
S-$Ti_3C_2T_x$/S	>70 [>4.5]	0.8−2.8	2 M NaTFSI in EC/PC + FEC [10]	$S_8 \leftrightarrow Na_2S_{8-4} \leftrightarrow Na_2S_{2-1}$	483.7 (600th) at 1C [≈100%]	62
N-doped C/Au/S	56.5 [NA]	0.8−2.8	1 M $NaClO_4$ in PC + FEC [NA]	$S_8 \leftrightarrow Na_2S_x \leftrightarrow Na_2S_4 \leftrightarrow Na_2S$	369 (2000th) at 10 A g^{-1} [≈100%]	63
Microporous carbon/S	47 [0.58−0.79]	0.5−3.0	1 M $NaClO_4$ in EC/PC + SiO_2-IL-ClO_4 [NA]	$S_8 \leftrightarrow Na_2S_2 \leftrightarrow Na_2S$	≈600 (100th) at 0.5C [96−99%]	64
Microporous carbon/S	40 [1]	0.5−2.9	1 M $NaClO_4$ in EC/PC + FEC [NA]	$S_{1-4} \leftrightarrow Na_2S$	≈680 (2000th) at 1C [≈100%]	49
Covalent S−C	40.07 [0.84]	0.01−3 (1st) 0.6−2.8	1 M $NaClO_4$ in EC/PC [NA]	$C-S_x \rightarrow Na_2S_x \rightarrow Na_2S$ (Short-chain covalent-S needed to be activated at the lower potential state)	452 (1000th) at 2.5A g^{-1} [≈100%]	65
			K−S System			
CMK-3/S	40.8 [NA]	1.2−2.4	1 M $KClO_4$ in TEGDME [NA]	$S_8 \leftrightarrow K_2S_x \leftrightarrow K_2S_3$	202.3 (50th) at 0.05A g^{-1} [93−102%]	47
CMK-3/S	76 [1.8−2.0]	1.2−3.0	5 M KTFSI in DEGDME + KNO_3 [45−50]	$S_8 \leftrightarrow K_2S_6 \leftrightarrow K_2S_5 \leftrightarrow K_2S_4 \leftrightarrow K_2S_3$	242 (10th) at 0.01A g^{-1} [≈100%]	66
K_2S_x + carbon film ($5 \leq x \leq 6$)	0.44 mg S per cell	1.2−2.4	0.5 M KTFSI in DEGDME [114]	$S \leftrightarrow K_2S_x \leftrightarrow K_2S_3$	376 (20th) at 0.056 A g^{-1} [87−97%]	67
S-N-Co_s-C polyhedron	62.4 [>0.5]	0.5−2.8	0.8 M KPF_6 in EC/DEC [NA]	$S_8 \leftrightarrow K_2S_6 \leftrightarrow K_2S_5 \leftrightarrow K_2S_4 \leftrightarrow K_2S_3$	355.3 (150th) at 0.2 A g^{-1} [≈97%]	68
Sulfurized polyacrylonitrile	39.3 [0.4−0.6]	0.1−3.0	1 M KOTF in EC/DEC [>200]	$S \leftrightarrow K_2S_{5-3}$ (3−0.8 V) $K_2S_{5-3} \leftrightarrow K_2S_{2-1}$ (0.8−0.1 V)	117 (200th) at 0.15 A g^{-1} [≈100%]	69
Microporous carbon/S	20 [<1]	0.5−3.0	0.8 M KPF_6 in EC/DEC [10]	$S_{1-3} \leftrightarrow K_2S_{2-3} \leftrightarrow K_2S$	869.9 (150th) at 0.02 A g^{-1} [93−97%]	50
Microporous carbon nanofiber/S	25 [<0.5]	0.5−3.0	0.8 M KPF_6 in EC/DEC [>200]	$S_{1-3} \leftrightarrow K_2S_{2-3} \leftrightarrow K_2S$	1002 (2000th) at 0.2 A g^{-1} [≈100%]	70

https://doi.org/10.1021/acs.chemrev.1c00838
Chem. Rev. 2022, 122, 8053−8125

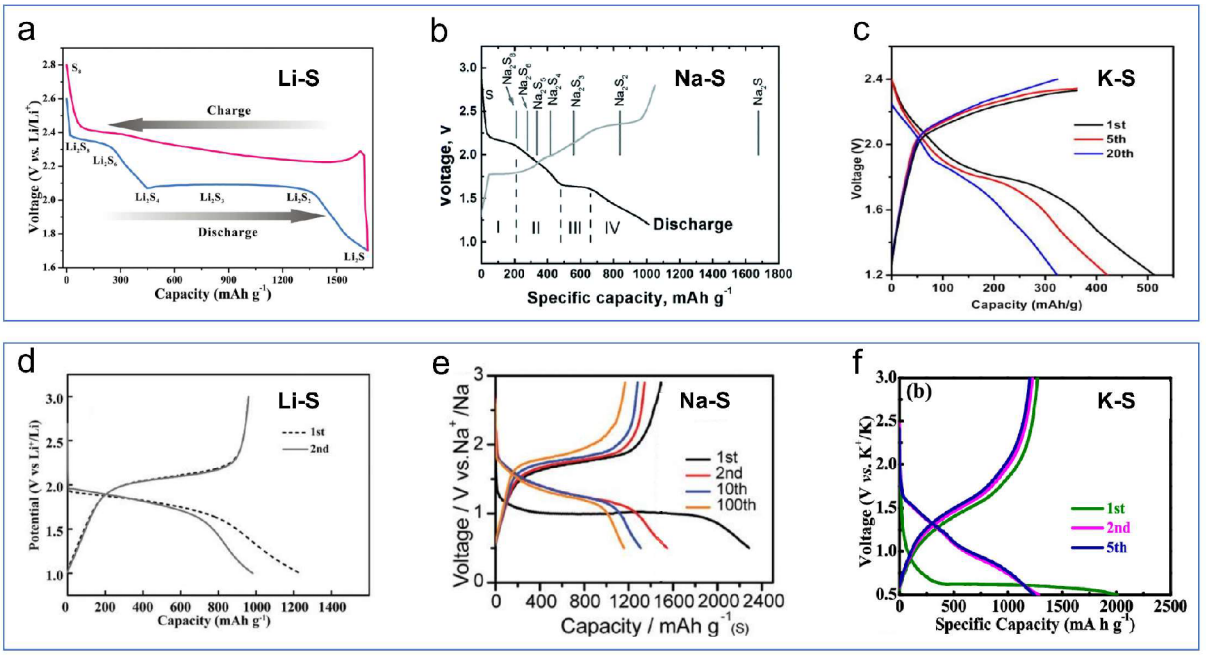

Figure 1. (a–c) Representative voltage profiles of cyclo-S_8-based cathodes for (a) Li–S, (b) Na–S, and (c) K–S metal batteries in ether-based electrolytes. (d and e) Representative voltage profiles of small molecule S_{2-4}-based cathodes for (d) Li–S, (e) Na–S, and (f) K–S metal batteries in ester-based electrolytes. Panel a is reproduced with permission from ref 45. Copyright 2019 Royal Society of Chemistry. Panel b is reproduced with permission from ref 46. Copyright 2020 Royal Society of Chemistry. Panel c is reproduced with permission from ref 47. Copyright 2017 American Chemical Society. Panel d is reproduced with permission from ref 48. Copyright 2014 John Wiley & Sons, Inc. Panel e is reproduced with permission from ref 49. Copyright 2020 John Wiley & Sons, Inc. Panel f is reproduced with permission from ref 50. Copyright 2019 American Chemical Society.

cathode, and in minimizing the crossover of species other than the active ions? To our knowledge, these pouch cell and related pressure questions have received minimal attention within the research community.

Per Figure 1a, a typical galvanostatic profile of Li–S displays two discharge plateaus. The upper discharge plateau is located at approximately 2.4 V *vs* Li/Li^+. This plateau corresponds to the opening of the cyclic octatomic sulfur ring (cyclo-S_8), followed by the transformation of lithium polysulfides from high-chain to low-chain forms by the sequence $S_8 \rightarrow Li_2S_8 \rightarrow Li_2S_6 \rightarrow Li_2S_4$. The complete reduction from elemental sulfur to electrolyte-soluble Li_2S_4 undergoes a half electron transfer per sulfur atom and contributes to a theoretical capacity of 418 mAh g^{-1}. The lower voltage plateau at approximately 2.1 V is related to the reaction from short-chain liquid Li_2S_4 to solid Li_2S_2 and finally to equilibrium solid Li_2S, making up the remaining capacity of 1255 mAh g^{-1}. The dip at the beginning of the lower discharge plateau results from the kinetically sluggish nucleation of solid Li_2S/Li_2S from liquid LiPSs. The reversible oxidation from Li_2S to S features the long charge plateaus at 2.3–2.4 V, with a second dip at the initial charging period representing the requisite overpotential to drive the conversion of Li_2S to polysulfide species. Meanwhile, the Li metal anode undergoes a reversible stripping/platting process during repeated discharge/charge processes.

Both the Na–S and K–S systems differ from Li–S in that the corresponding galvanostatic profiles have relatively less well-defined and more sloping plateaus, accompanied with a larger voltage hysteresis, as shown in Figure 1b and c. Per Table 1, the ionic radius increases in the order Li^+ (0.76 Å), Na^+ (1.02 Å), K^+ (1.38 Å), leading to the lower solid-state diffusivities of potassium and sodium ions versus that of lithium ions. This would impact the voltage features of the Na–S and K–S systems from a kinetics perspective, since solid-state concentration polarization would increase the overpotential for a given electrochemical reaction. Per Table 2, the higher volume changes associated with the formation of Na_2S/Na_2S_2 and K_2S_2/K_2S versus Li_2S_2/Li_2S inside the various carbon hosts would result in greater stresses opposing the reaction. This would likewise increase the overpotentials associated with discharging Na–S and K–S, moving the plateaus to lower voltages. Interestingly, neither the solid-state diffusivity limitation argument nor the solid-state volume expansion argument is applicable to the formation of liquid polysulfides (stoichiometries below K_2S_2/Na_2S_2), which also occur at lower voltages than for Li_2S_2. The more negative $E°(Li^+/Li)$ *vs* $E°(K^+/K)$ or $E°(Na^+/Na)$ would not explain this effect, since what is being considered is the polysulfide formation voltage relative to the corresponding metal redox. The lowered plateaus of the liquid Na and K polysulfides are likely related to activation polarization effects, namely the lower reactivity of solid S with Na^+ and K^+ within the electrolyte. Understanding the liquid-phase electrochemical reactions for Na–S and K–S, as well as contrasting them to what is known for Li–S, represents another interesting area for future research. To date much less is known about the soluble sodium polysulfides (NaPSs) and potassium polysulfides (KPSs) than their lithium counterparts. For instance, side-to-side analyses of identical cathodes tested against the three metals would identify the degree to which KPSs, NaPSs, and LiPSs dissolve, reversibly shuttle, and irreversibly react with the anodes. Both the redox and the transport behaviors of soluble NaPSs and KPSs in various ether and ester electrolytes need to be further understood. Moreover, in-depth analysis is needed

https://doi.org/10.1021/acs.chemrev.1c00838
Chem. Rev. 2022, 122, 8053–8125

for the reversible and irreversible reactions of KPSs, NaPSs, and LiPSs (although more is known) with the metal anodes at different states of charge, cycling conditions, rates, temperatures, *etc.*

During the charging process of the Li−S system, a prominent plateau appearing at 2.2−2.4 V corresponds to a relatively facile transformation of Li_2S back to S. In the K−S and Na−S systems, the concentration and activation polarization effects result in the charging plateau being less distinct, being more sloping, and having a relatively larger hysteresis versus discharge. The larger hysteresis would be a significant problem for commercial applications, since heat would be generated. An underappreciated source increasing overpotentials during both charge and discharge is the thicker and less stable SEI layer formed below ∼1 V on both the S cathode and the K and Na metal anodes versus their S−Li counterpart. Thus, with K and Na salts and with K and Na metal anodes, the SEI layer is known to be significantly less stable than with Li salts and Li metal.[12,42,43] A relatively thicker SEI layer, both initially and with extended cycling, will raise the cell impedance, leading to increased polarization during charge and discharge.[51,52] The role of anode SEI-related impedance in establishing the voltage profiles of K−S, Na−S, and Li−S cells has received only limited consideration. It should also be pointed out that cycling-induced SEI thickening is not necessarily uniform; in fact, it is likely heterogeneous across the electrode surface. The SEI is a micro- and nanoscale composite based on various organic and inorganic phases. Electroanalytical techniques such as impedance spectroscopy and overpotential analysis are able to indirectly evaluate SEI growth. Analytical methods such as sputter-down X-ray photoelectron spectroscopy (XPS) and time of flight secondary mass ion spectroscopy (TOF-SIMS) are able to resolve global variations in SEI structure normal to the electrode surface. However, it is the in-plane variations in the SEI thickness and structure that are perhaps the most meaningful for initiating electrochemical instabilities, such as growth of dendrites. Those may be tracked by site-specific methods such as cryo-stage focused ion beam (FIB) and transmission electron microscopy (TEM). Linking the local SEI structure with the electrochemical performance of full metal−sulfur batteries therefore represents an exciting emerging research topic and will be discussed further in this review.

Figure 1b displays a representative voltage profile of a room temperature Na−S cell in an ether-based electrolyte.[10] The authors identified the reaction intermediates using XPS and UV/vis absorption spectroscopy. They correspondingly proposed the following four continuous stages during the discharge process: (i) cyclo-S_8 first undergoes a solid−liquid phase transition to long-chain Na_2S_8, corresponding to the upper discharge plateau at around 2.2 V; (ii) the consequent transformation from long-chain Na_2S_8 to short-chain Na_2S_4 features the sloping region in the voltage range 2.20−1.65 V; (iii) the lower plateau at approximately 1.65−1.6 V reflects a liquid−solid reaction from soluble Na_2S_4 to insoluble Na_2S_2 or Na_2S; (iv) the solid−solid transition between Na_2S_2 and end-discharge product Na_2S proceeds in the last sloping potential, ranging from 1.6 to 1.2 V. Most discharge capacity is contributed by the sloping regions of the curve. For the charging process, the lower-order sodium sulfides (Na_2S_n, $1 \leq n \leq 2$) undergo the two-step conversion to higher-order sodium polysulfides (Na_2S_n, $4 \leq n \leq 8$) and finally back to elemental sulfur (S_8).

As Table 2 summarizes, the equilibrium K−S phase diagram shows that a series of stable phases of K_2S_n (n = 1, 2, 3, 4, 5, and 6) can form at room temperature.[38] As compared to Li−S (Li_2S serves as the only equilibrium phase) and Na−S (Na_2S_n, n = 1, 2, 4, and 5; stoichiometric Na_2S_3 is actually a mixture of equal amounts of Na_2S_2 and Na_2S_4), the phase transition in K−S is much more complicated and less understood.[12] In principle, each phase transition step between K_2S_n and K_2S_{n+1} will yield its own plateau. In conjunction with the more sluggish reaction kinetics and possibly lower solid-state potassium ion diffusivity, such series of "miniplateaus" would merge together into a single sloping capacitor-like profile, both during discharge and during charge. Most of these equilibrium phases have not been reported, and it is not known whether this is a thermodynamic or a kinetic limitation. An early version of a room temperature K−S cell was based on a cathode of sulfur impregnated into mesoporous CMK-3 carbon, a K metal anode, and 1 M $KClO_4$ in tetraethylene glycol dimethyl ether (TEGDME) as the electrolyte.[47] Figure 1c shows the corresponding sloping voltage profiles at cycles 1, 5, and 20. The discharge platform at 1.8 V corresponds to the transition from high-chain polysulfides to insoluble K_2S_3 phase, which was determined as the potassiation product by diffraction data. The K_2S_3 phase being the terminal discharge product has been reported by several groups (Table 3),[66,71] although it is not yet known whether the inability to form K_2S is a thermodynamic or a kinetic limitation. One explanation may be the severity of the potassiation-induced volume expansion, with the associated stress creating a nucleation barrier that is insurmountable at room temperature.[12] Stronger cation−anion electrostatic interaction between K^+ and S_4^{2-}/S_3^{2-}, owing to weaker K^+ solvation energy, would be another explanation the impediment of the K_2S_2 to K_2S solid-state phase transformation.[39]

The metastable allotropes of small sulfur molecules (S_{2-4}) either confined in carbon nanopores or covalently bonded to carbon could undergo a deep reduction beyond K_2S_3 even reaching K_2S,[50,70,72] indicating the higher intrinsic reactivity versus the cyclo-S_8. These results point to the reaction being thermodynamically feasible but kinetically limited, and hence being improvable with advanced separators. For example, Yu et al. reported enhanced cyclo-S_8 utilization when employing a single wall carbon nanotube (SWCNT)-functionalized separator, exceeding the theoretical capacity of K_2S_2 and approaching K_2S.[73] It is not obvious how (or why) the initial structure would influence the K_2S_3 to K_2S solid−solid transformation, since nominally S is fully reacted to K_2S_3 regardless of its initial state in the electrode. Understanding the relationship between the initial structure and the bonding state of the sulfur molecules within a given carbon host and the terminal potassiation products represents an interesting future research direction. Since carbon hosts can be relatively pure or heteroatom-rich, the sulfur molecules will possess a different degree of chemical interaction with the host walls. This may have a significant influence on both the intermediate and the terminal potassiation products and should be explored further.

Carbonate-based electrolytes are less employed in alkali metal−sulfur batteries than ether-based ones, as carbonate-type solvent molecules are more apt to suffer from nucleophilic attack by the dissociated long-chain polysulfide anions.[74] Such parasitic reactions result in rapid cell failure due to

https://doi.org/10.1021/acs.chemrev.1c00838
Chem. Rev. 2022, 122, 8053−8125

uncontrolled dissolution of the polysulfides. Per Table 3, to enable the utilization of carbonate-based electrolytes and take the battery architecture closer to the current commercial embodiments, the metastable allotropes of small sulfur molecules (S_{2-4}) are impregnated into the micropores ($D \leq$ 0.7 nm) of carbon hosts.[48,49,75−79] Alternatively, the S is covalently bonded to the carbon skeleton, virtually eliminating all dissolution. In the case of small S molecules in micropores, polysulfides are generated but remain trapped inside the pores. In the case of covalently bonded S (Table 3), liquid polysulfide formation is eliminated altogether along with the associated high-voltage portion of the discharge−charge plateaus, leading to a reduction in the reversible capacity, the cell voltage, and the cell energy. One classic example of such an approach is a sulfurized pyrolyzed poly(acrylonitrile) (S@pPAN) cathode, where the covalently bonded sulfur undergoes direct solid−solid conversion in ester-based electrolytes (Table 3).[80−83] Other examples of covalently bonded S systems include thioether-bond-functionalized carbon,[84] sulfurized carbon,[65] and so on,[85] all having analogous augmented voltage-capacity profiles. Parts d−f of Figure 1 represent the typical voltage profiles of small molecular sulfur allotropes in Li−S, Na−S, and K−S systems.[48−50] After an initial activation process, all the S_{2-4} to S^{2-} conversion reactions feature sloping curves with lower average redox voltages than the analogous S_8 to S^{2-} conversion reactions. This indicates a lowering of the cell energy as well, which is compounded by the difficulty of achieving greater than 50 wt %S inside a primarily microporous carbon host.[48,49,70,86]

Recently, the nucleophilic reactions between polysulfides and carbonate solvents in Na−S batteries were revealed to be less severe than those in Li−S batteries.[87] It was argued that the larger ionic radius of Na ions with lower solvation energy than that of Li ions contributed to the lower dissociation degree of Na^+−polysulfide$^-$ ion pairs.[88,89] Consequently the parasitic reactions between sodium polysulfide anions and carbonate solvents were more limited. With sodium, cyclo-S_8-based cathode architectures where sulfur is confined in mesoporous/microporous hosts or chemically interacts with polar hosts (*e.g.*, TiO_2, Mxene, or MOFs) have been shown to be compatible with the conventional carbonate solvents (*e.g.*, ethylene carbonate (EC), propylene carbonate (PC), and diethyl carbonate (DEC)), per Table 3.[62,63,90−92] Compared with ether solvents, carbonate solvents possess lower solubility for Na polysulfides, which can be further reduced through addition of fluoroethylene carbonate (FEC).[87] In such carbonate electrolytes, cyclo-S_8-based cathode architectures deliver the sloping voltage curves after initial activation. The lower average redox voltages indicate a possible quasi-solid-phase transformation mechanism,[64,93] although more work is needed to fully understand the reaction sequence. By analogy, K ions with the largest ionic radius of the three should possess the lowest solvation energies, as well as the least nucleophilic reactions between potassium polysulfides with carbonate solvents.[39] Yin et al. recently cycled cyclo-S_8 in a carbonate electrolyte (KPF_6 in EC/DEC), obtaining a retained capacity of 355 mAh g^{-1} at 150 cycles.[68] This was achieved by utilizing a metal−organic framework (MOF)-derived nitrogen doped cobalt nanocluster inlaid porous carbon as a sulfur host. The reaction sequence was reported as $S_8 \Rightarrow K_2S_6 \Rightarrow K_2S_5 \Rightarrow K_2S_4 \Rightarrow K_2S_3$. In general, more analytical and simulation work is required to fully understand the reaction sequence in both the Na−S and the K−S systems, especially as a function of host structure (microporous, mesoporous, and pore-free) and host chemistry (inert surface, polar surface, and covalent bonding).

3. POLYSULFIDE (PS) SHUTTLE AND SLUGGISH REACTION KINETICS IN METAL−SULFUR BATTERIES

Control of polysulfides is essential for metal−sulfur battery performance.[94] Studies have been widely conducted to investigate the properties of polysulfides and their corresponding influence on the cell redox processes. Characterization techniques including X-band ESR spectra, *in situ* UV−vis spectroscopy, and *in situ* X-ray absorption near edge structure (XANES) have identified polysulfide anions with varied sulfur atom numbers, such as S_8^{2-}, S_6^{2-}, S_4^{2-}, and S_2^{2-} dianions and the $S_3^{\bullet-}$ radical monoanion.[74,94−100] Due to their similar free energies, PS anions may coexist with each other in disproportionation equilibrium (*e.g.* $S_8^{2-} \leftrightarrow S_6^{2-} + {}^1/_4S_8$) and/or chain-breaking equilibrium (*e.g.* $S_6^{2-} \leftrightarrow 2S_3^{\bullet-}$).[95,100] The state of the PS species shows a strong dependence on the electrolyte solvent. For instance, electron pair donor solvents such as DMSO, DMA, and DMF are observed to stabilize the $S_3^{\bullet-}$ radical in the Li−S cell.[100] By contrast, with glyme-based electrolytes with low donor number such as DME and dioxolane (DOL), the $S_3^{\bullet-}$ radical is barely detectable.[100] The stabilization of the $S_3^{\bullet-}$ radical can provide additional chemical pathways through which the energy barrier of S redox is reduced.[61,99] In addition to the solvent, other factors such as the electrolyte salt, polysulfide chain length, and alkali ionic radius also play significant roles, affecting the corresponding solvation energy, dissociation/dissolubility, and redox kinetics of the PS species.[39,94] Steudel et al. reviewed the polysulfide dianions and related radical monoanions [$S_n^{\bullet-}$] evolved in the alkali metal−sulfur batteries in detail; readers are referred to that article for further discussion.[98]

In ether-based electrolytes, the intermediate high-order polysulfide species formed Li_2S_x ($4 \leq x \leq 8$) are highly soluble.[101] The soluble polysulfides species can function as redox mediators, exposing and activating the inner parts of the sulfur particles (*i.e.*, $S_8 + S_4^{2-} \rightarrow S_6^{2-}$) upon discharge or catalyzing the oxidation of insoluble sulfides upon charge (*i.e.*, $Li_2S + S_6^{2-} \rightarrow S_4^{2-}$).[9,102] Due to the high solubility and mobility of polysulfide species, the intermediate redox species (*i.e.*, S_8^{2-} and S_6^{2-}) formed upon discharge can diffuse out of the cathode and migrate toward the anode. This process occurs spontaneously, being driven by the chemical concentration gradient within the electrolyte. A confining host such as carbon micropores or a barrier layer such as a functional separator can physically and/or chemically block this process, however. The polysulfides may electrochemically react at the metallic anode surface, forming insoluble low-order sulfides that passivate the electrode.[103] Upon charging, the reduction of polysulfides can occur via two paths: $(n-2)Li_2S_n + 4Li \rightarrow nLi_2S_{n-2}$ versus $(n-2)Li_2S_n + 4Li^+ + 4e^- \rightarrow nLi_2S_{n-2}$.[104] The former does not require external source electrons, meaning that the metal ion corrodes at open circuit regardless of the state of charge. The reaction involving external electrons is reversed upon cell discharge, causing insoluble low-order sulfides to be transformed back to soluble sulfides, once again going into solution. This process does not result in charge storage but is instead parasitic, resulting in Coulombic efficiency and capacity loss that can be severe. It is not obvious that the above corrosion reaction is reversible under normal cycling conditions. It may be seen as the origin of the insulating passivation layer that

https://doi.org/10.1021/acs.chemrev.1c00838
Chem. Rev. 2022, 122, 8053−8125

forms on the anode after multiple cycles. Therefore, the role of polysulfide crossover is deleterious in two ways: the irreversible corrosion products on the anode will passivate it, while the reversible products will create ongoing parasitic reactions. While both affects are well recognized in Li−S literature, it would be highly beneficial to identify and further understand the extent of anode passivation for Na−S, as well as for the even less explored K−S. What is the extent of irreversible corrosion reactions, considering that Na and K are significantly more reactive than Li in all organic electrolytes? Moreover, what is the role of anode corrosion in the overall health of the cell during cycling? Could the impedance and overpotential rise associated with the passivating sulfide layers be deconvoluted from the rise due to other deleterious effects, such as cathode degradation?

Mikhaylik and Akridge proposed a mathematical expression to evaluate the degree of shuttle behavior in the Li−S system.[101] The charge shuttle factor (f_c) is expressed as $f_c = \frac{k_s q_H [S_{total}]}{I_c}$, where I_c, q_H, $[S_{total}]$, and k_s represent the charge current, specific capacity of sulfur contributed by the upper plateau (a constant value of 418 mAh g^{-1}), total sulfur concentration, and shuttle constant, respectively. Figure 2a represents the simulated charge profiles at different charge shuttle factors (f_c). When the charge current is high enough or the shuttle constant is low, f_c approaches zero and the cell can be charged completely, showing a sharp voltage increase and negligible shuttle effect. At $f_c > 1$, the cell shows an extensive voltage leveling representing an overcharge process. In principle, during cell cycling the parasitic shuttle process can proceed indefinitely. The process would involve concurrent polysulfide migration within the electrolyte, sulfur species redox processes at both electrodes, and reversible corrosion of the metal anode.[105]

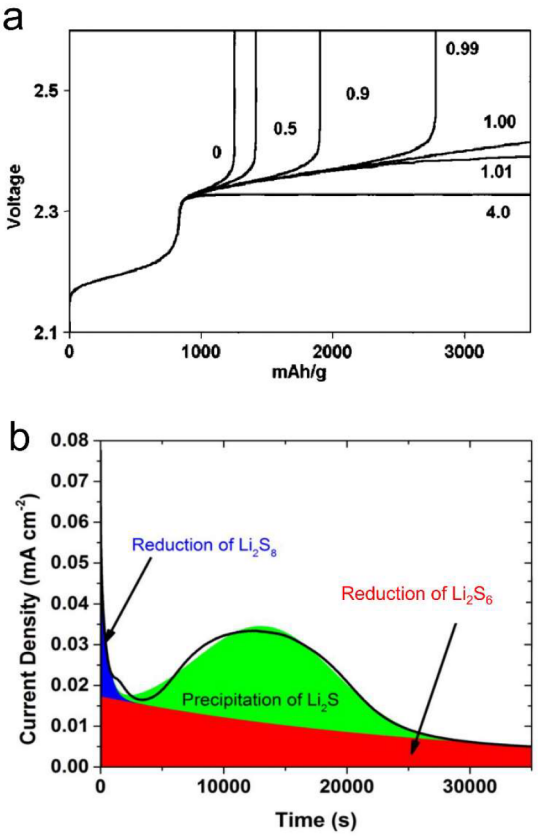

Figure 2. (a) Simulated charge profiles at different charge shuttle factors (f_c) = $k_s q_H [S_{total}]/I_c$. (b) Fitting of current versus time curve for the Li_2S deposition experiment. The curve (actual data in black) was fitted as the sum of two exponential functions, representing the reduction of Li_2S_8 and Li_2S_6 (blue and red, respectively), and a peak resulting from the electrodeposition of Li_2S. Panel a is reproduced with permission from ref 101. Copyright 2004 The Electrochemical Society. Panel b is reproduced with permission from ref 106. Copyright 2015 John Wiley & Sons, Inc.

The solubility of polysulfide species varies with salt types and solvents, resulting in significant differences in the severity of the shuttle.[74,107] The solubility for Na-based salts is substantially higher than that for Li counterparts. For example, Guo et al. reported that tetraethylene glycol dimethyl ether could dissolve about 0.18 M Li_2S_8 (equivalent to 1.44 M sulfur) at room temperature.[40] Ahn et al. reported a Na_2S_8 solubility of 1.32 M (equivalent to 10.56 M sulfur) in the same solvent.[41] This indicates that in ether-based electrolytes the detrimental shuttle effect for dissolved NaPSs may be substantially more severe than for LiPSs. This is at least part of the explanation regarding why Na−S cells generally cycle worse than Li−S cells. Lu et al. applied a rotating-ring-disk electrode to investigate the diffusion processes of the polysulfide in dimethyl sulfoxide (DMSO) model solvent.[39] With the decreasing solvation energy from Li^+ to K^+ and the decreasing size of the solvent−ion complex from Li^+-$(DMSO)_n$ to K^+-$(DMSO)_n$, the diffusion coefficients of the polysulfides oppositely increased (Table 2). The results helped to predict that the most extensive polysulfide shuttle effect occurs in K−S cells versus in Li−S and Na−S.

The polysulfide shuttle effect has been shown to operate in an ongoing manner during discharging and charging of Li−S.[108] It results in a series of issues including low CE and capacity loss during cycling, loss of active S in the cathode, and self-discharge at static conditions. Polysulfide crossover to the anode also leads to irreversible corrosion reactions of the metal surface and the associated formation of a lithium−sulfur passivation layer. Noked et al. investigated the reversibility of the lithium predeposited on copper, in the presence of Li_2S_8.[103] Even at a low polysulfide concentration of 0.04 M, the reversible stripping and plating of Li was obstructed. With the addition of 0.2 M Li_2S_8 into the ether electrolyte, the capacity retention dropped from 95% to 69% after 10 cycles. Mosslike deposits with the chemical composition of Li_xS_y were discernible on the anode copper collector surface. These passivating layers formed on the anode surface markedly increased the cell impedance, pointing to another source of failure due to PS dissolution into the electrolyte. The additive $LiNO_3$ has been widely employed as an electrolyte additive for Li−S cells. The compound forms Li_xNO_y and insoluble Li_xSO_y layers, which inhibit the reactions between lithium metal and sulfur species.[109,110] By analogy, $NaNO_3$ additives are also utilized for Na−S cells.[10,59,111] However, results by Kaskel et al. demonstrate that after about 20 cycles, the $NaNO_3$ additive is no longer effective.[112] The rapid consumption of nitrate ions during cycling is the likely explanation, in turn due to a combination of the higher solubility of NaPSs and the greater reactivity of the sodium metal anode *vs* lithium in comparable solvent−electrolyte combinations.[43]

Metal−sulfur cells are also plagued by a general sluggishness of the redox kinetics. Elemental sulfur and the discharge products are electrical insulators, as well as poor conductors of

https://doi.org/10.1021/acs.chemrev.1c00838
Chem. Rev. 2022, 122, 8053−8125

alkali ions. For example, σ_e= ~10^{-30} and ~10^{-13} S cm^{-1} for S and Li_2S, respectively. The high electronic and ionic resistances of the reactants render the cells with high polarization and prevent the redox reactions from running to completion without the addition of a large volume fraction of secondary conductive phase (typically carbon) and nanostructuring of the sulfur. As per the typical galvanostatic profile of the Li-cyclo-S_8 system (Figure 1a), the dip emerging at the beginning of the lower discharge plateau represents the necessary overpotential for initiating the nucleation process of solid Li_2S from liquid LiPSs.

To quantitatively evaluate the kinetics of Li_2S nucleation from LiPSs, authors performed the following the following experiment:[106] A Li−Li_2S_8 cell was galvanostatically discharged to a voltage of 2.06 V; the voltage was then kept at 2.05 V until the current dropped below a certain value. Per Figure 2b, the time dependence of the cathodic current features a characteristic curve with monotonically decreasing current followed by a current peak, the peak representing the nucleation and growth processes of Li_2S on the heterostructure surface. Electroanalytical kinetic analysis in combination with phase transformation theory revealed a 2D island nucleation model, with growth occurring at the three-phase boundary between the Li_2S islands, the conductive substrate, and the electrolyte.[106] It is known that the nucleation rate of Li_2S on a "routine" conductive surface is limited, contributing to the overall kinetic impediment of the system.[113] Upon charge, there is a large energy barrier and associated sluggish kinetics for Li_2S dissolution. This impediment combined with the slow ionic diffusivity and high electrical resistance of Li_2S/Li_2S_2 obstructs the complete conversion of the discharge products back to S_8.[114] With cycling, the nonconductive Li_2S_2/Li_2S particles accumulate at the cathode, gradually thickening and reducing the migration of Li ion through the interface. This in consequence hampers deeper discharge or charge in the batteries and thus results in a rapid capacity fade.

In practice, Na−S and K−S systems consistently display much larger charge−discharge hysteresis and lower practical capacity.[12,115] Most reported Na−S batteries in the literature show capacities below 1000 mAh g^{-1}, and the values are even less in K−S batteries. The kinetics in Na−S and K−S systems are more sluggish as compared to Li−S, which originates from multiple deficiencies. One is the strain effect, since the S species is not free-standing but rather contained within the pores of a relatively rigid host. The formation of Na_2S and K_2S is associated with 171% and 296% expansion, while with Li_2S this value is 80%. Other impediments are the solid-state diffusivity of Na and K ions. Table 1 shows the Li/Na/K ion diffusivities from a number of reports, obtained through diverse experimental techniques. In a broad range of electrode materials including hard carbon,[21,22,116] black phosphorus/graphite composite,[24] and tellurene,[23] Na and K ions show lower solid-state diffusivities. The low solid-state diffusivity of Na^+/K^+ in the carbon host and within the Na_2S_x/K_2S_x compounds will account for the kinetics' sluggishness. Another issue already discussed is the greater reactivity of the metal anodes and the associated SEI structure, as well as any Na and K corrosion products on the metal surface.

The K−S system has been particularly challenged in achieving rapid redox kinetics. A number of innovative strategies, including employing highly concentrated electrolytes, sulfurized polyacrylonitrile, microporous carbon confining small metastable sulfur allotropes (S_{2-4}), and so on, have not yielded "Li-like" rate capability (Table 3). Despite the challenging nature of K, consistent advances in both rate capability and cycling life are being achieved.[47,68] It is expected that with improved potassium-specific electrolyte formulations, the performance of K−S batteries will improve further.[66] Wu et al. applied a potassiated Nafion film (Nafion-K^+) as the cationic selective interlayer to suppress a polysulfide shuttle in a K−S cell.[71] Without this layer, the KPSs would diffuse across the bare Celgard separator and migrate to the K anode, leading to reversible parasitic reactions and irreversible anode corrosion. With the potassiated Nafion film the K metal anode remained shiny when extracted from the cell, indicating suppressed crossover. Despite this, the cell still suffered from substantial capacity decay, with 184 mAh g^{-1} remaining after 5 cycles. Their electroanalytical investigation revealed sluggish reduction reaction kinetics for the solid-phase K_2S_3 ($2K_2S_3 + 2e^- + 2K^+ \rightarrow 3K_2S_2$) and K_2S_2 ($K_2S_2 + 2e^- + 2K^+ \rightarrow 2K_2S$), with the overpotentials being as high as 0.8 V. Furthermore, the reaction pathway for charging K−S materials was found to be asymmetric with the discharge process. Upon charging, short-chain polysulfides (K_2S_{2-3}) would undergo a disproportionation reaction to produce K_2S and soluble S_4^{2-}. The short-chain K_2S_{1-3} was reduced by high-order S_6^{2-} intermediates to the more soluble form S_4^{2-}. Finally, the S_4^{2-} is electrochemically oxidized back to high-order polysulfides and sulfur. A portion of K_2S without the direct contact with electrolyte would become "dead sulfide" and not contribute to reversible capacities. In this way, the accessible pathway to soluble high-order S_4^{2-} intermediates was interrupted.

Lu et al.'s experimental and modeling results showed that the larger cation radius of K^+ contributed to the corresponding weaker solvation energy as compared to Li^+ and Na^+ and consequent stronger electrostatic interaction with S_4^{2-}/S_3^{2-}.[39] This helps to explain the strongly stabilized discharge products (*i.e.*, K_2S_3). Overall, much less is known about the intermediate redox sequence and the kinetic limitation with K−S and Na−S. This is summarized in Table 4, where Li−S is used as the baseline reference. Along those lines, studies that combine in-depth analytical methods with simulation are welcome. The Li−S system may be used as a convenient template for carrying out such work, since there is a long and established history of polysulfide analysis based on a number of experimental techniques and modeling methods such as Raman, X-ray diffraction (XRD), transmission X-ray microscopy, UV−vis spectroscopy, high-performance liquid chromatography, equivalent series resistance, and XANES.[45] Understanding the polysulfide sequence and exploring polysulfide adsorbents/electrocatalysts represent important steps in designing the next generation of separators to prevent species crossover, kinetically accelerate the terminal solid-phase formation upon discharge and S formation upon charge, promote uniform ionic flux, *etc.* These aspects will be discussed in detail in the subsequent sections of this review.

Considerable efforts have been devoted to enhancing sulfur-based cathode performance, including host engineering, electrolyte tailoring, binder functionalization, and separator modification. The core design principles of these strategies are to accelerate the sulfur redox kinetics and to suppress the migration of soluble polysulfide intermediates during cycling. In this review we closely examine functional separators and interlayers as a method for achieving one or both aims. For example, separators modified with the anionic groups such as SO_3^-, COO^-, and CO^- can block polysulfide migration

https://doi.org/10.1021/acs.chemrev.1c00838
Chem. Rev. 2022, 122, 8053−8125

Table 4. Research Progress Comparison of Li−S, Na−S, and K−S Systems, in Terms of Fundamental Reaction Chemistry, Polysulfide Properties, Electrocatalyst Exploration, and Cell Configuration

Research	Li−S	Na−S	K−S
Electrochemical reaction mechanisms	▲ Li−S redox chemistry has been well understood. ▲ Cells perform well-defined galvanostatic two-phase plateaus.	▲ In ether-based electrolytes, S performs an analogous reaction pathway to Li−S. ▲ In carbonate-based electrolytes, S transformation mechanism still remains ambiguous. ▲ Two-phase plateau is less distinct in galvanostatic profile.	▲ Complicated reaction mechanism. ▲ Poor understanding regarding kinetics/thermal limitations. ▲ K−S cells show less well-defined galvanostatic profiles, along with complex and successive phase transition between K_2S_n and K_2S_{n+1}.
Polysulfide properties	▲ LiPSs have been widely explored using first-principles calculations coupled with *in operando* testing. ▲ Various strategies have been developed to suppress shuttle effects, from aspects of host materials, separators, electrolytes, *etc.*	▲ *In situ* XRD or Raman spectroscopy is employed for identifying polysulfide intermediates. ▲ Emerging polysulfide adsorbents and electrocatalysts have been explored. ▲ NaPSs is more soluble in ether electrolytes than LiPSs yet suffers from less severe parasitic reactions with carbonate electrolytes.	▲ Scant exploration and understanding about the roles of K_2S_n. ▲ Carbon-based hosts show insufficient sulfur utilization. ▲ K−S cells delivered inferior Coulombic efficiencies.
Electrocatalyst exploration	▲ A broad range of sulfur redox mediators and corresponding catalytic mechanisms have been in-depth investigated.	▲ Increasing exploration of sulfiphilic electrocatalysts in ether- or carbonate-based electrolytes.	▲ There are a few reports of active electrocatalysts for expediating K−S redox.
Cell configurations	▲ Advanced configurations (*i.e.*, "Li-free anode" cell architectures) have been reported. ▲ Li−S cell is being explored targeting high-energy devices (high S loading, low E/S ratio).	▲ Na−S cell is still being explored in laboratory scale (low S loading, high E/S ratio).	▲ K−S cell is still being explored in laboratory scale. ▲ "Flooded" electrolyte is commonly employed.

through a distinct electrostatic repulsion mechanism while improving the cation diffusion kinetics in the electrolyte.[117−120] While it is possible to incorporate enhanced functionality directly into the cathode architectures, studies have demonstrated that employing a coated separator for this purpose can be more effective.[121,122] A key advantage that the incorporation of electrically conductive electrocatalytic phases gives to a separator is that it effectively functions as a secondary current collector that is in direct contact with the active materials in the cathode. During charging, an electrically conductive and electrocatalytic surface is especially important since Li_2S, Na_2S, and K_2S are electrically insulating. Because of the functional separator's location within the cell, the electrocatalytic phases are "first in line" at the reaction front and, hence, less limited by diffusional limitations. One potentially interesting and unexplored approach toward next-generation separators is to design three-dimensional interdigitated architectures, where the functional electrocatalytic phase extends from the separator into the bulk of the cathode, increasing the total number of electroactive sites and further reducing the diffusion distances.

4. METAL−SELENIUM BATTERIES AND CHALLENGES

Selenium reacts with alkali metals through a conversion-type reaction: $2M^+ + Se + 2e^- \leftrightarrow M_2Se$, M = Li, Na, and K.[13−15,123−126] Akin to sulfur, the intermediate reaction pathway of Se is associated with electrolytes, the host's porous structure, the Se chain length, and the alkali metal type.[127−133] In carbonate-based electrolytes, selenium and polyselenides (PSes) show relatively low solubility.[134] Amine and co-workers initially reported a Se/multiwalled carbon nanotubes (MWCNTs) composite as the cathode for LMBs and demonstrated the single-phase transformation of Se species in carbonate electrolyte (1.2 M $LiPF_6$ in EC/ethyl methyl carbonate (EMC)).[135] Our group reported selenium impregnated monolithic carbon as free-standing cathodes for lithium and sodium metal batteries, where Se was amorphous and was comprised of disordered short chains.[13] The carbon host was primarily composed of small mesopores and was effective in confining the sodium (NaPSes) and lithium (LiPSes) polyselenides during extended cycling. For the Li−Se system there are relatively flat discharge and charge plateaus at ≈1.8 and ≈1.9 V, respectively. The Na−Se system displays sloping plateaus. Based on solid-state nuclear magnetic resonance spectroscopy (SSNMR) results combined with high-resolution transmission electron microscopy (HRTEM), the following reaction sequence was established for sodiation of selenium (Se) encapsulated in a nanoporous carbon host:[128] SSNMR demonstrated that during the first sodiation, the Se chains were progressively cut to form an amorphous mixture of polyselenides of varying lengths. There was no evidence for discrete phase transitions during sodiation. The Se nearest the carbon pore surface was sodiated first, leading to the formation of a core−shell composition profile. It was demonstrated that the vast majority of the pore confined Se was amorphous, but with the site-specific presence of nanocrystalline equilibrium Na_2Se_2 (hcp) and Na_2Se (fcc) near the carbon pore surfaces.

Nevertheless, the low solubility of PSes in carbonates does not fully eliminate the shuttle effect, and hosts that physically or chemically confine PSes are still necessary for extended cyclability.[136] Wang employed a nitrogen, sulfur dual-doped hierarchical porous carbon (NSHPC) as the Se host, cycling against Na in carbonate electrolyte.[17] The postcycled anode

https://doi.org/10.1021/acs.chemrev.1c00838
Chem. Rev. 2022, 122, 8053−8125

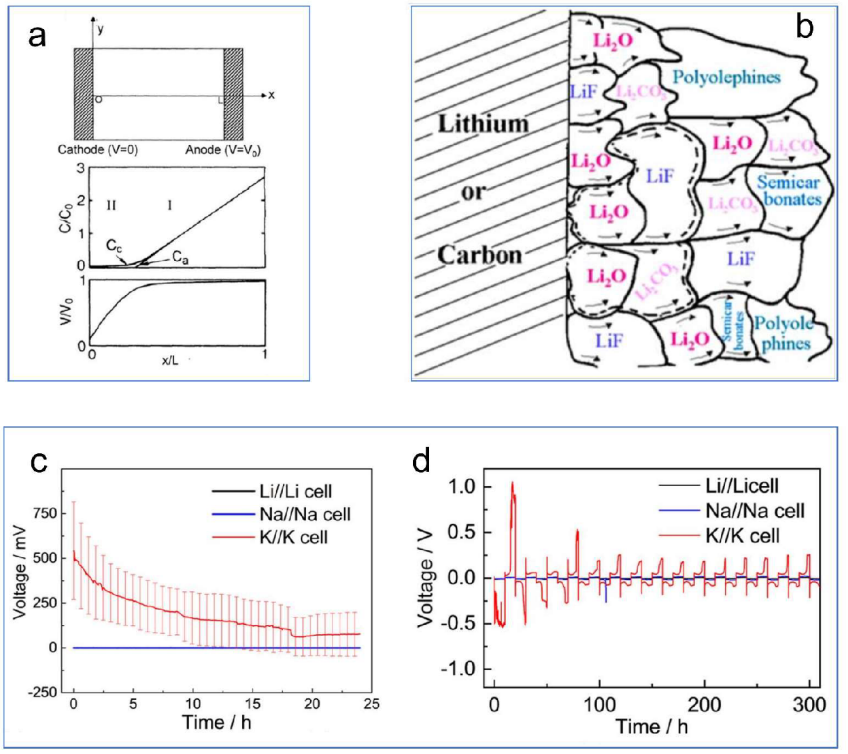

Figure 3. (a) Scheme of the cell (top); profiles of the ion concentrations and electrostatic potential based on theoretical simulation (bottom). (b) Mosaic model for the SEI on Li metal, showing the stable inorganic reduction products nearer the metal surface. Reproduced with permission from ref 148. Copyright 1997 The Electrochemical Society. (c) Open-circuit voltage (OCV) curves of two-electrode Li//Li, Na//Na, and K//K cells filled with 1.0 M $LiPF_6$/EC:DEC, 1.0 M $NaPF_6$/EC:DEC, and 0.8 M KPF_6/EC:DEC, respectively. (d) Voltage profiles of the symmetric cells during a continual plating−stripping process. Panel a is reproduced with permission from ref 145. Copyright 1990 American Physical Society. Panel b is reproduced with permission from ref 148. Copyright 1997 The Electrochemical Society. Panels c and d are reproduced with permission from ref 149. Copyright 2019 American Chemical Society.

showed rough surfaces with coarse Na_2Se agglomerates, indicating crossover of sodium polyselenides and their reduction on the metal surface. By coating a NSHPC/Se composite with interconnected polyaniline, the stability of Na−Se batteries was effectively promoted with 2.7% decay after 200 cycles. The polyaniline therefore appeared to be highly effective in blocking NaPSes' dissolution, representing an exciting secondary treatment of the electrode that can overcome the limitations of a nonideal host. The approach of secondary electrode coatings has the potential to be extremely useful since it may allow for stable cycling of Se that is infiltrated into large pores or potentially not infiltrated at all. As was discussed previously, a key downside to using micropore and small mesopore hosts is the relatively low mass loading that can be achieved, typically in the 50% range. Conversely, with large mesopores or even macropores much higher mass loadings are possible, with the secondary coating treatment being applied after infiltration. Creating Se cathode architectures based on large pore hosts but with secondary electrode coatings that will confine LiPSes, NaPSes, and potassium selenides (KPSes) represents a highly fruitful future research direction.

In ether-based electrolytes, the redox transformation of Se is analogous to S, with involvement of high-order polyselenides.[16,130] Taking the Li−Se system as an example, Se is first reduced to Li_2Se_n ($n \geq 4$) and then to Li_2Se_2/Li_2Se, featuring two plateaus at 2.1 and 1.9 V, respectively. During the charge process, Li_2Se is reversibly oxidized to Li_2Se_n ($n \geq 4$) and eventually back to Se. As PSes could easily dissolve in the ether electrolytes, there are more issues with crossover and shuttle and the associated cycling problems. Various porous carbon hosts have been dedicated to address the above issues by confining PSes inside the micropores and small mesopores, although with varying levels of effectiveness.[127,128,137] Moreover, dissolution, crossover, and shuttle have been mitigated through functional separators, as well as novel electrolyte and cell configurations.[16,136,138,139] Clearly, more research on both topics is welcome, with the learning obtained with the Li−S system being potentially transferable to the selenium systems.

5. DENDRITE GROWTH AND UNSTABLE SOLID ELECTROLYTE INTERPHASE (SEI)

A critical limitation of Li, Na, and K metal anodes is the formation and growth of metal dendrites, accompanied and in part caused by an unstable SEI.[140,141] Even prior to potentially catastrophic electrical shorting, dendrite growth will lead to low Coulombic efficiency and electrolyte consumption due to an unstable SEI and "dead metal" formation.[142,143] To compensate for corresponding losses caused by anode degradation, laboratory button cells typically employ an excess of metal and electrolyte, while having a low mass loading on the cathode so as to ensure a fairly shallow plating/striping regiment. While this approach is reasonable for fundamental studies, the achieved performance cannot be extrapolated to commercially representative pouch cells with less electrolyte and a higher cathode/anode mass ratio. Moreover, the gas generation−swelling concern also associated with SEI growth is masked by the rigid 2032-type stainless steel button cell. For

https://doi.org/10.1021/acs.chemrev.1c00838
Chem. Rev. 2022, 122, 8053−8125

near-commercial applications the negative/positive (N/P) areal capacity ratio approaches 1.[7,8] More studies with such N/P ratios are necessary and may yield very different performance results than with the less aggressive ratios. Moreover, more work is needed for the most aggressive case of all, which is the anode-free configuration where in effect the negative electrode is a bare current collector and all the Li, Na, and K is stored in the cathode. This is also the optimum configuration in terms of safety since the cell then is fabricated and stored in its discharged state. Without excess anode to artificially inflate cyclability, the electrochemical performance of anode-free full cells is limited almost entirely by the efficiency of lithium plating and stripping. In this case, the associated anode volume change would be infinite at every cycle. A stable SEI layer is therefore requisite for stabilizing anode deposition and reducing electrolyte decomposition. Otherwise, the ongoing electrolyte decomposition and SEI formation will result in quick depletion of the anode inventory in the cell. A representative anode-free Li−S full cell pairing a bare current collector on the anode side with the Li_2S cathode has recently been investigated.[8] To date there are far fewer analogous electrochemical configurations on the Na−S or K−S system, an area that is promising for exploration.

Several models have been proposed to explain dendrite growth from different aspects. Dendrite growth is considered self-enhancing. Monroe and Newman revealed the intensified electric field at Li dendrite tips, enabling the dendrites to preferentially grow along the protrusion direction by the so-called tip effect.[144] The space-charge model proposed by Chazalviel is widely accepted for describing the Li dendrite formation.[145] Per Figure 3a, the anion depletion in the vicinity of the electrode surface results in a large space-charge region, especially at high current density. The localized electric field in this region ramifies the growth of metallic Li electrodeposits. Such a timeline representing Li dendrite nucleation is called the Sand's time (τ) and calculated by

$$\tau = \pi D\left(\frac{zcF}{2Jt_a}\right)^2 \tag{1}$$

$$t_a = 1 - t_{Li^+} = \frac{\mu_a}{\mu_a + \mu_{Li^+}} \tag{2}$$

where D, z, c, F, J, and t_a correspond to the ambipolar diffusion coefficient, the valency, the salt concentration, Faraday's constant, the current density, and the transference number of anions. t_a relates to the transference number of Li^+ (t_{Li^+}) in the form of eq 2, where μ_a and μ_{Li^+} represent the mobilities of anions and Li^+, respectively. The equations afford a conceptual guide to delaying the emergence of metal dendrites, such as by dissipating the effective current density (J) with a high-specific-area conducting scaffold. The model represents an association between the local electric field at the metal−electrolyte interface and the concentration polarization of plating metal cations in bulk electrolyte. The above equations disclose that increasing the cation conductivity in the electrolyte and the transference number will postpone dendrite formation.[146,147]

As will be discussed, commercial polyolefin separators (polyethylene (PE), polypropylene (PP), *etc.*) will transmit solvated alkali ions toward the electrode in an inhomogeneous manner, due to nonuniformity of the porosity and nonideal electrolyte wetting. These heterogeneities of liquid-state ionic flux will in turn result in localized field effects in the vicinity of the metal anode. Thin foil metal anodes are fundamentally different in their geometry than powdered ion battery anodes based on graphite, *etc.* Due to the three-dimensional nature of the powdered electrodes, electrolyte wetting is enhanced, and the ion flux is homogenized. A planar metal foil with its surface area at least an order of magnitude lower than powder would be much more sensitive to wetting and ion flux nonuniformities.[150] With Na and K metal anodes, dendrites still persistently emerge at charging rates below the space-charge model predictions.[140] This is a known effect attributed to the unstable and nonuniform K- and Na-based SEI structure, especially in carbonate electrolytes. According to Table 1, K and Na ions possess faster liquid-state diffusivity than Li ions. This runs opposite to the Sand's time formulation, indicating that other factors (primarily the smaller SEI) drive dendrite emergence.

It is recognized that the structure and electrochemical stability of the SEI have key roles in determining the cycling stability of alkali metal anodes.[151−154] The SEI on the negative electrode's surface is a result of thermodynamically driven reduction of the electrolyte. The Li, Na, and K ions within the SEI are derived from solution cations as well as from the direct electrochemical/chemical corrosion of the metal anode.[155,156] Goodenough et al. put fourth now a classical thermodynamical theory for SEI formation:[157] In summary, when the lowest unoccupied molecular orbital (LUMO) of the anode lies above that of the electrolyte, electrons spontaneously transfer from the anode to the electrolyte, resulting in its reduction, *i.e.* the formation of the SEI. The SEI formation process is never ideally self-terminating, with potassium metal being more reactive than sodium, which is in turn more reactive than lithium in comparable electrolytes.[149,158] Figure 3b shows a classic Mosaic model employed to represent the SEI structure on the Li surface.[148] The inner layer close to the Li is mainly composed of inorganic species such as Li_2O, LiF, and Li_2CO_3, originated from the reactions of the salts and solvents.[159] The organic species such as $ROCO_2Li$, ROLi, and $RCOO_2Li$ make up the outer part of SEI layer. An analogous dual-layer structure in the SEI layer on the Na electrode was reported, and one can expect that it also applies to the K anode, although this is not fully determined yet.[160] While more complex models for the SEI on metal anodes have been proposed,[161] the Mosaic model appears to capture the essential inner inorganic versus outer organic structure commonly reported for Li, Na, and K anodes in standard carbonate and ether electrolytes.[162,163]

Analogous to a solid-state electrolyte, the SEI is ionically conductive but electrically insulating. Shi et al. proposed a two-layer/two-mechanism mode for Li ion diffusion through the SEI. The model was based on density functional theory (DFT) calculations combined with TOF-SIMS.[164] The Li cation first experiences a desolvation process occurring at the pore diffusion stage in the outer SEI layer. The cation then diffuses through the inner inorganic layer by a knock-off mechanism. The ion diffusion in Na-based and K-based SEI layers has been less explored experimentally or through modeling, with such studies being important moving forward. The geometrically and structurally heterogeneous SEI promotes uneven alkali ion diffusion, leading to heterogeneous growth/dissolution of the metal front.[140] In addition to the intrinsic heterogeneities within the SEI, extrinsic factors such as cracking may cause electrochemical hot spots, triggering dendritic growth. Features

https://doi.org/10.1021/acs.chemrev.1c00838
Chem. Rev. 2022, 122, 8053−8125

at the metal surface, such as dislocation steps, grain boundaries, and impurities, could drive dendrite growth as well.[165]

The native SEI layer on all three metals is generally considered unstable during repeated cycling, especially for deep stripping/plating, which leads to more volume changes, or at fast rates where the volume changes are rapid. For the various metal foils with a certain thickness, the corresponding theoretical volume changes can be estimated on the basis of the sulfur mass loading. When the S loading is 2 mg cm^{-2}, Li and Na foils with a thickness of 250 μm undergo volume changes of 6.5% and 11.8%, respectively (Table 5). Much more

Table 5. Theoretical Volume Changes for Li, Na, and K Planar Anodes with Specific Thicknesses of 250 and 100 μm, When Paired with Various Amounts of Sulfur[a]

Sulfur mass loading (mg cm^{-2})	Li volume change (%)	Na volume change (%)	K volume change (%)
Anode Thickness = 250 μm			
1	3.2	5.9	11.3
2	6.5	11.8	22.7
5	16.2	29.6	56.8
10	32.5	59.3	/
Anode Thickness = 100 μm			
1	8.1	14.8	28.4
2	16.2	29.6	56.8
5	40.6	74.2	/
10	81.2	/	/

[a]"/" represents N/P ratio is less than 1 (Metal anode is insufficient compared to sulfur cathode).

drastically, almost a quarter of the volume (22.7%) of the potassium with same thickness will be theoretically stripped and platted during cell operation. Per several high-visibility perspective articles, thin anode foil and high sulfur mass loading (*i.e.*, over 5 mg cm^{-2}) should be employed for practical cell operation.[7,166] At a thin anode thickness of 100 μm and a sulfur mass loading of 5 mg cm^{-2}, large interfacial fluctuations on the metal anode will result: 40.64% and 74.2% for Li and Na foils. Such repeated volume changes will mechanically disrupt the native SEI layer and are another reason why multifunctional separators are needed to ensure stable metal−sulfur battery performance.

The electrochemical reactivity of the SEI also plagues the stability of metal anodes during cycling. It is well established that with extended cycling the SEI grows, leading to an increasing electrochemical overpotential.[167] This effect is known to be most severe for K and least severe for Li in comparable electrolytes. Younesi et al. compared the SEI solubilities in Li and Na cells and proposed that the weaker Lewis acidity of Na resulted in higher electrocatalytic reactivity toward liquid electrolyte decomposition, as well as higher solubility of Na-based SEI components.[168] Two separate studies verified that Na-based and K-based SEI could be spontaneously formed at open-circuit potential, which is a manifestation of the metals' electrochemical reactivity.[143,152] Komaba and co-workers compared the electrochemical behaviors of various symmetric metal−metal cells (A//A cells, A = Li, Na, and K) with APF_6/EC/DEC electrolytes.[149] Per Figure 3c, the K//K cell represented the largest open-circuit potential (initially over 500 mV), which also drastically fluctuated with a large deviation of >100 mV (represented as error bars) during the relaxation period. Figure 3d presents the voltage profiles of the symmetric cells during successive metal plating−stripping at 25 μA cm^{-2}. The Li and Na cells show voltage polarization of less than 5 and 10 mV, respectively. By contrast, the K cell displayed polarization of 100 mV and above, with voltage spikes of nearly 1 V in the initial few cycles. This behavior originates from SEI instability although the exact cause of the early spike is not fully understood.

To improve the stability of metal anodes, various strategies have been employed, including designing new electrolytes and additives, modifying the current collector, fabricating functional hosts, and incorporating artificial SEI layers.[43,150,169−171] Favorable modification of the SEI structure can be achieved through electrolyte additives, such as the well-documented formation of the LiF phase adjacent to the Li metal due to fluoroethylene carbonate. For Na metal and K metal, FEC has yielded mixed results, an effect attributed in some studies to its rapid consumption from the electrolyte due to a continuous thickening of the SEI.[149,172] The structure (crystalline *vs* amorphous) and morphology (continuous *vs* discrete) of the NaF and KF phases need further analysis, as this may also be important in explaining the efficacy of FEC with the two metals. The artificial SEI approach can be roughly subdivided into (i) coating the metal anode directly with a secondary material and (ii) employing a membrane that is fully or partially incorporated into the SEI during electrochemical testing. For approach (i) low-temperature chemical vapor deposition (CVD) methods such as atomic layer deposition (ALD) and molecular layer deposition (MLD) are often employed. Since K melts at 64 °C and is even more reactive with air and moisture than Li, it is extremely challenging to coat the anode directly. Likewise, directly depositing artificial SEI layers on Na metal also represents a greater challenge than on Li metal. Coating the separator and then having the layer become *in situ* transferred onto the metal surface during cycling are agnostic to whether the anode is Li, Na, or K, in principle being equally applicable to all three. Such a transfer method avoids having to pretreat the metal anodes before assembling the cell, making functional separators a potentially scalable technology. For example, our recent work on functional separators with K metal anodes focused on double-coated tape-cast microscale AlF_3 on polypropylene (AlF_3@PP).[173] This layer resulted in a distinctly stable artificial SEI film containing KF, AlF_3, and Al_2O_3 phases on a K metal surface, which for a range of electrolytes promoted electrolyte wetting on the current collector, stabilized the SEI, and prevented dendrites. Studies are needed on scale up of functional separators including roll-to-roll (R2R) manufacturing, as well as cell assembly issues related to incorporating functional separators into commercially representative pouch cells of various dimensions.

From a holistic view, the failure to achieve effective sulfur or selenium immobilization in the cathode can further exasperate the anode instability. For carbon hosts with poor PSs or PSes confinement, insulating layers such as Li_2S_2/Li_2S have been reported on postcycled metal anode surfaces.[17,174−176] Several reports did report positive roles of Li_2S_x/Li_2Se_x/Na_2S_x in stabilizing the SEI,[177−179] which implies that some limited crossover may be beneficial. However, a high concentration of PSs has been reported to induce massive cracks and dendrites on anodes.[177] More work is needed to understand the role of "thin" sulfide and selenide passivation layers that actually stabilize the metal surface, versus "thick" layers that promote

https://doi.org/10.1021/acs.chemrev.1c00838
Chem. Rev. 2022, 122, 8053−8125

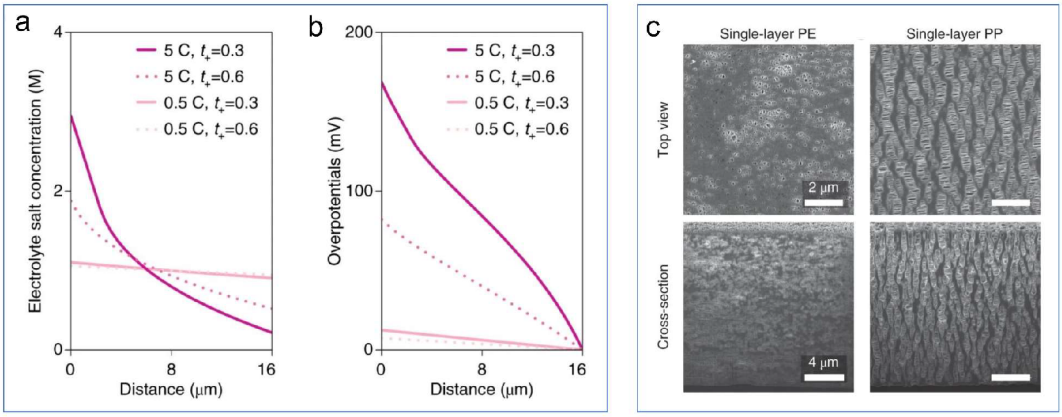

Figure 4. (a and b) COMSOL simulations of (a) electrolyte salt concentration and (b) electrolyte potential as a function of distance across the separator in a symmetric Li versus Li cell (to exclude effects of electrode structure. (c) Surface (top) and cross-sectional (bottom) scanning electron micrographs of PE and PP separators. Reproduced with permission from ref 180. Copyright 2018 Springer Nature.

dendrites or effectively size the plating and stripping reactions altogether.

6. PROPERTIES AND LIMITATIONS OF CONVENTIONAL SEPARATORS

With liquid electrolyte filling its pores, a separator takes on a key role in the ionic transport process. Moreover, the separator properties significantly impact the total electrolyte resistance of the cells. Wood et al. categorized such conductivity-related properties into two aspects: the intrinsic separator structure and the separator−electrolyte interface interactions.[180] These two factors affect the electrolyte distribution, salt dissociation, and ion desolvation, impacting the electrolyte ionic conductivity and the ion transference number. The features of the separator structure that affect these properties are its porosity ε, which is the fraction of pore volume to total volume, and tortuosity τ, which is a dimensionless quantity describing the influence of the morphology of the solid phase on ion flow. These in turn determine the separator's structure-dependent scaling parameter $\delta_{geo,eff}$, which is the ratio of ε to τ, per eq 3. The $\delta_{geo,eff}$ can be calculated using diffusion simulations on 3D reconstructions. A geometric effective ionic transport conductivity ($\sigma_{geo,eff}$) can be derived based on eq 4, where σ_{el} represents the ionic conductivity of the liquid electrolyte. Assuming a porosity of 40% (a typical value for polyolefin separators) and a tortuosity of 2.5, δ is calculated to be 0.16, indicating relatively slow ionic conduction throughout the separator.

$$\delta_{geo,eff} = \frac{\varepsilon}{\tau} \tag{3}$$

$$\sigma_{geo,eff} = \delta_{geo,eff}\sigma_{el} \tag{4}$$

$$\sigma_{eff} = \delta_{eff}\sigma_{el} = \frac{1}{N_M} \times \sigma_{el} \tag{5}$$

Electrochemical impedance spectroscopy can be applied for measuring the ionic conductivity in the electrolyte across the separator (σ_{eff}). An effective transport coefficient δ_{eff} can be determined as per eq 5, with N_M being the MacMullin number. The δ_{eff} differs from the geometrically effective transport parameter ($\delta_{geo,eff}$), with the discrepancy originating from the separator surface−electrolyte interactions. The interactions result from the functional groups on the separator's surface and the anion, cation, and solvent molecule species in the electrolyte. The interactions are considered to exist as ionic, polar, hydrophobic, or van der Waals interactions. An empirical rule is that enhancing the interactions can promote the degree of electrolyte uptake of the separator, that is, improve its electrolyte wettability. In addition, salt dissociation and ion desolvation may be facilitated by the strong chemical interactions between the separator and electrolyte, with the effect of improving the ion transference number and ionic conductivity. For instance, Cui and co-workers fabricated a g-C_3N_4-modified separator, which chemically interacted with the lithium-based electrolyte.[181] The Li^+ desolvation process was facilitated by the formation of numerous transient Li−N bonds, resulting in a much reduced energy barrier for Li deposition on the current collector. Overall, one should take into account both the structure and the chemistry of the separator when predicting its ion conduction performance. For instance, coating the separator with polar materials may inevitably reduce its porosity and the value of $\sigma_{geo,eff}$. However, the enhanced separator−electrolyte interaction may offset this impact and give rise to an improved effective ionic conductivity (σ_{eff}). Fundamental research on how the various functional layers on separators influence these parameters would be beneficial. Moreover, it is not fully understood the degree to which these parameters influence the ultimate cycling and rate performance of metal batteries. For example, are surface modifications that lead to improved wetting and higher ionic conductivity responsible for suppressing dendrites, or are these secondary effects behind the role of modifications in stabilizing the SEI? Or are they inter-related and synergistic; that is, does improved electrolyte wetting and a higher ionic conductivity naturally lead to a more uniform and stable SEI? Recent work has demonstrated a strong causal link between electrolyte wetting and SEI morphology for the case of geometrically roughened current collectors.[182] It would be useful to further understand this effect for the case of separators with varying electrolyte wettabilities.

The cation transference number (t_+) represents the fraction of the ionic current carried by cations and is associated with the ionic concentration gradients in the bulk electrolyte.[183] The impact of the cation transference number on cell performance was revealed by COMSOL simulations.[180] Figure 4a and b shows the electrolyte salt concentration and electrolyte overpotential gradient across a 16-μm-thick

https://doi.org/10.1021/acs.chemrev.1c00838
Chem. Rev. 2022, 122, 8053−8125

Table 6. Summary of the Physical and Electrochemical Properties of Conventional Polyolefin Separators (Celgard) and Glass Frit Separators (Whatman), as Specified by the Manufacturer's Product Model

Separator	Porosity (%)	Thickness (μm)	Average pore diameter (μm)	Gurley (JIS) (s)	Liquid electrolyte	Electrolyte uptake (wt %)/Contact angle (deg)	Ionic conductivity (mS cm^{-1})/ Transference number	Ref
PP 2400	41	25	0.043	620	1 M LiTFSI in DOL/DME + $LiNO_3$	70/37	0.32/0.38	187
PP 2400	41	25	0.043	620	4 M KFSI in DME	294/63	0.089/0.43	173
PP 2075	48	20	NA	300	1 M LiTFSI in DOL/DME + $LiNO_3$	NA/40	0.311/NA	188
PP 2500	55	25	0.064	200	1 M $LiPF_6$ in EC/DMC/EMC	98.6/45	0.77/0.283	189
PP 2500	55	25	0.064	200	1 M NaTFSI in PC/FEC	81.9/80.6	5.9×10^{-4}/0.21	190
PE 2730	43	20	NA	240	1 M $LiPF_6$ in EC/DMC/EMC/VC	82/43.7	0.32/NA	191
PE 2730	43	20	NA	240	1 M $NaClO_4$ in EC/DMC/EMC	94/NA	0.16/0.17	192
PP/PE/PP 2325	39	25	0.034	620	1 M $LiPF_6$ in EC/DEC	113/66	0.86/0.32	193
PP/PE/PP 2320	39	20	0.028	530	1 M LiTFSI in DOL/DME + $LiNO_3$	68/NA	0.82/NA	192
PP/PE/PP 2340	45	38	0.035	780	1 M LiTFSI in DOL/DME + $LiNO_3$	NA/68	0.4/NA	194
GF/A	65.5	260	1.6	4.3	1 M $NaClO_4$ in PC	NA	NA/0.27	195
GF/C	66	260	1.2	6.7	1 M $NaClO_4$ in EC/PC	360/NA	1.674/0.91	196
GF/D	NA	675	2.7	2.6	1 M $NaClO_4$ in EC/PC/FEC	NA	6.45/NA	197

separator membrane ($\delta = 0.16$) during slow (0.5C) and fast (5 C) charging, assuming cation transference numbers of 0.3 and 0.6. At low current (0.5C), the electrolyte salt concentration is uniform across the separator, with minimal electrolyte overpotentials (around 10 mV). Significant ionic gradients and corresponding overpotentials emerge at high current (5 C), and both are more pronounced when the transference number is 0.3 rather than 0.6. The large ion concentration gradient is due to the sluggish cation diffusion in the electrolyte and is associated with overpotentials as high as 180 mV. Assuming a nominal cell voltage of 3.2 V, the electrolyte resistance leads to a voltage loss of ~6%.

$$J_{\text{lim}} = \frac{Z_c C_0 F \Phi D_{\text{solution}}}{\tau L t^-} \quad (6)$$

Wu et al. recently derived a separator-involving equation (eq 6) for calculating the limiting current density (J_{lim}) in a lithium electrode, which closely relates to the ion concentration behavior at the anode.[184] The variable Z_c is the charge number of the cation ($Z_c = 1$), C_0 is the bulk electrolyte concentration ($C_0 = 1$), F is the Faraday constant, Φ is the volume fraction of void space, D_{solution} is the diffusion coefficient of the solution, L is the thickness of the separator, τ is the tortuosity of the diffusion path, and t_- is the transference number of the anions ($t_- = 1 - t_+$), respectively. As indicated by the equation, the separator can determine the limiting current density of the anode from the aspect of both structure (τ, L) and the corresponding interaction with the electrolyte (t_+).

Table 6 summarizes the physical properties of the polyolefin (Celgard) and glass frit (GF) separators (Whatman), listing the corresponding electrolyte wetting and ionic conduction behaviors in representative electrolytes. For the polyolefin separators such as PP and PE their intrinsically hydrophobic nature yields poor wettability by polar electrolytes. Consequently, the inside pores of a separator may be empty or filled with limited electrolytes, meaning blocked ion transport pathways. This results in a low ionic conductivity (σ_{eff}) and a low alkali ion transference number (t_+), which is typically in the range of 0.3−0.4 for Li^+.[185] It may be observed that high electrolyte resistance would result in a large energy loss during transport and decreased redox kinetics. For alkali metal anodes, it can be inferred that a low t_+ value favors metal dendrite formation based on space-charge considerations, including the classic Sands' time formulation.[146,147] A separator with poor wettability is apt to induce an inhomogeneous electrolyte distribution including containing nonwetted sections. This will result in inhomogeneous liquid-state cation diffusion, which would be problematic for metal anodes where dendrites are more prevalent than for ion anodes. Again, the extent to which this drives dendrite growth in full metal sulfur and metal selenium cells is not understood, as the SEI-related factors may be more dominant. When polysulfides dissolve into the electrolyte, the increase in electrolyte viscosity lowers the ionic diffusion and potentially degrades the electrolyte wetting between the separator and the anode.[186] This is another area ripe for further analysis: the extent to which sulfur or selenium cathode degradation processes influence ion transport behavior and ultimately dendrite formation. It is highly probable that a full understanding of cell failure requires a holistic approach, where cathode effects influence the anode and *vise versa*. It is known than pristine polyolefin separators are vulnerable to metal dendrite penetration, nominally because they provide insufficient mechanical restrain.[144] However, considering the high homologous temperature of Li, Na, and K during testing, various low-stress (*e.g.*, Coble, Nabarro-Herring, and Harper-Dorn) and high-stress (power law dislocation climb) creep mechanisms would allow the metal dendrite to breach much stronger interfaces. Electrolyte ion transport and wetting effects may therefore be critical regardless of the separator's elastic and plastic properties.

Per Table 6, polyolefin separators possess a macroporous structure with pore sizes around 50−100 nm, while glass frits

https://doi.org/10.1021/acs.chemrev.1c00838
Chem. Rev. 2022, 122, 8053−8125

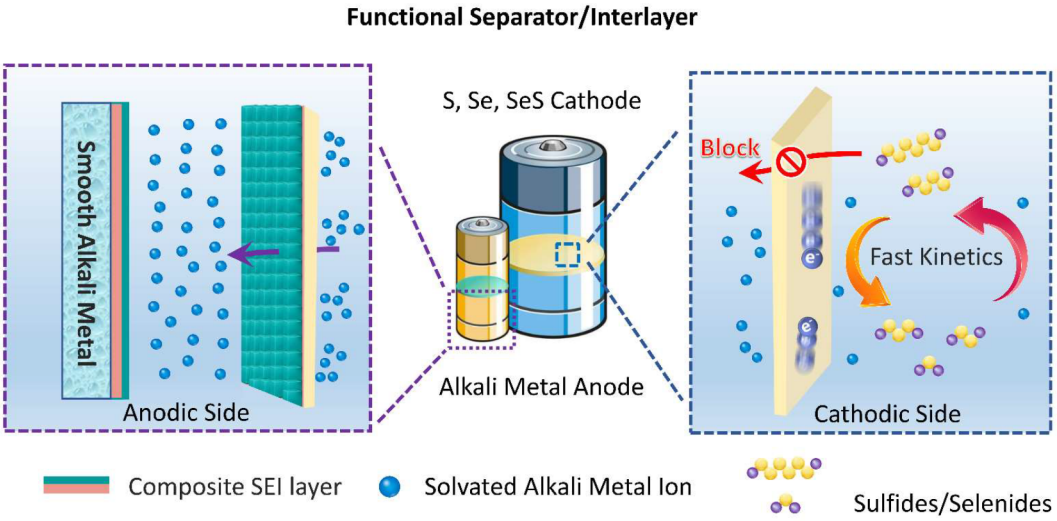

Figure 5. Schematic illustration of functional separators in rechargeable alkali metal−sulfur/selenium batteries.

have openings even in the 1.2−2.7 μm range. Figure 4c illustrates these dimensions, showing that it is straightforward for the polysulfides to migrate through either structure. If a dense and insulating layer of solid sulfides, *e.g.*, Li_2S and Li_2S_2, forms on the electrode surface, passivation can result. The electrically insulating polymer or glass frit separator will not sustain an appreciable electrical current necessary for dissolving the solid polysulfide species. Progressively more sulfur fails to be utilized with increasing cycle number, with the passivating layer thickening and further deteriorating the cell performance.[121] For the above reasons, the baseline untreated polymer separators pose significant problems for metal−sulfur batteries, more so than they would for conventional ion batteries with ceramic cathodes and graphite or silicon anodes. The unsatisfactory performance of untreated separators appears to be worse with Na−S and K−S versus Li−S cells, with the battery community consistently favoring glass frit separators for both. However, due to their large pore size, the glass fiber frits employed for Na−S and K−S show no ability to block polysulfides. They are also not effective in blocking dendrites despite the high elastic modulus of glass. Facile dendrite growth occurs through the larger openings of the frits, without the need to mechanically "punch through" the structures.[198] The Se- and SeS-based systems encounter analogous problems based on the inability of commercial separators to block polyselenide (PSe) crossover.

Figure 5 shows an "ideal" functional metal−sulfur/selenium separator. It is expected to promote electrolyte wetting on itself and on both electrodes, catalyze the redox kinetics at the cathode, homogenize the ion flux across it, suppress soluble species crossover from the cathode to the anode, and suppress dendrite growth at the anode. These positive functional separator attributes will be discussed next in regard to Li−S, Na−S, and K−S batteries and Se-based analogs.

7. FUNCTIONAL SEPARATOR AND INTERLAYER ADJACENT TO THE CATHODE

On the cathode side, the utilization of active sulfur/selenium is hindered by shuttle of polysulfides/polyselenides, passivation of the electrode on its surface due to precipitation of solid sulfides/selenides, and kinetically sluggish redox kinetics. Functional separators and interlayers are receiving increasing scientific focus as a means to simultaneously control these issues. Per Figure 6, the strategies can be categorized as one or

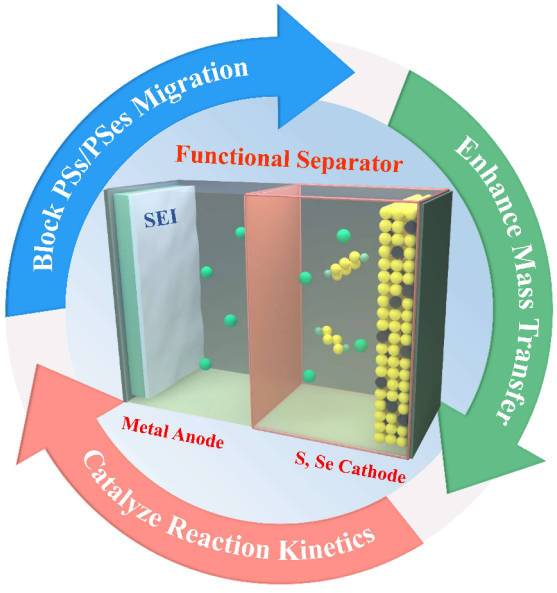

Figure 6. Summary of the strategies employed for designing functional separators/interlayers to enhance the electrochemical performance of sulfur-based and related cathodes.

a combination of blocking PSs/PSes' migration across the separator, promoting interfacial charge and mass transfer for the redox reactions, and acting as an electrocatalyst that accelerates the redox processes. Functional separators that block PSs/PSes while being electrically insulating and noncatalytic are established. Likewise, electrically conductive but nonelectrocatalytic separators are established too. An obvious future research direction is to create functional separator architectures that are explicitly designed to simultaneously address all three aspects, achieving optimum performance in each category. This is a complicated endeavor since various functional coatings are most effective in one or at most two out of the three categories. The solution may consist of multiphase structures, including multilayers where, for example, the outer layer is electrocatalytic while the inner

https://doi.org/10.1021/acs.chemrev.1c00838
Chem. Rev. 2022, 122, 8053−8125

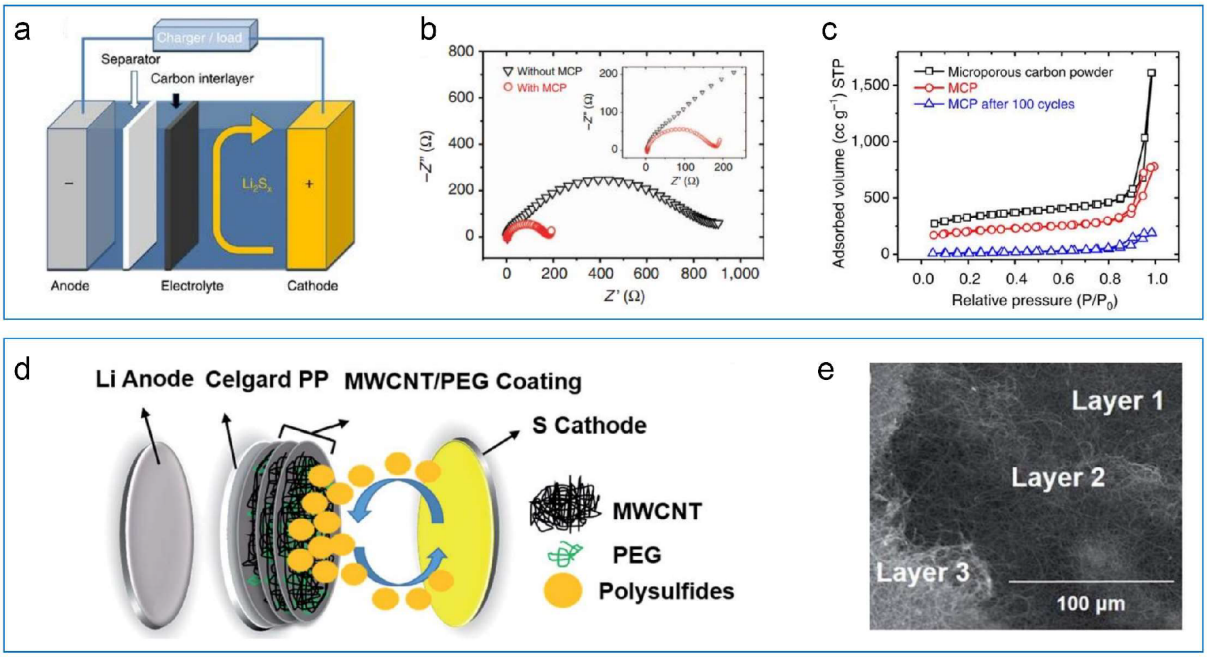

Figure 7. (a) Schematic configuration of a Li−S cell with a bifunctional microporous carbon paper (MCP) interlayer inserted between the sulfur cathode and the separator. (b) Electrochemical impedance spectroscopy plots of Li−S cells with and without MCP. (c) Isotherms of the microporous carbon powder, MCP, and MCP as an interlayer in the Li−S cell at the 1C rate after 100 cycles. (d) Schematic configuration of the layer-by-layer MWCNT/PEG-coated separator. (e) Scanning electron microscopy (SEM) images of the scratched fresh separators with MWCNT/PEG coatings. Panels a−c are reproduced with permission from ref 200. Copyright 2012 Springer Nature. Panels d and e are reproduced with permission from ref 215. Copyright 2016 Royal Society of Chemistry.

layer(s) blocks PSs/PSes and promotes ion transfer. Conversely, the functional coatings may be a single layer architecture but with catalytic phases embedded into or dispersed on the surface of the PSs/PSes blocking matrix. There are numerous other embodiments of multifunctional systems, with wet synthesis and vacuum deposition methods being ideally suited for such research.

7.1. Blocking the PSs/PSes' Migration across the Separator

7.1.1. Physical Interactions. For blocking the PSs/PSes' migration across the separator, an intuitive approach is to cover the macropores with functional layers which physically inhibit the diffusional crossover but still allow the alkali ion diffusion. Theoretical calculations estimate the radii of the solvated Li_2S_4, Li_2S_6, and Li_2S_8 to be 5.71 Å, 6.60 Å, and 7.21 Å, respectively.[137] By contrast, the Stokes radii of Li^+, Na^+, and K^+ in propylene carbonate solvents are 4.8 Å, 4.6 Å, and 3.6 Å.[199] Comparing the above PS numbers with the pore sizes of separators and the openings available with multifunctional separators (textural properties of carbons and graphenes, space between particles and between layers, *etc.*), it is apparent in most cases that physical passage across the separator is probable. The dimensions of the polysulfides are sufficiently small that only micropores would be effective physical blockers. While many materials are predominantly microporous, there are always some mesopores and macropores, even if these are the openings between individual particulates, sheets, *etc.* In fact, "physical blockers" with a broad range of pore size distributions have been experimentally demonstrated to be effective. The efficacy likely derives from a chemical interaction between the polysulfides and the functional layers, which operates in parallel to the physical blocking and prevents crossover through relatively large pores. It is the firm opinion of this article's authors that chemical trapping, to a varying extent, is always necessary for effective confinement.

Manthiram et al. first reported the application of porous MWCNT paper inserted between the cathode and the separator for blocking the shuttle of LiPS intermediates across the separator.[34] The high electrical conductivity of the carbon interlayer also endowed the cell with reduced interfacial resistance, allowing it to act, in effect, as a secondary current collector. With this interlayer, the cell exhibited significantly improved initial discharge capacity and cyclability versus the baseline:1446 mAh g^{-1} *vs* 671 mAh g^{-1} at 0.2C and 962 mAh g^{-1} *vs* 330 mAh g^{-1} after 50 cycles at 0.2C. In subsequent work, the same group employed microporous carbon paper (MCP) to mitigate the detrimental shuttling effect. Those results are illustrated in Figure 7a.[200] Figure 7b indicated the decrease in the charge-transfer resistance of the battery with MCP. The MCP had both micropore and small mesopore (less than 5 nm) and enabled the Li−S cell to retain over 1000 mAh g^{-1} after 100 cycles at the 1C rate. Figure 7c reveals the reduced surface area of MCP after cycles, due to the capture of soluble LiPSs within pores, which could, in principle, be recycled. To validate the potential of separator/interlayer modification, the authors further compared the electrochemical performances of different cell configurations, one based on a sulfur/microporous carbon (MPC) composite cathode with a pristine separator and another based on a pure sulfur cathode with an MPC-coated separator.[122] The first configuration showed the faster capacity fading and poorer sulfur utilization during cycling than the second configuration: a fade from 1060 mAh g^{-1} to 570 mAh g^{-1} after 50 cycles at 0.2C versus from 1214 mAh g^{-1} to 707 mAh g^{-1} after 200 cycles at 0.2C. Inspired by these pioneering works, various porous carbons, from one-dimensional to three-dimensional, have been

https://doi.org/10.1021/acs.chemrev.1c00838
Chem. Rev. 2022, 122, 8053−8125

Table 7. Summary of Functional Separators/Interlayers Created to Immobilize PSs or PSes and Their Performance Characteristics

Separator[a]	Film mass loading (mg cm^{-2}) /Film thickness (μm)	Cathode	Active materials loading (mg cm^{-2})	Liquid electrolyte	Cyclability (mAh g^{-1}) after n cycles	Ref
			Li−S			
PP + MWCNTs	NA	S	NA	1.85 M LiOTf in DOL/DME + $LiNO_3$	855 (100th) at 0.5C	34
PP + microporous carbon paper	NA	S	NA	1.85 M LiOTf in DOL/DME + $LiNO_3$	846 (150th) at 2C	200
PP/Super P carbon	0.2/20	S	1.1−1.3	1.85 M LiOTf in DOL/DME + $LiNO_3$	828 (200th) at 0.2C	35
PP/mesoporous carbon	0.5/27	S	1.55	1 M LiTFSI in DOL/DME + $LiNO_3$	1021 (100th) at 0.2C	213
PP/MWCNTs@PEG	0.26/6.7	S	1.6	1 M LiTFSI in DOL/DME + $LiNO_3$	490 (500th) at 1C	203
PP/PE/PP + UCM	NA/100	S/LCM	1.35	1 M LiTFSI in DOL/DME + $LiNO_3$	691 (300th) at 0.5C	219
PP/porous graphene	0.54/10	S/CNT	1.8−2.0	1 M LiTFSI in DOL/DME + $LiNO_3$	877 (150th) at 0.5C	208
PP/2D carbon	0.16/15	S	1	1 M LiTFSI in DOL/DME + $LiNO_3$	683 (500th) at 0.5C	209
PP/MOF(Ni_3(HITP)$_2$)	0.066/0.34	S/CNTs	8	1 M LiTFSI in DOL/DME + $LiNO_3$	905 (200th) at 0.5C	220
Celgard Separator/ Cu_2(CuTCPP)	0.1/3	S/Carbon black	2.0	1 M LiTFSI in DOL/DME + $LiNO_3$	604 (900th) at 1C	221
PP + BN/Graphene	NA/1	S/CNTs	NA	1 M LiTFSI in DOL/DME + $LiNO_3$	700 (1000th) at 1C	222
PP/Co_9S_8	NA/∼15	S	2	1.85 M LiOTf in DOL/DME + $LiNO_3$	530 (1000th) at 1C	223
PP/Laponite nanosheets	0.7/3.5	S	1.0−1.2	1 M LiTFSI in DOL/DME + $LiNO_3$	756 (500th) at 1C	224
PP/MoP/rGO	0.45/10	S/CNTs/ Acetylene black	3.88	1 M LiTFSI in DOL/DME + $LiNO_3$	760 (300th) at 0.5C	225
PP/Red phosphorus/ Carbon	0.3/8	S/C	2	1 M LiTFSI in DOL/DME + $LiNO_3$	729.6 (500th) at 1C	226
			Li−Se			
DMTA-COF + ceramic	NA	Se	3	1 M LiTFSI in DOL/DME + $LiNO_3$	126 (700th) at 6C	227
PP/CTAB-CNTs-$Ti_3C_2T_x$	0.09/0.27	Se/Carbon black	2.1	1 M LiTFSI in DOL/DME + $LiNO_3$	485 (100th) at 0.1C	16
PP/Graphene	0.3/5	Se	4	1 M LiTFSI in DOL/DME + $LiNO_3$	331 (1000th) at 0.5C	228
PP + N,S-doped Graphene	0.65/32	Li_2Se_8	5	1 M LiTFSI in DOL/DME + $LiNO_3$	330.7 (500th) at 1C	229
			Li−SeS_2			
PP + Graphene/TiN	NA	SeS_2/MWCNTs	2.3	1 M LiTFSI in DOL/DME + $LiNO_3$	511 (500th) at 1A g^{-1}	230
Celgard Separator/ TPB-DMTP-COF	0.2/14	SeS_2/MWCNTs	4	1 M LiTFSI in DOL/DME + $LiNO_3$	416.3 (800th) at 1C	231
Celgard Separator/Super P	NA	SeS_2/Super P	2	1 M LiTFSI in DOL/DME + $LiNO_3$	365.7 (200th) at 0.5C	231
			Na−Se			
GF/Porous Carbon	NA	Se/Activated CNFs	4.4	1 M $NaClO_4$ in EC/DMC	334 (200th) at 5C	136
PP/CTAB-CNTs-$Ti_3C_2T_x$	0.09/0.27	Se/Carbon black	1.8	1 M $NaClO_4$ in EC/DEC	450 (300th) at 0.5C	16
			Na−S			
GF/FPNs-G	NA/10	S/Porous carbon	0.68	1 M $NaClO_4$ in EC/PC	396 (800th) at 0.5C	232
GF + Teflon-lined carbon	NA	S/CNTs/ Graphene	NA	1 M $NaClO_4$ in EC/PC	650 (100th) at 0.1C	233
GF+PVdF-HFP-BN	NA/207.2	S	0.8−1	1 M $NaClO_4$ in TEGDME	570 (100th) at 0.5 A g^{-1}	234

[a]"Separator + Material" represents the case of introducing the self-standing interlayer into the interface; "Separator/Material" represents the case of directly coating the functional material on the separator.

employed. Carbon nanofibers (CNFs),[174,201−205] carbon tubes,[206,207] porous graphene,[208] carbon flakes,[209] hierarchical carbon spheres,[210] acetylene black mesh,[211] mesoporous carbon,[212,213] and carbon black[35,214] have been incorporated onto the separator to block LiPSs, LiPSes, NaPSs, and NaPSes species. The associated results are compiled in Table 7.

Such approaches have also been extended to Na metal systems. Jiang et al. demonstrated the feasibility of fabricating a PSes barrier for Na−Se batteries. KOH-activated carbon black

https://doi.org/10.1021/acs.chemrev.1c00838
Chem. Rev. 2022, 122, 8053−8125

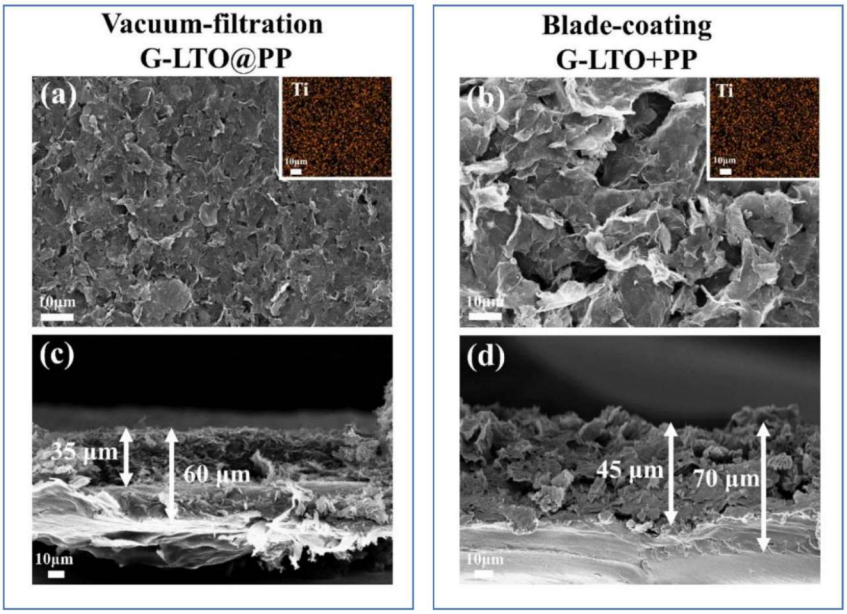

Figure 8. (a and b) SEM images of the surfaces of fresh G-LTO@PP and G-LTO+PP separators. (c and d) Cross-sectional SEM images of fresh G-LTO@PP and G-LTO+PP separators. Reproduced with permission from ref 235. Copyright 2016 Elsevier.

was coated on a glass frit separator, with an areal loading of 0.3 mg cm^{-2}.[136] The porous carbon coating blocked the free migration of high-order sodium polyselenides through the separator. No obvious color change was observed on the back side of the postcycled carbon-coated separator. As a result of suppressed PSes migration, Na−Se batteries with the functional separator displayed minimal self-discharge. Capacities of 599, 578, 572, 571, 567, 566, and 561 mAh g^{-1} were retained after storage for 0, 1, 2, 3, 4, 5, and 6 months in the charged state. In comparison, the pristine separator resulted in rapid capacity fade in the charged state, going from 598 to 340 mAh g^{-1} after six months. This approach, using KOH-activated porous carbon, serves as a good example of why there is likely a chemical interaction in addition to the physical one. It is well-known that KOH activation introduces significant O and OH functional groups to the porous carbon surface.[15,216−218] Therefore, what the PSes saw was a reactive polar surface, rather than the ideally inert surface of a pure carbon. More research is needed to understand the role of carbon's surface moieties, always present to some extent on the pore surface, in attracting various polysulfides and polyselenides. For a given carbon-based functional separator architecture, would its efficacy in preventing crossover depend on the type of surface functionality coverage? What about the case where there are "only" O and -OH groups that are an incidental byproduct of carbon processing?

To date there is no clear consensus regarding what porous structure and pore size distribution in a carbon would make for an optimum physical polysulfides/polyselenides barrier. Micropores are known to be effective in capturing, storing the soluble sulfur or selenium species, and keeping it accessible as an active material for further reutilization.[219] The larger mesopores are generally inferior in their trapping efficiency than the micropores. However, they may channel the electrolyte containing the dissolved PSs/PSes into the microporous trapping sites (pores are interconnected) and facilitate the reactivation of the trapped active material.[202] As mentioned earlier, the chemical functionality of the surfaces is likely the missing link in providing a comprehensive taxonomy of the various carbons' functional properties. Other carbon macroscopic properties that should be further considered are the particle/tube/sphere *etc.* packing, the interlayer thickness, and the total mass loading. The most facile diffusional pathway of dissolved species is along the largest gaps, which could be the space between the packed particles rather than through the particles themselves. Given that such spacing is fairly large, being on the same scale as the particle sizes, surface-functionality-driven chemical interactions appear even more important for preventing crossover.

Per Figure 7d, Luo et al. designed a layer-by-layer separator coating comprising multiwalled nonporous carbon nanotubes/polyethylene glycol (MWCNTs/PEG).[215] Figure 7e shows the corresponding microscopic structure. The nonporous nanotubes with low surface area supplied separator with limited LiPSs trapping sites. Instead, the LiPS confinement was nominally due to the high tortuosity created by the interwoven MWCNT framework and the layer-by-layer structure.

Yang and co-workers designed a hybrid coating of $Li_4Ti_5O_{12}$ (LTO) nanospheres between graphene layers on a separator for blocking LiPS migration, in which the space between the nanospheres served as ionic conductive channels.[235] The method of coating was found to play an important role in polysulfide immobilization by affecting the stack structure of graphene. Per Figure 8a and c, the vacuum-filtration method induced an oriented stack of graphene parallel to the separator, with a coating thickness of 35 μm (termed as G-LTO@PP). For the separator prepared by blade-coating (G-LTO+PP), graphene stacked in a disordered manner, per Figure 8b and d. The coating was thicker (45 μm) and looser, where open channels favored the facile electrolyte flow. As a result of comparatively smaller inner spaces in the G-LTO@PP separator, the diffusion of polysulfides across it occurred more slowly than across the G-LTO+PP separator. Corresponding rate and cycling performances revealed the improved sulfur utilization ascribed to the optimized separator coating. The cell with the G-LTO@PP separator delivered a reversible

https://doi.org/10.1021/acs.chemrev.1c00838
Chem. Rev. 2022, 122, 8053−8125

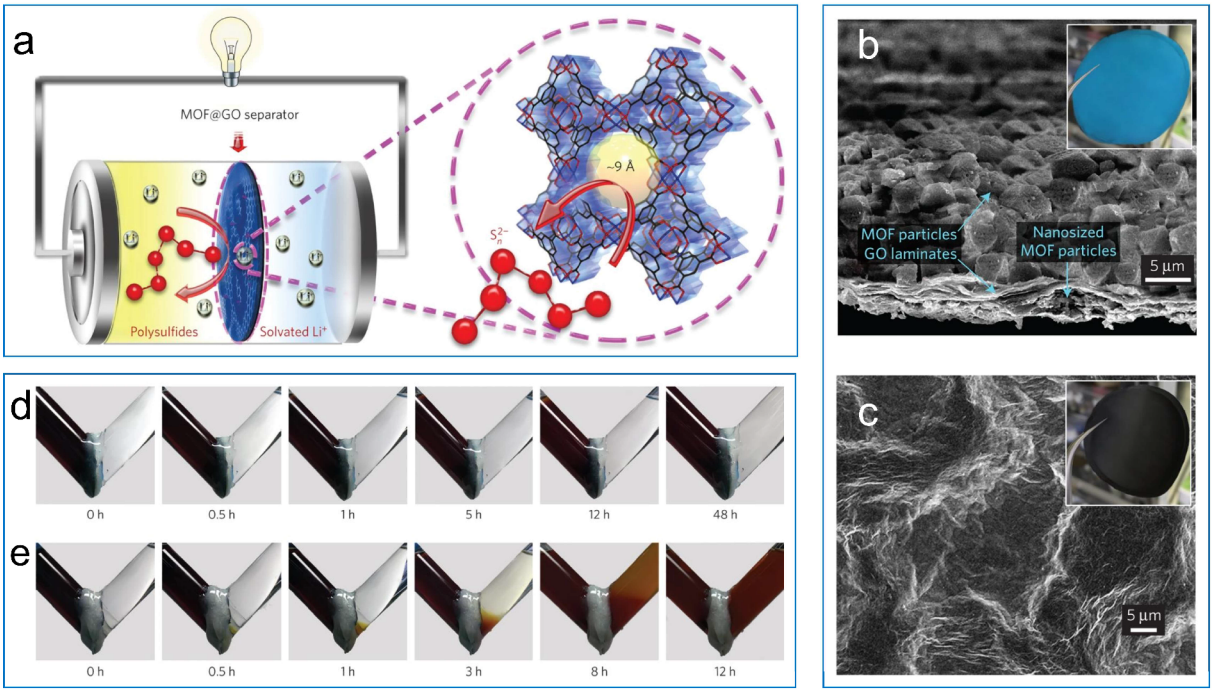

Figure 9. (a) Schematic of MOF@GO separators in lithium−sulfur batteries. (b) SEM image of the multilayered MOF@GO separator. The inset shows a digital photo along the MOF side. (c) SEM image of the GO layer. The inset shows a digital photo along the GO side. Polysulfide permeation measurements in the V-type permeation devices with (d) a MOF@GO separator and (e) a GO separator. Reproduced with permission from ref 244. Copyright 2016 Springer Nature.

capacity of 709 mAh g^{-1} at 2C and a retention of 85.6% after 300 cycles at 0.3C, versus 467 mAh g^{-1} and 52.4% with G-LTO+PP.

The chemically inert micrometer-scale pores of commercial separators are too large to block LiPSs. Researchers have employed organic polymerization on the pore walls of the polyolefin separator to improve the blocking. Polymers adhere to the separator walls and result in a shrinkage in the mean pore size. For instance, Sun et al. designed a polypyrrole (Ppy) modification layer on a Celgard separator, leading to pores in the 30−50 nm range.[187] Other polymers including polydopamine and polymerized nylon-66 have been employed as well with some success.[236,237] Yu et al. incorporated a specific polymer with intrinsic nanoporosity (termed as PIN) into the pores of the PP separator, significantly narrowing the pore size distribution.[238] Complementary molecular dynamics (MD) simulation revealed that the pore size of PIN was less than 2 nm, which would enable more efficient LiPS blocking. Experiments verified its potential in abating polysulfide crossover, allowing for 81.7% capacity retention after 200 cycles at 0.1C, versus only 4.5% in the pristine separator baseline.

Luo et al. demonstrated an increase in working ion resistance (from 3.6 Ω to 5.1 Ω) after coating polymerized nylon-66 into a graphene-coated polypropylene separator.[237] As a consequence, the Li−S cells had lower reversible capacity at fast charge (0.5C and 1C) than those with graphene-coated polypropylene but without nylon. These results were an excellent demonstration that too small a porosity is actually deleterious for cell performance and implies that better performance is achieved with larger separator pores, but which are chemically active enough to trap the crossover species. The compromised ionic conduction across the separator results from decreased total porosity ε (fraction of pore volume to total volume) and from increased tortuosity τ, which is related to the pore size distribution as well as to the packing characteristics. This can be inferred from eqs 3 and 4. An emerging strategy is to promote separator surface−electrolyte interactions by employing strongly polar and electrolyte-philic polymers. This may remedy the negative impact from pore volume and tortuosity factors, leading to enhanced ionic conductivity (σ_{eff}) in a modified separator. For instance, a Ppy-modified separator wetted by liquid electrolyte was shown to display improved ionic conductivity versus a regular Celgard separator (0.39 *vs* 0.32 mS cm^{-1}), despite a significant shrinkage in the pore sizes (micron scale *vs* 30−50 nm).[187] The improved ionic conductivity relates to the hydrophilic surfaces of the polypyrrole, which was also demonstrated by improved electrolyte uptake versus the baseline (108% *vs* 70%).

Metal−organic frameworks possess large surface areas and highly ordered pores with tunable nanoporosity. Metal−organic frameworks are based on a coordination network, comprising inorganic nodes which form the "corners" of the pores and organic linkers that connect these nodes together. The metal's coordination preference and ligand type both determine the size and shape of pores by dictating the coordination number and the ligand orientation.[239] Covalent organic frameworks (COFs) are porous organic polymers with ordered pores. Covalent organic frameworks are composed of light elements (such as H, C, B, N, and O), in which the building blocks are connected by covalent bonds.[240−243] Metal−organic frameworks and COFs with nanosized channels can be suitable separator coating materials for Li−S and other metal batteries and beyond. While nominally their efficacy derives from the size difference between pores and soluble species, it is likely that chemical interactions also contribute to the trapping mechanisms.

https://doi.org/10.1021/acs.chemrev.1c00838
Chem. Rev. 2022, 122, 8053−8125

Zhou et al. worked to improve Li−S batteries, coating the separator with GO and $Cu_3(BTC)_2$ MOFs (HKUST-1, BTC = 1,3,5-benzenetricarboxylic acid), as shown in Figure 9a and b.[244] The MOFs contained ordered microporous channels with a size window of only 9 Å. In order to verify the LiPS blocking function of the MOF layer, they conducted permeation experiments by employing V-shaped devices, in which Li_2S_6 solutions (left side) and Li_2S_6-free blank electrolyte were separated by different separators. These results are shown in Figure 9d and e. The prepared MOF@GO separator could intercept LiPSs, while the sole GO interlayer (Figure 9c) had poor suppression in LiPSs permeation, nominally because its spacing allowed passage. The battery with a MOF@GO separator held an initial capacity of 1207 mAh g^{-1} at 1C and a slight fade of 15 mAh g^{-1} from the 100th to the 1500th cycles. The battery with the GO separator exhibited a lower capacity retention rate of only approximately 23%.

Targeting rechargeable Li−SeS_2 batteries, Wang et al. prepared a TPB-DMTP-COF-coated separator (TPB = 1,3,5-tri(4-aminophenyl)benzene, DMTP = 2,5-dimethoxyterephthalaldehyde).[231] Nitrogen adsorption/desorption isotherms revealed an intrinsic pore size of 3 nm within TPB-DMTP-COF, which is larger than the dimensions of polysulfides and, likely, polyselenides. It was found that the pore size reduced to 0.9 nm after soaking the COF in the Li_2S_6/LiTFSI solution (LiTFSI = lithium bis(trifluoromethanesulfonyl)imide) but remained unchanged while soaking in the Li_2S_6 solution without lithium salt. The shrinkage of pores was inferred to be a result of the preferential adsorption of LiTFSI salt in the channels of COFs. This, in consequence, contributed to an increased polysulfide blocking effect, with little transport of Li_2S_6 species across the separator found after a 48 h permeation experiment. Accordingly, the Li−SeS_2 cell with a TPB-DMTP-COF-coated separator delivered a higher capacity of 849.2 mA h g^{-1} at 0.5C, versus 327.4 mAh g^{-1} in the case of a pristine separator. This study raises an interesting important point that it is not only the size of the intrinsic pores in the functional separator that matters but also how this size is modified during electrochemical testing through the adsorption of secondary species from the electrolyte. This is another aspect that should be further studied for a range of cathode and electrolyte systems. Starting with a known pore size distribution in the starting separator, what is the pore size distribution at cycle 1, cycle 10, cycle 100, *etc.*? A related query is how much of the observed capacity loss is attributable to separator pore blockage and the associated diffusional limitations of the working cations? Is there such as thing as being too effective; that is, while at first secondary species' adsorption leads to blocking of polysulfides and polyselenides, at a certain point is ionic flow also impeded? Are there secondary pretreatments that can take a fairly wide pore size distribution in the as-fabricated functional separator and further narrow it to the targeted dimensions? Conversely, could "clogging" species from the electrolyte be prevented from adsorbing beyond the targeted levels? In general, more work is needed to understand the evolution of porosity in functional separators with extended cycling, electrolyte types, additives, *etc*. Separator porosity changes should also be examined for as-received unmodified separators, since they are designed for LIBs with ceramic cathodes and carbonate electrolytes.

Despite the highly ordered pores within MOF and COF backbones, there are inevitable spaces between the particles which are much larger in size. Considering the standard theory of particle packing, a 66% packing density is achieved for monosized spheres with the open spaces between the particles being on the same scale as the particle sizes. This means that even for 10-nm-scale particulates, there is plenty of space for the crossover species to get through. Materials such as advanced 2D and 3D carbons are usually much larger, being up to tens of microns in their maximum dimensions. Based on physical blockage only, and assuming no secondary adsorption of species from the electrolyte, dissolved polysulfides and polyselenides species are very likely to pass through the separator along such gaps. The intermediate PS or PSe species are inherently polar while surfaces of pure carbons (no surface groups) are nonpolar. This leads to the weak van der Waals interaction with bonding energy ranging from −0.1 to −0.7 eV.[218] It necessitates the other materials with stronger interaction with intermediates, including carbons with heteratom moieties.

7.1.2. Chemical Interactions. Chemical interactions include polar−polar interaction, Lewis acid−base interaction, and catenation interaction, which can dependently or synergistically contribute to the strong affinity of polysulfides to functional separator materials. Figure 10 summarizes the affinities of nonpolar carbon and polar materials toward representative Li_2S_4 and Li_2S_6 species. The interaction appears much stronger in polar materials and, therefore, makes them promising candidates of effective polysulfides barriers (Table 7).

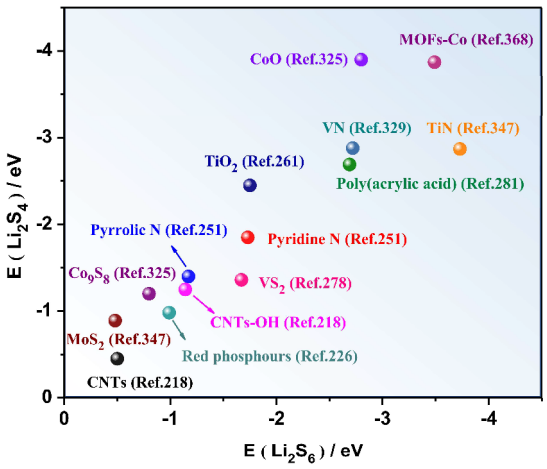

Figure 10. Binding energies of carbon and polar compounds with Li_2S_6 and Li_2S_4.

Polar molecules possess separate centers of positive and negative charge, which correspondingly results in an electric dipole or multipole. Polar molecules will strongly interact with each other (polar−polar interactions) through dipole−dipole intermolecular forces, which are much stronger than forces between polar and nonpolar molecules. Therefore, polar coatings on modified separators can strongly anchor similar polar polysulfide or polyselenide species. The dissociated PS and PSe anions can be considered as Lewis bases. Lewis acid−base interactions along with the formation of coordinate bonds are possible between these anions and various Lewis acids present on functional separators. This will cause soluble intermediates to be immobilized.

https://doi.org/10.1021/acs.chemrev.1c00838
Chem. Rev. 2022, 122, 8053−8125

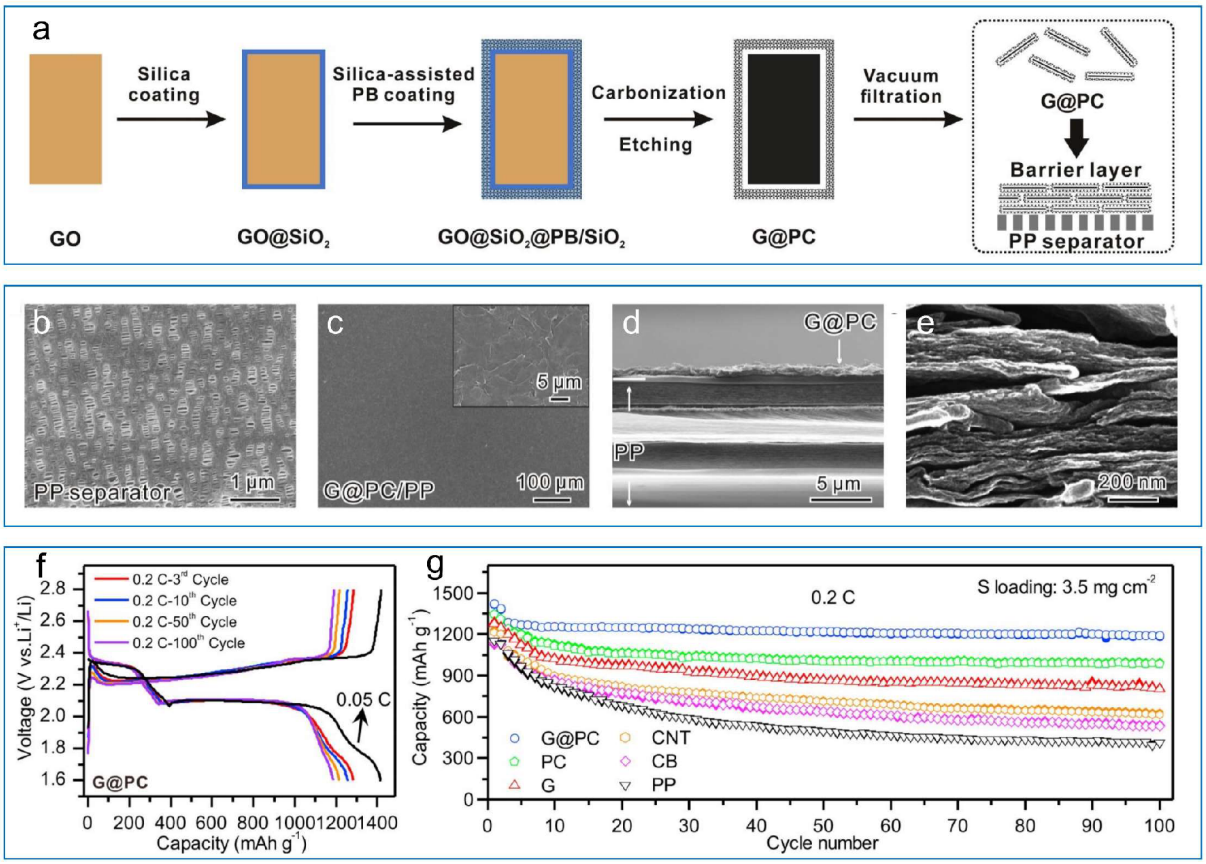

Figure 11. (a) Schematic illustrating the synthesis procedure for the G@PC functional layers. (b) SEM image of the pristine PP separator. (c) Top-down and (d) low- and (e) high-magnification cross-sectional SEM images of the G@PC/PP separator. (f) Charge/discharge curves of the G@PC/PP cell at 0.2C. (g) Cycling performances of the G@PC/PP, PC/PP, G/PP, CNT/PP, CB/PP, and PP cells at 0.2C. Reproduced with permission from ref 252. Copyright 2018 Elsevier.

Introduction of heteroatoms (such as nitrogen, oxygen, boron, phosphorus, sulfur, or codoping) into carbonaceous materials can offer tailored polarity and intense polar−polar or Lewis acid−base interactions with soluble PS and PSe species.[222] Heteroatom doped carbon interlayers or coatings on separators have been demonstrated to be effective in trapping of active species.[212,245] At the atomic scale, the difference in the electronegativities of carbon and heteroatoms (B, N, O, S, and P) can redistribute electrons and, hence, increase the polarity of the carbon. For instance, boron possesses lower electronegativity than carbon. When integrated into the carbon framework, the B doped sites lead to increased binding energy with sulfides (*i.e.*, Li_2S_2) compared to undoped carbon (1.535 eV *vs* 0.315 eV).[222] Conversely, the electronegative N atoms give basic surfaces. The pyridinic and pyrrolic N atoms with an extra pair of electrons can strongly interact with the electropositive alkali ions within PS or PSe species.[212,246−250] Taking Li−S as an example, the binding energy of Li_2S, Li_2S_2, Li_2S_4, Li_2S_6, and Li_2S_8 on pyridine N doped graphene is 2.29, 2.40, 1.85, 1.73, and 1.99 eV, respectively.[251] For pyrrolic N doped graphene, the Li_2S_x (x = 1, 2, 4, 6, and 8) binding energies are 1.68, 1.81, 1.40, 1.17, and 1.81 eV, respectively, far above that of pristine graphene, which is below 0.5 eV.[251]

Per Figure 11a, porous nitrogen doped carbon nanosheets were fabricated by a templating strategy and then were coated onto a separator by vacuum filtration (G@PC/PP).[252] Figure 11b−e shows that the nitrogen doped nanosheets were closely stacked with a "brick-wall" structure and a thickness of about 0.9 μm. The G@PC possessed a N content of 4.5 at %. Aided by both physical and chemical (due to N moieties) trapping of LiPSs, the Li−S cell with G@PC/PP delivered an initial reversible capacity of 1416 mAh g^{-1} at 0.05 C, substantially higher than with the pristine PP separator at 1126 mAh g^{-1}. Those results are illustrated in Figure 11f. As baselines, other low-N-content (2.0 at %) and undoped carbons were also adopted to modify separator using an analogous fabrication approach. As shown in Figure 11g, G@PC/PP exhibited an initial reversible capacity of 1285 mAh g^{-1} and a capacity retention of 92% after 100 cycles at 0.2C. A comparable functional separator but with 2% nitrogen content in the carbon gave an inferior capacity retention of 86% after 50 cycles, indicating the necessity of chemical interactions between N atoms and LiPSs.

Furthermore, a codoping strategy, *e.g.*, N and S, N and P, has been applied to separator modification, delivering a synergistic enhancement for PSs and PSes trapping over singly doped carbons.[253,254] On the basis of strong chemical confinement of polyselenides by nitrogen and sulfur atoms, a lightweight N,S-codoped graphene blocking layer was employed for Li−Se batteries.[229] The interlayer enabled a reversible capacity of 330.7 mAh g^{-1} at 1C after 500 cycles, while negligible capacity was retained when the interlayer was absent. Polar functional groups such as hydroxyl, epoxy, ether, ester, carboxyl, and amino groups can strongly bind with PSs and PSes. For instance, the electron-rich functional groups, including

https://doi.org/10.1021/acs.chemrev.1c00838
Chem. Rev. 2022, 122, 8053−8125

ketones, hydroxyl groups, and cyclic oxygen, possess binding energies ranging from −0.8 eV to −1.52 eV with Li_2S_4 and are apt to form a strong Li−O bond with LiPSs through Lewis acid−base interaction.[255] The corresponding interactions are higher than that between the nonpolar graphene and Li_2S_4, reported as −0.39 eV.[255] Carbon with polar group moieties was coated onto separator for more effective LiPS capture. Examples of such carbons are hydroxyl-functionalized carbon nanotubes (CNTOHs)[218] and carbon quantum dots with oxygenated functional groups.[256]

Polymer-coated separators show promise for immobilizing polysulfides, with their efficacy deriving from chemical interactions as well. Jiang et al. designed a functional composite separator comprising Fe^{3+}/polyacrylamide nanospheres (FPNs) and graphene, which enhanced the performance of Na−S batteries.[232] The polyacrylamide contained amide groups which served as the Lewis base. To demonstrate the chemical interaction between the polymer and soluble NaPS species, FPNs were added to a Na_2S_6-containing solution, which was analyzed by Fourier transform infrared (FTIR) spectra. New stretching vibration peaks attributed to the stretching vibrations of the Na−O/Na−N bonds appeared in the spectra, demonstrating the Lewis acid−base interaction between polyacrylamide and NaPSs. The functional separator displayed improved NaPS trapping and reutilization efficiency, leading to a higher long-term capacity retention over the baseline: 73% after 400 cycles at 0.1C versus 53% for the bare separator. Some polymeric binders only ensure the adhesion of functional materials onto the separator but also chemically interact with and immobilize the soluble species. Examples include polyethylene glycol (ether groups),[122,215] chitosan (hydroxyl and amino groups),[257,258] gum arabic (ketones, hydroxyl groups, and cyclic oxygen),[255] and poly(vinylpyrrolidone) (amide groups).[208]

Metal oxides such as Al_2O_3, SiO_2, TiO_2, SnO_2, and MnO_2 have been demonstrated as effective separator coatings due to their polar interactions with PSs.[175,259−264] Huang and co-workers employed a graphene sheet/TiO_2 film, which trapped LiPSs by physically (and likely chemically) interacting with the graphene and by chemical adsorption on the TiO_2 surface via formation of the S−Ti−O bond. This was highly effective in reducing the loss of active sulfur from the cathode.[176] The Li−S cells with solely the graphene film were significantly less stable. Nazar and co-workers confirmed that the oxygen groups of MnO_2 could react with polysulfides *in situ* to form surface-bound thiosulfate ($S_2O_3^{2-}$).[265] These groups could serve as a redox shuttle by anchoring long-chain LiPSs from solution by generating polythionate $[O_3S_2\text{-}(S)_{x-2}\text{-}S_2O_3]^{2-}$ complexes and reversibly converting them into insoluble short-chain LiPSs. The mechanism represents another chemical adsorption mode, termed catenation interaction, that prevents LiPS dissolution into the electrolyte. On the basis of dual chemical adsorption modes, Wang et al. developed a functional separator coated with MnO_2/graphene oxide/carbon nanotubes, termed G/M@CNT, for Li−S batteries.[175] The G/M@CNT film was effective at suppressing the self-discharge behavior of the cell, with 93% capacity retention after 20 days of storage. By contrast, the cell equipped with pristine separator delivered 26% retention, indicative of a major loss of active sulfur during the resting period. The authors also studied the cycled Li anodes in cells, employing SEM analysis. In the systems with the pristine separator, a 60-μm-thick passivation layer with a high S content was formed on the anode. However, the passivation layer of the cell with the G/M@CNT function separator was 20 μm and relatively smooth. These results revealed the impact of the separator−polysulfides interaction on the anode and also indicated that even the highly effective barrier films let some polysulfides across them. At the same time, these results demonstrated that a passivation layer on the anode is not extremely deleterious to performance, assuming that it does not grow too thick. Since most oxides are electrical insulators, their efficacy as an electrocatalyst is limited without a supporting conducting phase. For a functional separator to be effective as a secondary surface for the targeted electrochemical conversion reactions, there needs to be an electrically conductive phase in intimate contact with the cathode (but obviously not shorted to the anode). As a result, oxides with highly conductive components such as graphene, CNTs, and Mxene are employed to accelerate the reversible targeted redox kinetics with sulfur.[266,267]

Polysulfides' chemical affinity has also been demonstrated for phosphorus and for compounds such as transition metal phosphides, *e.g.* CoP, MoP, MoP_2, and Sn_4P_3. Both black phosphorus (BP) and red phosphorus (RP) allotropes strongly anchor LiPSs through chemical interaction of P with both Li and S.[226,268] Chen et al. reported that RP could react with LiPSs, forming ionically conductive Li_3PO_4, which is, in turn, a sulfur redox electrocatalyst.[226] The ionic transport conductance of the functional separator was incrementally increased from 6.9×10^{-4} S cm^{-1} to 9.7×10^{-4} S cm^{-1} although it is not obvious how Li_3PO_4 formation would enable this. After the same Li_2S_4 treatment, the baseline RP-free separator showed only a minimal increase in ionic conductivity, going from 6.8×10^{-4} S cm^{-1} to 7.0×10^{-4} S cm^{-1}. The sulfiphilic nature of metal atoms enables effective chemisorption of polysulfides through the formation of metal−sulfur bonds, such as the Mo−S bond between MoP_2/MoP and the polysulfides.[225,269−271]

Transition metal sulfides (TMSs), including Co_9S_8,[223] ZnS_2,[272] SnS,[272] MoS_2,[273] CoS,[274] ReS_2,[275] WS_2,[276] Sb_2S_3,[277] and VS_2,[278] have been employed for functional separator coating, having the general advantage of being electrocatalytically active with improved electrical conductivity over oxides. Cui et al. proposed that 2D layered metal disulfides could chemically confine LiPSs by forming a Li−S bond with Li_2S_x/Li_2S.[279] Likewise, in the Na−S system, Xu et al. observed strong chemical interaction between MoS_2 and Na_2S_6, with electrons being transferred from Na_2S_6 to Mo atoms.[280] Accordingly, the XPS Mo 3d peak was shifted to a lower binding energy. The authors fabricated hollow carbon spheres/MoS_2 (HCS/MoS_2)-coated glass fiber as the blocking barrier for sodium polysulfides. The large gaps between the glass fibers were covered after the compact coating by HCS/MoS_2 which had a thickness of around 10 μm. A reduction peak at 0.9 V emerged in the initial cyclic voltammetry (CV) curve of the Na−S cell with the modified separator. The peak was attributed to the irreversible intercalation of sodium ions into the layers of MoS_2. The authors argued that the formed sodiated MoS_2 was still effective in chemically adsorbing the polar polysulfides. With such a functional separator, the Na−S cell delivered significantly higher initial reversible capacity 1C than that with glass fiber, being 1090 mAh g^{-1} versus 633.3 mAh g^{-1}, as well as enhanced cycling life up to 1000 cycles.

Wang et al. engineered selenium cathode interfaces for Li−Se (ether-based electrolyte) and Na−Se batteries (carbonate-based electrolyte).[16] The authors created a cetrimonium

https://doi.org/10.1021/acs.chemrev.1c00838
Chem. Rev. 2022, 122, 8053−8125

Table 8. Recent Advances on Functional Separators/Interlayers That Immobilize PSs by Electrostatic Repulsion

Separator[a]	Film mass loading (mg cm^{-2}) /Film thickness (μm)	Cathode	Active materials loading (mg cm^{-2})	Liquid electrolyte	Cyclability (mAh g^{-1}) after n cycles	Ref
			Li−S			
PP/PE/PP/Nafion	0.7/1	S/CNTs	0.53	1 M LiTFSI in DOL/DME + $LiNO_3$	468 (500th) at 1C	117
PP/GO/Nafion	0.0532/∼0.13	S/G/CNTs	1.2	1 M LiTFSI in DOL/DME	800 (200th) at 0.5C	118
PP/PE/SO_3^-	0.7/0.8	S/Graphene	0.9−1.1	1 M LiTFSI in DOL/DME + $LiNO_3$	626 (1000th) at 0.25C	119
PP/Sulfonated acetylene black	0.13/10	S/C-PANI	3	1 M LiTFSI in DOL/DME + $LiNO_3$	939 (100th) at 0.75C	120
PP/Sulfonated UiO-66 MOFs/Nafion	1.1/4	S/rGO	1.7	1 M LiTFSI in DOL/DME	845.7 (200th) at 0.2C	285
PP/(rGO)/sodium lignosulfonate	0.2/NA	S/C	1.5	1 M LiTFSI in DOL/DME + $LiNO_3$	649 (500th) at 2C	284
Al_2O_3/PEP/Lithiated Nafion	NA/5	S/rGO	1	1 M LiTFSI in DOL/DME + $LiNO_3$	∼790 (1000th) at 1C	286
Al_2O_3/PP/MOFs/Sulfonic polymer	NA	S/CNTs	2.4	1 M LiTFSI in DOL/DME + $LiNO_3$	1000 (1000th) at 1C	283
PVDF/UiO-66-SO_3Li	NA/22	S/CMK3	2.0	1 M LiTFSI in DOL/DME + $LiNO_3$	580 (500th) at 0.5C	185
			Na−S			
PP/Sodiated Nafion	NA/0.5	S/C	2	1 M $NaClO_4$ in TEGDME	350 (20th) at 0.1C	287
Sodiated Nafion/CNFs	NA	Na_2S_6/CNFs/AC	∼0.85	1.5 M $NaClO_4$ in TEGDME + $NaNO_3$	550 (100th) at 0.2C	288
Sodiated Nafion/AC-CNFs	0.2/30	Na_2S/AC-CNFs	∼0.9	1.5 M $NaClO_4$ in TEGDME + $NaNO_3$	∼580 (100th) at 0.2C	289
GF/Al_2O_3-Nafion	NA/8.5	Na_2S_5/Carbon	NA	1 M NaOTf in TEGDME	250 (100th) at 0.1C	290
PMTFSINa-grafted PP	NA	S/Mesoporous C	0.5−0.8	1 M NaTFSI in PC/FEC	716 (200th) at 0.1C	174
			K−S			
PP/PE/PP + Potassiated Nafion + Carbon paper	NA	S/CNTs	0.478	KFSI in DME (n_{salt}:$n_{solvent}$ = 0.5)	720 (1st) at 0.05 A g^{-1} 184 (5th) at 0.05 A g^{-1}	71

[a]"Separator + Material" represents the case of introducing the self-standing interlayer into the interface; "Separator/Material" represents the case of directly coating the functional material on the separator.

bromide (CTAB)/carbon nanotube (CNT)/$Ti_3C_2T_x$ Mxene hybrid-modified polypropylene separator, termed CCNT/Mxene/PP. The Mxene displayed mild adsorption energies for Li_2Se_4 (E_b = −0.249 eV) and Li_2Se_6 (E_b = −0.359 eV) due to Lewis acid−base interactions between Ti sites and polyselenides species. The additional incorporation of CTAB induces stronger polyselenides' affinity (−1.764 eV for Li_2Se_4, −1.697 eV for Li_2Se_6). It was argued that the anchored CTAB molecules modified the Mxene substrate surface properties, such as charge density distribution and wettability, thus being responsible for the enhanced Lewis acid−base interaction. Accordingly, the CCNT/Mxene/PP separator showed stronger Ti−Se bond intensity in the corresponding XPS profile after the first cycle of Li−Se as compared to Mxene/PP. With strong chemical adsorption of polyselenides, the hybrid separators enabled minimal capacity decays for both Li−Se and Na−Se, being at 0.13% and 0.44% per cycle at 0.1C. The pristine PP separator had 0.75% and 1.00% decay for Li−Se and Na−Se systems, respectively.

Polar materials are also capable of improving the electrolyte wettability and ionic transport of the standard polyolefin separators (PP and PE) that are hydrophobic. The enhancement is achieved through polar−polar interactions. However, excessive coatings will compromise the alkali ion diffusion kinetics across the separator due to the decreased porosity and increased tortuosity. Conversely, there is also an implicit requirement that the incorporated functional layer sufficiently covers the surface such that PS/PSe trapping is retained. A series of ionic conductors, such as lithiated MoS_2,[281] laponite,[224] $Li_4Ti_5O_{12}$,[235] Li_3PO_4,[226] and LiF,[282] were incorporated into the carbon framework, for constructing favorable hybrid separators. These enhanced ionic transfer in addition to being electrocatalytic. It is doubtful, however, that the above materials, or similar structures, are able to provide solid-state ion conduction at rates above that of ion conduction through electrolyte-filled pores. The enhancement is likely to rather be a result of improved electrolyte wetting on these surfaces.

It has been reported that such functional layers undergo reversible lithiation and sodiation upon cell discharge.[175,261] One issue that needs to be further addressed with redox active functional species, such as various transition metal sulfides, is their actual contribution to the measured reversible capacity. Usually, this capacity contribution to the total capacity is neglected, which is reasonable for layers where the total mass loading is less than a tenth of the active material loading on the cathode. However, if the two mass loadings are on the same order of magnitude, what appears as enhanced stability of the cathode may in part be additional capacity from the separator. Therefore, it is important to track and account for the mass

https://doi.org/10.1021/acs.chemrev.1c00838
Chem. Rev. 2022, 122, 8053−8125

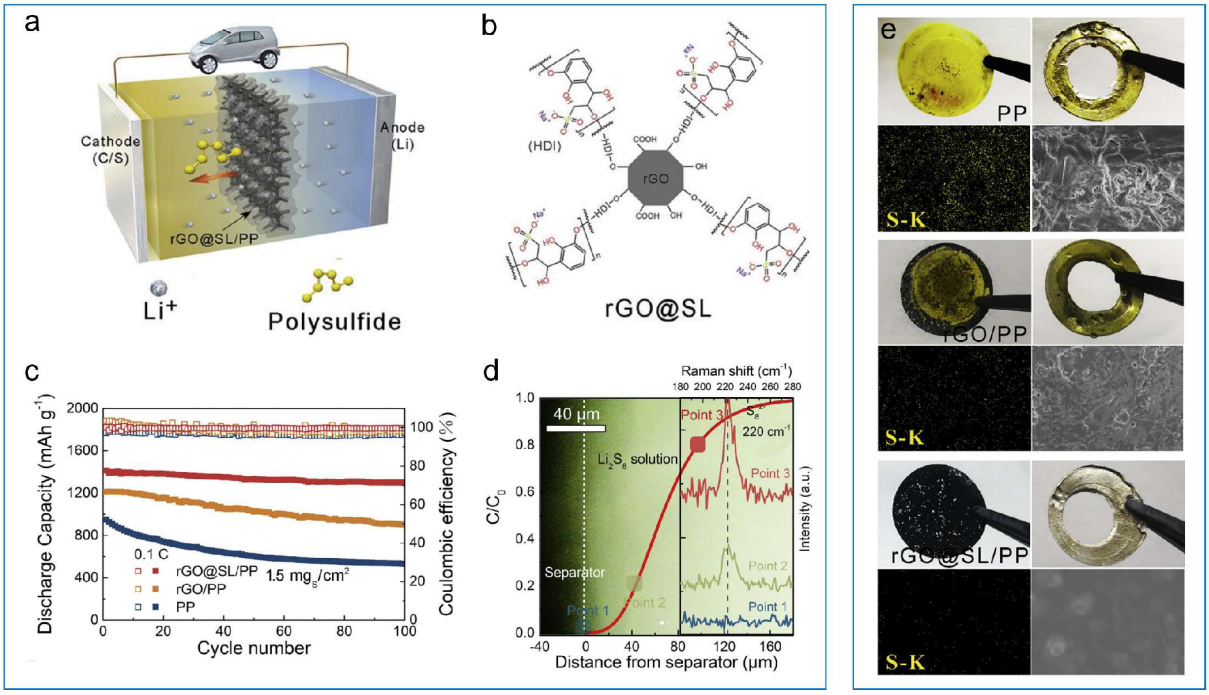

Figure 12. (a) Schematic diagram of the rGO@SL/PP separators for inhibiting the LiPS shuttling effect in Li−S batteries. (b) Molecular structure of rGO@SL. (c) Cycling performances and Columbic efficiencies at 0.1C for cells with PP, rGO/PP, and rGO@SL/PP separators. (d) Concentration of LiPSs at different potentials; the inset image shows the LiPS concentration evolution and the corresponding Raman spectra at points 1, 2, and 3. (e) Digital images and SEM images of the separators and Li metals after 10 cycles. A hole was created on Li foil to allow direct laser illumination on the separator. Reproduced with permission from ref 284. Copyright 2018 Elsevier.

loading of ion active materials on the separators. Employing thick redox active functional layers should not be perceived as "cheating", however, as long as the extra weight is entered into the capacity calculations. Rather, having what is, in effect, a redox active bilayer, with the primary active material on current collector plus a different material on the separator, may be viewed as a clever method for boosting the overall areal capacity and energy. Therefore, more research focusing on thick (yet ion and electrolyte permeable) redox active functional coating is encouraged.

7.1.3. Electrostatic Repulsion. A strategy based on electrostatic repulsion has been established for achieving permselectivity. This strategy employs a charge repulsion effect between the anionic groups such as SO_3^-, COO^-, and CO^- on the functional separator and the solution-dissolved polysulfide anions (S_x^{2-}) for achieving permselectivity. Various studies to employ this approach to inhibit crossover are summarized in Table 8. Moreover, the anionic functional groups have been reported to improve the kinetics of cation diffusion in the electrolyte, contributing to the lower chemical polarization and improved rate capability.[283,284]

Zhang and co-workers employed Nafion film coatings on separators to improve the performance of Li−S batteries, since Nafion contains anionic sulfonate-ended perfluoroalkyl ether groups.[117] The film acted as a cation permselectivity sieve which allowed Li^+ ions but rejected polysulfides due to the electrostatic repulsion. A Nafion loading of 0.7 mg cm^{-2} was necessary to achieve performance, balancing conformality with not increasing the diffusional polarization with thicker films. The functionalized separator stabilized the fade at 0.08% per cycle at 1C for over 500 cycles, versus the baseline at 0.13% decay per cycle. The authors developed an ultrathin repulsive layer composed of graphene oxide (GO) and Nafion.[118] The GO was loaded at 0.0032 mg cm^{-2} and served as a compact substrate enabling for the uniquely low mass loading of Nafion at 0.05 mg cm^{-2}.

Various anionic functional-group-terminated materials, including acetylene black,[120] modified MOFs,[185,283,285] graphene,[284] and MWCNT,[205,291] have been demonstrated to improve the permselectivity of the separator as well. Per Figure 12a and b, Duan et al. combined rGO with lignosulfonate (SL), which had abundant sulfonic groups by a cross-linking reaction, and then coated the composite (rGO@SL) onto a PP separator.[284] The measured negative surface zeta potential of −75.14 mV indicated that there would be an electrostatic repulsion between polysulfide anions and the modified separator, which was ascribed to the grafted sulfonic groups ($SL\text{-}SO_3^-$). Theoretical stimulation quantified the interaction energies between $SL\text{-}SO_3^-$ and LiPSs anions, which appeared more repulsive as the chain length of the polysulfides increased. The calculated values were 0.94 eV, 0.72 eV, 0.64 eV, and 0.46 eV for S_8^{2-}, S_6^{2-}, S_4^{2-}, and S_2^{2-}, respectively. Figure 12d shows the concentration of LiPSs adjacent to the separator and the corresponding Raman signal. Polysulfides were almost negligibly present near the rGO@SL surface but increased in concentration with distance. According to Figure 12c the cell with the rGO@SL/PP separator delivered a stable performance with a capacity fade of 0.08% per cycle. A separator with a coating of rGO/PP and an unmodified PP separator displayed fades of 0.3% and 0.5%, respectively. The postcycled separators and Li anodes were compared, as shown in Figure 12e. After 10 cycles both the pristine and rGO/PP separators appeared yellow, with the corresponding Li anodes exhibiting dendrite-like morphologies. By contrast, no LiPS species were detected on the rGO@SL/PP separator or the

https://doi.org/10.1021/acs.chemrev.1c00838
Chem. Rev. 2022, 122, 8053−8125

corresponding Li anode (confirmed by element mapping), while the Li metal remained smooth.

The use of electrostatic repulsion to modify separators has also been explored with inorganic materials, such as with negatively charged montmorillonite.[292] Kim and co-workers intentionally applied an electric field to polarize ferroelectric barium titanium oxide ($BaTiO_3$ or BTO).[293] The polarized BTO embedded in the PE separator consequently displayed strong and persistent polysulfide repulsion. As a result, overcharging of the Li−S cell was reduced by a factor of 3. For the PE-BTO separator without pretreatment in an electric field, the LiPSs shuttling was still extensive, supporting the key role of electrostatic repulsion.

Zhou's group investigated the "pore-size effect" of MOF-functionalized separators for Li−S batteries, employing operando Raman spectroscopy. It was verified that the polysulfides adsorbed on metal sites inside MOF channels rendered extra "sulfur loss" and low initial CE, with irreversible formation of metal−S_x^{2-} bonds.[283] The Lewis acid−base interaction was more apparent for the MOF separators with higher pore sizes of 9.0 Å (Ms-9.0), compared to the counterparts with pore sizes of 2.9 and 3.4 Å (Ms-2.9 and Ms-3.4). In consequence, this led to more sulfur loss in Ms-9.0 and inferior cell capacity, which was 200 mAh g^{-1} lower than the cells with Ms-2.9 and Ms-3.4 at 0.1C. However, Ms-2.9 and Ms-3.4 separators were encountered with more sluggish Li^+ ions transport arising from narrowed pore sizes. With the expectation of reducing sulfur loss and retaining facile Li^+ ion transport, a negatively charged sulfonic polymer (NSP) was incorporated into the channels of Ms-9.0. The electrostatic repulsion of functional channels reduced the irreversible metal−sulfur interaction. Moreover, the Li^+ transference number of Ms-9.0 was promoted from 0.68 to 0.82 by the sulfonic modification. The optimized separator structure enabled the Li−S cell to deliver an initial reversible capacity of 1279 mAh g^{-1} with a decay rate of 0.022% per cycle over 1000 cycles. The same group also investigated the interplay between chemical interactions and electrostatic repulsion. On the basis of Raman spectroscopy, the polar $VOPO_4$ treated with LiPSs was demonstrated to evolve into a polysulfide-phobic interface.[294]

In the case of Na−S and K−S systems, the cation permselective Nafion films are generally pretreated with sodium or potassium ions and aqueous hydroxide solutions, which ensures ion conductivity in the sodiated or potassiated film.[71,287] The earliest application of sodiated Nafion film in suppressing NaPSs' shuttling was reported by Kaskel and co-workers, employing a cathode of sulfur mixed with MWCNTs.[287] The electrostatic repulsion from the $-SO_3^-$ blocked the dissolved NaPSs, analogously as it would with the lithium system. Manthiram et al. proposed that the Nafion film could physically block the migration of the dissolved NaPSs across it, as the van der Waals size (0.5−5.0 nm) of the NaPSs was estimated to be on the same order of magnitude as the inherent porosity of the film.[289] Accordingly, the Na ion selective separator was applied in two different Na−S systems, a Na_2S cathode or Na_2S_6 polysulfide catholyte.[288,289] The Nafion-based film promoted deep discharge of the Na−S batteries.[288] The cell with the functional separator delivered a higher retained capacity as compared to the one with a pristine separator, 550 mAh g^{-1} after 100 cycles at 0.2C versus 200 mAh g^{-1}after 55 cycles.

Employing the potassiated Nafion film (Nafion-K^+) as cationic selective interlayer suppressed the polysulfides' shuttle in a K−S cell, minimizing overcharge as well as anode degradation.[71] However, the cell with Nafion-K^+ film still suffered from the substantial capacity decay, with 184 mAh g^{-1} remaining after five cycles. The difference in its efficacy versus Li−S and Na−S seems to be an indication that the K−S failure may not necessarily be due to polysulfide shuttle. The other limitations, such as sluggish reaction kinetics, may impede the high sulfur utilization. Further analysis is needed to understand the failure mechanisms in the K−S system. Additionally, electrocatalytic materials for accelerated K−S redox kinetics should be explored, since there are few reports currently available.

7.2. Promoting Interfacial Charge and Mass Transfer

The inherently low electronic conductivities of sulfur (5×10^{-30} S cm^{-1}) and of the discharge products (10^{-13} S cm^{-1} for Li_2S) inevitably result in sluggish redox kinetics, higher polarization, and poor active materials utilization especially at high sulfur loadings. The secondary carbon phase(s) within a typical cathode will form a conductive network that compensates for this. However, when a dense layer of Li_2S, Na_2S, or K_2S is not inside the carbon host but at the separator−cathode interface, ionic flow to the underlying unreacted material can effectively cease. Although the outer sulfide layer should remain electrically connected to the underlying current collector through the mutually contacting carbon host, it is the blocked ionic diffusion that leads to an impedance rise and a capacity decay. As the sulfide layer thickens, its IR losses increase, resulting in the inability to dissolve the layer upon cell charging. Having the functional separator serve as a secondary electrically conductive interface aids the overall redox kinetics, including by allowing for sufficient electrical conductivity so as to dissolve the sulfide layer. Some reports have demonstrated the advantage of pasting carbon on polymeric separators over incorporating them into the cathode for promoting sulfur utilization and cycling stability.[121,122] Ionic flow can be facilitated through the actual functional separator, which then acts as a fast path for the Li^+, Na^+, and K^+ to reach the active materials inside the host. In general, however, it is believed that the overriding role of an electrically conductive functional layer is to dissolve the blocking Li_2S, Na_2S, and K_2S surface layers.

Figure 13a illustrates how such a functional separator prevents the accumulation of a dense passivating layer and the consequent clogging of the ionic channels. According to Table 9, various carbons and conductive polymeric films have been employed for functionalizing the separator, including microporous carbon paper,[200] a Super P carbon-coated separator,[295] a graphene-embedded carbon fiber (GFC) film,[250] a polypyrrole film,[187] and a 3D graphene/carbon nanotube composite framework.[296]

Cui et al. designed a 2-μm-thick Super P carbon coating for the separator to prevent the formation of the sulfide blocking layer in a Li−S cell.[295] The carbonaceous film was too thin to effectively obstruct the migration of LiPSs to the anode, allowing LiPSs to diffuse back and forth and to precipitate on the separator−cathode interface. As a result of the electronically conductive network, only small bridge-like structures were observed at the interface of the cathode and the Super P-modified separator after 50 cycles. The presence of inactive S-related species layers could be prevented by other conductive

https://doi.org/10.1021/acs.chemrev.1c00838
Chem. Rev. 2022, 122, 8053−8125

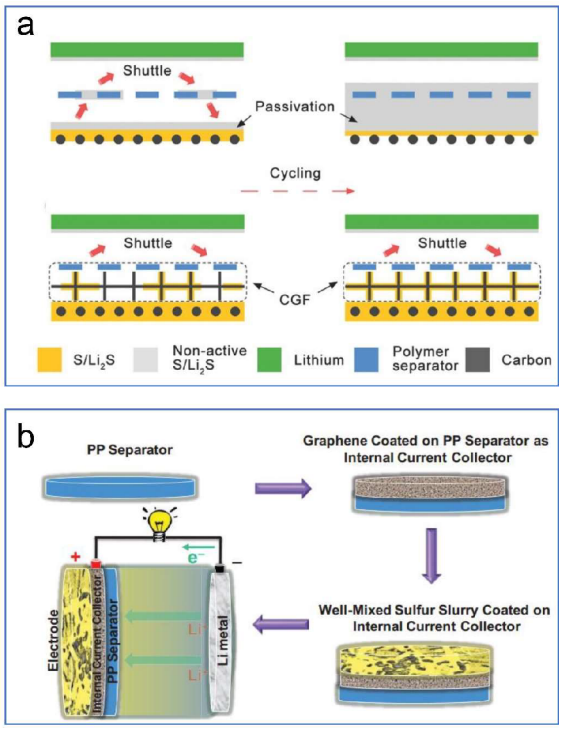

Figure 13. (a) Schematic illustration of how a functional separator with an electrical coating prevents the formation of an electrically and ionically insulating sulfide blocking layer at the cathode−separator interface. (b) Schematic of the electrode configuration using an integrated structure of sulfur and G@PP separator and the corresponding battery assembly. Panel a is reproduced with permission from ref 121. Copyright 2015 John Wiley & Sons, Inc. Panel b is reproduced with permission from ref 299. Copyright 2014 John Wiley & Sons, Inc.

coatings as well, including Ketjen black and MCNTs. However, the sulfur layers were not dissolved by insulating coatings such as TiO_2 and Al_2O_3.

Various studies have demonstrated the utility of an electrically conductive layer at the separator−cathode interface.[174,245,274,297,300−304] For instance, the Li−S cell with a carbon nanofiber@mesoporous δ-MnO_2 nanosheet-coated separator (HM separator) was reported to retain a reversible capacity of 856 mAh g^{-1} after 200 cycles.[266] However, its counterpart with a MnO_2-coated separator retained 265 mAh g^{-1}, supporting the key role of the conducting carbon phase. Zhang et al. examined the actual LiPSs transformation sites on the functional separator coated with a spider-web-like nanocomposite.[305] The nanocomposite was based on mesoporous silica ($mSiO_2$) nanospheres and Co nanoparticles that were threaded by interconnected nitrogen-doped carbon nanotubes (NCNTs). Experiments revealed that the LiPSs intermediates were mainly adsorbed and desorbed on the $mSiO_2$ nanosphere surfaces, due to the strong chemical interactions. However, the discharge products (Li_2S_2/Li_2S) were deposited on the conductive networks rather than nonconductive $mSiO_2$ nanospheres. This study elegantly illustrates the essential role of multiphase−multifunctionality architectures in optimizing functional separator performance. More studies involving similar site-specific analysis are needed, with a range of possible analytical techniques such as SEM, TEM, atomic force microscopy (AFM), and tip-enhanced Raman spectroscopy being well suited to probe the local phase formation. More broadly, it is evident that the best performing functional separators are multiphase nanocomposites, with each phase serving a complementary function, *e.g.* a phase for electrical conductivity, a phase for chemical polysulfide trapping, and a phase for electrocatalytic conversion, all interspersed at the nanoscale.

Li and Cheng et al. created an integrated separator−current collector that replaced a standard Al for the cathode side

Table 9. Recent Advances in Functional Separators/Interlayers Based on a Conductive Network at the Cathode−Separator Interface

Separator[a]	Film mass loading (mg cm^{-2})/ Film thickness (μm)	Cathode	Active materials loading (mg cm^{-2})	Liquid electrolyte	Cyclability (mAh g^{-1}) after *n* cycles	Ref
			Li−S			
PP/Super P carbon	0.5/1	S	1.5−2	1 M LiTFSI in DOL/ DME + $LiNO_3$	600 (200th) at 0.1C	295
Separator + GFC	NA	S	1.2	1 M LiTFSI in DOL/ DME + $LiNO_3$	698 (300th) at 1C	250
PE + GO/CNTs	1.1/30	S	1	1 M LiTFSI in DOL/ DME + $LiNO_3$	671 (300th) at 0.2C	297
PP/Cellular grapheme framework	0.3/30	S	1.2	1 M LiTFSI in DOL/ DME + $LiNO_3$	800 (300th) at 0.5C	121
PP + G/CNTs	0.2/15.2	S/G/CNTs	1.64	1 M LiTFSI in DOL/ DME + $LiNO_3$	445 (500th) at 2C	296
GF/$Ti_3C_2T_x$/CNTs-PEI	0.2/NA	S/$Ti_3C_2T_x$ /CNTs-PEI	2.6	1 M LiTFSI in DOL/ DME + $LiNO_3$	980 (500th) at 1C	298
PP/2D VS_2	0.14/∼5	S	1.5	1 M LiTFSI in DOL/ DME + $LiNO_3$	908 (300th) at 0.2C	278
			Na−S			
Separator + CNTs (or CNFs, or CCFs) film	NA	S	NA	1.5 M $NaClO_4$ in TEGDME + $NaNO_3$	∼ 400 (20th)	10
			K−S			
Celgard Separator + SWCNTs	0.2	S/CNFs	1	KOTf in TEGDME	600 (500th) at 0.2C	73

[a]"Separator + Material" represents the case of introducing the self-standing interlayer into interface; "Separator/Material" represents the case of directly coating the functional material on the separator.

https://doi.org/10.1021/acs.chemrev.1c00838
Chem. Rev. 2022, 122, 8053−8125

Table 10. Recent Advances on the Functional Separators/Interlayers Facilitating Redox Kinetics as Electrocatalysts

Separator[a]	Film mass loading (mg cm^{-2}) /Film thickness (μm)	Cathode	Active materials loading (mg cm^{-2})	Liquid Electrolyte	Cyclability (mAh g^{-1}) after n cycles	Ref
			Li−S			
PP/RuO_2/Carbon	0.3/16	S	NA	1 M LiTFSI in DOL/DME + $LiNO_3$	859 (100th) at 0.2C	314
PP/KB@Ir	0.2/20	S	0.8	1 M LiTFSI in DOL/DME + $LiNO_3$	452 (500th) at 1C	315
PP/MoP/rGO	0.45/10	S/CNTs/AB	3.6−3.88	1 M LiTFSI in DOL/DME + $LiNO_3$	760 (500th) at 0.5C	225
PP/PE/PP/MoS_2/PAA	0.1/3	S	4	1 M LiTFSI in DOL/DME + $LiNO_3$	450 (400th) at 1C	281
PP/Co-N_x/Graphene	0.2/4.1	S/CNTs	1	1 M LiTFSI in DOL/DME + $LiNO_3$	612 (500th) at 2C	316
PP/NbN/NG	0.21/10	S/Ketjen Black	1.5	1 M LiTFSI in DOL/DME + $LiNO_3$	714.5 (400th) at 1C	317
PP/NG/Fe SACs	0.1/7	Li_2S_6/CNF	4.5	1 M LiTFSI in DOL/DME + $LiNO_3$	892 (750th) at 0.5C	318
PP/S-doped TiN	0.35/25	S/rGO	0.9−1.1	1 M LiTFSI in DOL/DME + $LiNO_3$	713.5 (500th) at 1C	319
PP/Ce-MOF/CNTs	0.4/8	S/Ketjen Black	6	1 M LiTFSI in DOL/DME + $LiNO_3$	886.4 (200th) at 0.1C	320
PP/ReS_2-NG	0.09/0.5	S/CNTs	3.27	1 M LiTFSI in DOL/DME + $LiNO_3$	416.8 (800th) at 2C	275
PP/Sb_2Se_{3-x}/rGO	0.5/32	S/CNTs	1.8	1 M LiTFSI in DOL/DME + $LiNO_3$	847 (500th) at 1C	321
PP/TiO_{2-x}	0.12/0.5	S/rGO	3.6	1 M LiTFSI in DOL/DME + $LiNO_3$	631 (500th) at 2C	322
PP/Ti_3C_2@iCON	0.1/5	S/CNTs	1.2	1 M LiTFSI in DOL/DME + $LiNO_3$	706 (2000th) at 2C	323
PP/TiO_2-TiN	0.23/9	S/MWCNTs	1.2	1 M LiTFSI in DOL/DME + $LiNO_3$	704 (2000th) at 1C	324
PP/Co_9S_8/CoO	0.3/18	S/Graphene	2.5	1 M LiTFSI in DOL/DME + $LiNO_3$	471.8 (1000th) at 1C	325
PP/TiO_2/$Ti_3C_2T_x$/G	0.15/5	S/CMK-3	1.2	1 M LiTFSI in DOL/DME + $LiNO_3$	800 (1000th) at 2C	267
PP/MoO_2/Mo_2N	0.51/9	S/Carbon Black	4.0	1 M LiTFSI in DOL/DME + $LiNO_3$	590 (100th) at 0.2C	326
			Na−S			
GF/HCS/MoS_2	NA/10	S/HCS/MoS_2	0.5−1	1 M $NaClO_4$ in TEGDME	246 (1000th) at 1C	280
PP/PMTFSINa/$Ti_{3-x}CNT_y$	NA	S/Mesoporous C	0.5−0.8	1 M NaTFSI in PC/FEC	962 (200th) at 0.1C	190
GF/2H-$MoSe_2$/N-HCS/GO	0.56/NA	S/2H-$MoSe_2$/N-HCS	0.64	1 M $NaClO_4$ in EC/DEC	484 (500th) at 0.5C	327

[a]"Separator + Material" represents the case of introducing the self-standing interlayer into interface; "Separator/Material" represents the case of directly coating the functional material on the separator.

within a Li−S cell.[299] This architecture is illustrated in Figure 13b, where graphene was directly coated onto a separator followed by filling it with a slurry of sulfur, the architecture termed S-G@PP. As a result, one side of the separator acted also as a current collector, without the need for a supporting Al foil. The flexible structure led to a much lower charge-transfer resistance than for a conventional cell configuration that was employed as a baseline, being at 56 Ω versus 291 Ω. The electrical conductivity of the integrated electrode remained at around 800 S m^{-1} after 50000 bending cycles. A Li−S cell based on the integrated electrode achieved an energy of 1116 Wh kg^{-1} (taking into account the weight of the separator) at a current of 0.3 A g^{-1}. This is more than twice the energy when the cathode was based on an Al foil-S + PP separator cell, which is 450 Wh kg^{-1}. Wu et al. reported an Mxene-based integrated structure, based on delaminated Ti_3C_2 nanosheets coated on a polypropylene separator (d-Ti_3C_2/PP) and alkalized Ti_3C_2 nanoribbons as the S host.[306] The integrated electrode delivered an energy of 833 Wh kg^{-1} after 50 cycles at 0.5C. Research on new architectures and associated mechanistic insights for integrated separator−collector architectures is an exciting future research direction, with relatively few publications in the area to date.

Yu et al. applied various conductive carbonaceous films such as carbon nanofibers (CNFs), carbon nanotubes (CNTs), and commercially available carbon foams (CCFs) to enhance the performance of Na−S cells.[10] The CCFs outperformed the other two carbon interlayers, enabling an initial reversible capacity value more than 1000 mAh g^{-1} upon deep discharge to 1.2 V. The final discharge products consisted of a mixture of Na_2S_2 and Na_2S, indicating improved but yet still not full sulfur utilization. The authors coated SWCNTs onto a Gelgard separator and employed it for improving the performance of a K−S battery.[73] Upon a discharge down to 1.0 V, the battery with the Gelgard/SWCNT separator delivered a reversible capacity of 1140 mAh g^{-1}, versus 600 mAh g^{-1} for the uncoated baseline. A capacity of 1140 mAh g^{-1} corresponds to 65% sulfur utilization, which exceeds the theoretical capacity of K_2S_2 and approached that of K_2S. Through UV−vis spectroscopy and XPS, the authors observed the formation of

https://doi.org/10.1021/acs.chemrev.1c00838
Chem. Rev. 2022, 122, 8053−8125

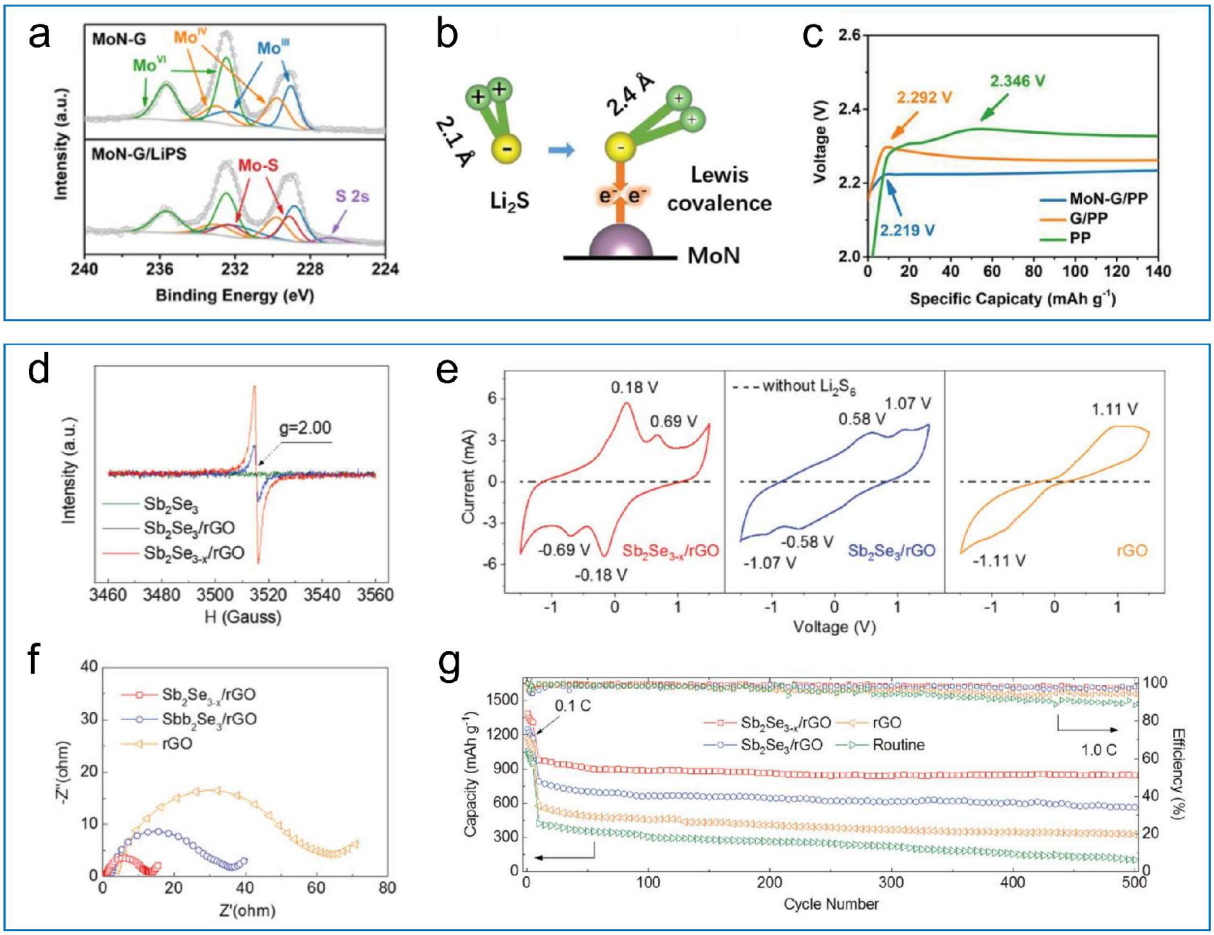

Figure 14. (a) Mo 3d XPS spectra of MoN-G and MoN-G/LiPS. (b) Representation of the covalence-activation mechanism on MoN. (c) Galvanostatic charge curves of the cells with MoN-G/PP, G/PP, and bare PP separators at 0.1C. (d) EPR spectra of Sb_2Se_3, Sb_2Se_3/rGO, and Sb_2Se_{3-x}/rGO. (e) CV curves and (f) electrical Impedance spectroscopy (EIS) spectra of symmetric cells with Sb_2Se_{3-x}/rGO, Sb_2Se_3/rGO, and rGO electrodes. (g) Cycling behavior at 1C of cells with Sb_2Se_{3-x}/rGO, Sb_2Se_3/rGO, and rGO-modifed and routine separators with a sulfur loading of 1.8 mg cm^{-2}. Panels a–c are reproduced with permission from ref 330. Copyright 2019 John Wiley & Sons, Inc. Panels d–g are reproduced with permission from ref 321. Copyright 2019 John Wiley & Sons, Inc.

polysulfide phases of K_2S_6, K_2S_4, and terminal K_2S. The efficacy of the separator was attributed to combined capture of the dissolved polysulfides by physical interaction and the role of the SWCNT as a secondary current collector.

The ionic mass transport across a separator also affects the cell polarization. Nonpolar polyolefin separators such as PP and PE are poorly wetted by polar electrolytes and consequently yield sluggish ionic conduction kinetics. A two-dimensional COF with abundant methoxy functional groups was designed as a separator coating for Li-SeS_2 batteries.[231] It was found that the channels of the COF are preferentially occupied by the LiTFSI salt due to the C–H···F hydrogen bonding and O···Li interactions. As a result of strong separator–electrolyte interaction, the cell with the COF-coated separator delivered improved Li^+ migration coefficients over the pristine separator, 3.47×10^{-10} cm^{-2} s^{-1} versus 1.11×10^{-10} cm^{-2} s^{-1}. With simultaneous blocking of polysulfide/polyselenide crossover, the COF-coated separator resulted in a reversible capacity of 684 mA h g^{-1} at 1C, while employing a relatively high SeS_2 mass loading of 4 mg cm^{-2}. A broad range of polar materials such as O/N/F-containing polymers and carbons have been applied as functional separator, improving electrolyte wettability and ionic conduction.[307−310] For example, a series of Janus separators with separator–electrode interfaces have been successfully employed.[187]

7.3. Facilitating Redox Kinetics as Electrocatalysts

In all alkali metal–sulfur batteries to some extent, sulfur displays sluggish redox kinetics. Moreover, the formation of Li_2S_2/Li_2S, Na_2S_2/Na_2S, and K_2S_2/K_2S passivation layers at the interface will exacerbate the polarization and decrease the reversible capacity. The explicit incorporation of electrocatalysts into the functional separator is a promising strategy to improve the sulfur redox kinetics. Summarized in Table 10, the electrocatalyst candidates for separator modification range from metal-free materials to metal compounds and their composites.[298,311−313] Not all nanostructured phases are effective electrocatalysts with sulfur. Despite strongly anchoring polysulfides, the insulating inorganics showed inferior electrocatalytic performance toward high sulfur utilization in comparison with metal sulfides and nitrides that were conducting.[295] In some cases, to achieve fast electron transfer, conductive networks such as CNTs and graphene were introduced.[266]

Cai et al. investigated the electrocatalytic effect of open metal sites toward LiPSs transformation.[320] Two types of Ce-MOFs with different coordination numbers of carboxyl ligands

https://doi.org/10.1021/acs.chemrev.1c00838
Chem. Rev. 2022, 122, 8053−8125

were compared. In the hexanuclear Ce(IV) clusters [$Ce_6(\mu_3$-$O)_4(\mu_3$-$OH)_4$(-$CO_2)_6$] (Ce-MOF-2), six unsaturated coordination sites were left. The open metal sites in Ce-MOF-2 enabled corresponding stronger adsorption for polysulfides than the counterpart [$Ce_6(\mu_3$-$O)_4(\mu_3$-$OH)_4$(-$CO_2)_{12}$] (Ce-MOF-1) comprising saturated coordination sites. The electrocatalytic effect was evaluated by the cyclic voltammetry of Li_2S_6 symmetric cells with different separators. The Ce-MOF-2/CNT separator rendered higher redox current densities, while Ce-MOF-1/CNT only showed a slight current response. This verified the role of open metal atoms in MOFs as active electrocatalytic sites. A Li−S cell based on the Ce-MOF-2/CNT separator retained a capacity of 839 mAh g^{-1} over 800 cycles at 1C, while only 349 mAh g^{-1} was retained with the Ce-MOF-1/CNT-based cell.

Based on polar interaction with polysulfides, various conductive metal carbides, nitrides, phosphides, sulfides, and selenides also act as electrocatalysts for the sulfur redox reaction.[225,269−271,328,329] Fan and Zhang et al. investigated the electrocatalytic mechanism of metal nitrides for Li−S redox, based on a functional interlayer of MoN supported on graphene, termed MoN-G.[330] The XPS result shown in Figure 14a demonstrates that MoN chemically interacted with LiPSs due to the Mo atoms being Lewis acid sites, along with the formation of a Mo−S bond. Associated DFT simulations demonstrated the high adsorption energies of Li_2S_4 (−7.33 eV) and Li_2S (−6.18 eV) on MoN, which favored Li_2S nucleation. Per Figure 14b and c, the Li−S bond distance of Li_2S was elongated after the adsorption on the MoN surface as a result of strong Mo−S interaction, which was beneficial for weakening the Li−S bond and reducing the energy barrier for Li_2S decomposition. The authors pointed out that such a covalence-activation mechanism could extend to other Lewis acid exposed surfaces such as WC (001) and ZrN (111) as well. A separate study examined the Li_2S nucleation−growth−decomposition process over the niobium nitride/N-doped graphene (NbN/NG) composite coated on a separator.[317] The results demonstrated the requisite role of polysulfides' affinity for electrocatalytic materials.

Jiang designed a functional glass fiber separator with 2H-$MoSe_2$/nitrogen-doped hollow carbon spheres/graphene oxide composite coating (2H-$MoSe_2$/N-HCS/GO + GF), as a polysulfide barrier and reaction electrocatalyst for Na−S batteries.[327] Through cyclic voltammetry under different scan rates, the authors compared the interfacial Na ion diffusion kinetics. Accordingly, the 2H-$MoSe_2$/N-HCS/GO + GF separator delivered 1−2 orders of magnitude higher Na ion diffusion coefficients in Na−S cells versus pristine GF or N-HCS/GO + GF separators. The combined experimental and modeling results demonstrated strong NaPS adsorption and a low Na_2S diffusion energy barrier (0.21 eV) on 2H-$MoSe_2$. This accelerated the sulfur redox process, promoting both rate capability and cycling life in the Na−S cells.

Various defective sulfur hosts including MoS_{2-x},[331] $Fe_{3-x}C$,[332] and Nb_2O_{5-x}[333] were successively fabricated as functional separator electrocatalytic phases. Chen et al. applied defect engineering to tailor the electronic structure of antimony selenide (Sb_2Se_3), for building a multifunctional LiPSs barrier.[321] Selenium vacancies (V_{se}'s) were induced through chemical reduction and consequent thermal shock and were verified through an EPR signal with a g-value of 2.00. These results are shown in Figure 14d. Based on first-principles calculations, a shallow donor level (defect level) emerged within the band gap of Sb_2Se_{3-x}, such that the electronic conductivity could be increased. A higher binding energy of Sb_2Se_{3-x} with Li_2S_6 (−2.33 eV) than with Sb_2Se_3 (−0.49 eV) was also derived from the calculations. To further evaluate the charge/mass transfer and redox kinetics on defect-rich Sb_2Se_{3-x}, the authors tested the Li_2S_6 symmetric cell with different electrodes. Per Figure 14e, two pairs of intense redox peaks were observed in the CV profile of the Sb_2Se_{3-x}/rGO cell, while Sb_2Se_3/rGO and rGO cells exhibited larger voltage hysteresis and a lower current response. Figure 14f shows that the Sb_2Se_{3-x}/rGO symmetric cell has the lowest charge-transfer resistance in EIS spectra. The results validated the fastest reaction kinetics for the LiPSs' conversion on the Sb_2Se_{3-x}/rGO surface, aided by the vacancy defects. The Sb_2Se_{3-x}/rGO-modified separator improved the redox kinetics in the Li−S cell, with a retained capacity of 847 mAh g^{-1} after 500 cycles at 1C versus 565 mAh g^{-1} for the baseline Sb_2Se_3/rGO-modified separator. These results are shown in Figure 14g. Mai el al. fabricated the defective TiO_2 nanosheets with oxygen vacancies (Ovs-TiO_2), employing this material as a functional coating on PP for Li−S.[322] It was reported that the unsaturated bonds due to the oxygen vacancies improved LiPSs' chemisorption as well as the overall redox kinetics. Huang et al. demonstrated an improved chemical interaction between lithium polysulfide species and the antisite defects in $Bi_2Te_{2.7}Se_{0.3}$.[334] From these promising results it can be stated that defect engineering represents an exciting emerging research direction which should be further pursued. It is probable that with sufficient defects, many mediocre electrocatalytic materials can achieve state-of-the-art performance in terms of driving the Li−S redox processes and, in parallel, minimizing crossover. While there are limited studies in defect engineering of the Li−S system, the Na−S and K−S systems remain relatively unexplored. Defect-engineered electrocatalytic secondary collectors represent a uniquely promising path for improving the redox kinetics and cyclability for Na−S and K−S systems, especially since their intrinsic performances are often reported as unsatisfactory.

Authors have reported functional separator approaches based on various cooperative mechanisms. A typical cooperative mechanism may be based on a biphasic interface composed of lithiophilic nitrogen-doped graphene (NG) and a sulfiphilic multimetallic layered hydroxide (LDH).[335] The LDH@NG heterostructure on the PP separator acted as the efficient electrocatalyst for electrochemical LiPSs' conversion. It was argued that the NG acted as a surface Li^+-transfer medium enabled by N dopants. Its role as an electrical conductor (N boosts the conductivity of carbon) should also be recognized. A baseline bare LDH displayed the limited electrochemical activity during the Li_2S deposition tests. Nitrogen-doped carbons have been employed as stand-alone phases and within a more complex multiphase network to accelerate the sulfur redox process.[275] Moreover, metal-embedded nitrogen-doped carbons (M-N-C) have been demonstrated to facilitating sulfur redox kinetics, having seen application in other fields such as the hydrogen evolution reaction and oxygen reduction reaction.[336,337] The metal can be in the form of nanoparticles or as individual atoms dispersed on conducting carbon surfaces.[316,318,338] Single atom catalysts (SACs) feature the isolated metal center coordinated with nitrogen dopants, forming metal-N-C moieties. This theoretically enables the maximization of metallic atom utilization efficiency.[339−341]

https://doi.org/10.1021/acs.chemrev.1c00838
Chem. Rev. 2022, 122, 8053−8125

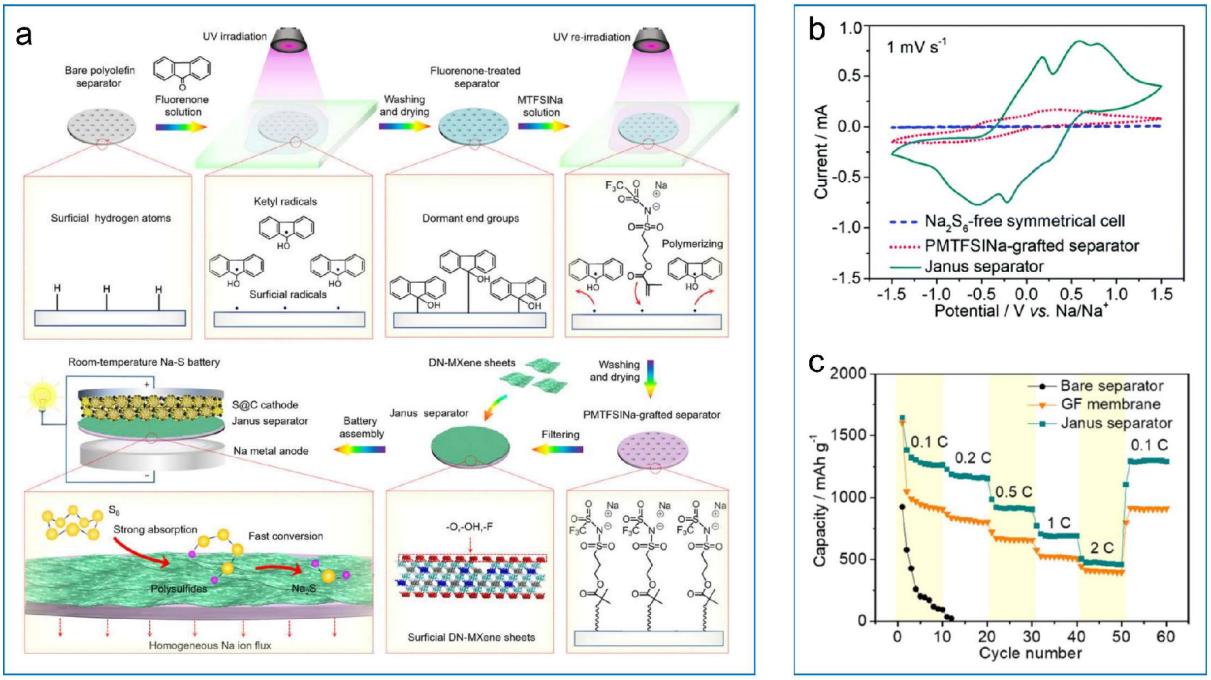

Figure 15. (a) Illustration of the preparation of PMTFSINa-graftedlDN-Mxene-coated separators for room-temperature Na−S batteries. (b) CV curves of Na_2S_6-free and Na_2S_6 symmetrical cells with a PMTFSINa-grafted separator and Janus separator at a scan rate of 1 mVs^{-1}. (c). Rate performances of the NalS@C cells using bare a Celgard 2500 separator, GF membrane, and Janus separator. Reproduced with permission from ref 190. Copyright 2020 John Wiley & Sons, Inc.

Chen et al. fabricated a functional separator modified with single nickel (Ni) atoms on nitrogen-doped graphene (Ni@NG) for Li−S batteries.[342] Through extended X-ray absorption fine structure (EXAFS) and X-ray absorption near edge structure (XANES) analysis, a Ni-N_4 molecular structure was identified. The Ni-N_4 moiety was verified to be electrocatalytic both for sulfur reduction with lithium and for lithium sulfide oxidation. This was based on electrochemical testing of Li_2S_6 in symmetric cells and Li−S in full cells. The voltage polarization in the full cell was only 384 mV at 5C, somewhat lower than the measured 430 mV for Ni particles/NG and the 530 mV for a NG without any Ni. Xie and co-workers studied various SACs (Fe/Co/Ni SACs) for Li−S separator modification.[318] The SAC-modified separator was found to deliver superior performance with the Li−S battery retaining 83.7% capacity (892 mAh g^{-1}) after 750 cycles at 0.5C, at a sulfur loading of 4.5 mg cm^{-2}.

Zhou developed a multifunctional NaPS barrier for rechargeable sodium−sulfur batteries by coating single-ion-conducting polymer and the defect-rich and nitrogen-containing $Ti_{3-x}CNT_y$ Mxene (DN-Mxene) onto a Celgard 2500 separator.[190] Per Figure 15a, the authors took advantage of the ultraviolet (UV)-induced surface graft polymerization for modifying the pristine polyolefin separator with a poly(1-[3-(methacryloyloxy)propylsulfonyl]-1-(trifluoromethanesulfonyl)imide sodium) (PMTFSINa) layer. The grafted PMTFSINa layer ensured increased electrolyte uptake with 274.3% *vs* 81.9% for the pristine polyolefin separator baseline. The Na ion transference number was also increased to 0.58 versus 0.21 for the baseline. According to Figure 15b the DN-Mxene accelerated the conversion kinetics between the polysulfides and Na_2S, as revealed by the higher current response of the composite separator (green line). Per Figure 15c, PMTFSINa and DN-Mxene cooperatively promoted the interfacial mass transfer and sulfur immobilization/conversion, yielding a superior rate performance with the Na−S cell.

A binary cooperative mechanism has been reported with various heterostructures such as VO_2-VN (VN=vanadium nitride),[343] Co_9S_8/CoO,[325] and MoO_x-MoC.[344] The oxides are believed to serve as the polysulfide anchoring mediator while the nitrides, sulfides, and carbides are the electrocatalytically active sites. Even for phosphides, sulfides, and nitrides their outer oxidation layer is believed to have a complementary role during sulfur species redox. For example, it was reported that the outer surface Co-O-P species enabled Co sites to chemically bind with the negatively charged S sites of LiPSs by strong Co−S bonding.[345] It is not obvious how a fully oxidized surface will still maintain the electrocatalytic role, so likely, the oxidation is only partial. Huang observed an electrochemically induced sulfurization of the Co_4N catalysts in Li−S cells.[346] After electrochemical cycling, the resultant mosaic-like hybrid catalysts were based on a combination of Co_4N and various CoS_x phases.

Yang et al. reported a TiO_2-TiN heterostructure which integrated the strong LiPS adsorptive ability of TiO_2 and superior catalytic activity of TiN, thus enabling smooth trapping−diffusion−conversion of LiPSs across the interface.[324] The group also developed a TiO_2-$Ti_3C_2T_x$ heterostructure through a hydrothermal treatment of $Ti_3C_2T_x$, combining it with graphene (GN) for the final functional separator coating.[267] Per Figure 16a−f, the $Ti_3C_2T_x$ nanosheets were continuously oxidized to TiO_2 nanoparticles as hydrothermal time advanced, and the transformation was fully completed after 8 h. Per Figure 16g the heterostructure with the oxidation time of 4 h could almost decolorize the LiPS solution. When coupled with the sulfur cathode and cycled for 200 cycles, $Ti_3C_2T_x$(4 h)-GN exhibited more evident peaks

https://doi.org/10.1021/acs.chemrev.1c00838
Chem. Rev. 2022, 122, 8053−8125

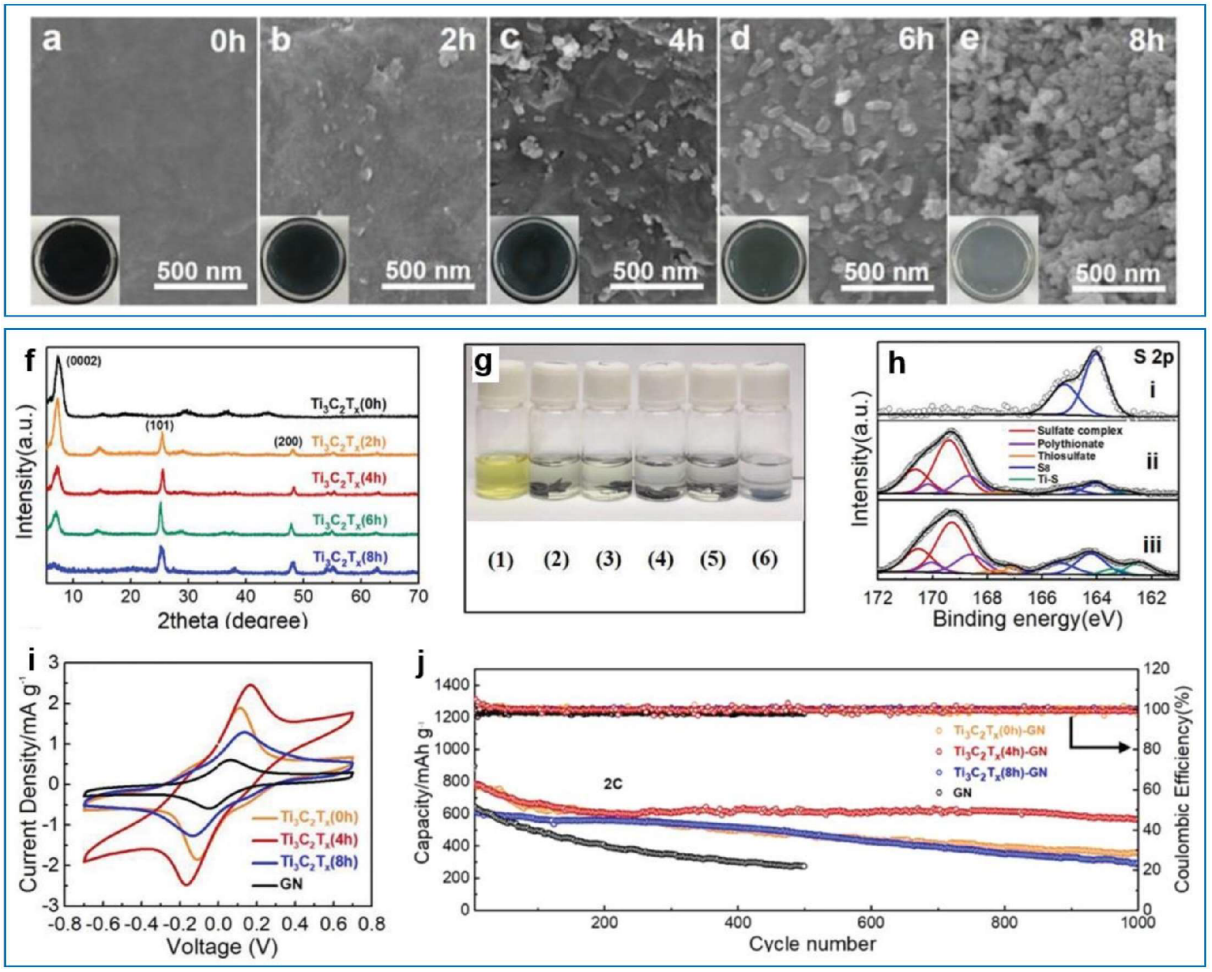

Figure 16. (a–e) SEM images and corresponding color changes of the colloidal solutions with different oxidation times from 0 to 8 h. (f) XRD patterns of $Ti_3C_2T_x$ NSs with different oxidation times from 0 to 8 h. (g) Photograph of Li_2S_6 adsorption by different samples in DME solution after 24 h. (1–6): Blank Li_2S_6, $Ti_3C_2T_x$(0 h), $Ti_3C_2T_x$(2 h), $Ti_3C_2T_x$(4 h), $Ti_3C_2T_x$(6 h), and $Ti_3C_2T_x$(8 h). (h) S 2p spectra of (i) elemental sulfur, (ii) $Ti_3C_2T_x$(0 h)-GN after cycling, and (iii) Ti3C2T_x(4 h)-GN after 200 cycles at 2.35 V. (i) CV profiles of symmetrical Li_2S_6 cell assembly with different heterostructures at the sweep rate 10 mV s^{-1}. (j) Long-term cycling stability at 2C of various interlayers. Reproduced with permission from ref 267. Copyright 2019 John Wiley & Sons, Inc.

assigned to Ti–S bonds and S_8. This is shown in the corresponding S 2p XPS spectrum as compared to $Ti_3C_2T_x$(0 h)-GN, per Figure 16h. It was therefore argued that the TiO_2-$Ti_3C_2T_x$ heterostructure displayed a combination of a strong anchoring effect toward the sulfur species and a facile conversion of LiPSs back to S_8. Figure 16i reveals the favorable redox kinetics on the heterostructure, of which the current response surpassed baseline $Ti_3C_2T_x$ or TiO_2. The Li–S cell with $Ti_3C_2T_x$(4 h)-GN displayed an initial reversible capacity of 800 mAh g^{-1} at 2C and a low fade rate of 0.028% per cycle over 1000 cycles. These results are shown in Figure 16j. Various heterostructures, such as Co_9S_8/CoO,[325] MoS_2/TiN,[347] MoO_2/Mo_2N,[326] and TiN/TiS,[319] have also been employed to modify the separator.

The exploration of electrocatalytic separators for Na–S and K–S as well as for Se-based systems is at a much earlier stage that for Li–S. For the Na–S system, various sulfiphilic sites, including NiS_2,[348] MnO_2,[111] Au,[63] Fe, Cu, and Ni metal clusters,[349] have been explored. Multisulfiphilic sites combining ZnS with CoS_2 exhibited unexpectedly effective Na–S electrocatalysis, where nominally the CoS_2 provided strong adsorption affinity toward polysulfides and ZnS was favorable for decreasing the redox energy barrier.[350] The exploration of new phases and the basic understanding of electrocatalysis for K–S is far behind that of Li–S and Na–S. A single electrocatalyst for the K–S system may or may not be effective as expected, depending on the true extent of the shuttle or redox sluggishness in causing premature failure. Heterostructures with synergetic electrocatalytic mechanisms represent a promising pursuit for K–S, where the kinetics are especially sluggish.

More needs to be understood regarding the fate of the nanoscale phases containing metal atoms (oxides, sulfides, phosphides, and nitrides) deposited onto the functional separator surface. Likely, the less thermodynamically stable structures will oxidize during extended cycling, which is especially the case for many nitrides which are significantly less stable than their oxide counterparts (*e.g.* VN). Does cycling or even storage induced oxidation of the nanoscale phases alter their functionality, transforming them from being electrocatalytic to merely chemically anchoring? It is not obvious why a fully oxidized surface would maintain its electrocatalytic functionality unless the oxide was also active. It may be that a

https://doi.org/10.1021/acs.chemrev.1c00838
Chem. Rev. 2022, 122, 8053–8125

partially oxidized sulfide, phosphide, nitride, *etc.* is highly redox active, while a fully oxidized analog is relatively inert.

Extended analytical and simulation research is needed to understand the role of ternary (*e.g.* oxynitride) materials in both electrocatalysis and anchoring of the polysulfides and polyselenides. The actual fate of the sulfide, phosphide, and nitride nanophases on the separator needs to be further understood as a function of both testing and electrolyte types. After 10, 100, or even 1000 cycles, is the functional separator material even close in structure and chemistry to what was originally synthesized on the separator? Interestingly, since the functional separator phases are electrically connected to the cathode, it is likely they too will undergo phase transitions as a function of applied voltage. These phases may have different functionality depending on whether the cell is being charged or discharged, or even at various states of charge within each regime. Analytical methods on postmortem specimens including XPS, high-angle annular dark-field scanning transmission electron microscopy (HAADF-STEM) combined with electron energy loss spectroscopy (EELS), as well as various synchrotron methods should be able to identify these changes. In parallel, *in situ* synchrotron methods should be able to probe the phase stability versus phase evolution during cell testing. Once the structures are relatively well characterized, simulation should be employed to understand the nuances of electrocatalysis *vs* anchoring for a given structure.

From a practical utilization perspective, the lean-electrolyte condition (E/S ratio of <5 μL mg^{-1}) is being pursued for the Li−S system. As the E/S ratio decreases, the ionic conductivity of the electrolyte decreases due to the increased viscosity caused by a higher concentration of polysulfides.[44,351] Li_2S_2/Li_2S may directly precipitate from a highly concentrated LiPSs solution through the chemical reaction pathway, thus without tightly binding to the conductive backbone. The increased diffusional and charge-transfer resistances will result in more severe polarization. Therefore, the pursuit for superior electrocatalysts under lean-electrolyte conditions becomes particularly important and remains open to exploration.

8. FUNCTIONAL SEPARATOR ADJACENT TO THE ALKALI METAL ANODE

With metal anodes, dendrite growth and the associated unstable SEI are significant problems. With conventional separators, poor electrolyte wetting and uneven pore size distribution result in inhomogeneous ionic flux, aggravating both issues. Tailoring the separator or interlayer is a novel and promising strategy to hinder metal dendrite formation and ensure a long-term cycling performance of alkali metal batteries. While there is a wide number of materials and architectures that have been employed, their role in improving performance may be broadly separated into homogenizing ionic flux to the anode surface, stabilizing the SEI by forming a composite structure, and refining the metallic nucleation sites, as summarized in Figure 17. In fact, the three functionalities are interrelated, with the most effective separator and interlayer materials providing at least two out of the three benefits.

8.1. Modifing Alkali Ion Flux to the Anode Surface

Conventional polyolefin separators possess an inhomogeneous pore distribution and poor electrolyte wettability, which are especially problematic for metal anodes. With conventional powdered graphite, those issues still exist but are mitigated to some extent due to their roughened geometry that naturally promotes wetting.[182] Likewise, an inhomogeneous pore size distribution, leading to nonuniform ion flux, is more of a problem with a planar metal anode than with a thick powdered graphite one. With an inhomogeneous ionic flux to the metal surface, the resultant localized electric field will result in heterogeneous metal deposition and ultimately dendrites. The alkali cation transference numbers (t_+) are generally below 0.5,[191] further promoting dendrite growth per the theories previously discussed.[145]

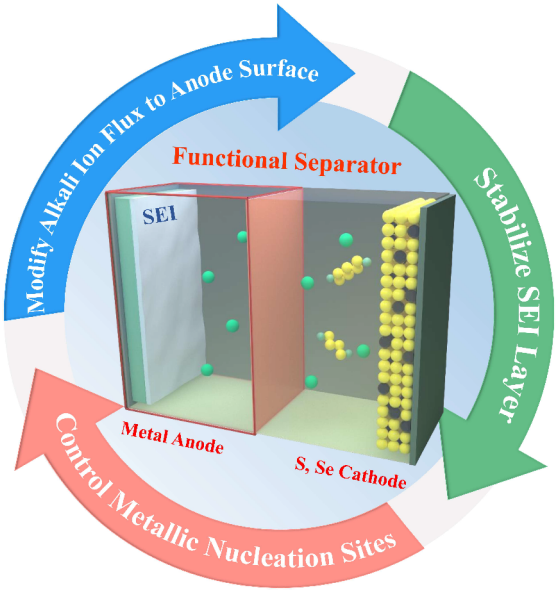

Figure 17. Summary of strategies in functional separators/interlayers for promoting alkali metal anode performance.

The uniformity of the ionic flux across the separator can be improved by introducing ion redistributor phases on the separator. To date, there have been various types of nanostructured ion redistributor phases for a range of Li and Na electrodes, as summarized in Table 11. Example phases include Al_2O_3,[286] nanoporous SiO_2 nanosheets,[352] graphene oxide nanosheets,[353] layered double hydroxide nanosheets,[354] and mesoporous cellulose nanofibers.[355] In principle, the pores and interparticle spaces within functional coatings are capable of channeling the electrolyte and redistributing the ionic flux uniformly.[352,356−358] This should, in turn, promote more uniform nucleation/growth−dissolution of the metal front, reducing the tendency to form dendrites. Zhang et al. utilized a solid-state fast ionic conductor [Al-doped $Li_{6.75}La_3Zr_{1.75}Ta_{0.25}O_{12}$ (LLZTO)] as a Li^+ redistributor coating on the separator.[359] The motivation for this garnet-type structure was its multiple ion conduction channels, including within the crystal structure, along the grain boundaries, and through the interfaces between particles. Improved symmetric cell stability in both carbonate- and ether-based electrolytes was obtained with the LLZTO ion redistributor versus with a bare separator or with a nonconductive Al_2O_3-modified separator. The conductive ionic redistributor can be a solid-state electrolyte with interfacial stability toward metal or an *in situ* formed layer such as a (lithiated/sodiated/potassiated) alloy with high solid-state ionic diffusivity.[360,361] The above findings support the utility of employing various solid-state ionic conductors at the separator, opening the possibility for numerous variants of this approach.

https://doi.org/10.1021/acs.chemrev.1c00838
Chem. Rev. 2022, 122, 8053−8125

Table 11. Survey of Functional Separator Coatings Designed to Enhance the Flux of Alkali Ions to the Anode Surface

Separator[a]	Liquid electrolyte	Electrolyte uptake (wt %) /Contact angle (deg)	Ionic conductivity (mS cm^{-1}) /Transference number	Electrochemical performance (Symmetric cell)	Ref
		Li Anode			
PE/Polydopamine	1 M $LiClO_4$ in EC/PC	112/39	0.3/NA	NA	362
PE/ZrO_2/POSS	1 M $LiPF_6$ in EC/DEC/EMC	340/17	0.46/0.6	NA	363
GF/GO	1 M $LiPF_6$ in EC/DMC	NA	NA	1 mA cm^{-2}, 1 mAh cm^{-2}, 160 cycles	353
PE/Polyphenol-polyamine	1 M $LiPF_6$ in EC/DMC/EMC + VC	128/11.5	0.42/0.49	1 mA cm^{-2}, 1 mAh cm^{-2}, 300 cycles	191
Overoxidised polypyrrole paper	1 M $LiPF_6$ in EC/DEC	NA	1.1/NA	0.5 mA cm^{-2}, 0.5 mAh cm^{-2}, 300 cycles	307
Celgard separator + g-C_3N_4 film	1 M LiTFSI in DOL/DME + $LiNO_3$	53.1/17.2	NA	1 mA cm^{-2}, 1 mAh cm^{-2}, 115 cycles	181
PP/LLZTO/PVDF/$LiClO_4$	1 M LiTFSI in DOL/DME	NA	0.14/0.66	1 mA cm^{-2}, 1 mAh cm^{-2}, 500 cycles	360
PP/silicone nanofilaments	1 M $LiPF_6$ in EC/DMC	287.8/0	1.02/0.59	1 mA cm^{-2}, 1 mAh cm^{-2}, 125 cycles	364
		Na Anode			
PP/Porous SiO_2 nanosheets	0.5 M $NaClO_4$ in EC/DEC	NA	NA	0.5 mA cm^{-2}, 0.75 mAh cm^{-2}, 140 cycles	352
Regenerated eggshell membrane	1 M $NaClO_4$ in PC	290/23.6	NA	NA	365
PP/PMTFSINa layer	1 M NaTFSI in PC/FEC	274.3/45.5	0.46/0.58	0.2 mA cm^{-2}, 0.6 mAh cm^{-2}, 83 cycles	190

[a]"Separator+Material" represents the case of introducing the self-standing interlayer into the interface; "Separator/Material" represents the case of directly coating the functional material on the separator.

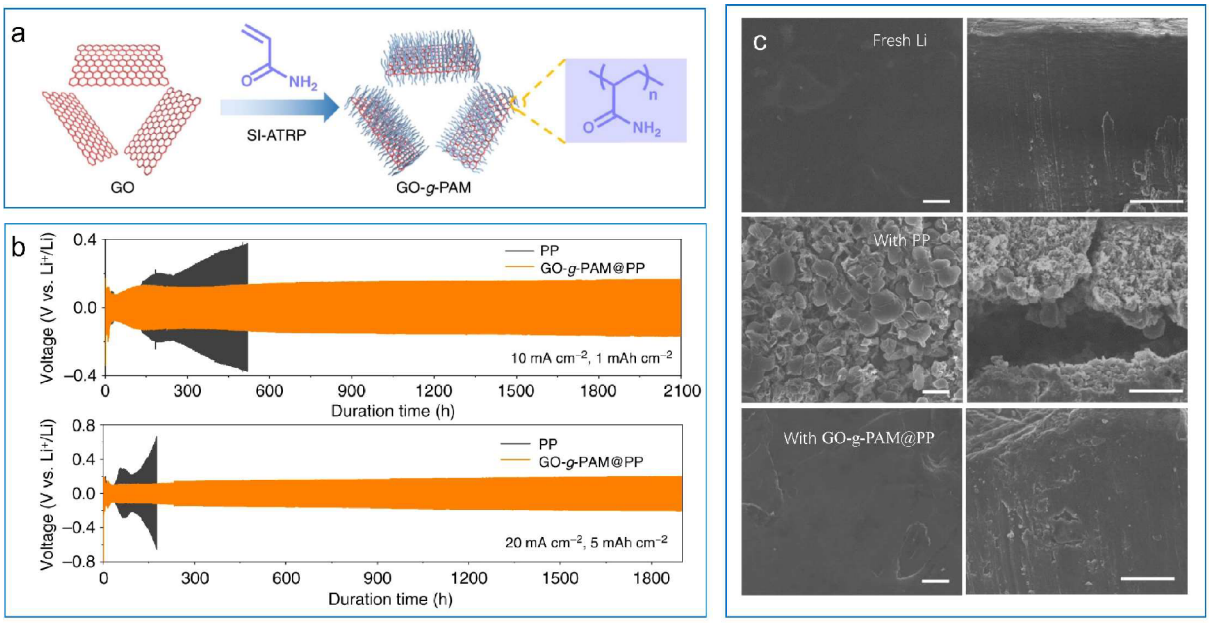

Figure 18. (a) Schematic illustration of the synthesis of GO-*g*-PAM molecular brushes. (b) Associated Li symmetric cell cycling data presented at varying current densities and capacities, comparing the GO-*g*-PAM modified separator and the PP baseline. (c) Top-view (left side, scale bars: 10 μm) and cross-sectional (right side, scale bars: 50 μm) SEM images of a fresh Li metal anode and Li metal anodes assembled with PP and GO-*g*-PAM@PP separators after 100 cycles. Reproduced with permission from ref 366. Copyright 2019 Springer Nature.

One issue that needs to be understood further is the extent to which ionic flux occurs through the solid-state electrolyte (SSE) phases, rather than through electrolyte-wetted interfaces. Apart from highly optimized sulfides, most solid-state ionic conductors display room temperature ionic diffusivities markedly lower than the conventional liquid electrolytes. It is not obvious that the ionic flux through bulk LLZTO, for example, would be on the same order of magnitude as through the electrolyte-filled pores or electrolyte-filled particle−particle interfaces. A typical powder packing density is around 67%, which implies ample continuous electrolyte-filled volume within the functional layer. More research is needed to understand how factors such as solid-state conductor layer thickness, solid-state conductor particle size, particle packing, interparticle pore size distribution, as well as intrinsic porosity all affect the ionic transport characteristics. Moreover, what needs to be understood further is the phase stability of the SSE in contact with the metal anode, especially after prolonged

https://doi.org/10.1021/acs.chemrev.1c00838
Chem. Rev. 2022, 122, 8053−8125

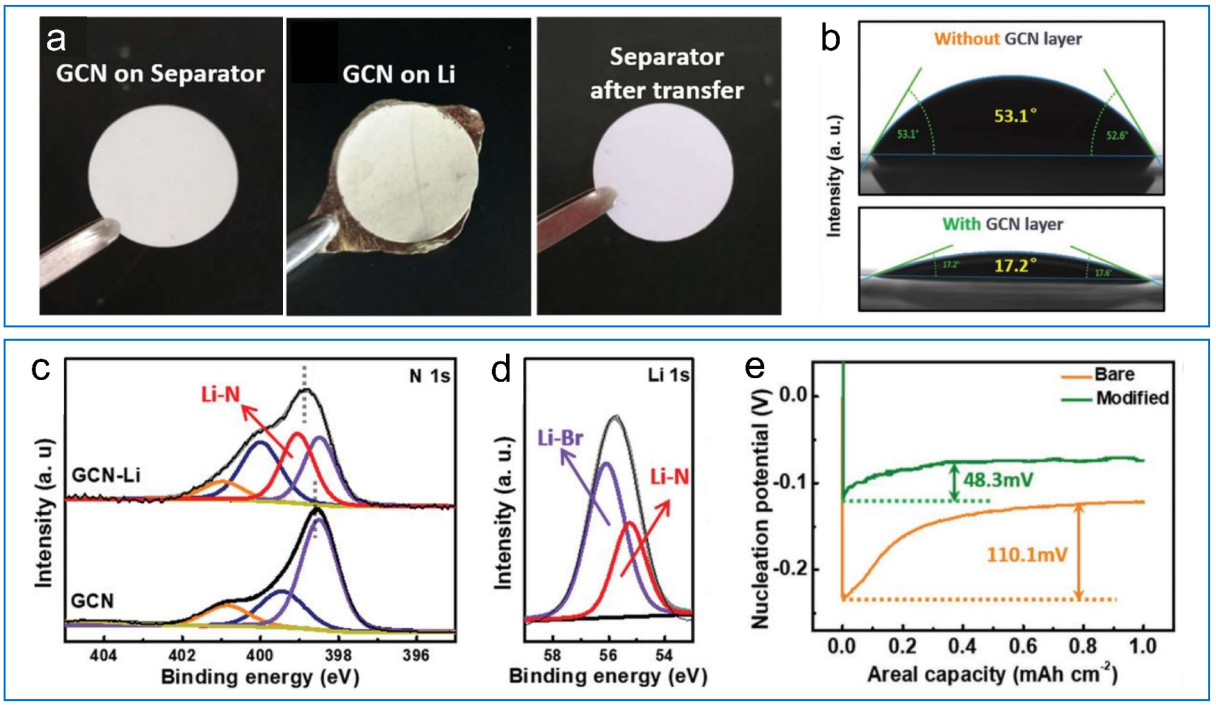

Figure 19. (a) Photographs of graphene-like carbon nitride (GCN) over the separator (left), GCN on Li metal after transfer employing electrolyte wetting (middle), and separator after transfer (right). (b) Contact angles of electrolyte on Li metal without and with a GCN layer. (c and d) N 1s XPS spectra and Li 1s XPS spectra of GCN before and after Li-salt solution treatment. (e) Nucleation overpotentials of asymmetric cells using GCN and baseline uncoated anodes. Reproduced with permission from ref 181. Copyright 2019 John Wiley & Sons, Inc.

cycling. Neither the oxide nor the sulfide SSEs are thermodynamically stable when in contact with alkali metals, although kinetic stability is possible especially with oxides such as LLZTO. For most of the interpretations of the role of SSEs in homogenizing the ionic flux, the working assumption is that the phase(s) present during cycling are the initial ones introduced as separator coatings. However, that may not be the case, especially in the region that counts the most, which is the SSE−metal anode interface. What is the role of SSE−metal anode reaction layers in homogenizing the ionic flux? Do the reactions thus improve the overall stability of the anode, or do they hinder it, being the explanation for the eventual degradation of voltage stability? The SSE−metal interface is a dynamic one, which also includes ongoing SEI growth and the incorporation of the SSE into the SEI layer. How much is a composite SEI, that incorporates a portion of the SSE into in, responsible for the stabilization effect? How does a composite SEI refine the ionic flux, since, in effect, the metal−separator interface is entirely solid with not "free" electrolyte in contact with the anode? What is the overall role of the SEI layer in creating flux heterogeneities and promoting dendrites, versus homogenizing the flux and promoting a geometrically uniform metal front? At a high level, is a functional separator layer at the metal anode really another approach for augmenting the properties of the native SEI or does it have an altogether distinct function beyond creating an artificial SEI that promotes more uniform ion flux while also being more robust mechanically? What is the role of truly inert insulator phases, such as Al_2O_3, that can be physically incorporated into the SEI structure but nominally do not react with the metal anode?

By employing polar materials as functional coating, the ionic flux across the separator is chemically modified. This effect is in addition to the physical and SEI modification effects that would happen in parallel. One additional benefit that polar materials possess is that they promote enhanced wetting and uptake by the electrolyte, which further enhances the ionic flux across the separator. Park and Choi et al. designed a polydopamine-coated PE separator which turned PE surfaces hydrophilic. This increased the Li-based electrolyte uptake from 15 ± 2.7% to 112 ± 3.1% and the ionic conductivity from 0.04×10^{-3} S cm^{-1} to 0.3×10^{-3} S cm^{-1}.[362] A broad range of polar materials ranging from O/N/F-containing polymers/carbons to inorganics, including Prussian blue,[358] MoS_2,[195] and VS_2,[274] have been employed, as also illustrated in Table 11.

A two-dimensional molecular brushes-functionalized separator (GO-*g*-PAM) was constructed with the "hairy" polyacrylamide (PAM) chains grafted on GO surfaces, providing rich polar groups including C ═O and N−H.[366] A schematic for the architecture is provided in Figure 18a. The polar moieties within PAM chains nominally acted to both homogenize and accelerate Li^+ ion transport. As shown in Figure 18b the symmetric Li||Li cells with the GO-*g*-PAM@PP separator achieved extended cycling with stable voltage plateaus even at high current densities (up to 20 mA cm^{-2}), outperforming the baseline cells with unmodified PP separator. The effect of the GO-*g*-PAM on lithium deposition was further illustrated by comparing the morphology of the metal anodes after 100 cycles, as shown in Figure 18c. For the baseline cell with a standard PP separator, the anode surface consisted of loosely stacked mossy Li with a highly porous structure. By contrast, uniform and dense Li deposition was observed with the GO-*g*-PAM@PP separator. The functional groups in GO-*g*-PAM@PP are expected to react with the surface of the metal anode and to accordingly modify the SEI structure. How this influences the plating−stripping stability is not fully under-

https://doi.org/10.1021/acs.chemrev.1c00838
Chem. Rev. 2022, 122, 8053−8125

Table 12. Survey of Janus-Type Functional Separators/Interlayers for Li−S Cells

Separator[a]	Electrolyte uptake (wt %) /Contact angle (deg)	Ionic conductivity (mS cm^{-1}) /Transference number	Electrochemical performance (Symmetric cell)	Full cell cyclability (mAh g^{-1}) after *n* cycles	Ref
PP/PE/PP + XC72	NA	NA	1 mA cm^{-2}, 1 mAh cm^{-2}, 90 cycles	730 (500th) at 2C	356
Celgard/Polypyrrole separator	108/9	0.39/0.47	1 mA cm^{-2}, 1 mAh cm^{-2}, 175 cycles	805 (250th) at 0.5C	187
PP/2D VS_2	NA/10.5	NA/0.69	5 mA cm^{-2}, 0.5 mAh cm^{-2}, 400 cycles	908 (300th) at 0.2C	278
GF/$Ti_3C_2T_x$@CNTs-PEI	NA	4.18/NA	5 mA cm^{-2}, 1 mAh cm^{-2}, 250 cycles	980 (500th) at 1C	298
B/2D MOF-Co separator	90/NA	NA/0.53	2 mA cm^{-2}, 1 mAh cm^{-2}, 400 cycles	703 (200th) at 0.5C	368
(MOF) UiO-66-SO_3Li − (PVDF) membrane	NA/6	NA/0.66	5 mA cm^{-2}, 0.5 mAh cm^{-2}, 2000 cycles	580 (500th) at 0.5C	185
Gelatin-based nanofabric	700/0	4.9/0.73	0.5 mA cm^{-2}, 0.5 mAh cm^{-2}, 500 cycles	577 (300th) at 0.5A g^{-1}	369
PP/SNFs/PDA	NA/0	0.991/0.75	1 mA cm^{-2}, 1 mAh cm^{-2}, 1150 cycles	736.6 (1000th) at 1C	370

[a]"Separator + Material" represents the case of introducing the self-standing interlayer into the interface; "Separator/Material" represents the case of directly coating the functional material on the separator.

stood and presents a broadly interesting topic for further analysis.

To date, there is no mathematical framework to precisely explain how ionic flux is impacted by the separator's surface properties. An empirical hypothesis is that the degree of dissociation of the electrolyte's salt and the ions' solvation shells may be dependent on the interaction between electrolyte components and functional groups on the separator's surface.[180] Strong interaction with the modified separator may weaken the electrostatic interactions between the anion and the cation in the electrolyte, in effect promoting stronger dissociation.[190,360,364] Furthermore, the modified separator may have a desolvation effect, stripping the solvation shell from the cation.[191,367] Yuan examined the relative Raman signal of associated Li^+-EC molecules versus free EC in 1 M $LiPF_6$ in EC/DEC/EMC soaked separators.[363] The modified PE separator displayed a suppressed relative signal of associated Li^+-EC molecules compared to the unmodified PE reference. The modified separator also resulted in enhanced ionic conductivity and lower voltage drops across the modified separator.

Cui et al. recently investigated the interactions between the N-species in a graphene-like carbon nitride (GCN, g-C_3N_4) interlayer and the Li-based electrolyte/anode.[181] Per Figure 19a, the GCN layer was first modified on a separator via vacuum filtrating the g-C_3N_4 suspension over it and then autotransferring it to a Li anode surface during the cell assembly process. This was feasible due to the high lithiophilicity of the the GCN layer combined with its poor mechanical adhesion with the separator. With GCN layer, the anode displayed a significantly improved electrolyte wettability, with the contact angle being reduced from 53.1° to 17.2°, per Figure 19b. According to Figure 19c and d, XPS analysis demonstrates that Li−N bonds were formed after the GCN nanosheet underwent Li-salt solution treatment. According to Figure 19e, the Li nucleation overpotential and the back-calculated activation energies with versus without the GCN layer were 48.3 mV/6.766 kJ mol^{-1} versus 110.1 mV/11.118 kJ mol^{-1}, respectively. It was argued that the GCN layer could facilitate the ionic desolvation process by forming numerous transient Li−N bonds before deposition. This then led to a much smaller energy barrier for Li deposition. Accordingly, the GCN-modified Li−Cu asymmetric cell displayed a stable voltage hysteresis of less than 110 mV and maintained a CE of over 99% for 900 cycles, while the baseline deteriorated after 60 cycles.

Yan et al. fabricated various interlayers including a fibrillar PVDF film (f-PVDF) with an interpenetrated porous structure and abundant polar C−F polar function groups.[308] The architecture was tested against Na metal. Such structural and chemical properties resulted in superior electrolyte uptake (960%) as well as improved ionic flux for the f-PVDF-coated separator. Stable sodium deposition/stripping was attained with the f-PVDF film, suppressing the Na dendrites' growth on the metallic anode. Other specimens tested include a PVDF (c-PVDF) membrane without pores, the porous PVDF (p-PVDF) membrane with similar pore structure to the PP separator, a poly(ethylene oxide) (PEO) film with weaker polar function groups, and a commercial polytetrafluoroethylene (PTFE) film with poor electrolyte uptake (30%). All these counterparts gave rise to an overall inferior electrochemical performance with the same Na metal anodes. It has been reported that biomass-derived polymer separators with a narrow pore size distribution and strong affinity to electrolyte solutions also significantly improved the electrochemical performance of metal anodes.[307,365] It should be also emphasized that in terms of a separator's structural and chemical properties, many similar functional attributes improve the performance of both anodes and cathodes. For instance, introducing polar moieties into a separator may suppress both dendrites and the crossover of polysulfides, with the two being likely related. Per Table 12, it can be observed that Janus separators are able to ameliorate both types of deleterious processes for the Li−S system, with varying levels of efficacy.

Authors reported a functional separator coating based in a single-ion conductive polymer, which is enriched with immobilizing anions on the backbone through a covalent bond or Lewis acid−base interaction. One example of this is the well-known Nafion film.[147] Such polymers feature high alkali ion transference number (t_+), indicating superior cation mobility. On the metal anode side, a higher transference number can suppress the space-charge formation and consequent dendrite growth.[371] Zhou et al. designed a single-ion-conducting polyolefin separator for Na−S batteries.

https://doi.org/10.1021/acs.chemrev.1c00838
Chem. Rev. 2022, 122, 8053−8125

The separator contained rich -$SO_2N^{(-)}SO_2^-$ anionic centers, which resulted in increasing electrolyte uptake from 81.9% to 274.3%.[190] The corresponding Na ion transference number was accordingly higher than both pristine PP and GF membrane, being at 0.58 *vs* 0.21 and 0.27. Cycling of Na||Na symmetric cells verified the longer life span (500 h *vs* 139 h) and lower polarization using the single-ion-conducting separator versus the GF membrane. The immobilized anions on a separator will also excerpt an electrostatic repulsion force against polysulfide anions, allowing dual functionality that also improves the cathode performance.

Targeting a Janus separator for Li−S batteries, Pan et al. designed the MOF(UiO-66-SO_3Li)-based single-ion conductive polymer, which contained the anion (-SO_3^-)-immobilized Li^+ transport tunnels.[185] The narrow pore size of about 6 Å was proposed to homogenize the Li^+ ion flux. In addition, the sulfonate (SO_3^-) anionic groups within the tunnels facilitated the ionic transport kinetics, with the intrinsic Li^+ transference number (tested without additional Li salts) reaching 0.96. When tested in conventional electrolyte with additional Li salts, the anion-immobilized separator still had a higher t_{Li^+} than the commercial PP separator, with the value being 0.66 *vs* 0.41. Such a kinetic superiority was reported as the source of the low overpotentials in the Li||Li symmetric cell, being 13 mV, 17 mV, and 42 mV for 0.5 mA cm^{-2}, 2.0 mA cm^{-2}, and 5.0 mA cm^{-2}, respectively. The bifunctional separator contributed to a retained capacity of 580 mAh g^{-1} after 500 cycles at 0.5C, superior to the PP baseline with 230 mAh g^{-1} retention. It should also be noted that glass frit membranes with their usual macroscopic pores lead to uncontrolled dendrite growth for Na and K systems and an associated thick and nonuniform SEI layer.[198] Therefore, having an initially high ion flux to the anode is not an effective solution to dendrite growth by itself. As was argued earlier, the stabilization of the SEI layer through a physical composite-type effect or via some chemical/electrochemical modification is essential for anode cycling stability. Enhanced ion flux is certainly beneficial but is not the entire story for maintaining planar metal−electrolyte interfaces.

8.2. Physically Protective Layers

Per the mechanical blocking theory established by Monroe and Newman, metal dendrites can be suppressed if the elastic modulus of the blocking material is 1.8 times higher than that of the metal (theory done for Li).[144] Therefore, a protective layer with a higher elastic stiffness could be introduced and, in principle, prevent dendrite growth. The shear moduli of Li, Na, and K metal are 4.2, 3.3, and 1.3 GPa, respectively. This gives an estimate of the stiffness needed for a protective layer to mechanically block dendrites. Various protective layers, such as Al_2O_3,[286] MoS_2,[281] SiO_2,[372] poly(*p*-phenylene benzobisoxazole) (PBO) nanofiber,[202] and NaF,[373] have been incorporated either on the separator surface or in self-standing form to improve cycling stability.[31] While the modulus effect is likely real, there does not seem to a be a direct correlation between the elastic stiffness of the secondary phase per se and its ability to stabilize the metal−electrolyte interface. Alumina is very elastically stiff with a Young's modulus of 330 GPa, while MoS_2 is a dry lubricant that can be readily sheared along its basal planes due to the weak van der Waals bonding holding the layers in place. Yet both have been demonstrated to be effective in preventing dendrites. It is the opinion of this article's authors that the key mechanical feature that needs to be considered when estimating the efficacy of the secondary layer is its effect on the toughness (combination of strength and ductility) of the SEI. Both the free-standing functional layers and the layers attached to separators are ultimately incorporated into the SEI structure. For inert phases this may occur by SEI overgrowth, while for reactive phases it may occur as a combination of SEI overgrowth and reaction of the layer with the metal anodes. In either case an artificial SEI composite results, with phase content and phase distribution distinct from the baseline scenario of a PP or other type of commercial separator.[141] At ambient conditions, the homologous temperature for Li, Na, and K is 0.66, 0.80, and 0.89. This indicates that dendrites will also actively propagate via various dislocation and diffusional creep mechanisms, being in effect extruded through the paths of least resistance within the SEI and the separator. This is probably why glass frit separators are so ineffective in blocking the growth of Na and K metal dendrites: While being relatively stiff (Young's modulus of 50−90 GPa), the frits are macroporous, allowing the metal to be extruded through the openings. The diffusional deformation and growth of dendrites also put in doubt whether elastic properties alone are an effective descriptor for dendrite blocking. The metal anode community may perhaps move to a more complex descriptor of blocking ability, perhaps considering the ability of a modified SEI composite to impede creep deformation of dendrites or their diffusional growth. Since most SEI structures in liquid electrolytes are inorganic/organic composites, would a viscoelastic descriptor of mechanical stabilization be sought?

Huang et al. developed an artificial soft−rigid protective layer (APL) composed of poly(vinylidene-*co*-hexafluoropropylene) (PVDF-HFP) and lithium fluoride (LiF), for stabilizing the Li metal anode.[374] The LiF resulted in APL having an elastic modulus of 6.72 GPa, which far exceeded the values of the LiF-free PVDF-HFP film, natural SEI film, or a conventional separator. It was found that such a soft−rigid protective interlayer endowed the Li||Cu asymmetric cell with improved cyclability at 0.5 mA cm^{-2} and 1.0 mAh cm^{-2} (120 cycles, CE: 97.2%) versus the baseline PP separator (60 cycles, CE: 65%) or PVDF-HFP (80 cycles, CE: 80%). The authors analyzed the Li metal deposit morphologies after depositing 1.0 mAh cm^{-2} of Li in the Li||Cu half-cell. The Li adhered both to the PVDF-HFP layer and to the APL but resulted in loose needle-like Li dendrites on the bare Cu foil without protective layer. The boundary between deposited Li and the APL was flat versus geometrically fluctuated for the case of PVDF-HFP. The difference was ascribed to the mechanical robustness of rigid LiF. This is certainly a valid interpretation of the interfacial differences, although other factors such as wetting on the Li metal on LiF and differences in ion transport kinetics would be contributors as well. More analysis is sought to understand the role of different mechanical properties (elastic stiffness, instantaneous strength and ductility, and creep deformation resistance) on the ability of individual layers or discrete phases in suppressing dendrites.

Li, Mitlin, and co-workers fabricated a strontium fluoride (SrF_2) microsphere-coated separator, being motivated by the material's high elastic stiffness and chemical stability relative to the electrolyte.[375] While the layer was initially deposited on the separator, during cycling it detached and wound up, being almost entirely fixed to the Li metal anode surface. The SrF_2 microsphere coating stabilizes the SEI growth kinetics during cycling, creating a composite of SrF_2 particles imbedded within

https://doi.org/10.1021/acs.chemrev.1c00838
Chem. Rev. 2022, 122, 8053−8125

Table 13. Recent Advances on Functional Separators/Interlayers Promoting a Composite or Otherwise Modified SEI Structure

Separator[a]	Liquid electrolyte	SEI features	Electrochemical performance (Symmetric cell)	Ref
		Li Anode		
PE/SrF_2	1 M $LiPF_6$ in EC/DEC/DMC	SrF_2 are trapped within the SEI	0.25 mA cm^{-2}, 0.5 mAh cm^{-2}, 90 cycles	375
PVdF-HFP-Garlic	1 M $LiPF_6$ in EC/DMC/DEC/EMC + VC	Ester-based polymers, R-SH (thiols), KF, and CuF_2 were incorporated into SEI	NA	378
PP/a-TiO_2-BDC	1 M LiTFSI in DOL/DME + $LiNO_3$	SEI was richer in C-O moieties and Li_3N	4 mA cm^{-2}, 4 mAh cm^{-2}, 250 cycles	379
PP/$MnCO_3$	1 M LiTFSI in DOL/DME + $LiNO_3$	Covering layer consisted of Mn, Li_2CO_3, and SEI species	5 mA cm^{-2}, 1 mAh cm^{-2}, 5000 cycles	380
PP/$PbZr_{0.52}Ti_{0.48}O_3$ (PZT)	1 M $LiPF_6$ in EC/DMC	Part of PZT got reduced by Li, forming Pb−Li alloy adhered to the Li foil	2 mA cm^{-2}, 2 mAh cm^{-2}, 100 cycles	381
PP/Lignosulfonate	1 M LiTFSI in DOL/DME + $LiNO_3$	Li_2S and organic aromatic groups were induced in SEI	1 mA cm^{-2}, 1 mAh cm^{-2}, 250 cycles	382
PP/Nanodiamonds (NDs)	1 M LiTFSI in DOL/DME + $LiNO_3$	NDs self-transferred to the Li surface became part of the SEI	1 mA cm^{-2}, 3 mAh cm^{-2}, 155 cycles	377
PP + MgO film	1 M LiTFSI in DOL/DME + $LiNO_3$	MgO near the Li surface was lithiated into Li−Mg alloy	10 mA cm^{-2}, 5 mAh cm^{-2}, 2500 cycles	361
PP/Graphite fluoride/PVDF	1 M LiTFSI in DOL/DME + $LiNO_3$	LiF and graphene were generated in the interface	5 mA cm^{-2}, 1 mAh cm^{-2}, 2500 cycles	383
PP/Si	1 M $LiPF_6$ in EC/DEC/FEC + VC	Li−Si alloy was formed, giving a Si-enriched SEI	0.5 mA cm^{-2}, 1 mAh cm^{-2}, 250 cycles	384
Xonotlite (XNs)-based separator	1 M LiTFSI in DOL/DME + $LiNO_3$	Part of XNs reacted into Li_xSiO_y which accumulated in SEI	5 mA cm^{-2}, 1 mAh cm^{-2}, 5000 cycles	385
		Na Anode		
PP + Graphene film	1 M $NaPF_6$-EC/PC	Graphene suppressed the reaction between Na and the electrolyte	2 mA cm^{-2}, 3 mAh cm^{-2}, 100 cycles	386
Lithium-activated PP/SnS-G	1 M $NaClO_4$-EC/DEC + FEC	Li-based SEI components (Li_2O, LiF, Li_2CO_3, *etc.*) were introduced, enabling faster Na^+ conduction	4 mA cm^{-2}, 2 mAh cm^{-2}, 500 cycles	387
		K Anode		
PP/AlF_3	4 M KFSI-DME	PP/AlF_3 induced a stable artificial SEI film containing KF, AlF_3, and Al_2O_3 on K surface	0.5 mA cm^{-2}, 0.5 mAh cm^{-2}, 1000 cycles	173

[a]"Separator+Material" represents the case of introducing the self-standing interlayer into interface; "Separator/Material" represents the case of directly coating the functional material on the separator.

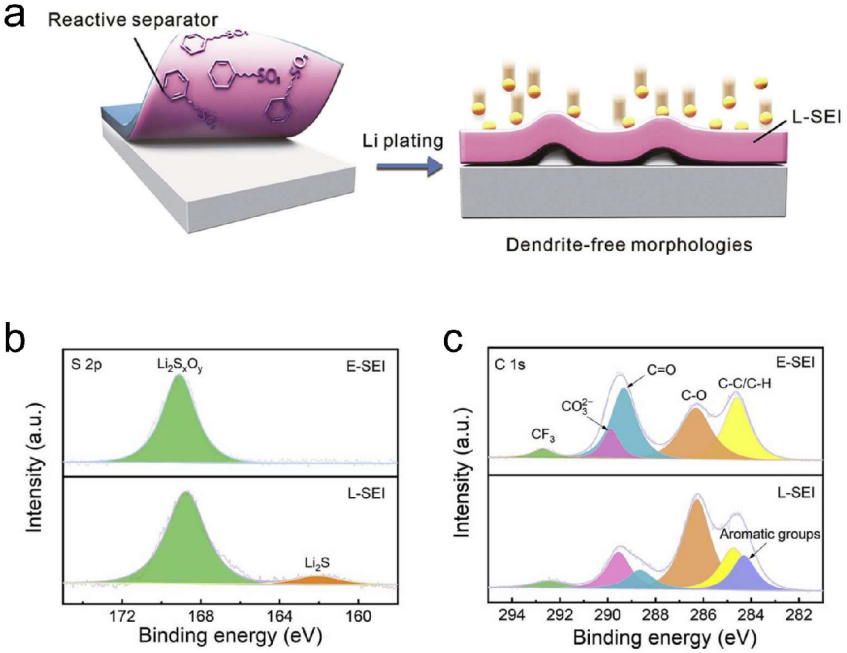

Figure 20. (a) Schematic illustration showing the beneficial effect of a lignosulfonate-derived SEI (L-SEI) on the Li plating behavior. (b and c) XPS spectra profiles of an L-SEI on Li anode displaying the S 2p and C 1s peaks, respectively. Reproduced with permission from ref 382. Copyright 2020 Elsevier.

https://doi.org/10.1021/acs.chemrev.1c00838
Chem. Rev. 2022, 122, 8053−8125

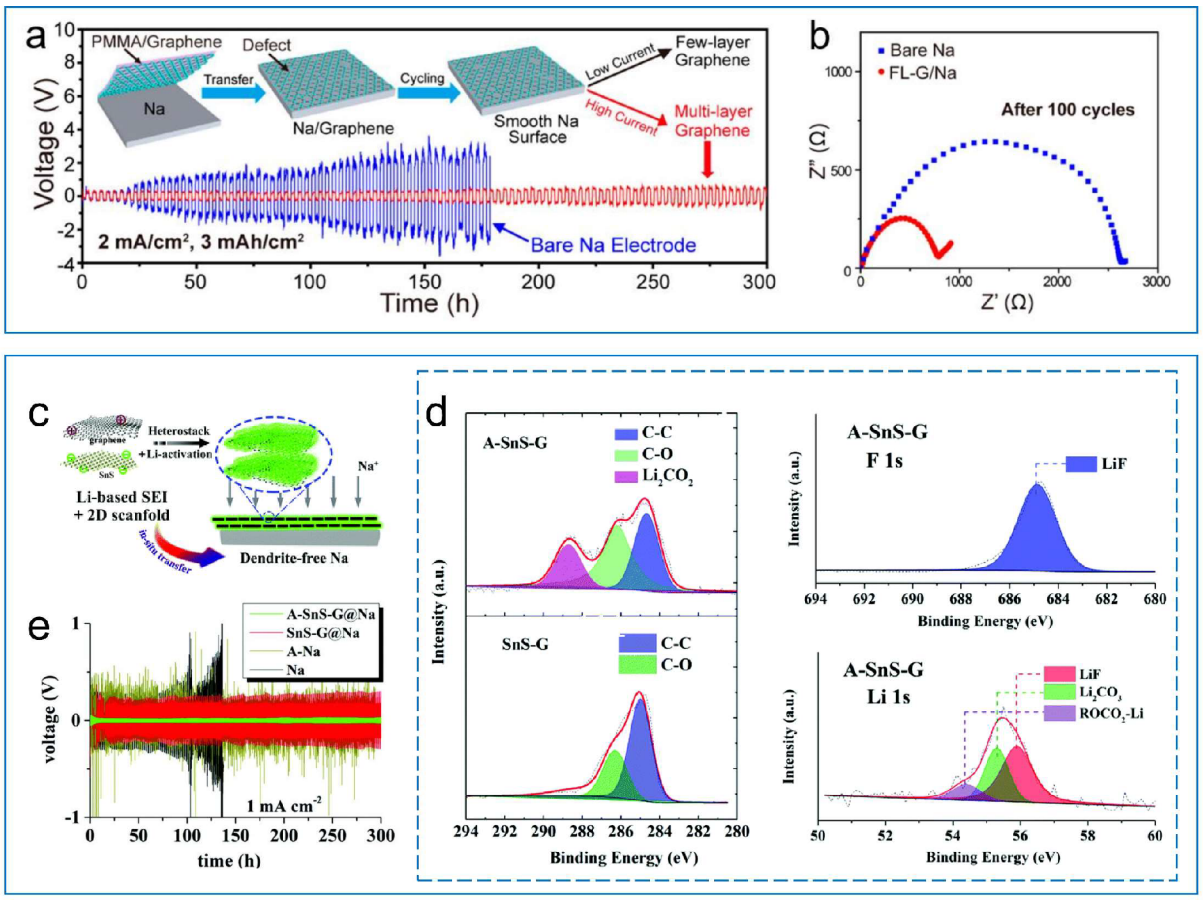

Figure 21. (a) Schematic and cycling data illustrating the performance enhancement achieved by employing defective graphene protective films in Na metal batteries. (b) Nyquist plots of the symmetric cells comparing the few-layer graphene (FL-G)/Na electrode and the baseline unprotected Na after 100 cycles. (c) Schematic illustration of sodium protection by a lithium-activated SnS/graphene nanocomposite membrane (A-SnS-G). (d) XPS C 1s, F 1s ,and Li 1s spectra of A-SnS-G after a single lithiation-delithiation cycle in $LiPF_6$-EC-EMC-DEC-FEC electrolyte. (e) Electrochemical performance of symmetric cells based on A-SnS-G@Na and baselines Sn-G@Na, A-Na, and Na tested at 1 mA cm^{-2}. Panels a and b are reproduced with permission from ref 386. Copyright 2017 American Chemical Society. Panels c and d are reproduced with permission from ref 387. Copyright 2020 Royal Society of Chemistry.

the SEI. It was argued that such a protective composite with a "soft" SEI matrix and "hard" ceramic SrF_2 reinforcement was physically tough and could mechanically stabilize the interface. Density functional theory simulations showed that the Li^+ ions preferred to adsorb onto the SrF_2 surface, which would homogenize the lithium ion flux, further promoting a planar plating−dissolving interface. With both a mechanical and an ion transport impact, the SrF_2-coated separator effectively inhibited dendrite growth and improved the electrochemical performance of full LMBs. This study served as a useful illustration of the multifunctional role that many coatings and interlayers have in improving metal anode performance. It is likely that most of the effective functional layers possess multiple roles, including the mechanical benefit, the ion transport benefit, and the electrolyte wetting benefit. Which benefit is reported often depends on the authors' viewpoint and the confirmatory analyses−simulations performed. For example, authors employed a nonwoven rGO fiber-aramid separator for improving the electrochemical performance of Li metal anodes.[376] The "F-doped" rGO surface induced the formation of LiF on the metal surface, which dramatically improved the stability of the SEI. The rGO surface would also promote enhanced wetting versus a baseline polymer separator and probably resulted in an improved ionic flux. These factors all would contribute to enhanced cycling stability, promoting a more holistic view of the benefits imbued by a given functional layer architecture. Future research should focus on understanding the synergistic aspects of these benefits. Is it actually possible to achieve state-of-the-art electrochemical performance with functional layers that do not simultaneously improve the electrolyte wetting behavior, ion transport kinetics, and SEI toughness, as all three lag with standard separators−electrolytes?

Per Table 13, there have been several studies where an artificial SEI was created through a functional separator coating. Lu et al. recently reported a nanodiamond particle (ND)-embedded Li-SEI, created by the self-transfer from the ND-coated polypropylene separator (ND-PP) under mechanical stress.[377] The embedded NDs caused a factor of 5 decrease in SEI conductivity, which nominally would impede further reduction of the electrolyte at the SEI−liquid interface. The Young's modulus of ND-PP was raised to 30GPa. Both factors could, in principle, reduce the degree of dendrite growth, although other factors such as the role of the ND layer in forming a composite with the SEI were also likely important. This study serves as an illustrative example of the difficulty of ascribing the performance improvement to just one property of

https://doi.org/10.1021/acs.chemrev.1c00838
Chem. Rev. 2022, 122, 8053−8125

the functional separator, further supporting an argument for a holistic view of the needed attributes.

Materials with an intrinsic reactivity toward Li metal have been utilized as separator coatings.[361,378,382] As illustrated by the schematic in Figure 20a, Huang et al. integrated a reactive lignosulfonate film onto a separator surface in order to stabilize the cycling of Li metal.[382] Per the XPS analysis shown in Figure 20b and c the lignosulfonate-derived SEI (L-SEI) on the Li surface was determined to contain inorganic species (Li_2CO_3, LiF, and Li_2S) and the aromatic groups (C═C) inherited from lignosulfonate. These components effectively passivated the Li metal surface and resulted in a lower activation energy for Li ion diffusion through the SEI (60.8 kJ mol^{-1} *vs* 72.3 kJ mol^{-1} for the electrolyte-induced SEI). A symmetrical Li||Li cell with this protective layer showed stable voltage hysteresis (20 mV) for 400 h, at a current density of 1 mA cm^{-2} and a capacity of 1 mAh cm^{-2}. A full cell Li−S with an L-SEI displayed improved capacity retention as well. Authors have also explored reactive inorganics for constructing an artificial protective layer on the Li-metal surface, including $PbZr_{0.52}Ti_{0.48}O_3$,[381] $MnCO_3$,[380] MgO,[361] and silicon.[384] Many of these inorganic coatings are reduced by the Li foil, for example $Pb_{27}Zr_{14}Ti_{13}O_{81}$ + 2 Li → $Pb_{25}Li_2Zr_{14}Ti_{13}O_{80}$ + Pb + PbO. Such reactions typically occur over the initial cycles and will result in the layer becoming physically transferred from the separator to the Li foil surface, where it becomes incorporated into the modified SEI layer. From this vantage, the effect is similar to what was described previously for many coatings that were not originally intended to be reactive but were reduced by the metal surface nevertheless. Often, one result of these reactions is a reduced interfacial resistance of the metal anode as calculated from impedance analysis. The formed alloys and reaction layers would not have this effect unless in parallel there was a stabilization of the SEI layer. While more work is needed to understand the fate of the numerous reactive materials employed, microstructural analysis typically points to a new phase(s)/SEI composite formation. More needs to be understood about how the mechanical properties and ion transport properties of such composites are different versus the baseline SEI structure and how those differences translate into anode cycling stability and resistance to dendrite formation.

Cui et al. employed a reaction-protective separator strategy where Li dendrites in contact with the layer would be impeded by a lithiation reaction of the phase.[388] The functional separator possessed a sandwiched structure of Li-active silica being incorporated between two polymeric separators. Once a dendrite punctured the outer separator and contacted with the inner silica, the SiO_2 nanoparticles could be lithiated by the lithium dendrites, in effect stopping their advance. When Si was employed instead, the separator failed to protect the cell, actually reducing the battery life. One explanation for this effect is the kinetic difficulty of lithiating bulk Si, with the Li metal dendrite rather proceeding around the obstacle. In contrast, the SiO_2 particles are reactive with the Li metal, readily forming a Li_2O compound. TiO_2 nanoparticles were also demonstrated to stabilize the metal−electrolyte interface with both Na and Li.[389,390] TiO_2, however, is not expected to undergo a conversion reaction but would rather lithiate to form an amorphous Li−Ti solid solution.[391] Therefore, multiple reactivity types are potentially effective in blocking dendrite propagation.

Per Figure 21a, Li and co-workers directly transferred a free-standing graphene film with tunable thickness onto a Na metal surface.[386] Acting as a stable artificial SEI, the graphene reduced excessive SEI buildup, which occurred on a bare Na electrode in the carbonate electrolyte employed. As shown in Figure 21b, after 100 cycles at 0.5 mA cm^{-2}, the Na||Na symmetric cells protected by the graphene layers displayed significantly lower impedance than the baselines, with interfacial resistances being ∼800 *vs* ∼2600 Ohms. With an optimal graphene thickness of around 5 nm, a stable Na cycling behavior was achieved at a high current density of 2 mA/cm^2 with a cycling capacity of 3 mAh/cm^2, without any mossy or dendritic structures being present on the postcycled surface. The layers were likely incorporated into a composite SEI which was more stable during cycling. Liu and Mitlin reported an artificial SEI layer based on a Li-ion-activated SnS/graphene nanocomposite membrane (A-SnS-G), which allowed for deep stable cycling of a record-thin 100 mm Na metal anode. A schematic of the synthesis process is shown in Figure 21c.[387] The synthesis procedure was along the following lines: A PP separator coated with SnS-graphene alternating nanolayers was activated in lithium-based carbonate electrolyte (EC:EMC:-DEC = 1:1:1, 5% FEC) versus a Li electrode. The activation consisted of a single lithiation−delithiation cycle in a voltage range of 0.01−2.5 V *vs* Li/Li^+. After the activation process, SnS was transformed to amorphous sulfides and tin-based species (Li_2S and Sn), while still remaining well-dispersed within the graphene scaffold. These amorphous species are known to be inherently good Li and Na ionic conductors per prior literature reports. In addition, a Li-based SEI comprising substantial inorganic electrolyte decomposition products (*i.e.*, Li_2CO_3, Li_2O, $ROCO_2Li$, as well as LiF) was created in the membrane, as verified by the XPS results shown in Figure 21d. Of these phases, LiF is known as an effective mechanical stabilizer of the SEI. It is more effective than NaF, while displaying higher ionic conductivity, 10^{-7} S cm^{-1} *vs* 10^{-13} S cm^{-1}. As a result of these multiple synergistic contributions, the A-SnS-G composite membrane, which acted as an artificial SEI layer, allowed for extended cycling both of Na metal cells and of full Na metal batteries in a standard carbonate electrolyte (EC:DEC = 1:1, 5% FEC). Figure 21e shows the electrochemical performances of the symmetric Na||Na cells with various configurations, including several baselines that had inferior performance to A-SnS-G. Li and co-workers reported a simple and cost-effective approach to stabilizing Na and K metal anodes, via directly inserting a thin piece of commercial carbon paper (CP) between the anode and separator.[392] Upon contacting with Na metal or K metal, the carbon paper was sodiated or potassiated, forming a more stable SEI than the unprotected baseline.

An optimum SEI should be mechanically robust to tolerate the anode expansion/contraction during the plating/stripping process. It is recognized that the Na-based SEI is relatively unstable as compared to Li, while the K-based SEI is unstable even as compared to Na. For instance, fluoroethylene carbonate (FEC) can stabilize Li and Na anodes by forming a dense and mechanically strong LiF or NaF layer on surfaces, suppressing dendrite proliferation.[393−395] However, FEC generally does a poor job of protecting K metal anodes.[143,172] This was found to be associated with the excessive side reactions of the SEI and the fact that the FEC was consumed early in the cycling process. From such results, and from a broad survey of the existing literature, it may be surmised that the membrane solutions established for Li metal may not be as effective, especially for K. To date, there is minimal literature on functional membranes for K metal anodes that allow state-

https://doi.org/10.1021/acs.chemrev.1c00838
Chem. Rev. 2022, 122, 8053−8125

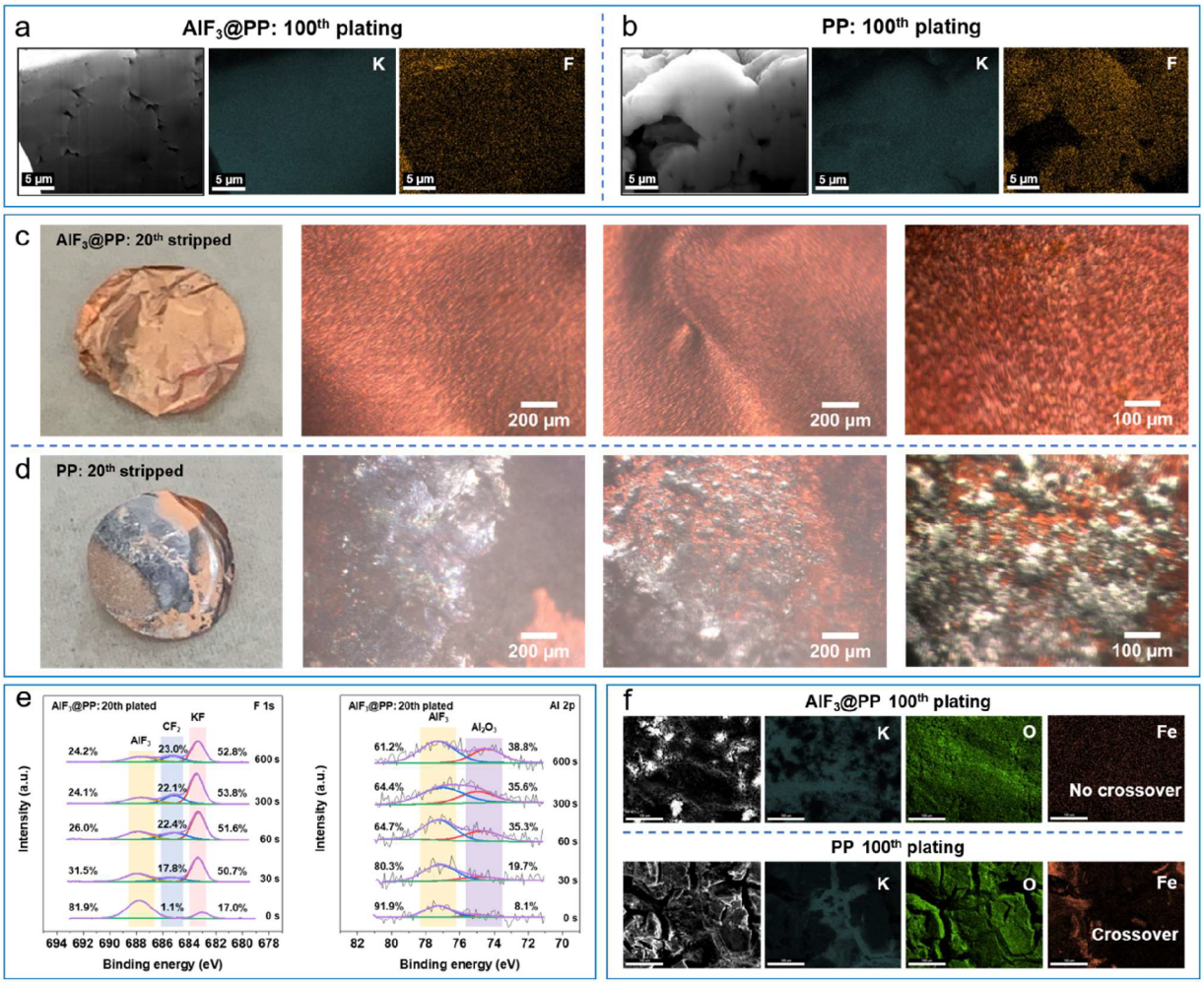

Figure 22. Cryo-FIB cross-sectional SEM images and EDXS K and F maps of (a) AlF_3@PP in the 100th plated condition and of (b) PP in the 100th plated condition. (c) Light optical images of AlF_3@PP at the 20th stripped condition. (d) Same analysis but performed for the baseline PP. (e) Sputter-down XPS analysis showing the F 1s and Al 2p spectra of the plated metal surface with AlF_3@PP, after 20 cycles. (f) Top-down SEM images and EDXS maps of the post-100-cycle metal anodes extracted from full batteries based on the potassium hexacyanoferrate(III) cathode, tested at 100 mA g^{-2}. Reproduced with permission from ref 173. Copyright 2021 John Wiley & Sons, Inc.

of-the-art performance. More research in this area is encouraged.

Authors recently published the first report of a multifunctional separator for potassium−metal batteries based on a double-coated tape-cast microscale AlF_3 on polypropylene, termed AlF_3@PP.[173] Analysis of asymmetric metal half-cells was performed in the ether-based electrolyte 4 M potassium bis(fluorosulfonyl) imide (KFSI) in dimethoxyethane (DME) electrolyte. Analysis of full batteries was performed in 0.8 M KPF_6 in ethylene carbonate (EC) and diethyl carbonate (DEC) (1:1, v/v). With AlF_3@PP, the postcycled plated metal surface was dendrite-free, while the postcycled fully stripped current collector surface was covered by a uniform SEI layer. Those results are shown in Figure 22a and c, including cryo-FIB cross-sectional analysis of the plated metal surface. Baseline PP half-cells displayed blocky dendrites interspersed with porosity at plating and copious dead metal interspersed with SEI clumps at stripping. Those results are shown in Figure 22b and d. During cycling, the AlF_3 from the separator became incorporated into an artificial SEI with enhanced cycling stability, partially reacting to form KF and Al_2O_3 phases within the modified structure. These SEI phases were verified by XPS analysis, and the results are shown in Figure 22e. When tested in a full battery, the AlF_3@PP also formed an artificial cathode electrolyte interphase that stabilized the potassium hexacyanoferrate(III) cathode. As shown in Figure 22f, the functional separator minimized both Fe crossover and corresponding cycling-induced anode pulverization. It was demonstrated that the AlF_3@PP had multiple additional electrochemical benefits, promoting complete electrolyte wetting, enhancing electrolyte uptake, and improving ion conductivity through the electrolyte-filled separator while increasing the ion transference number. Studies on multifunctional separators for potassium metal batteries are encouraged, with the field being minimally explored.

8.3. Controlling Metallic Nucleation Sites

Xie et al. proposed a novel strategy of adjusting the Li dendrite growth direction via using a functional separator as shown in Figure 23a.[396] The separator was coated with the prelithiated functionalized nanocarbon (FNC), which immobilized Li^+ ions on the surface, and was electrically connected to the Li metal electrode through the tabs. Per the *in situ* TEM experimental results shown in Figure 23b the conductive FNC served as an upper current collector. There, Li dendrites during plating

https://doi.org/10.1021/acs.chemrev.1c00838
Chem. Rev. 2022, 122, 8053−8125

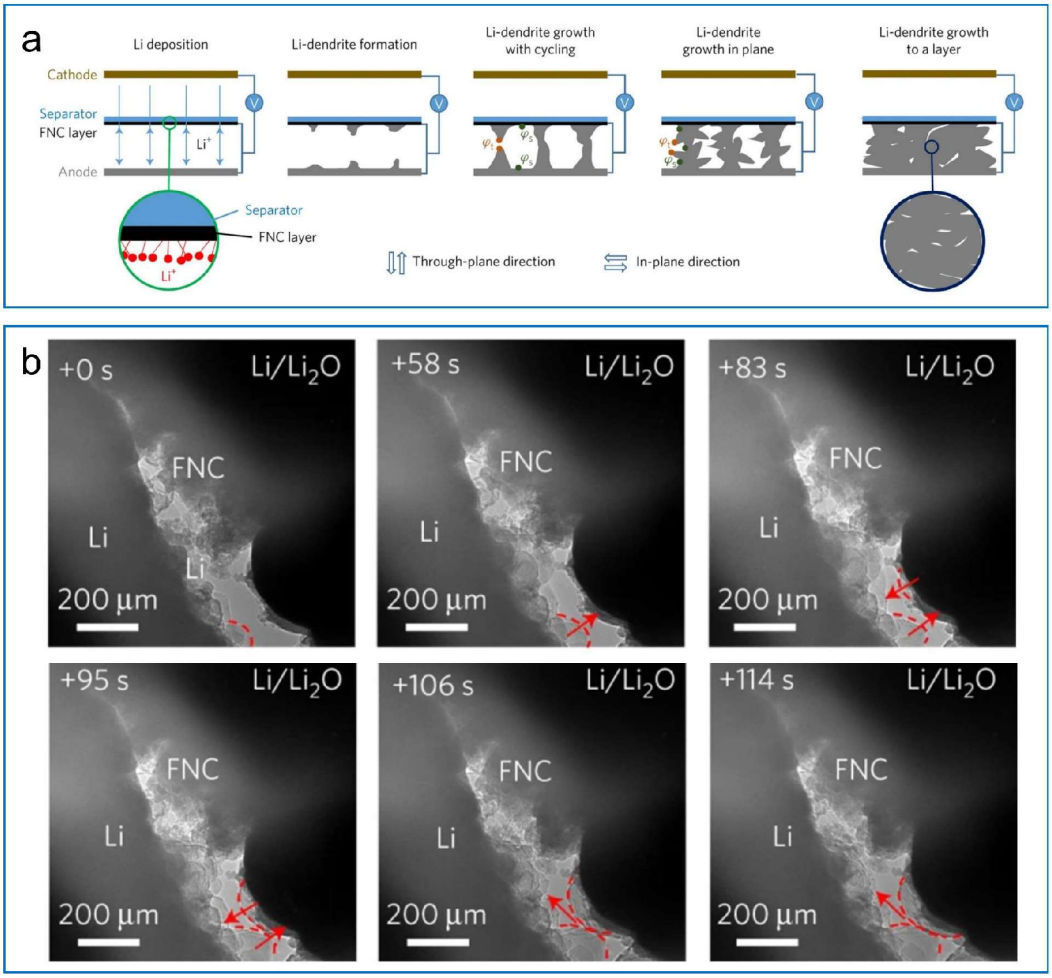

Figure 23. (a) Dendrite growth in a Li metal cell using a functionalized nanocarbon (FNC)-coated separator. (b) *In situ* TEM experimental results at 0 s, 58 s, 83 s, 95 s, 106 s, and 114 s. The red dashed curves show the profile of the Li dendrite; the arrows indicate the growth directions. Reproduced with permission from ref 396. Copyright 2017 Springer Nature.

formed (the red dashed curves appearing at 83 s) and grew out from the surface toward the anode (95 s), driven by the voltage difference between the tip and the base. When the dendrites formed on both surfaces of the FNC thin film and the Li anode met (106 s), the dendrite growth along the through-plane direction stopped and instead continued along the in-plane direction (114 s). In such a manner, a densely packed Li layer between the separator and Li anode was induced, with nonsharp geometries. The immobilized Li^+ ions played a vital role as the intentionally introduced nucleation sites for Li dendrite growth toward the anode. Zhang et al. demonstrated the feasibility of applying a Cu thin film (CuTF) as a functional coating on a PE separator, for modulating the Li deposition morphology via dendrite merging.[397] Various lithiophilic nanoparticles, including Mg,[398] Pt,[399] Ag,[400] and SnO_2,[401] have employed as Li nucleation sites that were coated onto the separator and nominally guided the dendrite growth direction. The enthalpy of an infinite solution ($\Delta_{sol}H^{\infty}$) of the alkali metal into the element can be used to predict the wetting property and the associated nucleation behavior.[141] Elements such as Ag, Mg, and Pt possess negative $\Delta_{sol}H^{\infty}$ values with Li, explaining improved electrochemical wetting and low plating overpotentials. The enthalpy of infinite solution criteria identified Au, Ba, Ge, Pt, and Sn as being sodiophilic and Au, Ge, and Sn as being potassiophilic. It remains to be known how many of these elements when incorporated onto the separator surface are effective in blocking dendrites by promoting metal nucleation and growth in the direction toward the current collector. There is one recent example of a Sn-coated separator that prevented dendrite growth and improved the cyclic stability of the Na metal anode.[402] This alloying theme seems ripe for further exploration, with the associated analytical and simulation studies being necessary. What is the precise mechanism(s) by which dendrites blocked by the reactive phases on the separator, even for the cases of the established SiO_2 and Sn?

Liu and Tao et al. employed atomic-resolution cryo-TEM and SEM, to study Li nucleation and growth under a trifluoroethanol-modified eggshell membrane (TESM).[403] The TESM film with rich polar functional groups improved the wettability of ether-based electrolytes, resulting in a contact angle of nearly 0° versus 44.2° for the baseline PP separator. XPS and FTIR analysis indicated that TESM may be incorporated into the SEI, forming a modified structure. SEM analysis revealed that Li was deposited with a uniform spherical morphology on the TESM-protected Cu electrode, whereas Li deposits with the baseline PP appeared dendritic. The Cryo-TEM revealed a difference in crystallographic texture between the two specimens, with ⟨110⟩ and ⟨211⟩ being the film texture with a TESM and ⟨110⟩, ⟨211⟩, and

https://doi.org/10.1021/acs.chemrev.1c00838
Chem. Rev. 2022, 122, 8053−8125

⟨111⟩ being the dendrite growth directions with the PP. A Li||Li symmetry with TESM protection had a cycle life of over 1200 h at 5 mA cm^{-2}, versus only 180 h for the baseline. While there is clearly a linkage between film texture and electrolyte wetting, further studies are needed to establish broad trends both in respect to planar film growth and in respect to dendrite orientation.

Hu et al. employed a BN-coated separator to stabilize the Li metal anode.[404,405] The authors claimed that a uniform temperature distribution was created on the thermally conductive BN surface, which contributed to uniform deposition/striping of the Li. Pol et al. improved the temperature distribution on a separator by coating it with a thermally conductive AlN layer.[406] The functional layer enabled superior Li deposition behavior and allowed for stability of Li metal batteries over 100 cycles, even at low temperatures of 0 and 10 °C. By contrast, batteries with an untreated separator quickly deteriorated during cycling. Several groups revealed that temperature is an important aspect in understanding the nucleation behavior of electrochemically plated metal.[407−409]

9. INTERLAYERS AND ARTIFICIAL SEI/CEI LAYERS FOR METAL−SULFUR SOLID-STATE BATTERIES (SSBS)

In this section, we discuss the application of functional interlayers and artificial SEIs/CEIs for solid-state electrolyte applications in metal−sulfur-based solid-state batteries. Solid-state electrolytes are gaining major attention as a replacement for liquid electrolytes and traditional separators, primarily due to their perceived increased safety. There has been significant progress in the solid-state alkali metal−sulfur batteries showing reasonable cycle life and capacity retention.[410] To a varying extent, all SSEs have the propensity to develop unstable interfaces both at the anode (mechanical separation, parasitic reduction reactions, and/or dendrites) and at the cathode (mechanical separation and parasitic oxidation reactions).[411−413] These interfacial effects increase impedance, giving fast charge and fast discharge limitations even with the most state-of-the-art SSEs. Solid-state electrolytes display electrochemical−mechanical coupling to a much greater extent than with liquid electrolyte systems, leading to complex failure modes not normally observed in the later.[412,414] Some manifestations of this coupling include cracking of the SSEs through the bulk, pulverization of cathode−SSE and anode−SSE interfaces, and generally poor or nonuniform physical contact between the cell components that worsen with extended cycling. To counter these effects, external stress is applied to promote diffusional and creep relaxation of the metal, to inhibit interfacial reactions that result in volume expansion, and to simply keep the pouch or PEEK cell components in physical contact.[415,416] While stainless steel button cells naturally exert several MPa of pressure upon the internal stack, more representative pouch cells do not bring any pressure unless it is externally applied. Research has shown that commercially representative pouch cell stack pressures of around 1 MPa are insufficient to stabilize SSB performance and that pressures up to ten times higher are needed, depending on the SSE type and cell configuration. This creates major problems when envisioning the transition of SSB technologies from the laboratory to a commercial product.

Functional interlayers and artificial SEIs and CEIs promise to alleviate this critical problem to some extent, reducing the parasitic reactions at both interfaces with sulfide SSEs or promoting better stack adhesion and improved metal wetting with oxide SSEs. This will be the focus of the discussion below. At a high level, numerous questions remain regarding the nature of the anode−SSE and the cathode−SSE interfaces and the associated electrochemical−mechanical coupling. An obvious concern is the ability to quantitatively analyze each interface so as to obtain key microstructural data that may be input into various multiscale models. Some of the emerging opportunities for direct analysis of the interfaces will be discussed in section 11 of this review. Historically there has been an emphasis on "global" electroanalytical and analytical approaches, which could provide quantitative information but only averaged over a relatively large sample area. For example, increasing EIS resistance values of a SSB can be due to one or a combination of multiple factors: This includes stress-driven, nonuniform self-diffusion-driven, or Kirkendall effect-driven voiding of the metal anode, localized fracture or more general pulverization of the SSE at either or at both electrode−SSE interfaces, growth of ionically insulating reaction layers at the interfaces, *etc*. While employing a three-electrode setup will provide information regarding the anode−SSE and the cathode−SSE state of health, there is still ambiguity regarding the microstructural origin of the impedance rise. Employing site-specific techniques such as cryo-stage FIB and cryo-stage TEM in combination with global electroanalytical (EIS, overpotential analysis) and analytical methods (synchrotron and X-ray, XPS, and TOF-SIMS) is likely the best path forward. For example, such a combined approach provided unique microstructural information regarding the role of AlF_3 multifunctional coatings in extending the cycling stability of potassium metal batteries, as well as specific early failure modes in baseline cells employing a conventional separator.[173]

It should be noted that hybrid inorganic−organic SSEs have also been widely employed. The reader is referred to several excellent review articles on this topic.[417−419] In principle, hybrid electrolytes synergize the advantages of inorganic SSEs and polymer SSEs to facilitate processing efficiency, while improving interfacial contact both initially and after extended cycling.[420−425] In practice, polymer-based secondary SSE phases are often a compromise, tremendously aiding battery fabrication but creating secondary issues related to polymer reduction/oxidation. The plating/stripping behavior of Li or Na at the oxide portion of the SSE may be quite different than at the polymer portion of the SSE, leading to inhomogeneous interfaces during extended cycling. Likewise, at the cathode the oxidation behavior of the polymer component will differ from the oxidation behavior of the inorganic portion, leading to additional inhomogeneity. Most polymer-based electrolytes display lower ionic conductivity than state-of-the-art inorganic SSEs, reducing the battery rate performance when added in appreciable amounts. An alternative and promising approach for hybrid electrolytes is to combine oxides such as lithium lanthanum zirconium oxide (LLZO) with minor additions of conventional liquid electrolytes, improving the interfacial contact at both electrodes, especially at the cathode. Surveying the supplemental portion of state-of-the-art performance ceramic SSB publications, it is evident how widely this approach is utilized, even when the manuscript title and abstract refer to the architecture as all-solid state.

https://doi.org/10.1021/acs.chemrev.1c00838
Chem. Rev. 2022, 122, 8053−8125

9.1. Inorganic Solid-State Electrolytes

Inorganic solid-state electrolytes can be categorized into oxide- and sulfide-based series. Oxide-based SSEs primarily include lithium−phosphorus oxynitride (LiPON), lithium lanthanum zirconium oxide (LLZO), lithium superionic conductors (LISICON), sodium superionic conductors (NASICON), and β''-alumina. These display comparatively wide electrochemical stability windows, primarily due to kinetic rather than thermodynamic stability, with β''-alumina being perhaps the thermodynamically stable exception.[426−428] These oxides display ionic conductivities in the range 10^{-6}−10^{-3} S cm^{-1}. Sulfide-based SSEs present comparatively higher ionic conductivities up to beyond 10^{-2} S cm^{-1} at room temperature.[429] Sulfides such as $Li_{10}GeP_2S_{12}$ (thio-LISICON, LGPS), Li_6PS_5Cl (argyrodite, LPSC), Li_2S-P_2S_5 (LPS), β-Li_3PS_4 (lithium thiophosphate, LPS), Na_3PS_4 (NPS), and Na_3SbS_4 (NAS) are widely studied, with argyrodite being promising due to its relative kinetic stability.[430] Solid inorganic electrolytes have near-unity cation transference numbers, which indicate they are only permeable to alkali ions but impermeable to polysulfide anions. With SSEs sulfur undergoes a direct solid−solid reaction pathway without the formation of polysulfide intermediates.[431] Thio-LISICON ($Li_{10}GeP_2S_{12}$[432] and $Li_{10}SnP_2S_{12}$[433]), Li_2S-P_2S_5 glass electrolyte,[434] and Na_3PS_4[435] have been explored for SSE-based metal−sulfur batteries. The full battery cells display a single sloping discharge plateau which is associated with direct conversion of S to Li_2S or to Na_2S.

Cathodes and anodes interfaced to oxide SSEs generally display a large interfacial resistance. For example, the interfacial resistance between NASICON and Na metal has been reported to be more than 10,000 Ω·cm^2.[436] To reduce this resistance, a minor amount of liquid electrolyte can be added to the interfaces, including with sulfide-based SSEs. For example, using such an approach, the interfacial resistance of the symmetric Li/$Li_{10}GeP_2S_{12}$(LGPS)/Li cell was reduced from over 2000 Ω·cm^2 to 142 Ω·cm^2.[437] This may be considered a hybrid approach, relying (primarily) on solid-state ionic conductivity through the bulk of the SSE but also improving the interfacial charge-transfer kinetics through the minority liquid. Figure 24 presents a hybrid Li−S battery configuration with two different liquid electrolytes separated by a solid-state $Li_{1+x+y}Al_xTi_{2-x}Si_yP_{3-y}O_{12}$ (LATP) film.[438] With such a "quasi-solid-state" battery, sulfur converts through a conventional solid−liquid dual-phase reaction route along with the recurrent formation and dissolution of the LiPSs. This indicates that there is enough liquid in the system that most of the ionic conduction derives from the it, rather than from the SSE. The key role of the LATP electrolyte would then be the inhibition of the polysulfide crossover to the anode. This quasi-solid-state Li−Li_2S battery delivered a stable capacity of more than 900 mA h g^{-1} for 150 cycles at 0.05C. Since the Li anode foil acted as an effectively infinite reservoir of Li ions, the battery CE approached 100% during cycling. In general, within quasi-solid-state batteries the polysulfides' shuttle effect seems to be substantially reduced.[439] Rather, the cells appear to be limited by the stability of the anode−electrolyte and cathode−electrolyte interfaces. With hybrid electrolytes, the problem of reduction at the anode and oxidation at the cathode appears to be compounded. Table 14 compares different ceramic electrolytes for metal−sulfur battery applications. The comparison is made in terms of room temperature bulk ionic conductivity, thermodynamically stable electrochemical window,[427] and observed interfacial stability (thermodynamic or kinetic) at the anode and at the cathode.

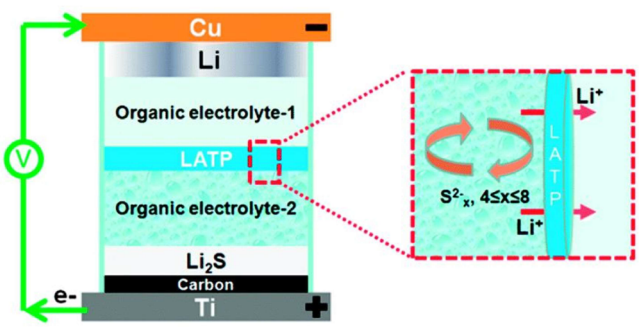

Figure 24. Schematic of the architecture for the LATP electrolyte-based quasi-solid-state Li−S battery. Reproduced with permission from ref 438. Copyright 2015 Royal Society of Chemistry.

Janek et al. summarized three different types of interface formation in terms of the interfacial stability of SSEs against metal anodes.[451] The three types of interfaces are shown in Figure 25. While the schematic focuses on the Li metal−SSE interface, the provided concepts are fully applicable to Na and K as well. The first case is a thermodynamically stable interface, shown in Figure 25a. The SSE is thermodynamically stable and completely unreactive when in contact with lithium metal. To our knowledge, such an interface does not exist when considering oxide or sulfide-based SSEs. Moreover, it would not necessarily be a desirable feature since a completely inert interface implies lithiophobicity and, hence, difficulty in maintaining wetting contact during plating/stripping. While higher Li content phases such as Li_2S, Li_3P, Li_3N, and LiF are thermodynamically stable against Li metal, they are poor ionic conductors and are, therefore, better suited as secondary artificial SEI layers.[411,427] Figure 25b presents a reactive and mixed conducting interphase (MCI) where ionically and electronically conductive interfacial reaction products are formed. Solid electrolytes containing high-valence cations (*i.e.*, Ti^{4+}, Ge^{4+}, Ta^{5+}, and Sb^{3+}) such as perovskite-type $Li_{0.33}La_{0.56}TiO_3$ (LLTO), NASICON-type LATP, $Li_{1.5}Al_{0.5}Ge_{1.5}(PO_4)_3$ (LAGP), LGPS, and NAS will form an MCI that is not self-passivating. This results in the continuous growth of a low-ion-conductivity interface with the associated increase in impedance and overpotentials. Figure 25c illustrates kinetically stable SSEs such as with LLZO and to some extent with argyrodite. A self-passivating interface is formed, with all or most of the reaction products (*e.g.* tetragonal LLZO and Li_3P) being electrical insulators. Ongoing growth of such an interface is limited, qualitatively being analogous to a stable SEI layer with liquid electrolytes. Despite a range of mechanical compatibility issues, LLZO displays excellent electrochemical compatibility with Li metal through the formation of a thermodynamically stable passivation layer. NASICON-type $Na_{1+x}Zr_2P_{3-x}Si_xO_{12}$ delivers practical stability against Na metal as a consequence of the decomposition product NaO_x suppressing further reactions.[452] In contrast, the interface between Na_3PS_4, Na_3SbS_4, and Na metal is highly reactive and unstable. The reduction products such as Na_3P and Na_3Sb phases possess a low band gap (0.4 and 0.68 eV), making them electronically conductive, with the result being a reacted interface that is not self-terminating.[453]

https://doi.org/10.1021/acs.chemrev.1c00838
Chem. Rev. 2022, 122, 8053−8125

Table 14. Comparison of Different Ceramic Electrolytes Employed for Metal−Sulfur Battery Applications

SIE type and representative material		σ_{ion} (S·cm^{-1})	Electrochemical windows (V *vs* Li/Li$^+$ or Na/Na$^+$)	Stability against metal anode	Stability against S cathode	Ref
Oxides-Based SIEs						
Perovskite	$Li_{0.33}La_{0.56}TiO_3$	7.00×10^{-5}	1.75−3.71	▶ Be thermodynamically unstable ▶ Reduction of Ti^{4+} to Ti^{3+} ▶ Oxidized Li insertion	▶ Be thermodynamically unstable ▶ Reduction of Ti^{4+} to Ti^{3+} by LiPSs	440
NASICON	$Li_{1.2}Al_{0.2}Ti_{1.8}(PO_4)_3$	5.00×10^{-3}	2.17−4.21	▶ Be thermodynamically unstable	▶ Be thermodynamically unstable	441
	$Li_{1.5}Al_{0.5}Ge_{1.5}(PO_4)_3$	1.80×10^{-4}	2.70−4.27	▶ Reduction of Ti^{4+} to Ti^{3+} or Ge^{4+} to Li−Ge alloy	▶ Reduction (*i.e.*, Ti^{4+} to Ti^{3+}) by LiPSs	442
	$Na_3Zr_2PSi_2O_{12}$	1.00×10^{-3}	1.11−3.41	▶ Be kinetically stable	Be thermodynamically stable	443, 444
Garnet	$Li_7La_3Zr_2O_{12}$	2.44×10^{-4}	0.05−2.91	▶ Be kinetically stable	▶ Be thermodynamically stable	445
Alumina	Na-β''-alumina	2.00×10^{-3}	0.1−3.80	▶ Be thermodynamically stable	▶ Be thermodynamically stable	446
Sulfide-Based SIEs						
Li_2S-P_2S_5 system	$0.7Li_2S$-$0.3P_2S_5$	1.40×10^{-3}	NA	▶ Be kinetically stable	▶ Be kinetically stable	447
	β-Li_3PS_4	1.60×10^{-4}	1.71−2.31			448
Argyrodite	Li_6PS_5Cl	4.60×10^{-3}	1.71−2.01	▶ Be kinetically stable	▶ Be kinetically stable	449
Thio-LISICON	$Li_{10}GeP_2S_{12}$	1.20×10^{-2}	1.71−2.14	▶ Be thermodynamically unstable ▶ Formation of MCI layer consisting of Li_3P, Li_2S, and Li−Ge alloy	▶ Be kinetically stable	429
Sulfde-based Na^+ conductor	Na_3PS_4	1.09×10^{-4}	1.55−2.25	▶ Be thermodynamically unstable	▶ Be kinetically stable	431
	Na_3SbS_4	1.48×10^{-3}	1.80−1.90	▶ Formation of MCI layer consisting of electron conductor (Na_3P or Sb−Na alloy)		450

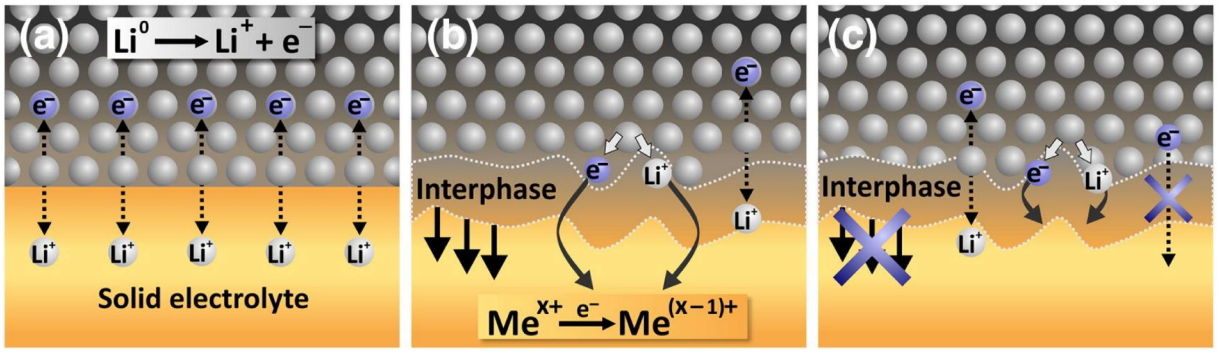

Figure 25. Types of interfaces between lithium metal and a solid lithium ion conductor: (a) nonreactive−thermodynamically stable interface; (b) reactive and mixed conducting interphase (MCI); (c) reactive and metastable solid electrolyte interphase (SEI). Reproduced with permission from ref 451. Copyright 2015 Elsevier.

Many oxide-based solid electrolytes and all sulfide-based ones also anodically decompose at the ceramic cathode voltages. With S-based batteries, the cathode voltage is lower, with less driving force for SSE decomposition. In cases where the sulfide SSE does decompose, several studies demonstrated that the decomposition may be partially reversible or that the decomposition products are redox-active.[411,454] When employing Li_6PS_5Cl, LGPS, and Na_3PS_4 as electrolytes for Li−S and Na−S batteries, it was found that the sulfides contributed to the extra reversible capacity within the operating voltage.[435,456,457] It is not obvious that this effect may be beneficial for practical batteries since the associated conversion reactions lead to large volume changes at every cycle. As an example of sulfides being employed for cathodes, a mixed Na_3PS_4−carbon catholyte delivered a reversible capacity of 140 mAh/$g_{Na_3PS_4}$ in the voltage range 0.5−3.0 V against a Na−Sn alloy anode.[431] The ball-milled composite cathode mixture of Na_3PS_4-nano-Na_2S-C exhibited an initial capacity of around 900 mAh/g when tested at 50 mA/g, which was based on the weight of Na_2S and exceeded its theoretical capacity of 687 mAh/g. Garnet LLZO,[458] NASICON-type $Li_{1+x}Y_xZr_{2-x}(PO_4)_3$ (LYZP),[459] and $Na_{1+x}Zr_2P_{3-x}Si_xO_{12}$ solid electrolytes[443] possess favorable thermodynamic stability versus sulfur cathodes, as well as kinetic compatibility with the anode. Alas, the oxides are less ionically conductive and suffer more from electrochemical−mechanical-coupling-related failures due to their brittle nature.

If employing a hybrid liquid−solid SSE, there is the additional concern that the SSE reacts with the intermediate sulfide species that is in the liquid solution. For instance, $Li_{1.3}Al_{0.3}Ti_{1.7}(PO_4)_3$ solid electrolyte displays a reduction potential of 2.5 V *vs* Li/Li$^+$ and will be lithiated when in contact with lithium polysulfide solution, accompanied by a reduction of Ti^{4+} to Ti^{3+}.[455] The crystal would expand anisotropically during the lithiation process, generating cracks. During cycling, the SSE grain boundaries would be corroded by polysulfide solution, resulting in the generation of additional pores within the structure and leading to polysulfide crossover. Likewise, LAGP is thermodynamically unstable against LiPSs

https://doi.org/10.1021/acs.chemrev.1c00838
Chem. Rev. 2022, 122, 8053−8125

species considering its high reduction potential of 2.7 V *vs* Li/Li^+.[439]

Employing alloy anodes such as Li−Sn, Li−In, and Na−Sn or passivating the metal anode surface with electronically insulating layers can reduce interfacial degradation.[433,435,450,460−462] For example, Ceder et al. employed surface hydration to stabilize the SSE−metal interface, which was achieved by exposing the Na_3SbS_4 electrolyte pellet to ambient air.[461] A concern with using alloy anodes rather than plating/stripping anodes is the reduction in the operating voltage window of the full cell, as well as the degradation of the alloy itself due to the ongoing volume changes. A key approach for stabilizing the SSE−metal interface is to introduce one or several interlayers between them, akin to membranes and artificial SEIs with liquid cells but designed to be ionically conductive but electrically insulating. One powerful example of this approach is by Wang et al., who introduced a lithiophilic−lithiophobic gradient interface layer between Li and LGPS. This was achieved by the sequential reduction of salts and solvent in $Mg(TFSI)_2$-LiTFSI-DME liquid electrolyte at the LGPS−Li interface.[463] The metal salts were first reduced by lithium, forming a lithiophilic Li_xMg-rich portion of the gradient layer at the metal surface, while a lithiophobic LiF-rich portion of the gradient layer formed toward the electrolyte. This gradient layer allowed the critical current to be increased from 0.6 mA cm^{-2} (capacity of 0.6 mAh cm^{-2}) to 1.3 mA cm^{-2} (capacity of 1.3 mAh cm^{-2}). Tu et al. developed an MoS_2-doped Li_2S-P_2S_5 glass−ceramic electrolyte ($Li_7P_{2.9}S_{10.85}Mo_{0.01}$) through a combined method of high-energy ball milling plus annealing.[464] This novel electrolyte exhibited an enhanced bulk ionic conductivity of 4.8 mS cm^{-1} at RT, in comparison with the $Li_7P_3S_{11}$ baseline of 2.5 mS cm^{-1}. Moreover, it displayed lower interfacial resistance along with higher stability against lithium metal. A Li−S all-solid-state battery with $Li_7P_{2.9}S_{10.85}Mo_{0.01}$ demonstrated an initial discharge capacity of 1020 mA h g^{-1} at 0.05C, versus 775 mA h g^{-1} with $Li_7P_3S_{11}$. Doping $Li_7P_3S_{11}$ with Mn and I ($Li_7P_{2.9}Mn_{0.1}S_{10.7}I_{0.3}$) resulted in a combination of improved ion conductivity of 5.6 mS cm^{-1} and improved electrochemical stability.[465] Corresponding Li−S SSBs exhibited a stable cycling performance with a capacity of around 800 mA h g^{-1} after 60 cycles at 0.05C. In a study of Na−S SSBs, NaI was introduced into Na_3SbS_4 to improve the ionic conductivity.[466] The optimized solid electrolyte of $0.9Na_3SbS_4$·0.1NaI displayed an ionic conductivity of 1.01×10^{-3} S cm^{-1} at 30 °C. With employment of the Fe_3S_4·S·$0.9Na_3SbS_4$·0.1NaI composite cathode and the sodium foil anode, the Na−S SSBs exhibited a favorable cycling stability with a reversible capacity of 410 mAh g^{-1} at 500 mA g^{-1} for 50 cycles. It also showed favorable rate capability with capacities of 952, 797, 514, and 446 mAh g^{-1} at 50, 100, 200, and 500 mA g^{-1}, respectively.

A high interface resistance is a critical factor limiting the electrochemical performance of solid-state metal−sulfur batteries. Despite the kinetic stability of the interface, oxide-based SSEs such as garnet-type LLZO and NASICON $Na_{1+x}Zr_2P_{3-x}Si_xO_{12}$ suffer from this problem.[436,467−469] Interfacial resistances in the kΩ cm^2 range are reported, being attributed to the poor wettability of alkali metals on oxides as well as their physical separation.[436] In addition, it is known that LLZO is prone to degradation when exposed to air.[470−472] The reaction between LLZO and moisture is conceptualized according to eqs 7 and 8:

$$Li_7La_3Zr_2O_{12} + xH_2O \rightarrow Li_{7-x}H_xLa_3Zr_2O_{12} + xLiOH \quad (7)$$

$$LiOH + 1/2CO_2 \rightarrow 1/2Li_2CO_3 + 1/2H_2O \quad (8)$$

The Li^+/H^+ exchange between garnet and moisture forms a Li^+ insulating Li_2CO_3 surface layer and blocks ion transfer at the interface, leading to a major increase in interface resistance.[473,474] In parallel, with oxides there is strong propensity for dendrite formation. The origin of dendrites in SSEs is thought to be quite different from how dendrites are envisioned to form in liquid systems. With oxide-based SSEs, dendrites are thought to originate from a combination of several mechanisms, including decreased grain boundary ionic conductivity leading to localized Li^+ concentrations, increased grain boundary electrical conductivity leading to field concentrations and localized conduction sufficient to nucleate metal, and poor wetting of the metal on the oxide surface.[475−477] To address these sources of dendrites, targeted strategies have focused on reducing the levels of porosity and grain boundary area, increasing the grain boundary ionic conductivity, reducing grain boundary electrical conductivity, and promoting wetting through metalphilic interfacial layers.[468] To improve lithium wettability while reducing the interfacial resistance, polymers have been employed.[478] Lithiophilic interlayers have also been based on a range of oxides, metals, and nitrides that display stronger chemical interaction with the metal than the SSE, including Al_2O_3,[471] Sb,[479] ZnO,[480] and Li_3N.[481] In order to remove the pristine thin Li ion insulating surface layers consisting of Li_2CO_3 and protons, Li et al. employed a carbon-assisting heat treatment on the garnet-type $Li_{6.5}La_3Zr_{1.5}Ta_{0.5}O_{12}$ (LLZT) solid electrolyte at 700 °C.[482] As a result, the interfacial impedance with lithium significantly decreased from 1210 Ω cm^2 to 28 Ω cm^2, and the resistance of the Li/LLZT/organic-electrolyte/S full cell was reduced from 1900 Ω cm^2 to 250 Ω cm^2. The hybrid Li−S cell displayed a reversible capacity of 970 at 100 μA cm^{-2}, retaining 800 mAh g^{-1} after 50 cycles at 200 μA cm^{-2}.

Hu et al. developed a three-dimensional (3D) bilayer garnet-type $Li_7La_{2.75}Ca_{0.25}Zr_{1.75}Nb_{0.25}O_{12}$ (LLCZNO) electrolyte framework for Li−S batteries, as shown in Figure 26.[478] The

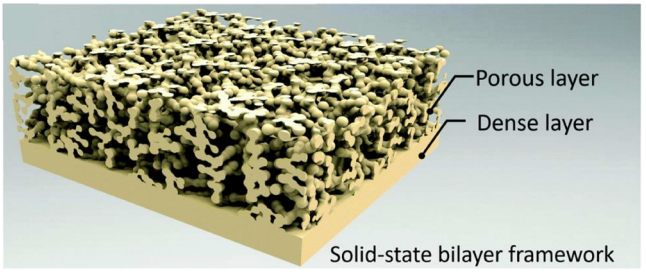

Figure 26. Schematic of the 3D bilayer garnet-type $Li_7La_{2.75}Ca_{0.25}Zr_{1.75}Nb_{0.25}O_{12}$ (LLCZNO) electrolyte framework. Reproduced with permission from ref 478. Copyright 2017 Royal Society of Chemistry.

70-μm-thick, porous layer hosted sulfur with a high mass loading of approximately 7.5 mg cm^{-2} and provided pathways for continuous ion transport. Meanwhile, a 35-μm dense layer separated Li metal and the cathode, providing mechanical rigidity. The same group also developed a trilayer garnet $Li_7La_3Zr_2O_{12}$ (LLZO) electrolyte framework with porous-dense-porous architecture for a hybrid Li−S battery.[458] Prior

https://doi.org/10.1021/acs.chemrev.1c00838
Chem. Rev. 2022, 122, 8053−8125

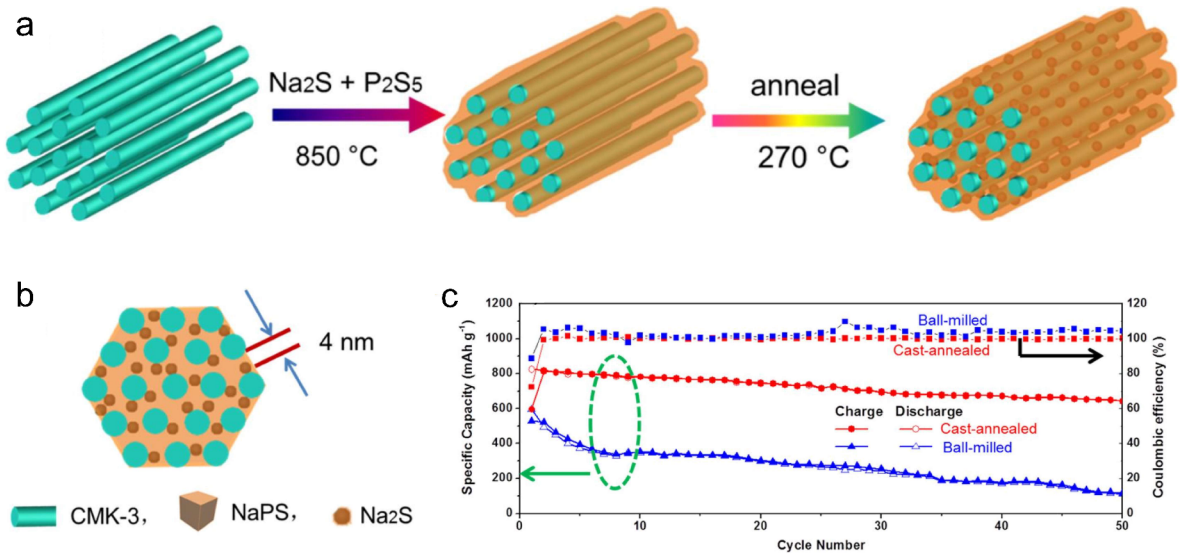

Figure 27. (a) Schematic illustration of the synthesis of a cast-annealed $Na_2S/Na_3PS_4/C$ composite cathode. (b) Front view of a single rod of the cast-annealed $Na_2S/Na_3PS_4/C$ composite. (c) Cycling properties the cast-annealed $Na_2S/Na_3PS_4/C$ nanocomposite cathodes and baseline ball-milled $Na_2S/Na_3PS_4/C$ composites, tested at of 50 mA g^{-1}. Reproduced with permission from ref 435. Copyright 2018 American Chemical Society.

to impregnation of the molten lithium, the anode side of the porous LLZO layer was ALD coated with 20 nm of zinc oxide. As a result, the porous electrolyte was fully wetted by lithium metal, ensuring low interfacial impedance. The total resistance of the resultant Li−S battery was less than 800 Ω cm^2. The cell showed stable electrochemical performance with a retained capacity of 1100 mA h g^{-1} after 50 cycles, which was equal to an energy density of 272 Wh/kg_{cell}.

A parallel challenge with S-based cathodes employing SSEs is to achieve a satisfactory combination ionic conductivity and electrical conductivity through the assembled cathode. With liquid electrolytes, achieving the former is less challenging since the electrolyte fully envelopes the cathode particles. With SSEs conformal coating of the cathode particles is not guaranteed and requires additional effort. Han et al. employed solution processing to fabricate a mixed conducting Li_2S electrode by dissolving Li_2S as the active material, polyvinylpyrrolidone (PVP) as the carbon precursor, and Li_6PS_5Cl as the solid electrolyte in ethanol, followed by a coprecipitation and thermal carbonization process at 550 °C.[483] The SSBs with Li_2S-Li_6PS_5Cl-C as the cathode, $80Li_2S{\cdot}20P_2S_5$ glass ceramic as the solid electrolyte, and Li−In alloy as the anode delivered a reversible capacity of 830 mAh g^{-1} at 50 mA g^{-1} after 60 cycles. In another study of a Na−S battery, Fan and co-workers utilized a cast-annealing process to obtain a robust Na_2S/Na_3PS_4/CMK-3 composite cathode with low interface resistance, as shown in Figure 27.[435] The Na_2S and P_2S_5 precursors were heated to 850 °C, forming a homogeneous liquid. After quenching and reannealing at 270 °C, the Na_2S nanoparticles were densely precipitated from the parent Na_3PS_4 solid electrolyte. The intimately contacting Na_3PS_4 and CMK-3 provided the mixed ionic/electronic conductive network that supported facile Na_2S conversion reactions. As a baseline, a $Na_2S/Na_3PS_4/C$ composite prepared by ball milling was also prepared. Figure 27c compares the performances of Na−S SSBs with these different cathode structures. The cast-annealed cathode delivered a superior reversible capacity of 650 mAh g^{-1} after 50 cycles at 60 °C, versus 110 mAh g^{-1} in the ball-milled case.

β''-Al_2O_3 solid electrolyte is thermodynamically stable against both metal anodes and sulfur cathodes.[484] A quasi-solid-state high-temperature (HT) potassium−sulfur (K−S) battery based on a K^+-conducting β''-Al_2O_3 solid electrolyte (K-BASE) was created by Lu et al., as shown in Figure 28a.[484] Molten-potassium-wetted K-BASE at 150 °C, which is markedly lower than the 400 °C necessary to achieve partial wetting of molten Na on the same electrolyte. The sulfur cathode was the potassium polysulfide (K_2S_5) catholyte in tetraglyme, with an overall sulfur concentration of 10 M. During discharge at 150 °C, the sulfur species were converted according to the following sequence: $K_2S_5 \rightarrow K_2S_4 + K_2S_3 \rightarrow K_2S_3 + K_2S_2$, with a capacity of 402 mAh g^{-1} and an energy density of 677 Wh kg^{-1}. The HT K−S cell operated for up to 1000 cycles with negligible capacity decay and favorable (98−100%) CE, and the results are shown in Figure 28b. This favorable performance was attributed to the permselectivity of the K-BASE electrolyte.

For polymer-based electrolytes, a typical anode protection strategy is focused on tailoring metallic salts and introducing reactive additives to mechanically and chemically stabilize the SEI layer.[485−488] This approach is also applicable for hybrid inorganic−organic SSE architectures. A few noteworthy examples of polymer modification strategies and hybrid approaches are summarized here, with previously cited review articles providing comprehensive discussions.[410,417−419] Armand et al. reported a significantly improved cycling performance of the PEO-based all-solid-state Li−S cell, by replacing conventional LiTFSI salt with LiFSI.[485] The inorganic F-SO^{2-} group in FSI^- could induce a robust and polysulfide-resistant SEI (rich LiF) film at the Li metal electrode as compared with the organic CF_3-SO^{2-} group in $TFSI^-$. The same group also developed an electrolyte additive lithium azide (LiN_3) into a PEO-based electrolyte that also stabilized the SEI.[488] A uniform Li_3N-rich SEI layer was *in situ* formed on the Li anode surface. Goodenough et al. developed a series of inorganic additives in SPEs, which can simultaneously improve the bulk ionic conductivity and stabilize the Li metal anode−polymer membrane inter-

https://doi.org/10.1021/acs.chemrev.1c00838
Chem. Rev. 2022, 122, 8053−8125

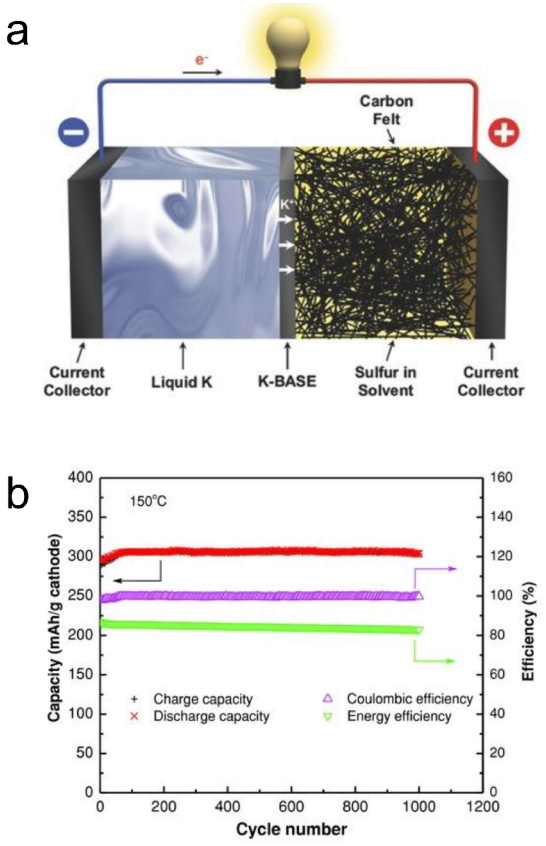

Figure 28. (a) Schematic of the quasi-solid-state high-temperature potassium−sulfur (K−S) battery. (b) Discharge/charge capacities and efficiencies of the K−S cell during cycling. Reproduced with permission from ref 484. Copyright 2015 John Wiley & Sons, Inc.

face.[487,489,490] Utilizing NASICON-type $LiZr_2(PO_4)_3$ (LZP) as a filler, $LiZr_2(PO_4)_3$ reacted with the metallic lithium anode to form an interphase layer composed of Li_8ZrO_6 and Li_3P.[490] This layer increased the wettability of the composite electrolyte by the metallic lithium anode and, meanwhile, reduced the interfacial contact resistance. The layer kinetically stabilized the interface by minimizing the reactions between the anode and the SSE. The symmetric cell with the composite electrolyte displayed only a minor increase in the interfacial resistance, going from 175 to 208 Ω cm^2 after 100 cycles at 40 °C.

10. PRACTICAL CONSIDERATIONS FOR FUNCTIONAL SEPARATORS

With functional separators one must also consider practical issues such as their impact on the overall cell specific energy and energy density, as well as the additional costs associated with the various functionalization schemes for commercial membranes. The additional weight and volume introduced by the functional separators and interlayers (and the extra electrolyte needed for wetting) should be accounted for. If the functional layer contains heavy transition metals, is thick, and/or is "fluffy" such that there is significant electrolyte uptake, the overall reduction of cell energy may be significant. Nanostructured functional layers such as various graphenes, carbon nanotubes, MOFs, *etc.* may contribute significantly to the cost of the metal−sulfur cell, reducing its competitiveness. Therefore, an industrially viable functional separator should be as lightweight as possible, for example with a loading of 0.1 mg cm^{-2} or less. The low mass loading will, in parallel, ensure that the functional layer contributes minimally to the total components weight, the weight due to the additional electrolyte, and the overall system cost. The high cost of some functional layers, such as electrocatalysts based on precious metals or adsorbents based on pristine monolayer graphene, may create cost issues even at these low mass loadings. To advance functional separator technology toward commercialization, analysis of functional separators also needs to be based on lean-electrolyte−high-mass-loading pouch cells, rather than flooded coin cells. We are aware of only several reports that explore functional separators at high sulfur loadings (>5 mg cm^{-2}), at lean-electrolyte conditions (<10 μL mg^{-1}), and with relatively thin alkali metal anode foils.[321,338,387] Even in those cases, analysis is performed on coin cells rather than on pouch cells.

Commercial separators are designed to have relatively low thermal stability, having their ion conducting seal off at elevated temperature, potentially suppressing catastrophic thermal runaway. For example, Celgard 2325 is a trilayer PP/PE/PP separator that displays this feature. The lower melting temperature (T_m = 120 °C) of the PE layer allows it to melt first and then fill the pores of the outer PP layers (T_m = 160 °C). This stops ion transport and current flow in the cell, while the PP layers continue to provide some mechanical protection from electrical shorting up to their melting point. Given such passive safety features in the commercial baselines, functional separators with modified interfaces need to be thoroughly evaluated. The safety-related parameters should include thermal resistance, flame retardancy, high-temperature melt integrity, and mechanical robustness.[491] Additional analysis would include (but is not limited to) combustion tests, thermogravimetric analysis−differential scanning calorimetry (TGA-DSC), and tensile strength and penetration tests that incorporate temperature and the electrolyte environment. Metal anodes have received justified negative publicity due to both dendrites and their intrinsically reactive surfaces. One consideration in their favor is that commercial embodiments of metal batteries would either employ a very thin film of the metal (*e.g.* 10−20 μm) to match the capacity of the cathode or be entirely "anode-free", with the active ions being stored directly in the cathode. The latter is even possible with sulfur-based batteries, for example by having a Li_2S-based cathode that is assembled in its discharged state. The use of functional separators for anode-free configurations has received only limited attention and is a critical area where further research is needed.

The technoeconomics of Li−S batteries have been treated in the literature, with readers being referred to the articles in refs 108 and 492−494. We are not aware of analogous studies that include the cost−benefit analysis of functional separators. Per the battery performance and cost (BatPaC) 4.0 model released from Argon National Laboratory,[495] the average cost of commercial PP−PE separators is $2 per m^2. Coating and/or surface modification of commercial separators would increase their cost, with the extent depending on the functionalization material and the application method (*e.g.* ALD, sputtering, and tape casting). Additional cost savings may be achieved by having the functional separator substitute for the current collector, although there would be difficulties integrating such architectures into existing pouch cell or cylindrical cell manufacturing processes. For example, coating PP or PE

https://doi.org/10.1021/acs.chemrev.1c00838
Chem. Rev. 2022, 122, 8053−8125

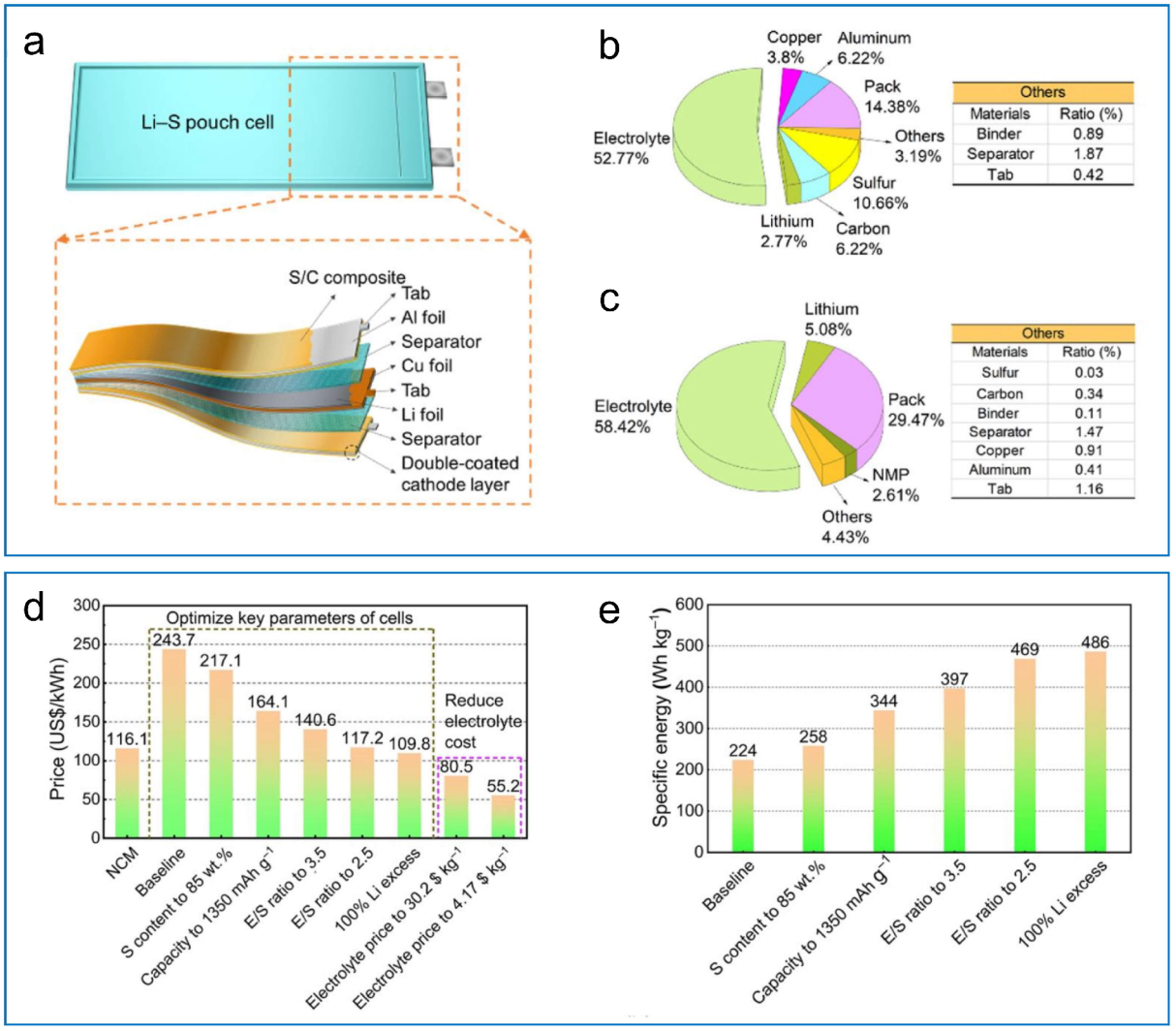

Figure 29. (a) Schematic illustration of a Li–S pouch cell. (b) Weight and (c) cost constitutions of a typical Li–S pouch cell. (d) Cell-level specific energy as a function of cell parameters. (e) Price per kW h of a Li–S pouch cell as a function of cell parameters and electrolyte prices. Reproduced with permission from ref 496. Copyright 2020 Elsevier.

with conducting carbon and further filling it with a slurry of sulfur can achieve an integrated separator–current collector–electrode.[299]

Kong et al. comprehensively evaluated how cell parameters could contribute to the specific energy and the cost of a Li–S pouch cell.[496] Figure 29a shows the structure of the as-designed Li–S pouch cell. The assumed parameters are the following: S loading = 4 mg cm^{-2}; E/S ratio = 4.5; N/P ratio = 5; sulfur capacity = 1000 mAh g^{-1}. According to this analysis a Li–S pouch cell is estimated to deliver a total capacity of 5.0 Ah and a specific energy of 224 Wh kg^{-1}. This is indicative that electrolytes take up a large portion of the Li–S pouch cell in terms of weight (52.77%) and cost (58.42%), as shown in Figure 29b and c. By comparison, the electrolyte weight and cost only account for 21.17% and 3.33% in a typical Li ion pouch cell based on a $LiNi_{0.5}Co_{0.2}Mn_{0.3}O_2$ (NCM) cathode and graphite (C) anode. Figure 29d and e presents the estimated cell-level specific energy and price of the optimized Li–S pouch cell from various aspects such as sulfur content, delivered capacity, E/S ratio, and lithium supply. The sulfur capacity has the possibility to reach 1350 mAh g^{-1} through engineering of the separator or host, which allows for a specific energy of 344 Wh kg^{-1}. The advanced Li–S pouch cells can attain specific energies of 397 and 469 Wh kg^{-1} by reducing the E/S ratio to 3.5 and 2.5, along with decreased costs of 140.6 US$ kWh^{-1} and 117.2 US$ kWh^{-1}, respectively. By curtailing the lithium supply from a 400% excess (N/P = 5) to 100% excess (N/P = 2), the specific energy can be boosted to 486 Wh kg^{-1} and the cost can accordingly drop to 109.8 US$ kWh^{-1}. These specific energy analyses indicate that realizing a projected specific energy of more than 500 Wh kg^{-1} requires pushing the critical cell parameters to their limits. To date, the critical missing link for commercialization of Li–S batteries is battery fabrication facilities. There is little available beyond the dedicated one or several PI laboratory setups for fabricating Li–S button or (less common) Li–S pouch cells. The vast majority of R&D battery foundries will not allow sulfur-based cathodes into the fabrication line as they will contaminate conventional LIBs even with changes in tooling. With covalently bonded sulfur–carbon systems such as SPAN and SSePAN, fabrication line contamination is less of an issue, although the perception of contamination and the associated hesitancy is still prevalent.

https://doi.org/10.1021/acs.chemrev.1c00838
Chem. Rev. 2022, 122, 8053–8125

Pure selenium is not found naturally; it is, rather, obtained by purifying byproducts of various mining operations or by being separated from sulfur deposits.[497,498] More than 90% of primary Se is derived from copper ores, and most of the other 10%, from lead ores. The fact that selenium is produced entirely as a byproduct means it will not be as promising as the sulfur cathode in large-scale commercialization. As a result, the supply of selenium is directly affected by the mining output of the primary materials such as copper. The average traded price of selenium in the United States in 2019 was \$44 kg^{-1}, making it potentially economical as a minority dopant to S[499] but likely not as the primary charge storage material since its cost is higher than for state-of-the-art oxide cathodes.

11. FUTURE OUTLOOK: MECHANICS AND ANALYTICAL METHODS FOR FUNCTIONAL SEPARATORS

11.1. Mechanics Considerations for Separators

In this section, we describe general considerations on the mechanics of separator materials, primarily from the perspective of existing polyolefin separators for conventional lithium batteries, given the dearth of information on emerging battery separator materials. There is a surprising range of perspectives on the desired mechanical attributes of separators, in part stemming from differing levels of understanding on the role that various properties play in separator performance. The function of the separator is not directly a mechanical role. The primary purpose of a conventional separator is twofold: (1) blocking direct electrical shorts from the anode to the cathode while (2) providing an easy pathway for ionic conduction. This requires an electrically insulating material that maintains a physical separation while also providing ionic conduction pathways that are as short as practical. There is an intrinsic trade-off between the openness of the woven or microporous polymer skeleton to facilitate fluid and ionic conductivity and the connectivity/density of the structure to promote structural integrity.[500] In addition, in alkali metal batteries, the separator plays a secondary role by influencing dendrite formation. Finally, multifunctional separators also employ surface coatings to suppress S uptake at the cathode side or unstable SEI formation at the anode.

Generally, a high stiffness is thought to be desirable as it prevents shape change of the poroelastic separator during the large volumetric distortions associated with battery cycling. Elastically driven shape changes correspond generally to a change in ionic conductivity: compressive strains serve to close off paths in the percolation network. In the elastic regime, the ionic conductivity κ of a stressed separator has been modeled[501] as a function of the unstressed conductivity κ_0 with a linear dependence on stress σ and an inverse dependence on modulus E:

$$\kappa = \kappa_0\left(1 + \frac{\sigma}{E}\right) \tag{9}$$

This rather simple model would likely only be an approximate solution, presumably lacking fidelity for large stress changes or for hierarchical pore networks. While this equation illustrates the desire for a high elastic modulus, the high stresses that are developed in the separator are necessarily transmitted to the cathode and anode on either side, thereby inducing larger potential deformation in those bodies. The extent of the elastic stress transmitted from the separator is ultimately limited by the yield strength and work hardening capacity of the separator relative to those properties of the cathode and anode.

The desire for high stiffness in the separator runs counter to the desire for a high volume fraction of porosity. At the continuum scale, the Gibson–Ashby model for cellular solids[502] suggests that the modulus of a porous structure E scales with the modulus of its fully dense solid E_s:

$$E = E_s C_e\left(\frac{\rho}{\rho_s}\right)^{n_e} \tag{10}$$

where ρ is the effective density of the porous solid and ρ_s is the corresponding full density at zero porosity with C_e and n_e as scaling constants for elastic behavior. For porous networks where the solid ligaments are bending dominated, $n_e \sim 2$. Here again, this first-order scaling law is only approximate, and modifications become important in the nanoporous regime where new physical mechanisms emerge.[503]

Experimentally, there are three pathways to measure mechanical properties including elastic response. Thin film compression is perhaps best suited to mimic the macroscopic mechanical configuration of most battery stacks. For example, Yan et al. used such a technique to explore the compressive stress–strain response of Celgard 2400 both in a dry condition and infiltrated with a dimethyl carbonate electrolyte.[504] They reported a compressive modulus of 191 GPa in air and 165 GPa with the addition of electrolyte. Nanoindentation allows a small sampling volume on the order of a cubic micrometer, comparable to the feature sizes of many separators and, thereby, amenable to mapping spatial variations in properties. With a sufficiently deep indent and correspondingly large sampling volume spanning many microstructural features, the average mechanical response can also be probed. For example, the effective modulus of several dry microporous separator materials was compared using nanoindentation, reporting a moduli range from 49 MPa for a SiO_2 + Al_2O_3 + PET separator to 1240 MPa for an Al_2O_3 + UHMWPE separator.[505] Finally, thin film tension tests represent the third common pathway to obtain mechanical properties. For example, Wang et al. used tension testing to observe the stress–strain response and corresponding porosity evolution for several commercially available Celgard and Asahi Hipore separator materials.[506] They found that dry-processed separators exhibited overall volumetric growth during tensile deformation and associated that behavior with pore growth, whereas wet-processed separators experienced pore collapse.

The aforementioned considerations treat elasticity in the time-independent sense. But many separator materials have a substantial viscoelastic response. The viscoelastic behavior causes the separator to respond more stiffly under rapid loading but also causes the separator to release stress over time when held at a constant strain state (*e.g.*, battery state). Recently, a generalized orthotropic viscoelastic model for polymeric separators, calibrated to Celgard 2400, was developed by Yan et al.[507] The viscoelastic response is very rapid upon initial loading, following an approximately logarithmic time scale. For perspective, the Celgard 2400 separator will halve its stress level (or double its strain level if in a stress-controlled scenario) in about 20 min. These time scales are comparable to, or shorter than, most battery cycle scenarios, and accordingly, the viscous response should not be discounted. A few years earlier, Chen et al. also demonstrated a

https://doi.org/10.1021/acs.chemrev.1c00838
Chem. Rev. 2022, 122, 8053–8125

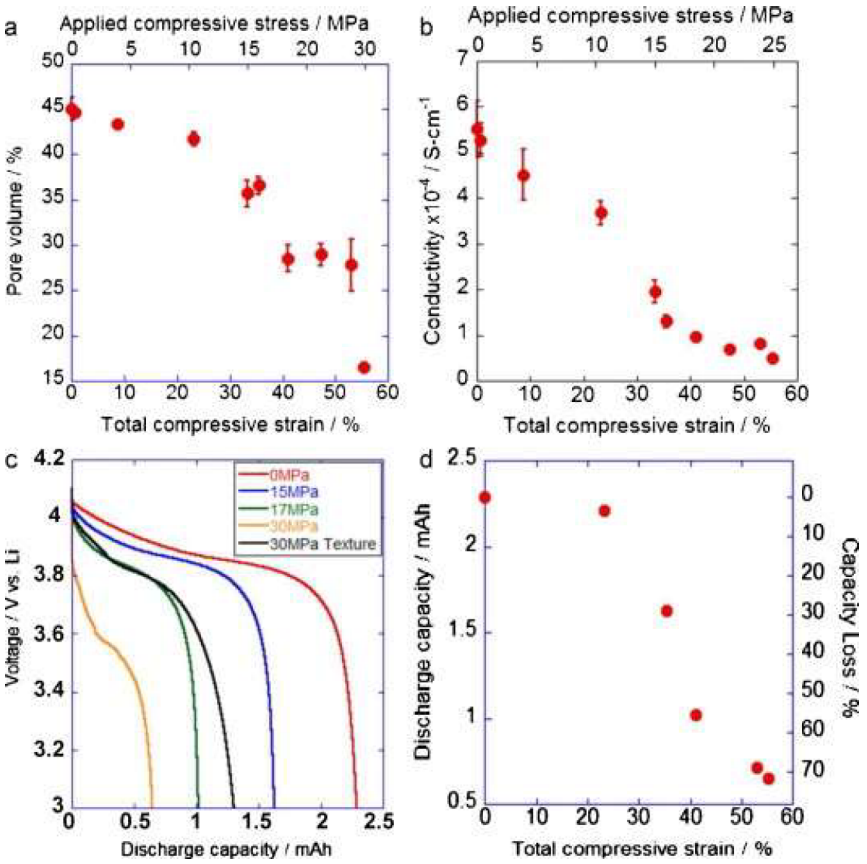

Figure 30. Applied compressive stress leads to permanent strain in the separator, pore collapse, and concomitant capacity loss in a Celgard 2340 separator. Reproduced with permission from ref 517. Copyright 2011 Elsevier.

viscous constitutive model for Celgard 2400 that could effectively capture the nonlinear behavior, stress-relaxation, and corresponding strain-rate sensitivity effects in the strain-rate regime of 10^{-5} to 5×10^{-3} s^{-1}.[508,509] Unlike the Yan model which was developed for a dry viscoelastic separator, the Chen work also evaluated the role of electrolyte concentration in effectively reducing the modulus through a swelling effect, as discussed in the next section.

Both the Yan and Chen models lacked an explicit temperature dependence. Thermal fluctuations are critical since their magnitude during battery cycling can have four mechanical effects: generally, as temperature rises, not only will the time constant for the viscous response shorten, but the time-independent "storage" modulus will also decrease.[510] In addition to the effect that thermal fluctuations play on intrinsic elastic separator properties, there is also a thermal expansion effect, causing a heat-induced strain, and, under idealized rigid confinement, a corresponding increase in stress or, alternatively, a subsequent co-deformation with the anode.

The mechanical properties are not controlled by the polymer skeleton alone. While many studies consider the dry properties of the separator, the role of the infiltrated electrolyte solvent is generally not negligible. In poroelasticity models for rate-dependent elastic properties,[511,512] the effective modulus of a fluid-infiltrated poroelastic separator depends on the porous polymer's permeability, the overall separator dimensions (proximity to free surfaces), the elastic properties of the polymer and the bulk modulus, and the viscosity of the fluid. The restricted fluid flow induces a strain-rate dependence of elastic properties beyond the intrinsic viscoelasticity of the polymer alone.[513] However, the viscous effect is negligible for strain rates typical of battery usage: In a study on the compressive modulus of Celgard 3501, the apparent modulus of the electrolyte-containing separator began to rise above that of the reference dry separator only at strain rates in excess of ~0.01 to 0.1 s^{-1}.[513]

Some, but not all, solvent−separator pairs cause swelling, leading to a corresponding reduction in stiffness. In an early study from 2011, the viscoelastic properties of polypropylene-based Celgard 2400 were evaluated using dynamic mechanical analysis (DMA) in both a dry environment and two electrolyte solutions.[514] Both the storage and loss moduli in the wet separator were reported to be approximately half that of the dry separator, although the effect was strongly anisotropic with considerably less swelling and modulus change in the transverse direction of the separator.

The relative susceptibility of a separator−electrolyte combination to swelling and stiffness loss has been rationalized on the basis of the Flory−Huggins interaction parameter that takes into account the free-volume-corrected solvent activity as a function of solvent mass fraction.[515] A simpler consideration of the cohesive energy based on a Hildebrand parameter did not show strong predictivity. What is less clear from these studies is the role of pore size, especially in the context of nanoscale interstices associated with some separators. Chen et al.'s study on Celgard 2400 also explored the effects of two different electrolyte solutions on the elastic modulus.[509] At low strain rates in the regime of 10^{-5} s^{-1} to 0.01 s^{-1}, the wet separators were substantially less stiff than the dry separator. The wet separators also exhibited reduced modulus as the

https://doi.org/10.1021/acs.chemrev.1c00838
Chem. Rev. 2022, 122, 8053−8125

concentration of the salt electrolyte was increased up to a maximum of 1.1 M. This is likely an illustration of the swelling effect on elastic modulus, rather than a poroelastic effect. To our knowledge, there is very little experimental evidence of the superimposed roles of thermal and poroelastic properties on time-dependent elastic behavior. A thermo-poro-viscoelastic model of polymeric separators was recently developed by Behrou,[516] although the effectiveness of this model is not yet clear as it has yet to be calibrated or validated against experimental observations. This model is a continuum-scale model, so scaling phenomena such as the effects of pore size distribution and network connectivity are captured only in the effective material properties, *i.e.*, permeability. Moreover, it is unclear if such a model will effectively capture the superimposed role of separator swelling on thermo-viscoelastic behavior.

A separator nominally functions in the elastic regime. For this reason, there is less focus in the literature on the yielding behavior of separators. The onset of yielding corresponds to densification: a permanent collapse of pores and ensuing loss in both fluid permeability and ionic conductivity. Accordingly, higher strengths allow larger elastic strains before the onset of permanent damage and for larger stresses to be transferred to the cathode and anode without permanent separator shape change. Hardness is closely related to yield strength and typically easier to measure. The previously mentioned nanoindentation study on several separator materials reported a hardness range from 1.4 MPa for PTFE to 66 MPa for Al_2O_3 + UHMWPE.[505]

The term "creep" often is used in the viscoplastic sense, describing permanent, irreversible deformation mechanisms. In separator studies, creep is also used to describe recoverable viscoelastic straining followed by recovery.[514] Peabody and Arnold reported that separator creep can induce capacity fade.[517] In constrained battery packages, when the electrode expands, it exerts compression on the separator that can cause irreversible pore closure, thereby impeding ion transport. For example, when a compressive stress of 20 MPa is exerted over 3 h on a Celgard 2340 separator, the separator experiences ∼45% compressive strain and a ∼ 33% reduction in pore volume, corresponding to a ∼ 60% loss in capacity, as illustrated in Figure 30. In an apparent contradiction, the authors oxymoronically described the observed creep phenomenon as "viscoelastic".[513,517] However, the observed pore collapse was not reversible, but permanent, and only observed through subsequent imaging in a scanning electron microscope after loading. Thus, the behavior seemingly should have been described as viscoplastic. The phenomenon of reduced ion transport from mechanically driven pore volume reduction has been described as "stress-induced",[518] and while this choice of terminology is understandable, the semantically rigorous description would be "strain-induced".

There is a general perception that higher strength separators should enhance the safety performance of batteries and resist the penetration of dendrites.[519,520] To that end, several options for enhancing the strength of conventional separators have been explored, such as reinforcing the polymers with oxide particles[521−523] or nanofibers.[520] However, the term "strength" or "mechanical strength" is often used only in a general sense, without qualifying the distinction between yield strength, *e.g.* the onset of permanent deformation, and ultimate tensile strength, *e.g.* the final rupture of a material. For perfectly brittle elastic materials, there is no distinction between yield and ultimate strengths. But for deformable separators the distinction is important: the yield strength is an indicator of shape changes coinciding with alteration of the ionic conductivity whereas the ultimate tensile strength triggers through-thickness crack formation. In ductile materials, yield strength and ultimate tensile strength often approximately scale with one another. However, as materials become more brittle, the yield strength and fracture resistance are often in conflict with one another.[524] Mechanistically, a low yield strength can enable plasticity mechanisms that enhance toughening and resistance to crack formation, thereby elevating the ultimate tensile strength.

Puncture resistance is particularly thought to be a key mechanical attribute, allowing the separator to resist perforation from dendrite growth. However, as with phase transition, it is unclear that dendrite growth could be substantially impeded by modest increases in puncture resistance—the constraining pressures would likely need to be substantial to suppress dendrites. A general standardized test method for testing the perforation of barrier films, ASTM F1306-90, is often used for separator characterization. Chen et al. developed a coupled penetration−tension method to evaluate battery separators under combined loading.[525] In that study, they explored the morphological role of anisotropic separator porosity on fracture, revealing that slitlike pores oriented in the machine direction serve to impede cracking by blunting, but in the transverse direction, pores link up and encourage cracking. In a subsequent study, the essential work of fracture was measured in both dry and wet conditions in two electrolytes, with both electrolytes having a deleterious effect on the work of fracture.[509] The authors postulate several possible explanations for the loss of fracture resistance including swelling-induced microcrack formation, a reduction in the local density of matrix fibers, and an interaction of the electrolyte with trace water causing significant acidity in the system. Owing to the viscoelastic, viscoplastic, and poroelastic properties of separators described previously, the puncture resistance is also strain-rate sensitive. For Celgard 2400, a deformation rate of 4 mm/s requires a puncture force that is about three times higher than that of the quasi-static puncture force observed at 0.004 mm/s.[526] While this strain-rate sensitivity is relevant for accident scenarios, the effect is likely negligible for normal use conditions and dendrite puncture.

There have been very few published studies on the cyclic response of even the most common polyolefin separators for existing lithium ion batteries. In a recent article, the repeated dynamic compression during charge−discharge cycling was observed to gradually induce a partial point electrolyte shortage for an undisclosed commercial separator.[527] In the study, the degraded performance was associated with a substantial reduction in electrolyte retention within the separator. While the study focused primarily on a tearing response under a single cycle (monotonic loading), there was no mention of a tearing or cracking response related to the cyclic loading. While numerous studies exist on the fatigue response of dense polypropylene and composites, there does not appear to be any substantial studies on microporous separators.[528,529] The existing literature on cyclic loading primarily is concerned with flexible batteries, where the physical strain is caused not by battery cycling but by external flexure of the battery cell.[530,531] These studies were on full battery stacks and did not isolate the behavior of the separator. With regard to coated separators for Li−S batteries, fatigue

https://doi.org/10.1021/acs.chemrev.1c00838
Chem. Rev. 2022, 122, 8053−8125

loading from battery cycling was cited as the source of microcrack formation,[532] although in that study the microcracks were not viewed to be critically detrimental. Given the importance of the poro-viscoelastic and viscoplastic behavior of separators and the early indications that separator fatigue may at least induce accelerated pore collapse if not cracking, the lack of cycling studies under dry and wet conditions appears to be an important oversight.

11.2. Spectroscopic Techniques for Separators

Many different methods are used in battery research for characterization and monitoring either *ex situ* or *in situ*/*operando*. For example, Raman and infrared spectroscopies provide structural and chemical information, and they are noninvasive and nondestructive techniques and have been widely used for battery research.[45,533,534] Chi et al. studied separator−electrolyte interaction by measuring the Raman spectra of an electrolyte-soaked PE separator, a $(ZrO_2/POSS)_3$-modified PE separator, and a $(ZrO_2/POSS)_3ZrO_2$-modified PE separator.[363] Li et al. used XRD, Raman, XPS, and Fourier transform infrared (FTIR) to characterize mesoporous nitrogen-doped carbon nanospheres as a sulfur matrix before and after impregnation with sulfur.[232] However, for *in situ*/*operando* analysis, there are practical challenges associated with such measurements, for which similar chemical environment and operation conditions should be maintained as per the true environment of a cell during operation. Development of experimental techniques for *in situ* and *operando* analysis is critical for understanding and studying battery mechanisms, dynamics, intercalation, phase transformations, interfacial reactions, and degradation.[535] As per Figure 31, here we

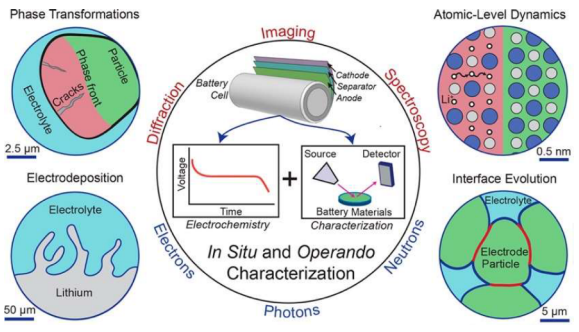

Figure 31. Schematic diagram of various characterization techniques for the different phenomena on various dimensions. Reproduced with permission from ref 535. Copyright 2020 American Chemical Society.

focus our discussion on vibrational spectroscopies (IR and Raman), X-ray-based methods (XRD and XPS), and nuclear magnetic resonance (NMR), and we provide a description of integration approaches of analytical instrumentation to enable measurement of physiochemical processes in real time.

In order to achieve *in situ*/*operando* characterization, complex measurement configurations and electrochemical cells with optical windows for spectral collection are required. Figure 32a shows an *in situ* Raman cell comprised of two electrodes with a separator in between and a reference electrode positioned on the edge of the separator.[536] The backside of the upper electrode is illuminated by the laser through a thin glass window, and the backscattered radiation is collected by the microscope lens. In this work, the electrochemical intercalation of tetraethylammonium (Et_4N^+) and tetrafluoroborate (BF_4^-) into and out of microcrystalline graphite was studied using the Raman cell. Lei et al. used *in situ* Raman to study the shuttling mechanism of negatively charged polysulfide species for three types of separators: standard PP, reduced graphene oxide on PP, and reduced graphene oxide/sodium lignosulfonate composite on PP.[284] The configuration of the Raman cell is presented in Figure 32b, and the collected time-resolved Raman spectra of a PP separator during a discharge process are shown in Figure 32c. To allow direct laser illumination on the separator and Raman signal collection from the separator−lithium interface, a hole was made on both negative case and lithium metal foil, and the Raman signal from the separator was collected at the side next to the lithium foil. Three Raman peaks for Li_2S_8 (at 150, 219, and 478 cm^{-1}) which correspond to long-chain PSs are initially observed when the discharge is initiated. Following that, the characteristic peak corresponding to S_8^{2-} gradually vanishes as discharging continues, and peaks (at 398 and 413 cm^{-1}) of the short-chain PSs Li_2S_6, Li_2S_3, and Li_2S_4 + Li_2S_5 start to appear. At the end of the process, peaks of Li_2S_4 + Li_2S_5 suggest that those are likely to deposit on the separator during the PS shuttling.

Integration of Raman with plasmonic structures resulted in surface-enhanced Raman spectroscopy (SERS), and integration of Raman with AFM resulted in development of tip-enhanced Raman spectroscopy (TERS). Typically, the Raman scattering signal is weak; therefore, sensitivity is low. In order to increase the sensitivity, plasmonic nanoparticles or nanostructures are utilized, where localized electromagnetic enhancement increases the measured Raman signal. Such a method is called SERS. When a special particle of a metallic core is coated with a thin oxide layer, then this technique is called shell-isolated nanoparticle-enhanced Raman spectroscopy (SHINERS). Chang et al. used SHINERS to systematically investigate the effect of the pore size of MOF separators.[283] The MOF layer was coated on a PP separator and sandwiched in the middle of the catholyte and anolyte glass fibers (GF-C and GF-A, respectively). Figure 32d shows the schematic of the measurement setup and the measurement points at which Raman spectra were collected. As this method requires distribution of plasmonic nanoparticles on the surface of the sample to be analyzed, it will not be possible to measure the exact real environment in a battery cell. He et al. used time-resolved *operando* SHNIERS to study the interaction between the polysulfide-adsorbed/saturated host surface and the dissolved polysulfide species in bulk solution.[294] An advanced spectroscopic method, such as TERS, has been used to determine the chemical composition, distribution of phases, and topography at nanoscale of an SEI formed on amorphous silicon at a lateral resolution of <10 nm and a sampling depth of <5 nm.[537] Figure 32e shows the schematic of the setup, where a Raman laser illuminates a gold-coated AFM tip, creating localized surface plasmon resonance which enhanced the electromagnetic field in the tip's proximity. However, implementation of such a technique for *in situ*/*operando* analysis is challenging due to the needed for contact of the AFM tip with the sample.

Attenuated total reflection (ATR)-FTIR relies on light propagation in an infrared transparent crystal, where an evanescent field extends a short distance into the medium in the proximity of the crystal's surface. When the surface of the crystal is coated with a thin layer of gold, it can be used as an electrode, and also its plasmonic effect enhances the electromagnetic field on gold's surface, which is termed surface-enhanced infrared absorption spectroscopy (SEIRAS). Raberg

https://doi.org/10.1021/acs.chemrev.1c00838
Chem. Rev. 2022, 122, 8053−8125

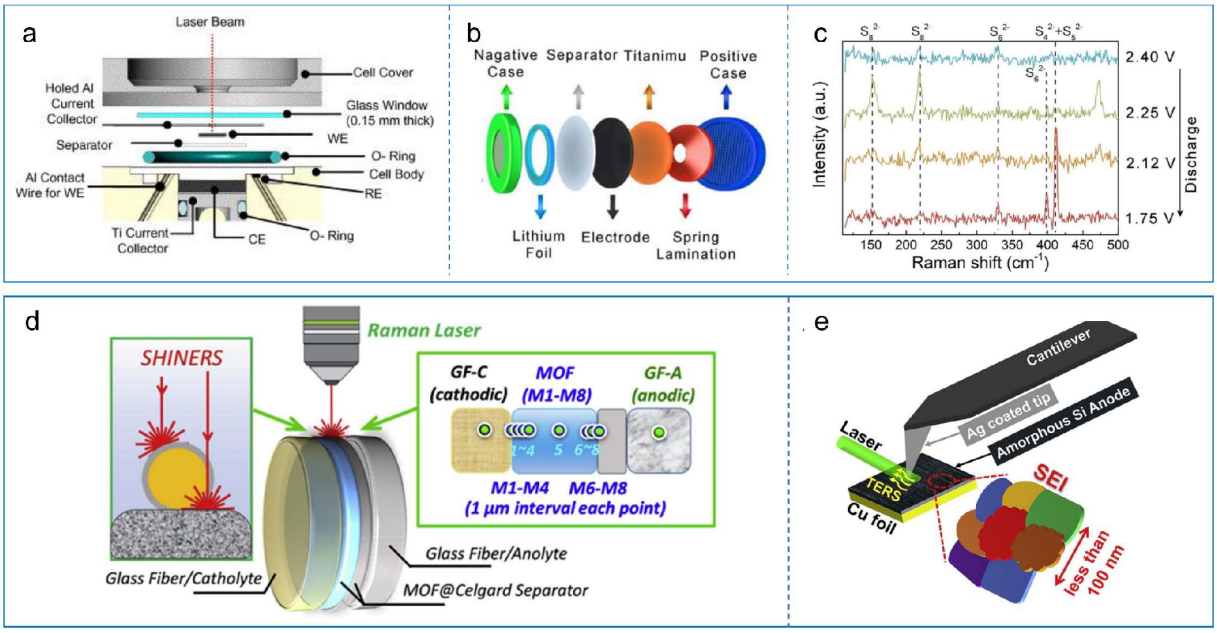

Figure 32. (a) Three-electrode *in situ* Raman cell showing the separate components (expanded, not to scale). (b) Cell configuration with a sealed glass window for *in situ* Raman analysis of PP-based separators. (c) Raman spectra for the discharge process for a PP separator. (d) Schematic of the surface-enhanced *operando* Raman characterization system SHINERS. (e) TERS setup combining AFM with a confocal side-illumination Raman spectrometer. Panel a is reproduced with permission from ref 536. Copyright 2006 Elsevier. Panels b and c are reproduced with permission from ref 284. Copyright 2018 Elsevier. Panel d is reproduced with permission from ref 283. Copyright 2020 Elsevier. Panel e is reproduced with permission from ref 537. Copyright 2019 Elsevier.

et al. used ATR-FTIR to study the *in situ* vibrational spectroscopy of the electric double layer (EDL), where they probed changes in the EDL composition as a function of potential.[538] Vivek et al. investigated lithium−oxygen and sodium−oxygen electrochemistry in acetonitrile and dimethyl sulfoxide by monitoring *in situ* the metastable, solvated, and surface adsorbed alkali metal−oxygen discharge species.[539] Challenges in optical−electrochemical cell design to ensure light preparation and collection from the desired component in the battery limit the applicability of the technique to study the separator, for example, which is internally positioned between the two electrodes.

X-ray-based methods are useful for qualitative and quantitative analysis and especially for phase and chemical changes in battery components. Those include XRD, XPS, X-ray absorption spectroscopy (XAS), X-ray reflectometry (XRR), and X-ray imaging. *In situ* analysis relies on an electrochemical cell with X-ray transparent windows, and those have been used to study various processes and interfacial phenomena for battery research.[94,534] Gorlin et al. performed XAS characterization of a Li_2S−Li battery using a spectro-electrochemical cell capable of spatially resolved measurements.[97] They successfully obtained information about both solid and solution phase intermediates produced in two locations of the cell, the Li_2S cathode and a glass fiber separator, which allowed them to discriminate between the changes in the concentration of the species in the separator and the changes in the composition of the species in both locations of the cell. Conder et al. demonstrated the direct observation of lithium polysulfides adsorbed on the surface of a glass fiber separator in the Li−S battery during operation by means of *operando* XRD.[540]

Solid-state nuclear magnetic resonance spectroscopy can be a useful tool to study multiple processes involved during electrochemical cycling. Information on structural and electronic changes of the materials is possible due to high chemical specificity and sensitivity to crystalline and amorphous phases. However, *in situ* operation presents challenges associated with the electrochemical cell, which should be placed inside the NMR coil, and the overall hardware setup design, which can be affected by interferences.[541] Moreover, the relatively slow response of NMR measurements and the micrometer scale information may limit the temporal and special resolution. On the other hand, NMR enables a direct observation of structural species within the entire sample volume, thus probing the anode, cathode, and electrolyte simultaneously.[542] *In situ*/*operando* or *ex situ* implementations have been explored in an alkali metal−sulfur system, for probing the evolution of the soluble and precipitated (poly)sulfides during electrochemical cycling.[64,543] The clear recognition regarding the sulfur redox mechanism, especially for the emerging Na−S and K−S systems, serves to guide the reasonable design of multifunctional separators.

11.3. Advanced Imaging Techniques for Separators

Indirect methods to probe the various organic and inorganic phases of the SEI are valuable in giving an overall picture of the evolution of the electrode−electrolyte interface. However, the understanding of local variations is critical to determine the mechanistic nature of counterproductive phenomena such as dendrite growth. For this, microanalysis techniques that provide real space images and high-resolution elemental and redox mapping are essential. Furthermore, in terms of the separator, inherent heterogeneities (*e.g.*, pore size) can be averaged out using ensemble techniques, which can skew our understanding of the material behavior. For polyolefin separators porosity can be heterogeneous, which is a main contributing factor toward nonuniform ionic flux and localized

https://doi.org/10.1021/acs.chemrev.1c00838
Chem. Rev. 2022, 122, 8053−8125

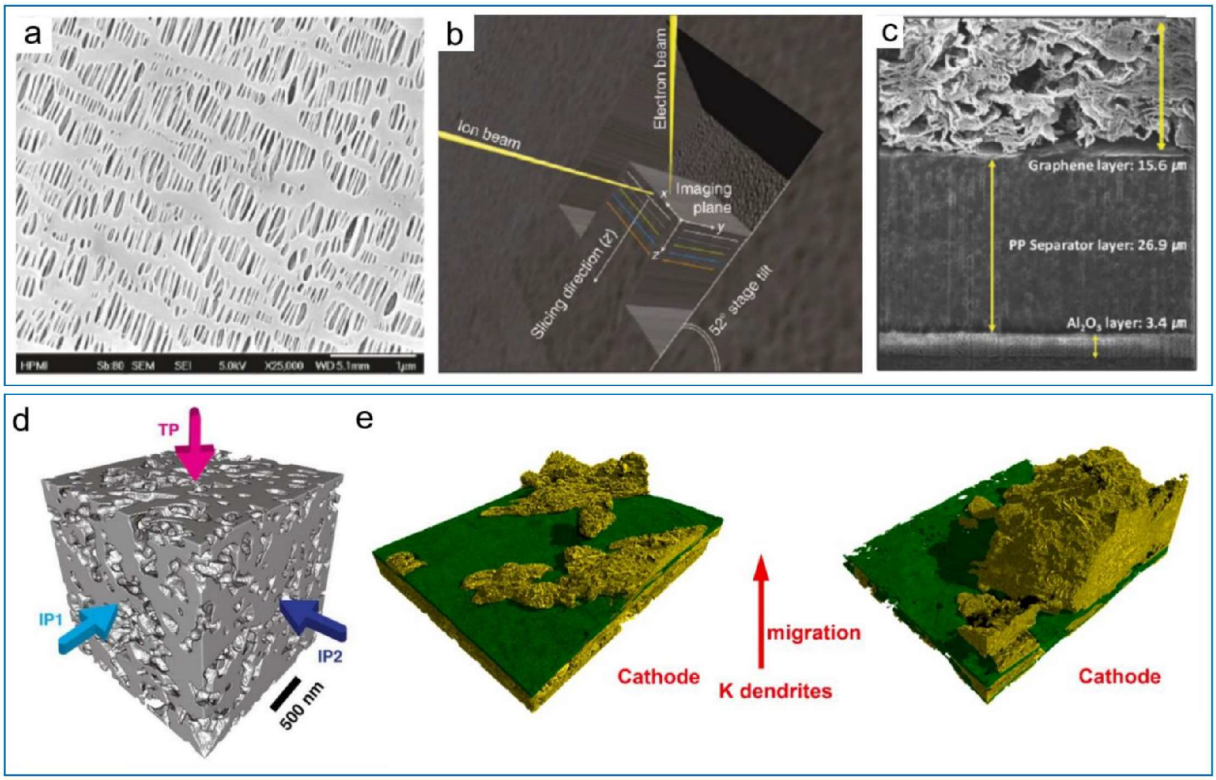

Figure 33. (a) Surface SEM images of the Celgard H2013 commercial separator trilayer (porosity 45%). (b) Typical sample and beam geometry and orientation for a SEM/FIB tomography experiment using serial cross-sectional milling. (c) Cross-sectional view of a dual-functional graphene/PP/Al_2O_3 (DF-GPA) separator. (d) 3D tomogram reconstruction showing a microstructure rendering of a PE16A separator; volume has a 2 μm edge length. (e) 3D reconstructed tomograms of K-based cells formed with a Celgard separator. Panel a is reproduced with permission from ref 544. Copyright 2018 Hindawi. Panel b is reproduced with permission from ref 545. Copyright 2011 Springer Nature. Panel c is reproduced with permission from ref 546. Copyright 2017 John Wiley & Sons, Inc. Panel d is reproduced with permission from ref 547. Copyright 2016 The Electrochemical Society. Panel e is reproduced with permission from ref 198. Copyright 2021 Elsevier.

concentration field, which can initiate dendrite growth. Site-specific analysis, especially when correlated to the known local chemical behavior of the cathode, the anode, and their interfaces, can provide a mechanistic understanding critical to evaluating and optimizing battery performance. Figure 3b shows the complex problem of phase identification in the SEI. Elemental analysis, such as X-ray energy dispersive spectroscopy (XEDS), can suffer from overlap of the X-ray lines, making quantification difficult. For crystallographic analysis the complex and varying crystal structures of each phase, polycrystallinity of local regions, strong diffuse amorphous signal, and sample instability under the beam all make indexing exceedingly difficult.

Scanning electron microscopy is a two-dimensional imaging technique that is readily available, is relatively cheap and easy to operate, and can give rapid feedback on the separator structure, as well as postcycling structural evolution (Figure 33a). Both polyolefin and glass frit separators present unique challenges in SEM. They are insulating and require a conductive coating to image, especially at high resolution. Furthermore, it is difficult to prepare and image a common cross cut section. Polyolefins will show some compression under a cutting blade no matter how sharp, and glass frits would require fracture, which can be difficult to precisely perform. Furthermore, the surface imaging that it enables should not be regarded as sufficient enough to determine structure−function relationships. The complexity of the internal 3D pore network of a separator may be suggested by the surface structure, but a complete understanding requires exposing the buried interface using focused ion beam milling. FIB milling is typically carried out by a highly focused Ga^+ ion beam and creates a cross section on the tens of micrometers scale after around 10 min of milling (Figure 33b). Likewise, to probe the important and unique interfaces of multifunctional separators, the layers must first be exposed using FIB milling techniques (Figure 33c). Since the nature of these interfaces is critical to understanding performance, they must be conserved during the FIB process. A too-high-powered Ga^+ ion beam can "delaminate" the interface, as well as introduce ion contamination into the interface, causing uncertainty in elemental and redox analysis. Therefore, each sample requires optimization of the imaging and milling conditions to eliminate sample preparation artifacts.

To accurately quantify the structure of a porous membrane, the features of interest must be much smaller than this length scale; that is, a statistically significant number of pores must be exposed and visualized to give confidence that the structure being observed is representative of the larger material. Serial cutting can be performed to systematically cross section the separator and create a series of images that then can be reconstructed to 3D tomogram (Figure 33d); although, it should be noted this is a destructive technique, at least at the local level. The length scale of the cross section can be increased by using a plasma FIB (hundreds of micrometers scale length after around 10 min of milling) or even newly developed laser milling systems (millimeter scale length after

https://doi.org/10.1021/acs.chemrev.1c00838
Chem. Rev. 2022, 122, 8053−8125

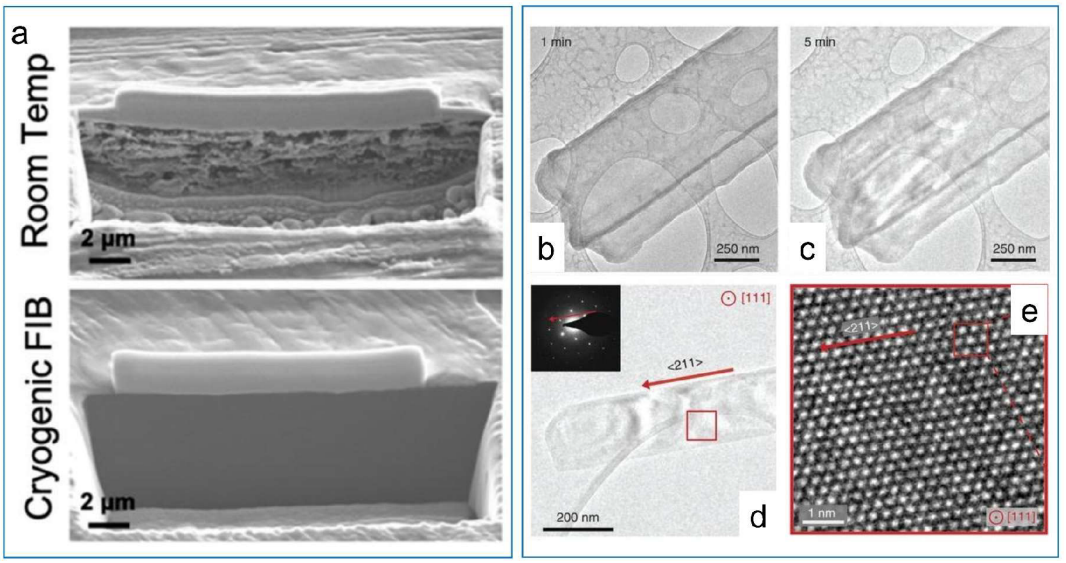

Figure 34. (a) SEM images showing the difference in FIB milling temperatures of a pristine Li foil. At cryogenic temperatures (−170 °C) artifacts from the Ga^+ ion beam are minimized to preserve a dense, uniform Li foil. (b−e) Cryo-TEM images of Li metal dendrites showing the effect of cryogenic temperatures on sample stability. Continuous electron-beam irradiation at a dose rate of ∼50 e^- $Å^{-2}$ s^{-1} shows no appreciable damage after 1 min (b) and 5 min (c) of exposure. Such sample stability of low-Z materials and the resulting atomic resolution imaging are critical to characterize the orientation and growth direction of the dendrite (d and e). Panel a reproduced with permission from ref 551. Copyright 2019 American Chemical Society. Panels b−e reproduced with permission from ref 163. Copyright 2017 Science.

around 10 min of milling). However, a volume of 8 μm^3 (2 μm × 2 μm × 2 μm) has recently been shown to be sufficient to properly microanalyze the ensemble properties of a PE separator, so the less expensive and more readily available Ga^+ ion FIB milling systems should be broadly applicable to separator characterization.[547] Larger length scales can also be probed by X-ray tomography; Figure 33e shows 3D reconstructions from *in situ* synchrotron X-ray tomography experiments.[198] These images show how the different densities and structures of K dendrites (yellow), *e.g.*, mosslike, treelike, or needle-like *etc.*, can deform and penetrate the Celgard separator (green).

If the pore sizes are increasingly small such that SEM cannot resolve them, especially with the lowered contrast inherent in polyolefins, then a lamella can be milled, lifted out, and thinned to be electron transparent for TEM.[548] In practice, a lamella of between 80−100 nm is sufficient for good characterization in a 300 keV accelerating voltage TEM. Milling thinner samples decreases pore overlap and allows for the use of a less intense (*i.e.*, destructive) e^- beam accelerating voltage (*e.g.*, 120 keV); however, this can introduce mechanical concerns. The FIB lamella can literally curl up on itself due to reduced rigidity and increased electrostatics. So a successful sample preparation becomes an interplay between increasing final resolution and sample stability, which is especially true for polymer materials. Once safely loaded onto the TEM, there are a number of techniques available to reduce beam−sample interactions: (1) cooling the sample to ∼ −190 °C using a cryogenic holder, (2) using low-dose imaging techniques, a series of tracking, focus, and exposure steps that allow the user to take an image of their sample with the lowest e^- dose possible,[549] and (3) direct detection cameras, which can count single electrons, greatly reducing the required e^- dose. These techniques are especially crucial for tomography, where a number of images are taken of the same region of interest at multiple tilt angles (±70°) and then reconstructed into a 3D tomogram. With enough care and imaging/milling optimization, MOFs and COFs can also be thinned to electron transparency for TEM analysis; however, their lifetime under the beam is very short, and even the above strategies for minimizing total e^- dose may not be enough for the sample to survive a tilt series.[550]

Recently, the use of cryogenic temperatures has proven itself to be critical for the characterization of energy materials. Performing analysis on instruments cooled to cryogenic temperatures (−190 °C to −140 °C) presents a number of distinct advantages over room temperature operation: (1) the oxidation of Li, Na, and K is drastically slowed, especially if the sample is kept both cool and under high vacuum, (2) soft material separators such as PP and PE become more rigid, which makes them easier to mill and reduces charging effects, and (3) beam−sample interactions are reduced, which is crucial for sample stability under both the electron and ion beams and for minimizing the inclusion of Ga^+ artifacts into the freshly exposed subsurface during milling.

Figure 34a shows a comparison from Lee et al. of FIB milling performed on Li foil samples at room temperature and at cryogenic temperatures (−170 °C).[551] Using standard room temperature techniques, there is a distinct structural change in the foil due to local melting events. Energy-dispersive X-ray spectroscopy (XEDS) mapping also showed a high degree of Ga inclusion. In contrast, performing milling at cryogenic temperatures produced no unwanted artifacts, and a dense, uniform, and pristine Li subsurface was exposed. Figure 34b−d by Li et al. shows the analysis of an incredibly air-sensitive Li dendrite grown directly on a Cu TEM grid.[163] The Li is electrochemically deposited onto the grid using standard battery conditions. The sample is washed and immediately flash frozen in liquid N_2, with the incredibly low temperatures slowing its reactivity enough to assume retention of its native electrochemical and structural state. Figure 34b and c shows time-dependent images of the dendrite under constant

https://doi.org/10.1021/acs.chemrev.1c00838
Chem. Rev. 2022, 122, 8053−8125

electron-beam irradiation at dose rates of ~50 e^{-} Å^{-2} s^{-1}, indicating good sample stability under cryogenic conditions. This is crucial to obtain good atomic resolution images (Figure 34c and d) that can be used to fully characterize the dendrite crystallography and growth direction.

One of the key benefits of performing characterization at cryogenic temperatures is the ability to preserve the solid−liquid interface. Zachman et al. preserved the solid−liquid interface in a lithium metal battery in order to perform structural and elemental mapping by cryogenic scanning transmission electron microscopy (cryo-STEM) (Figure 35).[552] Figure 35a and b shows electron transparent lamellae

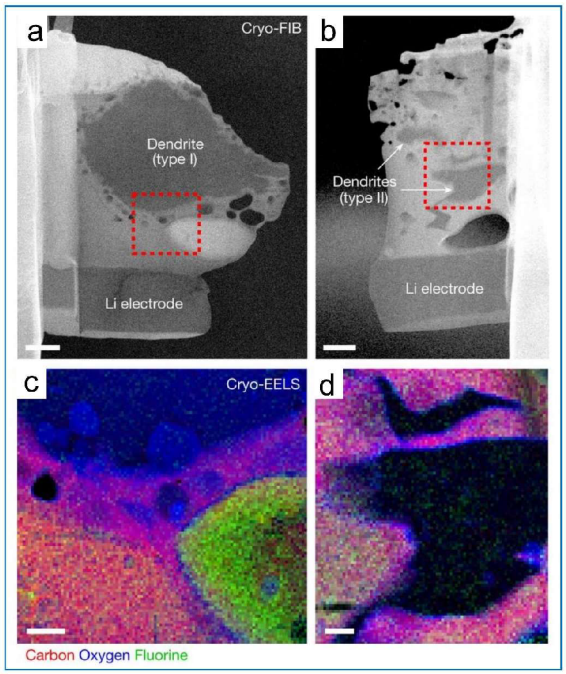

Figure 35. (a and b) Electron transparent cryogenic FIB lift-out lamellae of two different types of Li dendrite, complete with intact SEI and electrolyte layers. (c and d) Cryogenic electron energy loss spectroscopy elemental mapping showing that both SEIs are oxygen-rich; however the SEI in panel d contains no carbon. Likewise, the dendrite in panels a and c has an appreciable oxygen content, whereas the dendrite analyzed in panels b and d does not. Reproduced with permission from ref 552. Copyright 2018 Springer Nature.

prepared by cryo-FIB lift out techniques and imaged using cryo-STEM. Due to the inherent Z-contrast in STEM, the different regions of the interface (Li electrode, SEI, penetrating dendrite, and electrolyte) can be readily distinguished. Cryogenic electron energy loss spectroscopy (cryo-EELS) was used to create an elemental map of the sample. Unlike XEDS, which primarily identifies elements of interest, EELS can provide information on bonding environment and atomic configuration (oxidation state) and is better suited to lighter elements. Using this technique, they were able to identify two dendrite types with distinct compositions: one composed primarily of partially oxidized lithium and one corresponding to pure lithium hydride.

AUTHOR INFORMATION

Corresponding Authors

Hongchang Hao − *Materials Science and Engineering Program & Texas Materials Institute, The University of Texas at Austin, Austin, Texas 78712, United States*; Email: haohongchang@utexas.edu

David Mitlin − *Materials Science and Engineering Program & Texas Materials Institute, The University of Texas at Austin, Austin, Texas 78712, United States*; orcid.org/0000-0002-7556-3575; Email: david.mitlin2@utexas.edu

Authors

Tanya Hutter − *Materials Science and Engineering Program & Texas Materials Institute, The University of Texas at Austin, Austin, Texas 78712, United States*

Brad L. Boyce − *Center for Integrated Nanotechnologies, Sandia National Laboratories, Albuquerque, New Mexico 87110, United States*

John Watt − *Center for Integrated Nanotechnologies, Los Alamos National Laboratory, Los Alamos, New Mexico 87545, United States*

Pengcheng Liu − *Materials Science and Engineering Program & Texas Materials Institute, The University of Texas at Austin, Austin, Texas 78712, United States*; orcid.org/0000-0002-9530-9267

Complete contact information is available at: https://pubs.acs.org/10.1021/acs.chemrev.1c00838

Notes

The authors declare no competing financial interest.

Biographies

Hongchang Hao received his B.S. degree from Tianjin University in 2016 and his M.S. degree from University of the Chinese Academy of Sciences in 2019. He is currently pursuing his Ph. D. degree under the supervision of Prof. David Mitlin at The University of Texas at Austin. His current research interests are high-energy-density electrode materials, including sulfur cathodes and Li and Na metal anodes. His research interests also include catalysis.

Tanya Hutter is currently an Assistant Professor at the Walker Department of Mechanical Engineering at The University of Texas at Austin. She obtained a B.Sc. in Chemical Engineering in 2007 from Ben Gurion University, an M.Sc. in Materials Science and Engineering in 2009 from Tel Aviv University, and a Ph.D. in Physical Chemistry in 2013 from University of Cambridge.

Brad L. Boyce is a Distinguished Member of the Technical Staff at Sandia National Laboratories. Dr. Boyce received a B.S. degree from Michigan Technological University in 1996 in Metallurgical Engineering and M.S. and Ph.D. degrees in 1998 and 2001 from the University of California at Berkeley. Dr. Boyce joined the technical staff at Sandia in 2001, where his research interests lie in micromechanisms of material behavior. He was promoted to Principal Member of the Technical Staff in 2005 and received the Distinguished appointment in 2015. In 2017, Dr. Boyce joined the Center for Integrated Nanotechnologies in the *in situ* characterization and nanomechanics thrust. He has published over 140 peer reviewed articles and holds 6 patents. Dr. Boyce is a past recipient of the Hertz Foundation fellowship, the Brimacombe Medal, and the Marcus A. Grossman Young Author award.

John Watt is a Scientist at the Center for Integrated Nanotechnologies (CINT) at Los Alamos National Laboratory. He received his Ph.D.

https://doi.org/10.1021/acs.chemrev.1c00838
Chem. Rev. 2022, 122, 8053−8125

from Victoria University of Wellington, New Zealand, and held postdoctoral positions at both VUW and CINT Sandia. His research interests include the synthesis and characterization of soft matter, low-Z, and inorganic nanoparticles using cryogenic and *in situ* electron microscopy techniques.

Pengcheng Liu is currently a Humboldt Fellow and conducts scientific research at Technical University of Munich. Prior to that, he received his Ph.D. at Nanjing University of Aeronautics and Astronautics in 2017, and then he joined Prof. David Mitlin's group in 2018, working as a Postdoctoral Associate at The University of Texas at Austin. He is serving as the Guest Editor for the academic journal *Nano Materials Science* and is organizing the Special Issue "Special issue on emerging materials for carbon neutrality". Also, he is serving as the committee fellow for organizing the second Global Summit and Expo on Graphene and 2D Materials (*2DMAT2022*) in Edinburgh, Scotland. His current research interests the advanced alkali metal batteries, and focus is paid to the stable alkali metal anode and interface issues in nonaqueous and all-solid-state batteries.

David Mitlin is a David Allen Cockrell Endowed Professor at the Walker Department of Mechanical Engineering, The University of Texas at Austin. Prior to that, he was a Professor and General Electric Chair at Clarkson University and an Assistant, Associate, and Full Professor at the University of Alberta. Dr. Mitlin is an ISI Highly Cited Researcher (2018−onward), having published over 150 journal articles on various aspects of energy storage materials, on metallurgy and corrosion. Dr. Mitlin also serves as the Associate Editor for *Sustainable Energy and Fuels* - RSC. He grew up in upstate New York and southern Connecticut.

ACKNOWLEDGMENTS

This work was supported by the Los Alamos National Laboratory IMS Distinguished Faculty Scholar program, which was awarded in 2021 to D.M. This work was performed at the Center for Integrated Nanotechnologies, an Office of Science User Facility operated for the U.S. Department of Energy (DOE) Office of Science. Los Alamos National Laboratory, an affirmative action equal opportunity employer, is managed by Triad National Security, LLC for the U.S. Department of Energy's NNSA, under contract 89233218CNA000001. Sandia National Laboratories is a multimission laboratory managed and operated by National Technology & Engineering Solutions of Sandia, LLC, a wholly owned subsidiary of Honeywell International, Inc., for the U.S. DOE's National Nuclear Security Administration under contract DE-NA-0003525. The views expressed in the article do not necessarily represent the views of the U.S. DOE or the United States Government.

REFERENCES

(1) Manthiram, A. A Reflection on Lithium-Ion Battery Cathode Chemistry. *Nat. Commun.* **2020**, *11*, 1550.
(2) Goodenough, J. B.; Park, K. S. The Li-Ion Rechargeable Battery: A Perspective. *J. Am. Chem. Soc.* **2013**, *135*, 1167−1176.
(3) Hong, X.; Mei, J.; Wen, L.; Tong, Y.; Vasileff, A. J.; Wang, L.; Liang, J.; Sun, Z.; Dou, S. X. Nonlithium Metal-Sulfur Batteries: Steps Toward a Leap. *Adv. Mater.* **2019**, *31*, 1802822.
(4) Xu, J.; Ma, J.; Fan, Q.; Guo, S.; Dou, S. Recent Progress in the Design of Advanced Cathode Materials and Battery Models for High-Performance Lithium-X (X = O2, S, Se, Te, I2, Br2) Batteries. *Adv. Mater.* **2017**, *29*, 1606454.
(5) Ji, X.; Lee, K. T.; Nazar, L. F. A Highly Ordered Nanostructured Carbon-Sulphur Cathode for Lithium-Sulphur Batteries. *Nat. Mater.* **2009**, *8*, 500−506.
(6) Yin, Y. X.; Xin, S.; Guo, Y. G.; Wan, L. J. Lithium-Sulfur Batteries: Electrochemistry, Materials, and Prospects. *Angew. Chem., Int. Ed.* **2013**, *52*, 13186−13200.
(7) Albertus, P.; Babinec, S.; Litzelman, S.; Newman, A. Status and Challenges in Enabling the Lithium Metal Electrode for High-Energy and Low-Cost Rechargeable Batteries. *Nat. Energy* **2018**, *3*, 16−21.
(8) Nanda, S.; Bhargav, A.; Manthiram, A. Anode-free, Lean-Electrolyte Lithium-Sulfur Batteries Enabled by Tellurium-Stabilized Lithium Deposition. *Joule* **2020**, *4*, 1121−1135.
(9) Chung, S. H.; Manthiram, A. Current Status and Future Prospects of Metal-Sulfur Batteries. *Adv. Mater.* **2019**, *31*, 1901125.
(10) Yu, X.; Manthiram, A. Capacity Enhancement and Discharge Mechanisms of Room-Temperature Sodium-Sulfur Batteries. *ChemElectroChem.* **2014**, *1*, 1275−1280.
(11) Wang, Y. X.; Lai, W. H.; Chou, S. L.; Liu, H. K.; Dou, S. X. Remedies for Polysulfide Dissolution in Room-Temperature Sodium-Sulfur Batteries. *Adv. Mater.* **2020**, *32*, 1903952.
(12) Ding, J.; Zhang, H.; Fan, W.; Zhong, C.; Hu, W.; Mitlin, D. Review of Emerging Potassium-Sulfur Batteries. *Adv. Mater.* **2020**, *32*, 1908007.
(13) Ding, J.; Zhou, H.; Zhang, H.; Tong, L.; Mitlin, D. Selenium Impregnated Monolithic Carbons as Free-Standing Cathodes for High Volumetric Energy Lithium and Sodium Metal Batteries. *Adv. Energy Mater.* **2018**, *8*, 1701918.
(14) Ding, J.; Zhou, H.; Zhang, H.; Stephenson, T.; Li, Z.; Karpuzov, D.; Mitlin, D. Exceptional Energy and New Insight with a Sodium-Selenium Battery based on a Carbon Nanosheet Cathode and a Pseudographite Anode. *Energy Environ. Sci.* **2017**, *10*, 153−165.
(15) Yao, Y.; Chen, M.; Xu, R.; Zeng, S.; Yang, H.; Ye, S.; Liu, F.; Wu, X.; Yu, Y. CNT Interwoven Nitrogen and Oxygen Dual-Doped Porous Carbon Nanosheets as Free-Standing Electrodes for High-Performance Na-Se and K-Se Flexible Batteries. *Adv. Mater.* **2018**, *30*, 1805234.
(16) Zhang, F.; Guo, X.; Xiong, P.; Zhang, J.; Song, J.; Yan, K.; Gao, X.; Liu, H.; Wang, G. Interface Engineering of MXene Composite Separator for High-Performance Li-Se and Na-Se Batteries. *Adv. Energy Mater.* **2020**, *10*, 2000446.
(17) Zhang, F.; Xiong, P.; Guo, X.; Zhang, J.; Yang, W.; Wu, W.; Liu, H.; Wang, G. A Nitrogen, Sulphur Dual-Doped Hierarchical Porous Carbon with Interconnected Conductive Polyaniline Coating for High-Performance Sodium-Selenium Batteries. *Energy Storage Mater.* **2019**, *19*, 251−260.
(18) Pham, V. H.; Boscoboinik, J. A.; Stacchiola, D. J.; Self, E. C.; Manikandan, P.; Nagarajan, S.; Wang, Y.; Pol, V. G.; Nanda, J.; Paek, E.; et al. Selenium-Sulfur (SeS) Fast Charging Cathode for Sodium and Lithium Metal Batteries. *Energy Storage Mater.* **2019**, *20*, 71−79.
(19) Yao, Y.; Xu, R.; Chen, M.; Cheng, X.; Zeng, S.; Li, D.; Zhou, X.; Wu, X.; Yu, Y. Encapsulation of SeS2 into Nitrogen-Doped Free-Standing Carbon Nanofiber Film Enabling Long Cycle Life and High Energy Density K-SeS2 Battery. *ACS Nano* **2019**, *13*, 4695−4704.
(20) Li, Z.; Zhang, J. T.; Lu, Y.; Lou, X. W. A Pyrolyzed Polyacrylonitrile/Selenium Disulfide Composite Cathode with Remarkable Lithium and Sodium Storage Performances. *Sci. Adv.* **2018**, *4*, No. eaat1687.
(21) Guo, H.; Li, X.; Zhang, X.; Wang, H.; Wang, Z.; Peng, W. Diffusion Coefficient of Lithium in Artificial Graphite, Mesocarbon Microbeads, and Disordered Carbon. *New Carbon Mater.* **2007**, *22*, 7−10.
(22) Jian, Z.; Xing, Z.; Bommier, C.; Li, Z.; Ji, X. Hard Carbon Microspheres: Potassium-Ion Anode Versus Sodium-Ion Anode. *Adv. Energy Mater.* **2016**, *6*, 1501874.
(23) Jain, R.; Yuan, Y.; Singh, Y.; Basu, S.; Wang, D.; Yang, A.; Wang, X.; Rong, M.; Lee, H. J.; Frey, D.; et al. Alloying of Alkali Metals with Tellurene. *Adv. Energy Mater.* **2021**, *11*, 2003248.
(24) Jin, H.; Wang, H.; Qi, Z.; Bin, D. S.; Zhang, T.; Wan, Y.; Chen, J.; Chuang, C.; Lu, Y. R.; Chan, T. S.; et al. A Black Phosphorus-Graphite Composite Anode for Li-/Na-/K-Ion Batteries. *Angew. Chem., Int. Ed.* **2020**, *59*, 2318−2342.

https://doi.org/10.1021/acs.chemrev.1c00838
Chem. Rev. 2022, 122, 8053−8125

(25) Qian, J.; Henderson, W. A.; Xu, W.; Bhattacharya, P.; Engelhard, M.; Borodin, O.; Zhang, J. G. High Rate and Stable Cycling of Lithium Metal Anode. *Nat. Commun.* **2015**, *6*, 6362.
(26) Zheng, J.; Chen, S.; Zhao, W.; Song, J.; Engelhard, M. H.; Zhang, J. G. Extremely Stable Sodium Metal Batteries Enabled by Localized High-Concentration Electrolytes. *ACS Energy Lett.* **2018**, *3*, 315−321.
(27) Hosaka, T.; Kubota, K.; Kojima, H.; Komaba, S. Highly Concentrated Electrolyte Solutions for 4 V Class Potassium-Ion Batteries. *Chem. Commun.* **2018**, *54*, 8387−8390.
(28) Kubota, K.; Dahbi, M.; Hosaka, T.; Kumakura, S.; Komaba, S. Towards K-Ion and Na-Ion Batteries as "Beyond Li-Ion". *Chem. Rec.* **2018**, *18*, 459−479.
(29) Amara, S.; Toulc'Hoat, J.; Timperman, L.; Biller, A.; Galiano, H.; Marcel, C.; Ledigabel, M.; Anouti, M. Comparative Study of Alkali-Cation-Based (Li+, Na+, K+) Electrolytes in Acetonitrile and Alkylcarbonates. *ChemPhysChem* **2019**, *20*, 581−594.
(30) Deng, N.; Liu, Y.; Li, Q.; Yan, J.; Lei, W.; Wang, G.; Wang, L.; Liang, Y.; Kang, W.; Cheng, B. Functional Mechanism Analysis and Customized Structure Design of Interlayers for High Performance Li-S Battery. *Energy Storage Mater.* **2019**, *23*, 314−349.
(31) Zhang, W.; Tu, Z.; Qian, J.; Choudhury, S.; Archer, L. A.; Lu, Y. Design Principles of Functional Polymer Separators for High-Energy, Metal-Based Batteries. *Small* **2018**, *14*, 1703001.
(32) Jeong, Y. C.; Kim, J. H.; Nam, S.; Park, C. R.; Yang, S. J. Rational Design of Nanostructured Functional Interlayer/Separator for Advanced Li-S Batteries. *Adv. Funct. Mater.* **2018**, *28*, 1707411.
(33) Fan, L.; Li, M.; Li, X.; Xiao, W.; Chen, Z.; Lu, J. Interlayer Material Selection for Lithium-Sulfur Batteries. *Joule* **2019**, *3*, 361−386.
(34) Su, Y. S.; Manthiram, A. A New Approach to Improve Cycle Performance of Rechargeable Lithium-Sulfur Batteries by Inserting a Free-Standing MWCNT Interlayer. *Chem. Commun.* **2012**, *48*, 8817−8819.
(35) Chung, S. H.; Manthiram, A. Bifunctional Separator with a Light-Weight Carbon-Coating for Dynamically and Statically Stable Lithium-Sulfur Batteries. *Adv. Funct. Mater.* **2014**, *24*, 5299.
(36) Okamoto, H. The Li-S (Lithium-Sulfur) System. *J. Phase Equilib.* **1995**, *16*, 94−97.
(37) Sangster, J.; Pelton, A. D. The Na-S (Sodium-Sulfur) System. *J. Phase Equilib.* **1997**, *18*, 89.
(38) Sangster, J.; Pelton, A. D. The K-S (Potassium-Sulfur) System. *J. Phase Equilib.* **1997**, *18*, 82−88.
(39) Zou, Q.; Liang, Z.; Du, G. Y.; Liu, C. Y.; Li, E. Y.; Lu, Y. C. Cation-Directed Selective Polysulfide Stabilization in Alkali Metal-Sulfur Batteries. *J. Am. Chem. Soc.* **2018**, *140*, 10740−10748.
(40) Fu, C.; Wong, B. M.; Bozhilov, K. N.; Guo, J. Solid State Lithiation-Delithiation of Sulphur in Sub-Nano Confinement: A New Concept for Designing Lithium-Sulphur Batteries. *Chem. Sci.* **2016**, *7*, 1224−1232.
(41) Park, C. W.; Ahn, J. H.; Ryu, H. S.; Kim, K. W.; Ahn, H. J. Room-Temperature Solid-State Sodium/Sulfur Battery. *Electrochem. Solid-State Lett.* **2006**, *9*, A123.
(42) Liu, P.; Mitlin, D. Emerging Potassium Metal Anodes: Perspectives on Control of the Electrochemical Interfaces. *Acc. Chem. Res.* **2020**, *53*, 1161−1175.
(43) Lee, B.; Paek, E.; Mitlin, D.; Lee, S. W. Sodium Metal Anodes: Emerging Solutions to Dendrite Growth. *Chem. Rev.* **2019**, *119*, 5416−5460.
(44) Zhao, M.; Li, B. Q.; Peng, H. J.; Yuan, H.; Wei, J. Y.; Huang, J. Q. Lithium-Sulfur Batteries under Lean Electrolyte Conditions: Challenges and Opportunities. *Angew. Chem., Int. Ed.* **2020**, *59*, 12636−12652.
(45) Zhang, L.; Qian, T.; Zhu, X.; Hu, Z.; Wang, M.; Zhang, L.; Jiang, T.; Tian, J. H.; Yan, C. In Situ Optical Spectroscopy Characterization for Optimal Design of Lithium-Sulfur Batteries. *Chem. Soc. Rev.* **2019**, *48*, 5432−5453.
(46) Wang, Y.; Zhou, D.; Palomares, V.; Shanmukaraj, D.; Sun, B.; Tang, X.; Wang, C.; Armand, M.; Rojo, T.; Wang, G. Revitalising Sodium-Sulfur Batteries for Non-High-Temperature Operation: a Crucial Review. *Energy Environ. Sci.* **2020**, *13*, 3848−3879.
(47) Zhao, Q.; Hu, Y.; Zhang, K.; Chen, J. Potassium-Sulfur Batteries: A New Member of Room-Temperature Rechargeable Metal-Sulfur Batteries. *Inorg. Chem.* **2014**, *53*, 9000−9005.
(48) Hu, L.; Lu, Y.; Li, X.; Liang, J.; Huang, T.; Zhu, Y.; Qian, Y. Optimization of Microporous Carbon Structures for Lithium-Sulfur Battery Applications in Carbonate-Based Electrolyte. *Small* **2017**, *13*, 1603533.
(49) Guo, Q.; Li, S.; Liu, X.; Lu, H.; Chang, X.; Zhang, H.; Zhu, X.; Xia, Q.; Yan, C.; Xia, H. Ultrastable Sodium-Sulfur Batteries without Polysulfides Formation Using Slit Ultramicropore Carbon Carrier. *Adv. Sci.* **2020**, *7*, 1903246.
(50) Xiong, P.; Han, X.; Zhao, X.; Bai, P.; Liu, Y.; Sun, J.; Xu, Y. Room-Temperature Potassium-Sulfur Batteries Enabled by Microporous Carbon Stabilized Small-Molecule Sulfur Cathodes. *ACS Nano* **2019**, *13*, 2536−2543.
(51) Kumar, V.; Eng, A. Y. S.; Wang, Y.; Nguyen, D. T.; Ng, M. F.; Seh, Z. W. An Artificial Metal-Alloy Interphase for High-Rate and Long-Life Sodium-Sulfur Batteries. *Energy Storage Mater.* **2020**, *29*, 1−8.
(52) Bommier, C.; Ji, X. Electrolytes, SEI Formation, and Binders: A Review of Nonelectrode Factors for Sodium-Ion Battery Anodes. *Small* **2018**, *14*, 1703576.
(53) Wu, Q.; Zhou, X.; Xu, J.; Cao, F.; Li, C. Adenine Derivative Host with Interlaced 2D Structure and Dual Lithiophilic-Sulfiphilic Sites to Enable High-Loading Li-S Batteries. *ACS Nano* **2019**, *13*, 9520−9532.
(54) Wu, Q.; Yao, Z.; Zhou, X.; Xu, J.; Cao, F.; Li, C. Built-In Catalysis in Confined Nanoreactors for High-Loading Li-S Batteries. *ACS Nano* **2020**, *14*, 3365−3377.
(55) Huang, S.; Wang, Y.; Hu, J.; Lim, Y. V.; Kong, D.; Zheng, Y.; Ding, M.; Pam, M. E.; Yang, H. Y. Mechanism Investigation of High-Performance Li-Polysulfide Batteries Enabled by Tungsten Disulfide Nanopetals. *ACS Nano* **2018**, *12*, 9504−9512.
(56) He, B.; Rao, Z.; Cheng, Z.; Liu, D.; He, D.; Chen, J.; Miao, Z.; Yuan, L.; Li, Z.; Huang, Y. Rationally Design a Sulfur Cathode with Solid-Phase Conversion Mechanism for High Cycle-Stable Li-S Batteries. *Adv. Energy Mater.* **2021**, *11*, 2003690.
(57) Zhu, Q.; Zhao, Q.; An, Y.; Anasori, B.; Wang, H.; Xu, B. Ultra-Microporous Carbons Encapsulate Small Sulfur Molecules for High Performance Lithium-Sulfur Battery. *Nano Energy* **2017**, *33*, 402−409.
(58) Chen, X.; Peng, L.; Wang, L.; Yang, J.; Hao, Z.; Xiang, J.; Yuan, K.; Huang, Y.; Shan, B.; Yuan, L.; et al. Ether-Compatible Sulfurized Polyacrylonitrile Cathode with Excellent Performance Enabled by Fast Kinetics via Selenium Doping. *Nat. Commun.* **2019**, *10*, 1021.
(59) Ghosh, A.; Kumar, A.; Das, T.; Ghosh, A.; Chakraborty, S.; Kar, M.; MacFarlane, D. R.; Mitra, S. Lewis Acid-Base Interactions between Polysulfides and Boehmite Enables Stable Room-Temperature Sodium-Sulfur Batteries. *Adv. Funct. Mater.* **2020**, *30*, 2005669.
(60) Aslam, M. K.; Seymour, I. D.; Katyal, N.; Li, S.; Yang, T.; Bao, S. J.; Henkelman, G.; Xu, M. Metal Chalcogenide Hollow Polar Bipyramid Prisms as Efficient Sulfur Hosts for Na-S Batteries. *Nat. Commun.* **2020**, *11*, 5242.
(61) Kumar, A.; Ghosh, A.; Forsyth, M.; MacFarlane, D. R.; Mitra, S. Free-Radical Catalysis and Enhancement of the Redox Kinetics for Room-Temperature Sodium-Sulfur Batteries. *ACS Energy Lett.* **2020**, *5*, 2112−2121.
(62) Bao, W.; Shuck, C. E.; Zhang, W.; Guo, X.; Gogotsi, Y.; Wang, G. Boosting Performance of Na-S Batteries Using Sulfur-Doped Ti3C2Tx MXene Nanosheets with a Strong Affinity to Sodium Polysulfides. *ACS Nano* **2019**, *13*, 11500−11509.
(63) Wang, N.; Wang, Y.; Bai, Z.; Fang, Z.; Zhang, X.; Xu, Z.; Ding, Y.; Xu, X.; Du, Y.; Dou, S.; et al. High-Performance Room-Temperature Sodium-Sulfur Battery Enabled by Electrocatalytic Sodium Polysulfides Full Conversion. *Energy Environ. Sci.* **2020**, *13*, 562−570.

https://doi.org/10.1021/acs.chemrev.1c00838
Chem. Rev. 2022, 122, 8053−8125

(64) Wei, S.; Xu, S.; Agrawral, A.; Choudhury, S.; Lu, Y.; Tu, Z.; Ma, L.; Archer, L. A. A Stable Room-Temperature Sodium-Sulfur Battery. *Nat. Commun.* **2016**, *7*, 11722.
(65) Wu, T.; Jing, M.; Yang, L.; Zou, G.; Hou, H.; Zhang, Y.; Zhang, Y.; Cao, X.; Ji, X. Controllable Chain-Length for Covalent Sulfur-Carbon Materials Enabling Stable and High-Capacity Sodium Storage. *Adv. Energy Mater.* **2019**, *9*, 1803478.
(66) Wang, L.; Bao, J.; Liu, Q.; Sun, C. F. Concentrated Electrolytes Unlock the Full Energy Potential of Potassium-Sulfur Battery Chemistry. *Energy Storage Mater.* **2019**, *18*, 470−475.
(67) Hwang, J. Y.; Kim, H. M.; Yoon, C. S.; Sun, Y. K. Toward High-Safety Potassium-Sulfur Batteries Using a Potassium Polysulfide Catholyte and Metal-Free Anode. *ACS Energy Lett.* **2018**, *3*, 540−541.
(68) Ge, X.; Di, H.; Wang, P.; Miao, X.; Zhang, P.; Wang, H.; Ma, J.; Yin, L. Metal-Organic Framework-Derived Nitrogen-Doped Cobalt Nanocluster Inlaid Porous Carbon as High-Efficiency Catalyst for Advanced Potassium-Sulfur Batteries. *ACS Nano* **2020**, *14*, 16022−16035.
(69) Ma, R.; Fan, L.; Wang, J.; Lu, B. Confined and Covalent Sulfur for Stable Room Temperature Potassium-Sulfur Battery. *Electrochim. Acta* **2019**, *293*, 191−198.
(70) Zhao, X.; Hong, Y.; Cheng, M.; Wang, S.; Zheng, L.; Wang, J.; Xu, Y. High Performance Potassium-Sulfur Batteries and Their Reaction Mechanism. *J. Mater. Chem. A* **2020**, *8*, 10875−10884.
(71) Gu, S.; Xiao, N.; Wu, F.; Bai, Y.; Wu, C.; Wu, Y. Chemical Synthesis of K2S2 and K2S3 for Probing Electrochemical Mechanisms in K-S Batteries. *ACS Energy Lett.* **2018**, *3*, 2858−2864.
(72) Tao, L.; Yang, Y.; Wang, H.; Zheng, Y.; Hao, H.; Song, W.; Shi, J.; Huang, M.; Mitlin, D. Sulfur-Nitrogen Rich Carbon as Stable High Capacity Potassium Ion Battery Anode: Performance and Storage Mechanisms. *Energy Storage Mater.* **2020**, *27*, 212−225.
(73) Yu, X.; Manthiram, A. A Reversible Nonaqueous Room-Temperature Potassium-Sulfur Chemistry for Electrochemical Energy Storage. *Energy Storage Mater.* **2018**, *15*, 368−373.
(74) Gao, J.; Lowe, M. A.; Kiya, Y.; Abruña, H. D. Effects of Liquid Electrolytes on the Charge-Discharge Performance of Rechargeable Lithium/Sulfur Batteries: Electrochemical and in-Situ X-ray Absorption Spectroscopic Studies. *J. Phys. Chem. C* **2011**, *115*, 25132−25137.
(75) Xin, S.; Gu, L.; Zhao, N. H.; Yin, Y. X.; Zhou, L. J.; Guo, Y. G.; Wan, L. J. Smaller Sulfur Molecules Promise Better Lithium-Sulfur Batteries. *J. Am. Chem. Soc.* **2012**, *134*, 18510−18513.
(76) Xu, Y.; Wen, Y.; Zhu, Y.; Gaskell, K.; Cychosz, K. A.; Eichhorn, B.; Xu, K.; Wang, C. Confined Sulfur in Microporous Carbon Renders Superior Cycling Stability in Li/S Batteries. *Adv. Funct. Mater.* **2015**, *25*, 4312.
(77) Li, Z.; Yuan, L.; Yi, Z.; Sun, Y.; Liu, Y.; Jiang, Y.; Shen, Y.; Xin, Y.; Zhang, Z.; Huang, Y. Insight into the Electrode Mechanism in Lithium-Sulfur Batteries with Ordered Microporous Carbon Confined Sulfur as the Cathode. *Adv. Energy Mater.* **2014**, *4*, 1301473.
(78) Xin, S.; Yin, Y. X.; Guo, Y. G.; Wan, L. J. A High-Energy Room-Temperature Sodium-Sulfur Battery. *Adv. Mater.* **2014**, *26*, 1261.
(79) Carter, R.; Oakes, L.; Douglas, A.; Muralidharan, N.; Cohn, A. P.; Pint, C. L. A Sugar-Derived Room-Temperature Sodium Sulfur Battery with Long Term Cycling Stability. *Nano Lett.* **2017**, *17*, 1863−1869.
(80) Wang, L.; Chen, X.; Li, S.; Yang, J.; Sun, Y.; Peng, L.; Shan, B.; Xie, J. Effect of Eutectic Accelerator in Selenium-Doped Sulfurized Polyacrylonitrile for High Performance Room Temperature Sodium-Sulfur Batteries. *J. Mater. Chem. A* **2019**, *7*, 12732−12739.
(81) Ma, S.; Zuo, P.; Zhang, H.; Yu, Z.; Cui, C.; He, M.; Yin, G. Iodine-Doped Sulfurized Polyacrylonitrile with Enhanced Electrochemical Performance for Room Temperature Sodium/Potassium Sulfur Batteries. *Chem. Commun.* **2019**, *55*, 5267−5270.
(82) Wang, W.; Cao, Z.; Elia, G. A.; Wu, Y.; Wahyudi, W.; Abou-Hamad, E.; Emwas, A. H.; Cavallo, L.; Li, L. J.; Ming, J. Recognizing the Mechanism of Sulfurized Polyacrylonitrile Cathode Materials for Li-S Batteries and beyond in Al-S Batteries. *ACS Energy Lett.* **2018**, *3*, 2899−2907.
(83) Li, S.; Zeng, Z.; Yang, J.; Han, Z.; Hu, W.; Wang, L.; Ma, J.; Shan, B.; Xie, J. High Performance Room Temperature Sodium-Sulfur Battery by Eutectic Acceleration in Tellurium-Doped Sulfurized Polyacrylonitrile. *ACS Appl. Energy Mater.* **2019**, *2*, 2956−2964.
(84) Chen, K.; Li, H.; Xu, Y.; Liu, K.; Li, H.; Xu, X.; Qiu, X.; Liu, M. Untying Thioether Bond Structures Enabled by "Voltage-Scissors" for Stable Room Temperature Sodium-Sulfur Batteries. *Nanoscale* **2019**, *11*, 5967−5973.
(85) Yan, J.; Li, W.; Wang, R.; Feng, P.; Jiang, M.; Han, J.; Cao, S.; Zhang, Z.; Wang, K.; Jiang, K. An in Situ Prepared Covalent Sulfur-Carbon Composite Electrode for High-Performance Room-Temperature Sodium-Sulfur Batteries. *ACS Energy Lett.* **2020**, *5*, 1307−1315.
(86) Wu, C.; Lai, W.; Cai, X.; Chou, S.; Liu, H.; Wang, Y.; Dou, S. Carbonaceous Hosts for Sulfur Cathode in Alkali-Metal/S (Alkali Metal= Lithium, Sodium, Potassium) Batteries. *Small* **2021**, *17*, 2006504.
(87) Xu, X.; Zhou, D.; Qin, X.; Lin, K.; Kang, F.; Li, B.; Shanmukaraj, D.; Rojo, T.; Armand, M.; Wang, G. A Room-Temperature Sodium-Sulfur Battery with High Capacity and Stable Cycling Performance. *Nat. Commun.* **2018**, *9*, 3870.
(88) Bhattacharyya, D. N.; Lee, C. L.; Smid, J.; Szwarc, M. Studies of Ions and Ion Pairs in Tetrahydrofuran Solution. Alkali Metal Salts of Tetraphenylboride. *J. Phys. Chem.* **1965**, *69*, 608−611.
(89) Bhattacharyya, D. N.; Lee, C. L.; Smid, J.; Szwarc, M. Reactivities and Conductivities of Ions and Ion Pairs in Polymerization Processes. *J. Phys. Chem.* **1965**, *69*, 612−623.
(90) Ma, D.; Li, Y.; Yang, J.; Mi, H.; Luo, S.; Deng, L.; Yan, C.; Rauf, M.; Zhang, P.; Sun, X.; et al. New Strategy for Polysulfide Protection Based on Atomic Layer Deposition of TiO2 onto Ferroelectric-Encapsulated Cathode: Toward Ultrastable Free-Standing Room Temperature Sodium-Sulfur Batteries. *Adv. Funct. Mater.* **2018**, *28*, 1705537.
(91) Ye, C.; Jiao, Y.; Chao, D.; Ling, T.; Shan, J.; Zhang, B.; Gu, Q.; Davey, K.; Wang, H.; Qiao, S. Z. Electron-State Confinement of Polysulfides for Highly Stable Sodium-Sulfur Batteries. *Adv. Mater.* **2020**, *32*, 1907557.
(92) Yan, Z.; Liang, Y.; Hua, W.; Zhang, X. G.; Lai, W.; Hu, Z.; Wang, W.; Peng, J.; Indris, S.; Wang, Y.; et al. Multiregion Janus-Featured Cobalt Phosphide-Cobalt Composite for Highly Reversible Room-Temperature Sodium-Sulfur Batteries. *ACS Nano* **2020**, *14*, 10284−10293.
(93) Zhao, X.; Zhu, Q.; Xu, S. d.; Chen, L.; Zuo, Z.; Wang, X.; Liu, S.; Zhang, D. Fluoroethylene Carbonate as an Additive in a Carbonates-Based Electrolyte for Enhancing the Specific Capacity of Room-Temperature Sodium-Sulfur Cell. *J. Electroanal. Chem.* **2019**, *832*, 392−398.
(94) Li, G.; Wang, S.; Zhang, Y.; Li, M.; Chen, Z.; Lu, J. Revisiting the Role of Polysulfides in Lithium-Sulfur Batteries. *Adv. Mater.* **2018**, *30*, 1705590.
(95) Barchasz, C.; Molton, F.; Duboc, C.; Lepretre, J. C.; Patoux, S.; Alloin, F. Lithium/Sulfur Cell Discharge Mechanism: An Original Approach for Intermediate Species Identification. *Anal. Chem.* **2012**, *84*, 3973−3980.
(96) Dominko, R.; Vizintin, A.; Aquilanti, G.; Stievano, L.; Helen, M. J.; Munnangi, A. R.; Fichtner, M.; Arcon, I. Polysulfides Formation in Different Electrolytes from the Perspective of X-ray Absorption Spectroscopy. *J. Electrochem. Soc.* **2018**, *165*, A5014.
(97) Gorlin, Y.; Patel, M. U.; Freiberg, A.; He, Q.; Piana, M.; Tromp, M.; Gasteiger, H. A. Understanding the Charging Mechanism of Lithium-Sulfur Batteries Using Spatially Resolved Operando X-ray Absorption Spectroscopy. *J. Electrochem. Soc.* **2016**, *163*, A930.
(98) Steudel, R.; Chivers, T. The Role of Polysulfide Dianions and Radical Anions in the Chemical, Physical and Biological Sciences, Including Sulfur-Based Batteries. *Chem. Soc. Rev.* **2019**, *48*, 3279−3319.
(99) Cuisinier, M.; Hart, C.; Balasubramanian, M.; Garsuch, A.; Nazar, L. F. Radical or Not Radical: Revisiting Lithium-Sulfur Electrochemistry in Nonaqueous Electrolytes. *Adv. Energy Mater.* **2015**, *5*, 1401801.

https://doi.org/10.1021/acs.chemrev.1c00838
Chem. Rev. 2022, 122, 8053−8125

(100) He, Q.; Gorlin, Y.; Patel, M. U.; Gasteiger, H. A.; Lu, Y. C. Unraveling the Correlation between Solvent Properties and Sulfur Redox Behavior in Lithium-Sulfur Batteries. *J. Electrochem. Soc.* **2018**, *165*, A4027.
(101) Mikhaylik, Y. V.; Akridge, J. R. Polysulfide Shuttle Study in the Li/S Battery System. *J. Electrochem. Soc.* **2004**, *151*, A1969.
(102) Vizintin, A.; Chabanne, L.; Tchernychova, E.; Arčon, I.; Stievano, L.; Aquilanti, G.; Antonietti, M.; Fellinger, T. P.; Dominko, R. The Mechanism of Li2S Activation in Lithium-Sulfur Batteries: Can We Avoid the Polysulfide Formation? *J. Power Sources* **2017**, *344*, 208−217.
(103) Yemini, R.; Rosy; Noked, M. On the Efficacy of Anode Reversibility in Presence of Li2S8: A Case Study for Li-S Batteries. *J. Electrochem. Soc.* **2019**, *166*, A3098.
(104) Fang, R.; Xu, J.; Wang, D. W. Covalent Fixing of Sulfur in Metal-Sulfur Batteries. *Energy Environ. Sci.* **2020**, *13*, 432−471.
(105) Manthiram, A.; Fu, Y.; Chung, S. H.; Zu, C.; Su, Y. S. Rechargeable Lithium-Sulfur Batteries. *Chem. Rev.* **2014**, *114*, 11751−11787.
(106) Fan, F. Y.; Carter, W. C.; Chiang, Y. M. Mechanism and Kinetics of Li2S Precipitation in Lithium-Sulfur Batteries. *Adv. Mater.* **2015**, *27*, 5203.
(107) Pang, Q.; Shyamsunder, A.; Narayanan, B.; Kwok, C. Y.; Curtiss, L. A.; Nazar, L. F. Tuning the Electrolyte Network Structure to Invoke Quasi-Solid State Sulfur Conversion and Suppress Lithium Dendrite Formation in Li-S Batteries. *Nat. Energy* **2018**, *3*, 783−791.
(108) Fang, R.; Zhao, S.; Sun, Z.; Wang, D. W.; Cheng, H. M.; Li, F. More Reliable Lithium-Sulfur Batteries: Status, Solutions and Prospects. *Adv. Mater.* **2017**, *29*, 1606823.
(109) Xiong, S.; Xie, K.; Diao, Y.; Hong, X. Characterization of the Solid Electrolyte Interphase on Lithium Anode for Preventing the Shuttle Mechanism in Lithium-Sulfur Batteries. *J. Power Sources* **2014**, *246*, 840−845.
(110) Aurbach, D.; Pollak, E.; Elazari, R.; Salitra, G.; Kelley, C. S.; Affinito, J. On the Surface Chemical Aspects of Very High Energy Density, Rechargeable Li-Sulfur Batteries. *J. Electrochem. Soc.* **2009**, *156*, A694.
(111) Kumar, A.; Ghosh, A.; Roy, A.; Panda, M. R.; Forsyth, M.; MacFarlane, D. R.; Mitra, S. High-Energy Density Room Temperature Sodium-Sulfur Battery Enabled by Sodium Polysulfide Catholyte and Carbon Cloth Current Collector Decorated with MnO2 Nanoarrays. *Energy Storage Mater.* **2019**, *20*, 196−202.
(112) Kohl, M.; Borrmann, F.; Althues, H.; Kaskel, S. Hard Carbon Anodes and Novel Electrolytes for Long-Cycle-Life Room Temperature Sodium-Sulfur Full Cell Batteries. *Adv. Energy Mater.* **2016**, *6*, 1502185.
(113) Yuan, H.; Peng, H. J.; Li, B. Q.; Xie, J.; Kong, L.; Zhao, M.; Chen, X.; Huang, J. Q.; Zhang, Q. Conductive and Catalytic Triple-Phase Interfaces Enabling Uniform Nucleation in High-Rate Lithium-Sulfur Batteries. *Adv. Energy Mater.* **2019**, *9*, 1802768.
(114) Yan, J.; Liu, X.; Li, B. Capacity Fade Analysis of Sulfur Cathodes in Lithium-Sulfur Batteries. *Adv. Sci.* **2016**, *3* (12), 1600101.
(115) Bhardwaj, R. K.; Jayanthi, S.; Adarakatti, P. S.; Sood, A. K.; Bhattacharyya, A. J. Probing the Extent of Polysulfide Confinement Using a CoNi2S4 Additive Inside a Sulfur Cathode of a Na/Li-Sulfur Rechargeable Battery. *ACS Appl. Mater. Interfaces* **2020**, *12*, 28120−28128.
(116) Liu, Y.; Dai, H.; An, Y.; Fu, L.; An, Q.; Wu, Y. Facile and Scalable Synthesis of a Sulfur, Selenium and Nitrogen Co-Doped Hard Carbon Anode for High Performance Na- and K-Ion Batteries. *J. Mater. Chem. A* **2020**, *8*, 14993−15001.
(117) Huang, J. Q.; Zhang, Q.; Peng, H. J.; Liu, X. Y.; Qian, W. Z.; Wei, F. Ionic Shield for Polysulfides Towards Highly-Stable Lithium-Sulfur Batteries. *Energy Environ. Sci.* **2014**, *7*, 347−353.
(118) Zhuang, T. Z.; Huang, J. Q.; Peng, H. J.; He, L. Y.; Cheng, X. B.; Chen, C. M.; Zhang, Q. Rational Integration of Polypropylene/Graphene Oxide/Nafion as Ternary-Layered Separator to Retard the Shuttle of Polysulfides for Lithium-Sulfur Batteries. *Small* **2016**, *12*, 381−389.
(119) Abbas, S. A.; Ibrahem, M. A.; Hu, L. H.; Lin, C. N.; Fang, J.; Boopathi, K. M.; Wang, P. C.; Li, L. J.; Chu, C. W. Bifunctional Separator as a Polysulfide Mediator for Highly Stable Li-S Batteries. *J. Mater. Chem. A* **2016**, *4*, 9661−9669.
(120) Zeng, F.; Jin, Z.; Yuan, K.; Liu, S.; Cheng, X.; Wang, A.; Wang, W.; Yang, Y. S. High Performance Lithium-Sulfur Batteries with a Permselective Sulfonated Acetylene Black Modified Separator. *J. Mater. Chem. A* **2016**, *4*, 12319−12327.
(121) Peng, H. J.; Wang, D. W.; Huang, J. Q.; Cheng, X. B.; Yuan, Z.; Wei, F.; Zhang, Q. Janus Separator of Polypropylene-Supported Cellular Graphene Framework for Sulfur Cathodes with High Utilization in Lithium-Sulfur Batteries. *Adv. Sci.* **2016**, *3*, 1500268.
(122) Chung, S. H.; Manthiram, A. A Polyethylene Glycol-Supported Microporous Carbon Coating as a Polysulfide Trap for Utilizing Pure Sulfur Cathodes in Lithium-Sulfur Batteries. *Adv. Mater.* **2014**, *26*, 7352.
(123) Yang, X.; Wang, J.; Wang, S.; Wang, H.; Tomanec, O.; Zhi, C.; Zboril, R.; Yu, D. Y. W.; Rogach, A. Vapor-Infiltration Approach toward Selenium/Reduced Graphene Oxide Composites Enabling Stable and High-Capacity Sodium Storage. *ACS Nano* **2018**, *12*, 7397−7405.
(124) Yang, X.; Wang, H.; Yu, D. Y. W.; Rogach, A. L. Vacuum Calcination Induced Conversion of Selenium/Carbon Wires to Tubes for High-Performance Sodium-Selenium Batteries. *Adv. Funct. Mater.* **2018**, *28*, 1706609.
(125) Zeng, L.; Zeng, W.; Jiang, Y.; Wei, X.; Li, W.; Yang, C.; Zhu, Y.; Yu, Y. A Flexible Porous Carbon Nanofibers-Selenium Cathode with Superior Electrochemical Performance for Both Li-Se and Na-Se Batteries. *Adv. Energy Mater.* **2015**, *5*, 1401377.
(126) Liu, Y.; Tai, Z.; Zhang, Q.; Wang, H.; Pang, W. K.; Liu, H. K.; Konstantinov, K.; Guo, Z. A New Energy Storage System: Rechargeable Potassium-Selenium Battery. *Nano Energy* **2017**, *35*, 36−43.
(127) Xu, R.; Yao, Y.; Wang, H.; Yuan, Y.; Wang, J.; Yang, H.; Jiang, Y.; Shi, P.; Wu, X.; Peng, Z.; et al. Unraveling the Nature of Excellent Potassium Storage in Small-Molecule Se@Peapod-Like N-Doped Carbon Nanofibers. *Adv. Mater.* **2020**, *32*, 2003879.
(128) Perras, F. A.; Hwang, S.; Wang, Y.; Self, E. C.; Liu, P.; Biswas, R.; Nagarajan, S.; Pham, V. H.; Xu, Y.; Boscoboinik, J. A.; et al. Site-Specific Sodiation Mechanisms of Selenium in Microporous Carbon Host. *Nano Lett.* **2020**, *20*, 918−928.
(129) Zhou, X.; Gao, P.; Sun, S.; Bao, D.; Wang, Y.; Li, X.; Wu, T.; Chen, Y.; Yang, P. Amorphous, Crystalline and Crystalline/Amorphous Selenium Nanowires and Their Different (De)Lithiation Mechanisms. *Chem. Mater.* **2015**, *27*, 6730−6736.
(130) Tian, H.; Tian, H.; Wang, S.; Chen, S.; Zhang, F.; Song, L.; Liu, H.; Liu, J.; Wang, G. High-Power Lithium-Selenium Batteries Enabled by Atomic Cobalt Electrocatalyst in Hollow Carbon Cathode. *Nat. Commun.* **2020**, *11*, 5025.
(131) Wu, T.; Ding, Z.; Jing, M.; Zou, G.; Hou, H.; Tian, Y.; Jiang, Y.; Hong, W.; Ji, X. Chem-Bonding and Phys-Trapping Se Electrode for Long-Life Rechargeable Batteries. *Adv. Funct. Mater.* **2019**, *29*, 1809014.
(132) Li, Q.; Liu, H.; Yao, Z.; Cheng, J.; Li, T.; Li, Y.; Wolverton, C.; Wu, J.; Dravid, V. P. Electrochemistry of Selenium with Sodium and Lithium: Kinetics and Reaction Mechanism. *ACS Nano* **2016**, *10*, 8788−8795.
(133) Luo, C.; Wang, J.; Suo, L.; Mao, J.; Fan, X.; Wang, C. In Situ Formed Carbon Bonded and Encapsulated Selenium Composites for Li-Se and Na-Se Batteries. *J. Mater. Chem. A* **2015**, *3*, 555−561.
(134) Cui, Y.; Abouimrane, A.; Sun, C. J.; Ren, Y.; Amine, K. Li-Se Battery: Absence of Lithium Polyselenides in Carbonate Based Electrolyte. *Chem. Commun.* **2014**, *50*, 5576−5579.
(135) Abouimrane, A.; Dambournet, D.; Chapman, K. W.; Chupas, P. J.; Weng, W.; Amine, K. A New Class of Lithium and Sodium Rechargeable Batteries based on Selenium and Selenium-Sulfur as a Positive Electrode. *J. Am. Chem. Soc.* **2012**, *134*, 4505−4508.
(136) Wang, H.; Jiang, Y.; Manthiram, A. Long Cycle Life, Low Self-Discharge Sodium-Selenium Batteries with High Selenium Loading

https://doi.org/10.1021/acs.chemrev.1c00838
Chem. Rev. 2022, 122, 8053−8125

and Suppressed Polyselenide Shuttling. *Adv. Energy Mater.* **2018**, *8*, 1701953.
(137) Tang, W.; Chen, Z.; Tian, B.; Lee, H. W.; Zhao, X.; Fan, X.; Fan, Y.; Leng, K.; Peng, C.; Kim, M. H.; et al. In Situ Observation and Electrochemical Study of Encapsulated Sulfur Nanoparticles by MoS2 Flakes. *J. Am. Chem. Soc.* **2017**, *139*, 10133−10141.
(138) Liu, Q.; Deng, W.; Pan, Y.; Sun, C. F. Approaching the Voltage and Energy Density Limits of Potassium-Selenium Battery Chemistry in a Concentrated Ether-Based Electrolyte. *Chem. Sci.* **2020**, *11*, 6045−6052.
(139) Xu, G. L.; Sun, H.; Luo, C.; Estevez, L.; Zhuang, M.; Gao, H.; Amine, R.; Wang, H.; Zhang, X.; Sun, C. J.; et al. Solid-State Lithium/Selenium-Sulfur Chemistry Enabled via a Robust Solid-Electrolyte Interphase. *Adv. Energy Mater.* **2019**, *9*, 1802235.
(140) Liu, W.; Liu, P.; Mitlin, D. Review of Emerging Concepts in SEI Analysis and Artificial SEI Membranes for Lithium, Sodium, and Potassium Metal Battery Anodes. *Adv. Energy Mater.* **2020**, *10*, 2002297.
(141) Liu, W.; Liu, P.; Mitlin, D. Tutorial Review on Structure - Dendrite Growth Relations in Metal Battery Anode Supports. *Chem. Soc. Rev.* **2020**, *49*, 7284−7300.
(142) Wang, L.; Zhou, Z.; Yan, X.; Hou, F.; Wen, L.; Luo, W.; Liang, J.; Dou, S. X. Engineering of Lithium-Metal Anodes Towards a Safe and Stable Battery. *Energy Storage Mater.* **2018**, *14*, 22−48.
(143) Wu, F.; Yuan, Y. X.; Cheng, X. B.; Bai, Y.; Li, Y.; Wu, C.; Zhang, Q. Perspectives for Restraining Harsh Lithium Dendrite Growth: Towards Robust Lithium Metal Anodes. *Energy Storage Mater.* **2018**, *15*, 148−170.
(144) Monroe, C.; Newman, J. Dendrite Growth in Lithium/Polymer Systems: A Propagation Model for Liquid Electrolytes under Galvanostatic Conditions. *J. Electrochem. Soc.* **2003**, *150*, A1377.
(145) Chazalviel, J. Electrochemical Aspects of the Generation of Ramified Metallic Electrodeposits. *Phys. Rev. A* **1990**, *42*, 7355.
(146) Mao, X.; Shi, L.; Zhang, H.; Wang, Z.; Zhu, J.; Qiu, Z.; Zhao, Y.; Zhang, M.; Yuan, S. Polyethylene Separator Activated by Hybrid Coating Improving Li+ Ion Transference Number and Ionic Conductivity for Li-Metal Battery. *J. Power Sources* **2017**, *342*, 816−824.
(147) Lu, Y.; Tikekar, M.; Mohanty, R.; Hendrickson, K.; Ma, L.; Archer, L. A. Stable Cycling of Lithium Metal Batteries Using High Transference Number Electrolytes. *Adv. Energy Mater.* **2015**, *5*, 1402073.
(148) Peled, E.; Menkin, S. "SEI: Past, Present and Future.". *J. Electrochem. Soc.* **2017**, *164*, A1703.
(149) Hosaka, T.; Muratsubaki, S.; Kubota, K.; Onuma, H.; Komaba, S. Potassium Metal as Reliable Reference Electrodes of Nonaqueous Potassium Cells. *J. Phys. Chem. Lett.* **2019**, *10*, 3296−3300.
(150) Liu, P.; Wang, Y.; Gu, Q.; Nanda, J.; Watt, J.; Mitlin, D. Dendrite-Free Potassium Metal Anodes in a Carbonate Electrolyte. *Adv. Mater.* **2020**, *32*, 1906735.
(151) Liu, W.; Xia, Y.; Wang, W.; Wang, Y.; Jin, J.; Chen, Y.; Paek, E.; Mitlin, D. Pristine or Highly Defective? Understanding the Role of Graphene Structure for Stable Lithium Metal Plating. *Adv. Energy Mater.* **2019**, *9*, 1802918.
(152) Guo, W.; Han, Q.; Jiao, J.; Wu, W.; Zhu, X.; Chen, Z.; Zhao, Y. In Situ Construction of Robust Biphasic Surface Layers on Lithium Metal for Lithium-Sulfide Batteries with Long Cycle Life. *Angew. Chem., Int. Ed.* **2021**, *60*, 7267−7274.
(153) Shi, P.; Zhang, S.; Lu, G.; Wang, L.; Jiang, Y.; Liu, F.; Yao, Y.; Yang, H.; Ma, M.; Ye, S.; et al. Red Phosphorous-Derived Protective Layers with High Ionic Conductivity and Mechanical Strength on Dendrite-Free Sodium and Potassium Metal Anodes. *Adv. Energy Mater.* **2021**, *11*, 2003381.
(154) Liu, W.; Li, P.; Wang, W.; Zhu, D.; Chen, Y.; Pen, S.; Paek, E.; Mitlin, D. Directional Flow-Aided Sonochemistry Yields Graphene with Tunable Defects to Provide Fundamental Insight on Sodium Metal Plating Behavior. *ACS Nano* **2018**, *12*, 12255−12268.
(155) Dey, A. N. Electrochemical Alloying of Lithium in Organic Electrolytes. *J. Electrochem. Soc.* **1971**, *118*, 1547.
(156) Peled, E. Film Forming Reaction at the Lithium/Electrolyte Interface. *J. Power Sources* **1983**, *9*, 253−266.
(157) Goodenough, J. B.; Kim, Y. Challenges for Rechargeable Li Batteries. *Chem. Mater.* **2010**, *22*, 587−603.
(158) Iermakova, D. I.; Dugas, R.; Palacín, M. R.; Ponrouch, A. On the Comparative Stability of Li and Na Metal Anode Interfaces in Conventional Alkyl Carbonate Electrolytes. *J. Electrochem. Soc.* **2015**, *162*, A7060.
(159) Aurbach, D.; Markovsky, B.; Shechter, A.; Ein-Eli, Y.; Cohen, H. A Comparative Study of Synthetic Graphite and Li Electrodes in Electrolyte Solutions based on Ethylene Carbonate-Dimethyl Carbonate Mixtures. *J. Electrochem. Soc.* **1996**, *143*, 3809.
(160) Seh, Z. W.; Sun, J.; Sun, Y.; Cui, Y. A Highly Reversible Room-Temperature Sodium Metal Anode. *ACS Cent. Sci.* **2015**, *1*, 449−455.
(161) Zhou, Y.; Su, M.; Yu, X.; Zhang, Y.; Wang, J. G.; Ren, X.; Cao, R.; Xu, W.; Baer, D. R.; Du, Y.; et al. Real-Time Mass Spectrometric Characterization of the Solid-Electrolyte Interphase of a Lithium-Ion Battery. *Nat. Nanotechnol.* **2020**, *15*, 224−230.
(162) Nanda, J.; Yang, G.; Hou, T.; Voylov, D. N.; Li, X.; Ruther, R. E.; Naguib, M.; Persson, K.; Veith, G. M.; Sokolov, A. P. Unraveling the Nanoscale Heterogeneity of Solid Electrolyte Interphase Using Tip-Enhanced Raman Spectroscopy. *Joule* **2019**, *3*, 2001−2019.
(163) Li, Y.; Li, Y.; Pei, A.; Yan, K.; Sun, Y.; Cui, Y. Atomic Structure of Sensitive Battery Materials and Interfaces Revealed by Cryo-Electron Microscopy. *Science* **2017**, *358*, 506−510.
(164) Shi, S.; Lu, P.; Liu, Z.; Qi, Y.; Hector, L. G., Jr.; Li, H.; Harris, S. J. Direct Calculation of Li-Ion Transport in the Solid Electrolyte Interphase. *J. Am. Chem. Soc.* **2012**, *134*, 15476−15487.
(165) Cheng, X. B.; Zhang, R.; Zhao, C. Z.; Zhang, Q. Toward Safe Lithium Metal Anode in Rechargeable Batteries: A Review. *Chem. Rev.* **2017**, *117*, 10403−10473.
(166) Bhargav, A.; He, J.; Gupta, A.; Manthiram, A. Lithium-Sulfur Batteries: Attaining the Critical Metrics. *Joule* **2020**, *4*, 285−291.
(167) Dugas, R.; Ponrouch, A.; Gachot, G.; David, R.; Tarascon, J. M. Na Reactivity Toward Carbonate-Based Electrolytes: The Effect of FEC as Additive. *J. Electrochem. Soc.* **2016**, *163*, A2333.
(168) Mogensen, R.; Brandell, D.; Younesi, R. Solubility of the Solid Electrolyte Interphase (SEI) in Sodium Ion Batteries. *ACS Energy Lett.* **2016**, *1*, 1173−1178.
(169) Zhang, C.; Wang, A.; Zhang, J.; Guan, X.; Tang, W.; Luo, J. 2D Materials for Lithium/Sodium Metal Anodes. *Adv. Energy Mater.* **2018**, *8*, 1802833.
(170) Chi, S. S.; Qi, X. G.; Hu, Y. S.; Fan, L. Z. 3D Flexible Carbon Felt Host for Highly Stable Sodium Metal Anodes. *Adv. Energy Mater.* **2018**, *8*, 1702764.
(171) Luo, W.; Lin, C. F.; Zhao, O.; Noked, M.; Zhang, Y.; Rubloff, G. W.; Hu, L. Ultrathin Surface Coating Enables the Stable Sodium Metal Anode. *Adv. Energy Mater.* **2017**, *7*, 1601526.
(172) Zhang, W.; Pang, W. K.; Sencadas, V.; Guo, Z. Understanding High-Energy-Density Sn4P3 Anodes for Potassium-Ion Batteries. *Joule* **2018**, *2*, 1534−1547.
(173) Liu, P.; Hao, H.; Celio, H.; Cui, J.; Ren, M.; Wang, Y.; Dong, H.; Chowdhury, A. R.; Hutter, T.; Perras, F. A.; et al. Multifunctional Separator Allows Stable Cycling of Potassium Metal Anodes and of Potassium Metal Batteries. *Adv. Mater.* **2022**, *34*, 2105855.
(174) Li, Y.; Zhu, J.; Zhu, P.; Yan, C.; Jia, H.; Kiyak, Y.; Zang, J.; He, J.; Dirican, M.; Zhang, X. Glass Fiber Separator Coated by Porous Carbon Nanofiber Derived from Immiscible PAN/PMMA for High-Performance Lithium-Sulfur Batteries. *J. Membr. Sci.* **2018**, *552*, 31−42.
(175) Kong, W.; Yan, L.; Luo, Y.; Wang, D.; Jiang, K.; Li, Q.; Fan, S.; Wang, J. Ultrathin MnO2/Graphene Oxide/Carbon Nanotube Interlayer as Efficient Polysulfide-Trapping Shield for High-Performance Li-S Batteries. *Adv. Funct. Mater.* **2017**, *27*, 1606663.
(176) Xiao, Z.; Yang, Z.; Wang, L.; Nie, H.; Zhong, M.; Lai, Q.; Xu, X.; Zhang, L.; Huang, S. A Lightweight TiO2/Graphene Interlayer,

https://doi.org/10.1021/acs.chemrev.1c00838
Chem. Rev. 2022, 122, 8053−8125

Applied as a Highly Effective Polysulfide Absorbent for Fast, Long-Life Lithium-Sulfur Batteries. *Adv. Mater.* **2015**, *27*, 2891.
(177) Wang, H.; Wang, C.; Matios, E.; Li, W. Facile Stabilization of the Sodium Metal Anode with Additives: Unexpected Key Role of Sodium Polysulfide and Adverse Effect of Sodium Nitrate. *Angew. Chem., Int. Ed.* **2018**, *57*, 7734−7863.
(178) Yan, C.; Cheng, X. B.; Zhao, C. Z.; Huang, J. Q.; Yang, S. T.; Zhang, Q. Lithium Metal Protection Through In-Situ Formed Solid Electrolyte Interphase in Lithium-Sulfur Batteries: The Role of Polysulfides on Lithium Anode. *J. Power Sources* **2016**, *327*, 212−220.
(179) Liu, F.; Wang, L.; Zhang, Z.; Shi, P.; Feng, Y.; Yao, Y.; Ye, S.; Wang, H.; Wu, X.; Yu, Y. A Mixed Lithium-Ion Conductive Li2S/Li2Se Protection Layer for Stable Lithium Metal Anode. *Adv. Funct. Mater.* **2020**, *30*, 2001607.
(180) Lagadec, M. F.; Zahn, R.; Wood, V. Characterization and Performance Evaluation of Lithium-Ion Battery Separators. *Nat. Energy* **2019**, *4*, 16−25.
(181) Guo, Y.; Niu, P.; Liu, Y.; Ouyang, Y.; Li, D.; Zhai, T.; Li, H.; Cui, Y. An Autotransferable g-C3 N4 Li+-Modulating Layer toward Stable Lithium Anodes. *Adv. Mater.* **2019**, *31*, 1900342.
(182) Liu, P.; Wang, Y.; Hao, H.; Basu, S.; Feng, X.; Xu, Y.; Boscoboinik, J. A.; Nanda, J.; Watt, J.; Mitlin, D. Stable Potassium Metal Anodes with an All-Aluminum Current Collector through Improved Electrolyte Wetting. *Adv. Mater.* **2020**, *32*, 2002908.
(183) Doyle, M.; Fuller, T. F.; Newman, J. The Importance of the Lithium Ion Transference Number in Lithium/Polymer cells. *Electrochim. Acta* **1994**, *39*, 2073−2081.
(184) Yang, J.; Wang, C. Y.; Wang, C. C.; Chen, K. H.; Mou, C. Y.; Wu, H. L. Advanced Nanoporous Separators for Stable Lithium Metal Electrodeposition at Ultra-High Current Densities in Liquid Electrolytes. *J. Mater. Chem. A* **2020**, *8*, 5095−5104.
(185) Wang, Z.; Huang, W.; Hua, J.; Wang, Y.; Yi, H.; Zhao, W.; Zhao, Q.; Jia, H.; Fei, B.; Pan, F. An Anionic-MOF-Based Bifunctional Separator for Regulating Lithium Deposition and Suppressing Polysulfides Shuttle in Li-S Batteries. *Small Methods* **2020**, *4*, 2000082.
(186) Qin, F.; Wang, X.; Zhang, K.; Fang, J.; Li, J.; Lai, Y. High Areal Capacity Cathode and Electrolyte Reservoir Render Practical Li-S Batteries. *Nano Energy* **2017**, *38*, 137−146.
(187) Li, Y.; Wang, W.; Liu, X.; Mao, E.; Wang, M.; Li, G.; Fu, L.; Li, Z.; Eng, A. Y. S.; Seh, Z. W.; et al. Engineering Stable Electrode-Separator Interfaces with Ultrathin Conductive Polymer Layer for High-Energy-Density Li-S Batteries. *Energy Storage Mater.* **2019**, *23*, 261−268.
(188) Xiao, Z.; Li, Y.; Zhang, W.; Huang, H.; Gan, Y.; Zhang, J.; Liang, C.; Mao, Q.; Liao, P.; Jin, Y.; et al. Empowering Polypropylene Separator with Enhanced Polysulfide Adsorption and Reutilization Ability for High-Performance Li-S Batteries. *Mater. Res. Bull.* **2021**, *134*, 111108.
(189) Zhang, Y.; Yuan, J. J.; Song, Y. Z.; Yin, X.; Sun, C. C.; Zhu, L. P.; Zhu, B. K. Tannic Acid/Polyethyleneimine-Decorated Polypropylene Separators for Li-Ion Batteries and the Role of the Interfaces Between Separator and Electrolyte. *Electrochim. Acta* **2018**, *275*, 25−31.
(190) Zhou, D.; Tang, X.; Guo, X.; Li, P.; Shanmukaraj, D.; Liu, H.; Gao, X.; Wang, Y.; Rojo, T.; Armand, M.; et al. Polyolefin-Based Janus Separator for Rechargeable Sodium Batteries. *Angew. Chem., Int. Ed.* **2020**, *59*, 16725−16734.
(191) Song, Y. Z.; Yuan, J. J.; Yin, X.; Zhang, Y.; Lin, C. E.; Sun, C. C.; Fang, L. F.; Zhu, B.; Zhu, L. P. Effect of Polyphenol-Polyamine Treated Polyethylene Separator on the Ionic Conduction and Interface Properties for Lithium-Metal Anode Batteries. *J. Electroanal. Chem.* **2018**, *816*, 68−74.
(192) Zhu, Y.; Yang, Y.; Fu, L.; Wu, Y. A Porous Gel-Type Composite Membrane Reinforced by Nonwoven: Promising Polymer Electrolyte with High Performance for Sodium Ion Batteries. *Electrochim. Acta* **2017**, *224*, 405−411.
(193) Nie, L.; Li, Y.; Chen, S.; Li, K.; Huang, Y.; Zhu, Y.; Sun, Z.; Zhang, J.; He, Y.; Cui, M.; et al. Biofilm Nanofiber-Coated Separators for Dendrite-Free Lithium Metal Anode and Ultrahigh-Rate Lithium Batteries. *ACS Appl. Mater. Interfaces* **2019**, *11*, 32373−32380.
(194) Deng, N.; Liu, Y.; Li, Q.; Yan, J.; Zhang, L.; Wang, L.; Zhang, Y.; Cheng, B.; Lei, W.; Kang, W. Functional Double-Layer Membrane as Separator for Lithium-Sulfur Battery with Strong Catalytic Conversion and Excellent Polysulfide-Blocking. *Chem. Eng. J.* **2020**, *382*, 122918.
(195) Zhu, R.; Lin, S.; Jiao, J.; Ma, D.; Cai, Z.; Hany, K.; Hamouda, T. M.; Cai, Y. Magnetic and Mesoporous Fe3O4-Modified Glass Fiber Separator for High-Performance Lithium-Sulfur Battery. *Ionics* **2020**, *26*, 2325.
(196) Vijaya Kumar Saroja, A. P.; R, A. K.; Moharana, B. C.; M, K.; S, R. Design of Porous Calcium Phosphate based Gel Polymer Electrolyte for Quasi-Solid State Sodium Ion Battery. *J. Electroanal. Chem.* **2020**, *859*, 113864.
(197) Casas, X.; Niederberger, M.; Lizundia, E. A Sodium-Ion Battery Separator with Reversible Voltage Response Based on Water-Soluble Cellulose Derivatives. *ACS Appl. Mater. Interfaces* **2020**, *12*, 29264−29274.
(198) Ni, L.; Osenberg, M.; Liu, H.; Hilger, A.; Chen, L.; Zhou, D.; Dong, K.; Arlt, T.; Yao, X.; Wang, X.; et al. In Situ Visualizing the Interplay Between the Separator and Potassium Dendrite Growth by Synchrotron X-ray Tomography. *Nano Energy* **2021**, *83*, 105841.
(199) Matsuda, Y.; Nakashima, H.; Morita, M.; Takasu, Y. Behavior of Some Ions in Mixed Organic Electrolytes of High Energy Density Batteries. *J. Electrochem. Soc.* **1981**, *128*, 2552.
(200) Su, Y. S.; Manthiram, A. Lithium-Sulphur Batteries with a Microporous Carbon Paper as a Bifunctional Interlayer. *Nat. Commun.* **2012**, *3*, 1166.
(201) Zu, C.; Su, Y. S.; Fu, Y.; Manthiram, A. Improved Lithium-Sulfur Cells with a Treated Carbon Paper Interlayer. *Phys. Chem. Chem. Phys.* **2013**, *15*, 2291−2297.
(202) Singhal, R.; Chung, S. H.; Manthiram, A.; Kalra, V. A Free-Standing Carbon Nanofiber Interlayer for High-Performance Lithium-Sulfur Batteries. *J. Mater. Chem. A* **2015**, *3*, 4530−4538.
(203) Wang, G.; Lai, Y.; Zhang, Z.; Li, J.; Zhang, Z. Enhanced Rate Capability and Cycle Stability of Lithium-Sulfur Batteries with a Bifunctional MCNT@PEG-Modified Separator. *J. Mater. Chem. A* **2015**, *3*, 7139−7144.
(204) Hwang, J. Y.; Kim, H. M.; Lee, S. K.; Lee, J. H.; Abouimrane, A.; Khaleel, M. A.; Belharouak, I.; Manthiram, A.; Sun, Y. K. High-Energy, High-Rate, Lithium-Sulfur Batteries: Synergetic Effect of Hollow TiO2-Webbed Carbon Nanotubes and a Dual Functional Carbon-Paper Interlayer. *Adv. Energy Mater.* **2016**, *6*, 1501480.
(205) Chang, C. H.; Chung, S. H.; Nanda, S.; Manthiram, A. A Rationally Designed Polysulfide-Trapping Interface on the Polymeric Separator for High-Energy Li-S Batteries. *Mater. Today Energy* **2017**, *6*, 72−78.
(206) Huang, J. Q.; Chong, W. G.; Zheng, Q.; Xu, Z. L.; Cui, J.; Yao, S.; Wang, C.; Kim, J. K. Understanding the Roles of Activated Porous Carbon Nanotubes as Sulfur Support and Separator Coating for Lithium-Sulfur Batteries. *Electrochim. Acta* **2018**, *268*, 1−9.
(207) Chang, C. H.; Chung, S. H.; Manthiram, A. Effective Stabilization of a High-Loading Sulfur Cathode and a Lithium-Metal Anode in Li-S Batteries Utilizing SWCNT-Modulated Separators. *Small* **2016**, *12*, 174−179.
(208) Zhai, P. Y.; Peng, H. J.; Cheng, X. B.; Zhu, L.; Huang, J. Q.; Zhu, W.; Zhang, Q. Scaled-Up Fabrication of Porous-Graphene-Modified Separators for High-Capacity Lithium-Sulfur Batteries. *Energy Storage Mater.* **2017**, *7*, 56−63.
(209) Zheng, B.; Yu, L.; Zhao, Y.; Xi, J. Ultralight Carbon Flakes Modified Separator as an Effective Polysulfide Barrier for Lithium-Sulfur Batteries. *Electrochim. Acta* **2019**, *295*, 910−917.
(210) Liao, H.; Zhang, H.; Hong, H.; Li, Z.; Lin, Y. Novel Flower-Like Hierarchical Carbon Sphere with Multi-Scale Pores Coated on PP Separator for High-Performance Lithium-Sulfur Batteries. *Electrochim. Acta* **2017**, *257*, 210−216.
(211) Jeong, T. G.; Moon, Y. H.; Chun, H. H.; Kim, H. S.; Cho, B. W.; Kim, Y. T. Free Standing Acetylene Black Mesh to Capture

https://doi.org/10.1021/acs.chemrev.1c00838
Chem. Rev. 2022, 122, 8053−8125

Dissolved Polysulfide in Lithium Sulfur Batteries. *Chem. Commun.* **2013**, *49*, 11107−11109.
(212) Shao, H.; Ai, F.; Wang, W.; Zhang, H.; Wang, A.; Feng, W.; Huang, Y. Crab Shell-Derived Nitrogen-Doped Micro-/Mesoporous Carbon as an Effective Separator Coating for High Energy Lithium-Sulfur Batteries. *J. Mater. Chem. A* **2017**, *5*, 19892−19900.
(213) Balach, J.; Jaumann, T.; Klose, M.; Oswald, S.; Eckert, J.; Giebeler, L. Functional Mesoporous Carbon-Coated Separator for Long-Life, High-Energy Lithium-Sulfur Batteries. *Adv. Funct. Mater.* **2015**, *25*, 5285.
(214) Zhu, J.; Ge, Y.; Kim, D.; Lu, Y.; Chen, C.; Jiang, M.; Zhang, X. A Novel Separator Coated by Carbon for Achieving Exceptional High Performance Lithium-Sulfur Batteries. *Nano Energy* **2016**, *20*, 176−184.
(215) Luo, L.; Chung, S. H.; Manthiram, A. A Trifunctional Multi-Walled Carbon Nanotubes/Polyethylene Glycol (MWCNT/PEG)-Coated Separator Through a Layer-By-Layer Coating Strategy for High-Energy Li-S Batteries. *J. Mater. Chem. A* **2016**, *4*, 16805−16811.
(216) Zhao, X.; Yin, L.; Zhang, T.; Zhang, M.; Fang, Z.; Wang, C.; Wei, Y.; Chen, G.; Zhang, D.; Sun, Z.; et al. Heteroatoms Dual-Doped Hierarchical Porous Carbon-Selenium Composite for Durable Li-Se and Na-Se Batteries. *Nano Energy* **2018**, *49*, 137−146.
(217) Zhao, X.; Yin, L.; Yang, Z.; Chen, G.; Yue, H.; Zhang, D.; Sun, Z.; Li, F. An Alkali Metal-Selenium Battery with a Wide Temperature Range and Low Self-Discharge. *J. Mater. Chem. A* **2019**, *7*, 21774−21782.
(218) Ponraj, R.; Kannan, A. G.; Ahn, J. H.; Lee, J. H.; Kang, J.; Han, B.; Kim, D. W. Effective Trapping of Lithium Polysulfides Using a Functionalized Carbon Nanotube-Coated Separator for Lithium-Sulfur Cells with Enhanced Cycling Stability. *ACS Appl. Mater. Interfaces* **2017**, *9*, 38445−38454.
(219) Cui, Y.; Wu, X.; Wu, J.; Zeng, J.; Baker, A. P.; Lu, F.; Liang, X.; Ouyang, J.; Huang, J.; Liu, X.; et al. An Interlayer with Architecture that Limits Polysulfides Shuttle to Give a Stable Performance Li-S Battery. *Energy Storage Mater.* **2017**, *9*, 1−10.
(220) Zang, Y.; Pei, F.; Huang, J.; Fu, Z.; Xu, G.; Fang, X. Large-Area Preparation of Crack-Free Crystalline Microporous Conductive Membrane to Upgrade High Energy Lithium-Sulfur Batteries. *Adv. Energy Mater.* **2018**, *8*, 1802052.
(221) Tian, M.; Pei, F.; Yao, M.; Fu, Z.; Lin, L.; Wu, G.; Xu, G.; Kitagawa, H.; Fang, X. Ultrathin MOF Nanosheet Assembled Highly Oriented Microporous Membrane as an Interlayer for Lithium-Sulfur Batteries. *Energy Storage Mater.* **2019**, *21*, 14−21.
(222) Fan, Y.; Yang, Z.; Hua, W.; Liu, D.; Tao, T.; Rahman, M. M.; Lei, W.; Huang, S.; Chen, Y. Functionalized Boron Nitride Nanosheets/Graphene Interlayer for Fast and Long-Life Lithium-Sulfur Batteries. *Adv. Energy Mater.* **2017**, *7*, 1602380.
(223) He, J.; Chen, Y.; Manthiram, A. Vertical Co9S8 Hollow Nanowall Arrays Grown on a Celgard Separator as a Multifunctional Polysulfide Barrier for High-Performance Li-S Batteries. *Energy Environ. Sci.* **2018**, *11*, 2560−2568.
(224) Yang, Y.; Zhang, J. Highly Stable Lithium-Sulfur Batteries Based on Laponite Nanosheet-Coated Celgard Separators. *Adv. Energy Mater.* **2018**, *8*, 1801778.
(225) Li, M.; Wang, C.; Miao, L.; Xiang, J.; Wang, T.; Yuan, K.; Chen, J.; Huang, Y. A Separator-Based Lithium Polysulfide Recirculator for High-Loading and High-Performance Li-S Batteries. *J. Mater. Chem. A* **2018**, *6*, 5862−5869.
(226) Wang, Z.; Feng, M.; Sun, H.; Li, G.; Fu, Q.; Li, H.; Liu, J.; Sun, L.; Mauger, A.; Julien, C. M.; et al. Constructing Metal-Free and Cost-Effective Multifunctional Separator for High-Performance Lithium-Sulfur Batteries. *Nano Energy* **2019**, *59*, 390−398.
(227) Si, L.; Wang, J.; Li, G.; Hong, X.; Wei, Q.; Yang, Y.; Zhang, M.; Cai, Y. High Energy Density Lithium-Selenium Batteries Enabled by a Covalent Organic Framework-Coated Separator. *Mater. Lett.* **2019**, *246*, 144−148.
(228) Fang, R.; Zhou, G.; Pei, S.; Li, F.; Cheng, H. M. Localized Polyselenides in a Graphene-Coated Polymer Separator for High Rate and Ultralong Life Lithium-Selenium Batteries. *Chem. Commun.* **2015**, *51*, 3667−3670.
(229) Gu, X.; Xin, L.; Li, Y.; Dong, F.; Fu, M.; Hou, Y. Highly Reversible Li-Se Batteries with Ultra-Lightweight N,S-Codoped Graphene Blocking Layer. *Nano-Micro Lett.* **2018**, *10*, 1−10.
(230) Zhang, Y.; Guo, Y.; Wang, B.; Wei, Y.; Jing, P.; Wu, H.; Dai, Z.; Wang, M.; Zhang, Y. An Integrated Hybrid Interlayer for Polysulfides/Selenides Regulation Toward Advanced Li-SeS2 Batteries. *Carbon* **2020**, *161*, 413−422.
(231) Yang, Y.; Hong, X. J.; Song, C. L.; Li, G. H.; Zheng, Y. X.; Zhou, D. D.; Zhang, M.; Cai, Y. P.; Wang, H. Lithium Bis(Trifluoromethanesulfonyl)Imide Assisted Dual-Functional Separator Coating Materials based on Covalent Organic Frameworks for High-Performance Lithium-Selenium Sulfide Batteries. *J. Mater. Chem. A* **2019**, *7*, 16323−16329.
(232) Li, H.; Zhao, M.; Jin, B.; Wen, Z.; Liu, H. K.; Jiang, Q. Mesoporous Nitrogen-Doped Carbon Nanospheres as Sulfur Matrix and a Novel Chelate-Modified Separator for High-Performance Room-Temperature Na-S Batteries. *Small* **2020**, *16*, 1907464.
(233) Vijaya Kumar Saroja, A. P.; Muthusamy, K.; Sundara, R. Strong Surface Bonding of Polysulfides by Teflonized Carbon Matrix for Enhanced Performance in Room Temperature Sodium-Sulfur Battery. *Adv. Mater. Interfaces* **2019**, *6*, 1801873.
(234) Vijaya Kumar Saroja, A. P.; Rajamani, A.; Muthusamy, K.; Sundara, R. Repelling Polysulfides Using White Graphite Introduced Polymer Membrane as a Shielding Layer in Ambient Temperature Sodium Sulfur Battery. *Adv. Mater. Interfaces* **2019**, *6*, 1901497.
(235) Zhao, Y.; Liu, M.; Lv, W.; He, Y. B.; Wang, C.; Yun, Q.; Li, B.; Kang, F.; Yang, Q. H. Dense Coating of Li4Ti5O12 and Graphene Mixture on the Separator to Produce Long Cycle Life of Lithium-Sulfur Battery. *Nano Energy* **2016**, *30*, 1−8.
(236) Zhang, Z.; Zhang, Z.; Li, J.; Lai, Y. Polydopamine-Coated Separator for High-Performance Lithium-Sulfur Batteries. *J. Solid State Chem.* **2015**, *19*, 1709−1715.
(237) Ou, X.; Yu, Y.; Wu, R.; Tyagi, A.; Zhuang, M.; Ding, Y.; Abidi, I. H.; Wu, H.; Wang, F.; Luo, Z. Shuttle Suppression by Polymer-Sealed Graphene-Coated Polypropylene Separator. *ACS Appl. Mater. Interfaces* **2018**, *10*, 5534−5542.
(238) Yu, X.; Wu, H.; Koo, J. H.; Manthiram, A. Tailoring the Pore Size of a Polypropylene Separator with a Polymer Having Intrinsic Nanoporosity for Suppressing the Polysulfide Shuttle in Lithium-Sulfur Batteries. *Adv. Energy Mater.* **2020**, *10*, 1902872.
(239) Zhong, M.; Kong, L.; Zhao, K.; Zhang, Y. H.; Li, N.; Bu, X. H. Recent Progress of Nanoscale Metal-Organic Frameworks in Synthesis and Battery Applications. *Adv. Sci.* **2021**, *8*, 2001980.
(240) Ding, S. Y.; Wang, W. Covalent Organic Frameworks (COFs): From Design to Applications. *Chem. Soc. Rev.* **2013**, *42*, 548−568.
(241) Zhou, T.; Zhao, Y.; Choi, J. W.; Coskun, A. Lithium-Salt Mediated Synthesis of a Covalent Triazine Framework for Highly Stable Lithium Metal Batteries. *Angew. Chem., Int. Ed.* **2019**, *58*, 16795−16955.
(242) Zhao, Z.; Chen, W.; Impeng, S.; Li, M.; Wang, R.; Liu, Y.; Zhang, L.; Dong, L.; Unruangsri, J.; Peng, C. Covalent Organic Framework-Based Ultrathin Crystalline Porous Film: Manipulating Uniformity of Fluoride Distribution for Stabilizing Lithium Metal Anode. *J. Mater. Chem. A* **2020**, *8*, 3459−3467.
(243) Zheng, Y.; Xia, S.; Dong, F.; Sun, H.; Pang, Y.; Yang, J.; Huang, Y.; Zheng, S. High Performance Li Metal Anode Enabled by Robust Covalent Triazine Framework-Based Protective Layer. *Adv. Funct. Mater.* **2021**, *31*, 2006159.
(244) Bai, S.; Liu, X.; Zhu, K.; Wu, S.; Zhou, H. Metal-Organic Framework-Based Separator for Lithium-Sulfur Batteries. *Nat. Energy* **2016**, *1*, 1−6.
(245) Wu, F.; Qian, J.; Chen, R.; Ye, Y.; Sun, Z.; Xing, Y.; Li, L. Light-Weight Functional Layer on a Separator as a Polysulfide Immobilizer to Enhance Cycling Stability for Lithium-Sulfur Batteries. *J. Mater. Chem. A* **2016**, *4*, 17033−17041.
(246) Karuppiah, S.; Kalimuthu, B.; Nazrulla, M. A.; Krishnamurty, S.; Nallathamby, K. An Effective Polysulfide Trapping Polar Interlayer

https://doi.org/10.1021/acs.chemrev.1c00838
Chem. Rev. 2022, 122, 8053−8125

for High Rate Li-S Batteries. *J. Mater. Chem. A* **2019**, *7*, 10067−10076.
(247) Cai, J.; Song, Y.; Chen, X.; Sun, Z.; Yi, Y.; Sun, J.; Zhang, Q. MOF-Derived Conductive Carbon Nitrides for Separator-Modified Li-S Batteries and Flexible Supercapacitors. *J. Mater. Chem. A* **2020**, *8*, 1757−1766.
(248) Li, J.; Huang, Y.; Zhang, S.; Jia, W.; Wang, X.; Guo, Y.; Jia, D.; Wang, L. Decoration of Silica Nanoparticles on Polypropylene Separator for Lithium-Sulfur Batteries. *ACS Appl. Mater. Interfaces* **2017**, *9*, 7499−7504.
(249) Huangfu, Y.; Zheng, T.; Zhang, K.; She, X.; Xu, H.; Fang, Z.; Xie, K. Facile Fabrication of Permselective g-C3N4 Separator for Improved Lithium-Sulfur Batteries. *Electrochim. Acta* **2018**, *272*, 60−67.
(250) Chai, L.; Wang, J.; Wang, H.; Zhang, L.; Yu, W.; Mai, L. Porous Carbonized Graphene-Embedded Fungus Film as an Interlayer for Superior Li-S Batteries. *Nano Energy* **2015**, *17*, 224−232.
(251) Li, Q.; Song, Y.; Xu, R.; Zhang, L.; Gao, J.; Xia, Z.; Tian, Z.; Wei, N.; Rummeli, M. H.; Zou, X.; et al. Biotemplating Growth of Nepenthes-like N-Doped Graphene as a Bifunctional Polysulfide Scavenger for Li-S Batteries. *ACS Nano* **2018**, *12*, 10240−10250.
(252) Pei, F.; Lin, L.; Fu, A.; Mo, S.; Ou, D.; Fang, X.; Zheng, N. A Two-Dimensional Porous Carbon-Modified Separator for High-Energy-Density Li-S Batteries. *Joule* **2018**, *2*, 323−336.
(253) Zeng, P.; Huang, L.; Zhang, X.; Zhang, R.; Wu, L.; Chen, Y. Long-Life and High-Areal-Capacity Lithium-Sulfur Batteries Realized by a Honeycomb-Like N, P Dual-Doped Carbon Modified Separator. *Chem. Eng. J.* **2018**, *349*, 327−337.
(254) Balach, J.; Singh, H. K.; Gomoll, S.; Jaumann, T.; Klose, M.; Oswald, S.; Richter, M.; Eckert, J.; Giebeler, L. Synergistically Enhanced Polysulfide Chemisorption Using a Flexible Hybrid Separator with N and S Dual-Doped Mesoporous Carbon Coating for Advanced Lithium-Sulfur Batteries. *ACS Appl. Mater. Interfaces* **2016**, *8*, 14586−14595.
(255) Tu, S.; Chen, X.; Zhao, X.; Cheng, M.; Xiong, P.; He, Y.; Zhang, Q.; Xu, Y. A Polysulfide-Immobilizing Polymer Retards the Shuttling of Polysulfide Intermediates in Lithium-Sulfur Batteries. *Adv. Mater.* **2018**, *30*, 1804581.
(256) Pang, Y.; Wei, J.; Wang, Y.; Xia, Y. Synergetic Protective Effect of the Ultralight MWCNTs/NCQDs Modified Separator for Highly Stable Lithium-Sulfur Batteries. *Adv. Energy Mater.* **2018**, *8*, 1702288.
(257) Abbas, S. A.; Ding, J.; Wu, S. H.; Fang, J.; Boopathi, K. M.; Mohapatra, A.; Lee, L. W.; Wang, P. C.; Chang, C. C.; Chu, C. W. Modified Separator Performing Dual Physical/Chemical Roles to Inhibit Polysulfide Shuttle Resulting in Ultrastable Li-S Batteries. *ACS Nano* **2017**, *11*, 12436−12445.
(258) Jiang, S.; Chen, M.; Wang, X.; Wu, Z.; Zeng, P.; Huang, C.; Wang, Y. MoS2-Coated N-doped Mesoporous Carbon Spherical Composite Cathode and CNT/Chitosan Modified Separator for Advanced Lithium Sulfur Batteries. *ACS Sustain. Chem. Eng.* **2018**, *6*, 16828−16837.
(259) Liu, J.; Yuan, L.; Yuan, K.; Li, Z.; Hao, Z.; Xiang, J.; Huang, Y. SnO2 as a High-Efficiency Polysulfide Trap in Lithium-Sulfur Batteries. *Nanoscale* **2016**, *8*, 13638−13645.
(260) Kong, L.; Peng, H. J.; Huang, J. Q.; Zhu, W.; Zhang, G.; Zhang, Z. W.; Zhai, P. Y.; Sun, P.; Xie, J.; Zhang, Q. Beaver-Dam-Like Membrane: A Robust and Sulphifilic MgBO2(OH)/CNT/PP Nest Separator in Li-S Batteries. *Energy Storage Mater.* **2017**, *8*, 153−160.
(261) Xu, G.; Yan, Q. B.; Wang, S.; Kushima, A.; Bai, P.; Liu, K.; Zhang, X.; Tang, Z.; Li, J. A Thin Multifunctional Coating on a Separator Improves the Cyclability and Safety of Lithium Sulfur Batteries. *Chem. Sci.* **2017**, *8*, 6619−6625.
(262) Zhou, Y.; Hu, G.; Zhang, W.; Li, Q.; Zhao, Z.; Zhao, Y.; Li, F.; Geng, F. Cationic Two-Dimensional Sheets for an Ultralight Electrostatic Polysulfide Trap Toward High-Performance Lithium-Sulfur Batteries. *Energy Storage Mater.* **2017**, *9*, 39−46.
(263) Zhang, Z.; Lai, Y.; Zhang, Z.; Zhang, K.; Li, J. Al2O3-Coated Porous Separator for Enhanced Electrochemical Performance of Lithium Sulfur Batteries. *Electrochim. Acta* **2014**, *129*, 55−61.
(264) Xu, Q.; Hu, G. C.; Bi, H. L.; Xiang, H. F. A Trilayer Carbon Nanotube/Al2O3/Polypropylene Separator for Lithium-Sulfur Batteries. *Ionics* **2015**, *21*, 981−986.
(265) Liang, X.; Hart, C.; Pang, Q.; Garsuch, A.; Weiss, T.; Nazar, L. F. A Highly Efficient Polysulfide Mediator for Lithium-Sulfur Batteries. *Nat. Commun.* **2015**, *6*, 5682.
(266) Lai, Y.; Wang, P.; Qin, F.; Xu, M.; Li, J.; Zhang, K.; Zhang, Z. A Carbon Nanofiber@Mesoporous *δ*-MnO2 Nanosheet-Coated Separator for High-Performance Lithium-Sulfur Batteries. *Energy Storage Mater.* **2017**, *9*, 179−187.
(267) Jiao, L.; Zhang, C.; Geng, C.; Wu, S.; Li, H.; Lv, W.; Tao, Y.; Chen, Z.; Zhou, G.; Li, J.; et al. Capture and Catalytic Conversion of Polysulfides by In Situ Built TiO2-MXene Heterostructures for Lithium-Sulfur Batteries. *Adv. Energy Mater.* **2019**, *9*, 1900219.
(268) Sun, J.; Sun, Y.; Pasta, M.; Zhou, G.; Li, Y.; Liu, W.; Xiong, F.; Cui, Y. Entrapment of Polysulfides by a Black-Phosphorus-Modified Separator for Lithium-Sulfur Batteries. *Adv. Mater.* **2016**, *28*, 9797.
(269) Chen, X.; Ding, X.; Wang, C.; Feng, Z.; Xu, L.; Gao, X.; Zhai, Y.; Wang, D. A Multi-Shelled CoP Nanosphere Modified Separator for Highly Efficient Li-S Batteries. *Nanoscale* **2018**, *10*, 13694−13701.
(270) Sun, Z.; Wu, X. L.; Peng, Z.; Wang, J.; Gan, S.; Zhang, Y.; Han, D.; Niu, L. Compactly Coupled Nitrogen-Doped Carbon Nanosheets/Molybdenum Phosphide Nanocrystal Hollow Nanospheres as Polysulfide Reservoirs for High-Performance Lithium-Sulfur Chemistry. *Small* **2019**, *15*, 1902491.
(271) Luo, Y.; Luo, N.; Kong, W.; Wu, H.; Wang, K.; Fan, S.; Duan, W.; Wang, J. Multifunctional Interlayer Based on Molybdenum Diphosphide Catalyst and Carbon Nanotube Film for Lithium-Sulfur Batteries. *Small* **2018**, *14*, 1702853.
(272) Yao, W.; Zheng, W.; Xu, J.; Tian, C.; Han, K.; Sun, W.; Xiao, S. ZnS-SnS@ NC Heterostructure as robust Lithiophilicity and Sulfiphilicity Mediator toward High-Rate and Long-Life Lithium-Sulfur Batteries. *ACS Nano* **2021**, *15*, 7114−7130.
(273) Ghazi, Z. A.; He, X.; Khattak, A. M.; Khan, N. A.; Liang, B.; Iqbal, A.; Wang, J.; Sin, H.; Li, L.; Tang, Z. MoS2/Celgard Separator as Efficient Polysulfide Barrier for Long-Life Lithium-Sulfur Batteries. *Adv. Mater.* **2017**, *29*, 1606817.
(274) Yang, Y.; Wang, S.; Zhang, L.; Deng, Y.; Xu, H.; Qin, X.; Chen, G. CoS-Interposed and Ketjen Black-Embedded Carbon Nanofiber Framework as a Separator Modulation for High Performance Li-S Batteries. *Chem. Eng. J.* **2019**, *369*, 77−86.
(275) Wei, N.; Cai, J.; Wang, R.; Wang, M.; Lv, W.; Ci, H.; Sun, J.; Liu, Z. Elevated Polysulfide Regulation by an Ultralight All-CVD-Built ReS2@N-Doped Graphene Heterostructure Interlayer for Lithium-Sulfur Batteries. *Nano Energy* **2019**, *66*, 104190.
(276) Park, J.; Yu, B. C.; Park, J. S.; Choi, J. W.; Kim, C.; Sung, Y. E.; Goodenough, J. B. Tungsten Disulfide Catalysts Supported on a Carbon Cloth Interlayer for High Performance Li-S Battery. *Adv. Energy Mater.* **2017**, *7*, 1602567.
(277) Yao, S.; Cui, J.; Huang, J. Q.; Lu, Z.; Deng, Y.; Chong, W. G.; Wu, J.; Ihsan Ul Haq, M.; Ciucci, F.; Kim, J. K. Novel 2D Sb2S3 Nanosheet/CNT Coupling Layer for Exceptional Polysulfide Recycling Performance. *Adv. Energy Mater.* **2018**, *8*, 1800710.
(278) Wang, J.; Yi, S.; Liu, J.; Sun, S.; Liu, Y.; Yang, D.; Xi, K.; Gao, G.; Abdelkader, A.; Yan, W.; et al. Suppressing the Shuttle Effect and Dendrite Growth in Lithium-Sulfur Batteries. *ACS Nano* **2020**, *14*, 9819−9831.
(279) Zhou, G.; Tian, H.; Jin, Y.; Tao, X.; Liu, B.; Zhang, R.; Seh, Z. W.; Zhuo, D.; Liu, Y.; Sun, J.; et al. Catalytic Oxidation of Li2S on the Surface of Metal Sulfides for Li-S Batteries. *Proc. Natl. Acad. Sci. U.S.A.* **2017**, *114*, 840−845.
(280) Yang, T.; Guo, B.; Du, W.; Aslam, M. K.; Tao, M.; Zhong, W.; Chen, Y.; Bao, S. J.; Zhang, X.; Xu, M. Design and Construction of Sodium Polysulfides Defense System for Room-Temperature Na-S Battery. *Adv. Sci.* **2019**, *6*, 1901557.

https://doi.org/10.1021/acs.chemrev.1c00838
Chem. Rev. 2022, 122, 8053−8125

(281) Wu, J.; Zeng, H.; Li, X.; Xiang, X.; Liao, Y.; Xue, Z.; Ye, Y.; Xie, X. Ultralight Layer-by-Layer Self-Assembled MoS2-Polymer Modified Separator for Simultaneously Trapping Polysulfides and Suppressing Lithium Dendrites. *Adv. Energy Mater.* **2018**, *8*, 1802430.
(282) Ni, X.; Qian, T.; Liu, X.; Xu, N.; Liu, J.; Yan, C. High Lithium Ion Conductivity LiF/GO Solid Electrolyte Interphase Inhibiting the Shuttle of Lithium Polysulfides in Long-Life Li-S Batteries. *Adv. Funct. Mater.* **2018**, *28*, 1706513.
(283) Chang, Z.; Qiao, Y.; Wang, J.; Deng, H.; He, P.; Zhou, H. Fabricating Better Metal-Organic Frameworks Separators for Li-S Batteries: Pore Sizes Effects Inspired Channel Modification Strategy. *Energy Storage Mater.* **2020**, *25*, 164−171.
(284) Lei, T.; Chen, W.; Lv, W.; Huang, J.; Zhu, J.; Chu, J.; Yan, C.; Wu, C.; Yan, Y.; He, W.; et al. Inhibiting Polysulfide Shuttling with a Graphene Composite Separator for Highly Robust Lithium-Sulfur Batteries. *Joule* **2018**, *2*, 2091−2104.
(285) Kim, S. H.; Yeon, J. S.; Kim, R.; Choi, K. M.; Park, H. S. A Functional Separator Coated with Sulfonated Metal-Organic Framework/Nafion Hybrids for Li-S Batteries. *J. Mater. Chem. A* **2018**, *6*, 24971−24978.
(286) He, Y.; Wu, S.; Li, Q.; Zhou, H. Designing a Multifunctional Separator for High-Performance Li-S Batteries at Elevated Temperature. *Small* **2019**, *15*, 1904332.
(287) Bauer, I.; Kohl, M.; Althues, H.; Kaskel, S. Shuttle Suppression in Room Temperature Sodium-Sulfur Batteries Using Ion Selective Polymer Membranes. *Chem. Commun.* **2014**, *50*, 3208−3210.
(288) Yu, X.; Manthiram, A. Ambient-Temperature Sodium-Sulfur Batteries with a Sodiated Nafion Membrane and a Carbon Nanofiber-Activated Carbon Composite Electrode. *Adv. Energy Mater.* **2015**, *5*, 1500350.
(289) Yu, X.; Manthiram, A. Performance Enhancement and Mechanistic Studies of Room-Temperature Sodium-Sulfur Batteries with a Carbon-Coated Functional Nafion Separator and a Na2S/Activated Carbon Nanofiber Cathode. *Chem. Mater.* **2016**, *28*, 896−905.
(290) Ceylan Cengiz, E.; Erdol, Z.; Sakar, B.; Aslan, A.; Ata, A.; Ozturk, O.; Demir-Cakan, R. Investigation of the Effect of Using Al2O3-Nafion Barrier on Room-Temperature Na-S Batteries. *J. Phys. Chem. C* **2017**, *121*, 15120−15126.
(291) Shi, L.; Zeng, F.; Cheng, X.; Lam, K. H.; Wang, W.; Wang, A.; Jin, Z.; Wu, F.; Yang, Y. Enhanced Performance of Lithium-Sulfur Batteries with High Sulfur Loading Utilizing Ion Selective MWCNT/SPANI Modified Separator. *Chem. Eng. J.* **2018**, *334*, 305−312.
(292) Ahn, W.; Lim, S. N.; Lee, D. U.; Kim, K. B.; Chen, Z.; Yeon, S. H. Interaction Mechanism Between a Functionalized Protective Layer and Dissolved Polysulfide for Extended Cycle Life of Lithium Sulfur Batteries. *J. Mater. Chem. A* **2015**, *3*, 9461−9467.
(293) Yim, T.; Han, S. H.; Park, N. H.; Park, M. S.; Lee, J. H.; Shin, J.; Choi, J. W.; Jung, Y.; Jo, Y. N.; Yu, J. S.; et al. Effective Polysulfide Rejection by Dipole-Aligned BaTiO3-Coated Separator in Lithium-Sulfur Batteries. *Adv. Funct. Mater.* **2016**, *26*, 7817.
(294) He, Y.; Qiao, Y.; Chang, Z.; Cao, X.; Jia, M.; He, P.; Zhou, H. Developing A "Polysulfide-Phobic" Strategy to Restrain Shuttle Effect in Lithium-Sulfur Batteries. *Angew. Chem., Int. Ed.* **2019**, *58*, 11774−11904.
(295) Yao, H.; Yan, K.; Li, W.; Zheng, G.; Kong, D.; Seh, Z. W.; Narasimhan, V. K.; Liang, Z.; Cui, Y. Improved Lithium-Sulfur Batteries with a Conductive Coating on the Separator to Prevent the Accumulation of Inactive S-Related Species at the Cathode-Separator Interface. *Energy Environ. Sci.* **2014**, *7*, 3381−3390.
(296) Shi, H.; Zhao, X.; Wu, Z. S.; Dong, Y.; Lu, P.; Chen, J.; Ren, W.; Cheng, H. M.; Bao, X. Free-Standing Integrated Cathode Derived From 3D Graphene/Carbon Nanotube Aerogels Serving as Binder-Free Sulfur Host and Interlayer for Ultrahigh Volumetric-Energy-Density Lithium Sulfur Batteries. *Nano Energy* **2019**, *60*, 743−751.
(297) Huang, J. Q.; Xu, Z. L.; Abouali, S.; Akbari Garakani, M.; Kim, J. K. Porous Graphene Oxide/Carbon Nanotube Hybrid Films as Interlayer for Lithium-Sulfur Batteries. *Carbon* **2016**, *99*, 624−632.
(298) Guo, D.; Ming, F.; Su, H.; Wu, Y.; Wahyudi, W.; Li, M.; Hedhili, M. N.; Sheng, G.; Li, L. J.; Alshareef, H. N.; et al. MXene Based Self-Assembled Cathode and Antifouling Separator for High-Rate and Dendrite-Inhibited Li-S Battery. *Nano Energy* **2019**, *61*, 478−485.
(299) Zhou, G.; Li, L.; Wang, D. W.; Shan, X. Y.; Pei, S.; Li, F.; Cheng, H. M. A Flexible Sulfur-Graphene-Polypropylene Separator Integrated Electrode for Advanced Li-S Batteries. *Adv. Mater.* **2015**, *27*, 641.
(300) Huang, J. Q.; Zhang, B.; Xu, Z. L.; Abouali, S.; Akbari Garakani, M.; Huang, J.; Kim, J. K. Novel Interlayer made from Fe3C/Carbon Nanofiber Webs for High Performance Lithium-Sulfur Batteries. *J. Power Sources* **2015**, *285*, 43−50.
(301) Liang, G.; Wu, J.; Qin, X.; Liu, M.; Li, Q.; He, Y. B.; Kim, J. K.; Li, B.; Kang, F. Ultrafine TiO2 Decorated Carbon Nanofibers as Multifunctional Interlayer for High-Performance Lithium-Sulfur Battery. *ACS Appl. Mater. Interfaces* **2016**, *8*, 23105−23113.
(302) Wang, L.; He, Y. B.; Shen, L.; Lei, D.; Ma, J.; Ye, H.; Shi, K.; Li, B.; Kang, F. Ultra-Small Self-Discharge and Stable Lithium-Sulfur Batteries Achieved by Synergetic Effects of Multicomponent Sandwich-Type Composite Interlayer. *Nano Energy* **2018**, *50*, 367−375.
(303) Wu, F.; Zhao, S.; Chen, L.; Lu, Y.; Su, Y.; Jia, Y.; Bao, L.; Wang, J.; Chen, S.; Chen, R. Metal-Organic Frameworks Composites Threaded on the CNT Knitted Separator for Suppressing the Shuttle Effect of Lithium Sulfur Batteries. *Energy Storage Mater.* **2018**, *14*, 383−391.
(304) Li, N.; Chen, Z.; Chen, F.; Hu, G.; Wang, S.; Sun, Z.; Sun, X.; Li, F. From Interlayer to Lightweight Capping Layer: Rational Design of Mesoporous TiO2 Threaded with CNTs for Advanced Li-S Batteries. *Carbon* **2019**, *143*, 523−530.
(305) Fang, D.; Wang, Y.; Liu, X.; Yu, J.; Qian, C.; Chen, S.; Wang, X.; Zhang, S. Spider-Web-Inspired Nanocomposite-Modified Separator: Structural and Chemical Cooperativity Inhibiting the Shuttle Effect in Li-S Batteries. *ACS Nano* **2019**, *13*, 1563−1573.
(306) Dong, Y.; Zheng, S.; Qin, J.; Zhao, X.; Shi, H.; Wang, X.; Chen, J.; Wu, Z. S. All-MXene-Based Integrated Electrode Constructed by Ti3C2 Nanoribbon Framework Host and Nanosheet Interlayer for High-Energy-Density Li-S Batteries. *ACS Nano* **2018**, *12*, 2381−2388.
(307) Wang, Z.; Pan, R.; Xu, C.; Ruan, C.; Edström, K.; Strømme, M.; Nyholm, L. Conducting Polymer Paper-Derived Separators for Lithium Metal Batteries. *Energy Storage Mater.* **2018**, *13*, 283−292.
(308) Ma, J. L.; Yin, Y. B.; Liu, T.; Zhang, X. B.; Yan, J. M.; Jiang, Q. Suppressing Sodium Dendrites by Multifunctional Polyvinylidene Fluoride (PVDF) Interlayers with Nonthrough Pores and High Flux/Affinity of Sodium Ions toward Long Cycle Life Sodium Oxygen-Batteries. *Adv. Funct. Mater.* **2018**, *28*, 1703931.
(309) Chang, C. H.; Chung, S. H.; Manthiram, A. Dendrite-Free Lithium Anode via a Homogenous Li-Ion Distribution Enabled by a Kimwipe Paper. *Adv. Sustain. Syst.* **2017**, *1*, 1600034.
(310) Liu, W.; Mi, Y.; Weng, Z.; Zhong, Y.; Wu, Z.; Wang, H. Functional Metal-Organic Framework Boosting Lithium Metal Anode Performance via Chemical Interactions. *Chem. Sci.* **2017**, *8*, 4285−4291.
(311) Imtiaz, S.; Ali Zafar, Z.; Razaq, R.; Sun, D.; Xin, Y.; Li, Q.; Zhang, Z.; Zheng, L.; Huang, Y.; Anderson, J. A. Electrocatalysis on Separator Modified by Molybdenum Trioxide Nanobelts for Lithium-Sulfur Batteries. *Adv. Mater. Interfaces* **2018**, *5*, 1800243.
(312) Sun, Z.; Wang, T.; Zhang, Y.; Kempa, K.; Wang, X. Boosting the Electrochemical Performance of Lithium/Sulfur Batteries with the Carbon Nanotube/Fe3O4 Coated by Carbon Modified Separator. *Electrochim. Acta* **2019**, *327*, 134843.
(313) Deng, N.; Wang, L.; Feng, Y.; Liu, M.; Li, Q.; Wang, G.; Zhang, L.; Kang, W.; Cheng, B.; Liu, Y. Co-Based and Cu-Based MOFs Modified Separators to Strengthen the Kinetics of Redox Reaction and Inhibit Lithium-Dendrite for Long-Life Lithium-Sulfur Batteries. *Chem. Eng. J.* **2020**, *388*, 124241.

https://doi.org/10.1021/acs.chemrev.1c00838
Chem. Rev. 2022, 122, 8053−8125

(314) Balach, J.; Jaumann, T.; Muhlenhoff, S.; Eckert, J.; Giebeler, L. Enhanced Polysulphide Redox Reaction Using a RuO2 Nanoparticle-Decorated Mesoporous Carbon as Functional Separator Coating for Advanced Lithium-Sulphur Batteries. *Chem. Commun.* **2016**, *52*, 8134−8137.
(315) Zuo, P.; Hua, J.; He, M.; Zhang, H.; Qian, Z.; Ma, Y.; Du, C.; Cheng, X.; Gao, Y.; Yin, G. Facilitating the Redox Reaction of Polysulfides by an Electrocatalytic Layer-Modified Separator for Lithium-Sulfur Batteries. *J. Mater. Chem. A* **2017**, *5*, 10936−10945.
(316) Cheng, Z.; Pan, H.; Chen, J.; Meng, X.; Wang, R. Separator Modified by Cobalt-Embedded Carbon Nanosheets Enabling Chemisorption and Catalytic Effects of Polysulfides for High-Energy-Density Lithium-Sulfur Batteries. *Adv. Energy Mater.* **2019**, *9*, 1901609.
(317) Fan, S.; Huang, S.; Pam, M. E.; Chen, S.; Wu, Q.; Hu, J.; Wang, Y.; Ang, L. K.; Yan, C.; Shi, Y.; et al. Design Multifunctional Catalytic Interface: Toward Regulation of Polysulfide and Li2S Redox Conversion in Li-S Batteries. *Small* **2019**, *15*, 1906132.
(318) Zhang, K.; Chen, Z.; Ning, R.; Xi, S.; Tang, W.; Du, Y.; Liu, C.; Ren, Z.; Chi, X.; Bai, M.; et al. Single-Atom Coated Separator for Robust Lithium-Sulfur Batteries. *ACS Appl. Mater. Interfaces* **2019**, *11*, 25147−25154.
(319) Hao, B.; Li, H.; Lv, W.; Zhang, Y.; Niu, S.; Qi, Q.; Xiao, S.; Li, J.; Kang, F.; Yang, Q. H. Reviving Catalytic Activity of Nitrides by the Doping of the Inert Surface Layer to Promote Polysulfide Conversion in Lithium-Sulfur Batteries. *Nano Energy* **2019**, *60*, 305−311.
(320) Hong, X. J.; Song, C. L.; Yang, Y.; Tan, H. C.; Li, G. H.; Cai, Y. P.; Wang, H. Cerium Based Metal-Organic Frameworks as an Efficient Separator Coating Catalyzing the Conversion of Polysulfides for High Performance Lithium-Sulfur Batteries. *ACS Nano* **2019**, *13*, 1923−1931.
(321) Tian, Y.; Li, G.; Zhang, Y.; Luo, D.; Wang, X.; Zhao, Y.; Liu, H.; Ji, P.; Du, X.; Li, J.; et al. Low-Bandgap Se-Deficient Antimony Selenide as a Multifunctional Polysulfide Barrier toward High-Performance Lithium-Sulfur Batteries. *Adv. Mater.* **2020**, *32*, 1904876.
(322) Li, Z.; Zhou, C.; Hua, J.; Hong, X.; Sun, C.; Li, H. W.; Xu, X.; Mai, L. Engineering Oxygen Vacancies in a Polysulfide-Blocking Layer with Enhanced Catalytic Ability. *Adv. Mater.* **2020**, *32*, 1907444.
(323) Li, P.; Lv, H.; Li, Z.; Meng, X.; Lin, Z.; Wang, R.; Li, X. The Electrostatic Attraction and Catalytic Effect Enabled by Ionic-Covalent Organic Nanosheets on MXene for Separator Modification of Lithium-Sulfur Batteries. *Adv. Mater.* **2021**, *33*, 2007803.
(324) Zhou, T.; Lv, W.; Li, J.; Zhou, G.; Zhao, Y.; Fan, S.; Liu, B.; Li, B.; Kang, F.; Yang, Q. H. Twinborn TiO2-TiN Heterostructures Enabling Smooth Trapping-Diffusion-Conversion of Polysulfides Towards Ultralong Life Lithium-Sulfur Batteries. *Energy Environ. Sci.* **2017**, *10*, 1694−1703.
(325) Wang, N.; Chen, B.; Qin, K.; Liu, E.; Shi, C.; He, C.; Zhao, N. Rational Design of Co9S8/CoO Heterostructures with Well-Defined Interfaces for Lithium Sulfur Batteries: A Study of Synergistic Adsorption-Electrocatalysis Function. *Nano Energy* **2019**, *60*, 332−339.
(326) Yang, J. L.; Zhao, S. X.; Lu, Y. M.; Zeng, X. T.; Lv, W.; Cao, G. Z. In-Situ Topochemical Nitridation Derivative MoO2-Mo2N Binary Nanobelts as Multifunctional Interlayer for Fast-Kinetic Li-Sulfur Batteries. *Nano Energy* **2020**, *68*, 104356.
(327) Dong, C.; Zhou, H.; Jin, B.; Gao, W.; Lang, X.; Li, J.; Jiang, Q. Enabling High-Performance Room-Temperature Sodium/Sulfur Batteries with Few-Layer 2H-MoSe2 Embellished Nitrogen-Doped Hollow Carbon Spheres as Polysulfide Barriers. *J. Mater. Chem. A* **2021**, *9*, 3451−3463.
(328) Zhou, J.; Liu, X.; Zhu, L.; Zhou, J.; Guan, Y.; Chen, L.; Niu, S.; Cai, J.; Sun, D.; Zhu, Y.; et al. Deciphering the Modulation Essence of p Bands in Co-Based Compounds on Li-S Chemistry. *Joule* **2018**, *2*, 2681−2693.
(329) Song, Y.; Zhao, S.; Chen, Y.; Cai, J.; Li, J.; Yang, Q.; Sun, J.; Liu, Z. Enhanced Sulfur Redox and Polysulfide Regulation via Porous VN-Modified Separator for Li-S Batteries. *ACS Appl. Mater. Interfaces* **2019**, *11*, 5687−5694.
(330) Tian, D.; Song, X.; Wang, M.; Wu, X.; Qiu, Y.; Guan, B.; Xu, X.; Fan, L.; Zhang, N.; Sun, K. MoN Supported on Graphene as a Bifunctional Interlayer for Advanced Li-S Batteries. *Adv. Energy Mater.* **2019**, *9*, 1901940.
(331) Lin, H.; Yang, L.; Jiang, X.; Li, G.; Zhang, T.; Yao, Q.; Zheng, G. W.; Lee, J. Y. Electrocatalysis of Polysulfide Conversion by Sulfur-Deficient MoS2 Nanoflakes for Lithium-Sulfur Batteries. *Energy Environ. Sci.* **2017**, *10*, 1476−1486.
(332) Zhang, Y.; Li, G.; Wang, J.; Cui, G.; Wei, X.; Shui, L.; Kempa, K.; Zhou, G.; Wang, X.; Chen, Z. Hierarchical Defective Fe3-xC@C Hollow Microsphere Enables Fast and Long-Lasting Lithium-Sulfur Batteries. *Adv. Funct. Mater.* **2020**, *30*, 2001165.
(333) Luo, D.; Zhang, Z.; Li, G.; Cheng, S.; Li, S.; Li, J.; Gao, R.; Li, M.; Sy, S.; Deng, Y. P.; et al. Revealing the Rapid Electrocatalytic Behavior of Ultrafine Amorphous Defective Nb2O5-x Nanocluster toward Superior Li-S Performance. *ACS Nano* **2020**, *14*, 4849−4860.
(334) He, D.; Meng, J.; Chen, X.; Liao, Y.; Cheng, Z.; Yuan, L.; Li, Z.; Huang, Y. Ultrathin Conductive Interlayer with High-Density Antisite Defects for Advanced Lithium-Sulfur Batteries. *Adv. Funct. Mater.* **2021**, *31*, 2001201.
(335) Peng, H. J.; Zhang, Z. W.; Huang, J. Q.; Zhang, G.; Xie, J.; Xu, W. T.; Shi, J. L.; Chen, X.; Cheng, X. B.; Zhang, Q. A Cooperative Interface for Highly Efficient Lithium-Sulfur Batteries. *Adv. Mater.* **2016**, *28*, 9551.
(336) Chen, G.; Song, X.; Wang, S.; Wang, Y.; Gao, T.; Ding, L. X.; Wang, H. A Multifunctional Separator Modified with Cobalt and Nitrogen Co-Doped Porous Carbon Nanofibers for Li-S Batteries. *J. Membr. Sci.* **2018**, *548*, 247−253.
(337) Wang, R.; Yang, J.; Chen, X.; Zhao, Y.; Zhao, W.; Qian, G.; Li, S.; Xiao, Y.; Chen, H.; Ye, Y. Highly Dispersed Cobalt Clusters in Nitrogen-Doped Porous Carbon Enable Multiple Effects for High-Performance Li-S Battery. *Adv. Energy Mater.* **2020**, *10*, 1903550.
(338) Qian, J.; Wang, F.; Li, Y.; Wang, S.; Zhao, Y.; Li, W.; Xing, Y.; Deng, L.; Sun, Q.; Li, L. Electrocatalytic Interlayer with Fast Lithium-Polysulfides Diffusion for Lithium-Sulfur Batteries to Enhance Electrochemical Kinetics under Lean Electrolyte Conditions. *Adv. Funct. Mater.* **2020**, *30*, 2000742.
(339) Li, Y.; Wu, J.; Zhang, B.; Wang, W.; Zhang, G.; Seh, Z. W.; Zhang, N.; Sun, J.; Huang, L.; Jiang, J.; et al. Fast Conversion and Controlled Deposition of Lithium (Poly)Sulfides in Lithium-Sulfur Batteries Using High-Loading Cobalt Single Atoms. *Energy Storage Mater.* **2020**, *30*, 250−259.
(340) Li, Y.; Chen, G.; Mou, J.; Liu, Y.; Xue, S.; Tan, T.; Zhong, W.; Deng, Q.; Li, T.; Hu, J. Cobalt Single Atoms Supported on N-Doped Carbon as an Active and Resilient Sulfur Host for Lithium-Sulfur Batteries. *Energy Storage Mater.* **2020**, *28*, 196−204.
(341) Du, Z.; Chen, X.; Hu, W.; Chuang, C.; Xie, S.; Hu, A.; Yan, W.; Kong, X.; Wu, X.; Ji, H. Cobalt in Nitrogen-Doped Graphene as Single-Atom Catalyst for High-Sulfur Content Lithium-Sulfur Batteries. *J. Am. Chem. Soc.* **2019**, *141*, 3977−3985.
(342) Zhang, L.; Liu, D.; Muhammad, Z.; Wan, F.; Xie, W.; Wang, Y.; Song, L.; Niu, Z.; Chen, J. Single Nickel Atoms on Nitrogen-Doped Graphene Enabling Enhanced Kinetics of Lithium-Sulfur Batteries. *Adv. Mater.* **2019**, *31*, 1903955.
(343) Song, Y.; Zhao, W.; Kong, L.; Zhang, L.; Zhu, X.; Shao, Y.; Ding, F.; Zhang, Q.; Sun, J.; Liu, Z. Synchronous Immobilization and Conversion of Polysulfides on a VO2-VN Binary Host Targeting High Sulfur Load Li-S Batteries. *Energy Environ. Sci.* **2018**, *11*, 2620−2630.
(344) Fang, R.; Zhao, S.; Sun, Z.; Wang, D. W.; Amal, R.; Wang, S.; Cheng, H. M.; Li, F. Polysulfide Immobilization and Conversion on a Conductive Polar MoC@MoOx Material for Lithium-Sulfur Batteries. *Energy Storage Mater.* **2018**, *10*, 56−61.
(345) Zhong, Y.; Yin, L.; He, P.; Liu, W.; Wu, Z.; Wang, H. Surface Chemistry in Cobalt Phosphide-Stabilized Lithium-Sulfur Batteries. *J. Am. Chem. Soc.* **2018**, *140*, 1455−1459.
(346) Zhao, M.; Peng, H. J.; Li, B. Q.; Chen, X.; Xie, J.; Liu, X.; Zhang, Q.; Huang, J. Q. Electrochemical Phase Evolution of Metal-Based Pre-Catalysts for High-Rate Polysulfide Conversion. *Angew. Chem., Int. Ed.* **2020**, *59*, 9011−9102.

https://doi.org/10.1021/acs.chemrev.1c00838
Chem. Rev. 2022, 122, 8053−8125

(347) Waqas, M.; Han, Y.; Chen, D.; Ali, S.; Zhen, C.; Feng, C.; Yuan, B.; Han, J.; He, W. Molecular 'Capturing' and 'Seizing' MoS2/TiN Interlayers Suppress Polysulfide Shuttling and Self-Discharge of Li-S Batteries. *Energy Storage Mater.* **2020**, *27*, 333−341.
(348) Yan, Z.; Xiao, J.; Lai, W.; Wang, L.; Gebert, F.; Wang, Y.; Gu, Q.; Liu, H.; Chou, S. L.; Liu, H.; et al. Nickel Sulfide Nanocrystals on Nitrogen-Doped Porous Carbon Nanotubes with High-Efficiency Electrocatalysis for Room-Temperature Sodium-Sulfur Batteries. *Nat. Commun.* **2019**, *10*, 4793.
(349) Zhang, B. W.; Sheng, T.; Wang, Y. X.; Chou, S.; Davey, K.; Dou, S. X.; Qiao, S. Z. Long-Life Room-Temperature Sodium-Sulfur Batteries by Virtue of Transition-Metal-Nanocluster-Sulfur Interactions. *Angew. Chem., Int. Ed.* **2019**, *58*, 1484−1502.
(350) Liu, H.; Pei, W.; Lai, W. H.; Yan, Z.; Yang, H.; Lei, Y.; Wang, Y. X.; Gu, Q.; Zhou, S.; Chou, S. Electrocatalyzing S Cathodes via Multisulfiphilic Sites for Superior Room-Temperature Sodium-Sulfur Batteries. *ACS Nano* **2020**, *14*, 7259−7268.
(351) Zhao, M.; Li, B. Q.; Zhang, X. Q.; Huang, J. Q.; Zhang, Q. A Perspective toward Practical Lithium-Sulfur Batteries. *ACS Cent. Sci.* **2020**, *6*, 1095−1104.
(352) Kim, P. J.; Kim, K.; Pol, V. G. Uniform Metal-Ion Flux Through Interface-Modified Membrane for Highly Stable Metal Batteries. *Electrochim. Acta* **2018**, *283*, 517−527.
(353) Foroozan, T.; Soto, F. A.; Yurkiv, V.; Sharifi-Asl, S.; Deivanayagam, R.; Huang, Z.; Rojaee, R.; Mashayek, F.; Balbuena, P. B.; Shahbazian-Yassar, R. Synergistic Effect of Graphene Oxide for Impeding the Dendritic Plating of Li. *Adv. Funct. Mater.* **2018**, *28*, 1705917.
(354) Cui, J.; Li, Z.; Li, J.; Li, S.; Liu, J.; Shao, M.; Wei, M. An Atomic-Confined-Space Separator for High Performance Lithium-Sulfur Batteries. *J. Mater. Chem. A* **2020**, *8*, 1896−1903.
(355) Pan, R.; Xu, X.; Sun, R.; Wang, Z.; Lindh, J.; Edstrom, K.; Stromme, M.; Nyholm, L. Nanocellulose Modified Polyethylene Separators for Lithium Metal Batteries. *Small* **2018**, *14*, 1704371.
(356) Ye, Y.; Wang, L.; Guan, L.; Wu, F.; Qian, J.; Zhao, T.; Zhang, X.; Xing, Y.; Shi, J.; Li, L.; et al. A Modularly-Assembled Interlayer to Entrap Polysulfides and Protect Lithium Metal Anode for High Areal Capacity Lithium-Sulfur Batteries. *Energy Storage Mater.* **2017**, *9*, 126−133.
(357) Yu, B. C.; Park, K.; Jang, J. H.; Goodenough, J. B. Cellulose-Based Porous Membrane for Suppressing Li Dendrite Formation in Lithium-Sulfur Battery. *ACS Energy Lett.* **2016**, *1*, 633−637.
(358) Wu, X.; Liu, N.; Guo, Z.; Wang, M.; Qiu, Y.; Tian, D.; Guan, B.; Fan, L.; Zhang, N. Constructing Multi-Functional Janus Separator toward Highly Stable Lithium Batteries. *Energy Storage Mater.* **2020**, *28*, 153−159.
(359) Zhao, C. Z.; Chen, P. Y.; Zhang, R.; Zhang, Q. An Ion Redistributor for Dendrite-Free Lithium Metal Anodes. *Sci. Adv.* **2018**, *4*, No. eaat3446.
(360) Huo, H.; Li, X.; Chen, Y.; Liang, J.; Deng, S.; Gao, X.; Doyle-Davis, K.; Li, R.; Guo, X.; Shen, Y.; et al. Bifunctional Composite Separator with a Solid-State-Battery Strategy for Dendrite-Free Lithium Metal Batteries. *Energy Storage Mater.* **2020**, *29*, 361−366.
(361) Zhou, Y.; Zhang, X.; Ding, Y.; Bae, J.; Guo, X.; Zhao, Y.; Yu, G. Redistributing Li-Ion Flux by Parallelly Aligned Holey Nanosheets for Dendrite-Free Li Metal Anodes. *Adv. Mater.* **2020**, *32*, 2003920.
(362) Ryou, M. H.; Lee, D. J.; Lee, J. N.; Lee, Y. M.; Park, J. K.; Choi, J. W. Excellent Cycle Life of Lithium-Metal Anodes in Lithium-Ion Batteries with Mussel-Inspired Polydopamine-Coated Separators. *Adv. Energy Mater.* **2012**, *2*, 645.
(363) Chi, M.; Shi, L.; Wang, Z.; Zhu, J.; Mao, X.; Zhao, Y.; Zhang, M.; Sun, L.; Yuan, S. Excellent Rate Capability and Cycle Life of Li Metal Batteries with ZrO2/POSS Multilayer-Assembled PE Separators. *Nano Energy* **2016**, *28*, 1−11.
(364) Yang, Y.; Li, B.; Li, L.; Seeger, S.; Zhang, J. A SuperLEphilic/Superhydrophobic and Thermostable Separator Based on Silicone Nanofilaments for Li Metal Batteries. *iScience* **2019**, *16*, 420−432.
(365) Ma, L.; Chen, R.; Hu, Y.; Zhang, W.; Zhu, G.; Zhao, P.; Chen, T.; Wang, C.; Yan, W.; Wang, Y. Nanoporous and Lyophilic Battery Separator From Regenerated Eggshell Membrane with Effective Suppression of Dendritic Lithium Growth. *Energy Storage Mater.* **2018**, *14*, 258−266.
(366) Li, C.; Liu, S.; Shi, C.; Liang, G.; Lu, Z.; Fu, R.; Wu, D. Two-Dimensional Molecular Brush-Functionalized Porous Bilayer Composite Separators toward Ultrastable High-Current Density Lithium Metal Anodes. *Nat. Commun.* **2019**, *10*, 1363.
(367) Wang, Y.; Shi, L.; Zhou, H.; Wang, Z.; Li, R.; Zhu, J.; Qiu, Z.; Zhao, Y.; Zhang, M.; Yuan, S. Polyethylene Separators Modified by Ultrathin Hybrid Films Enhancing Lithium Ion Transport Performance and Li-Metal Anode Stability. *Electrochim. Acta* **2018**, *259*, 386−394.
(368) Li, Y.; Lin, S.; Wang, D.; Gao, T.; Song, J.; Zhou, P.; Xu, Z.; Yang, Z.; Xiao, N.; Guo, S. Single Atom Array Mimic on Ultrathin MOF Nanosheets Boosts the Safety and Life of Lithium-Sulfur Batteries. *Adv. Mater.* **2020**, *32*, 1906722.
(369) Chen, M.; Chen, Z.; Fu, X.; Zhong, W. H. A Janus Protein-Based Nanofabric for Trapping Polysulfides and Stabilizing Lithium Metal in Lithium-Sulfur Batteries. *J. Mater. Chem. A* **2020**, *8*, 7377−7389.
(370) Yang, Y.; Wang, W.; Li, L.; Li, B.; Zhang, J. Stable Cycling of Li-S Batteries by Simultaneously Suppressing Li-Dendrite Growth and Polysulfide Shuttling Enabled by a Bioinspired Separator. *J. Mater. Chem. A* **2020**, *8*, 3692−3700.
(371) Zhang, C.; Shen, L.; Shen, J.; Liu, F.; Chen, G.; Tao, R.; Ma, S.; Peng, Y.; Lu, Y. Anion-Sorbent Composite Separators for High-Rate Lithium-Ion Batteries. *Adv. Mater.* **2019**, *31*, 1808338.
(372) Liang, J.; Chen, Q.; Liao, X.; Yao, P.; Zhu, B.; Lv, G.; Wang, X.; Chen, X.; Zhu, J. A Nano-Shield Design for Separators to Resist Dendrite Formation in Lithium-Metal Batteries. *Angew. Chem., Int. Ed.* **2020**, *59*, 6561−6566.
(373) Wang, S.; Jie, Y.; Sun, Z.; Cai, W.; Chen, Y.; Huang, F.; Liu, Y.; Li, X.; Du, R.; Cao, R.; et al. An Implantable Artificial Protective Layer Enables Stable Sodium Metal Anodes. *ACS Appl. Energy Mater.* **2020**, *3*, 8688−8694.
(374) Xu, R.; Zhang, X. Q.; Cheng, X. B.; Peng, H. J.; Zhao, C. Z.; Yan, C.; Huang, J. Q. Artificial Soft-Rigid Protective Layer for Dendrite-Free Lithium Metal Anode. *Adv. Funct. Mater.* **2018**, *28*, 1705838.
(375) Li, X.; Liu, Y.; Pan, Y.; Wang, M.; Chen, J.; Xu, H.; Huang, Y.; Lau, W. M.; Shan, A.; Zheng, J.; et al. A Functional SrF2 Coated Separator Enabling a Robust and Dendrite-Free Solid Electrolyte Interphase on a Lithium Metal Anode. *J. Mater. Chem. A* **2019**, *7*, 21349−21361.
(376) Gong, Y. J.; Heo, J. W.; Lee, H.; Kim, H.; Cho, J.; Pyo, S.; Yun, H.; Kim, H.; Park, S. Y.; Yoo, J. Nonwoven RGO Fiber-Aramid Separator for High-Speed Charging and Discharging of Li Metal Anode. *Adv. Energy Mater.* **2020**, *10*, 2001479.
(377) Shen, Z.; Zhang, W.; Li, S.; Mao, S.; Wang, X.; Chen, F.; Lu, Y. Tuning the Interfacial Electronic Conductivity by Artificial Electron Tunneling Barriers for Practical Lithium Metal Batteries. *Nano Lett.* **2020**, *20*, 6606−6613.
(378) Boateng, B.; Han, Y.; Zhen, C.; Zeng, G.; Chen, N.; Chen, D.; Feng, C.; Han, J.; Xiong, J.; Duan, X. Organosulfur Compounds Enable Uniform Lithium Plating and Long-Term Battery Cycling Stability. *Nano Lett.* **2020**, *20*, 2594−2601.
(379) Zhong, Y.; Lin, F.; Wang, M.; Zhang, Y.; Ma, Q.; Lin, J.; Feng, Z.; Wang, H. Metal Organic Framework Derivative Improving Lithium Metal Anode Cycling. *Adv. Funct. Mater.* **2020**, *30*, 1907579.
(380) Yan, J.; Liu, F.; Hu, Z.; Gao, J.; Zhou, W.; Huo, H.; Zhou, J.; Li, L. Realizing Dendrite-Free Lithium Deposition with a Composite Separator. *Nano Lett.* **2020**, *20*, 3798−3807.
(381) Hu, Z.; Liu, F.; Gao, J.; Zhou, W.; Huo, H.; Zhou, J.; Li, L. Dendrite-Free Lithium Plating Induced by In Situ Transferring Protection Layer from Separator. *Adv. Funct. Mater.* **2020**, *30*, 1907020.
(382) Liu, J.; Xu, R.; Yan, C.; Yuan, H.; Ding, J. F.; Xiao, Y.; Yuan, T. Q.; Huang, J. Q. In Situ Regulated Solid Electrolyte Interphase via

https://doi.org/10.1021/acs.chemrev.1c00838
Chem. Rev. 2022, 122, 8053−8125

Reactive Separators for Highly Efficient Lithium Metal Batteries. *Energy Storage Mater.* **2020**, *30*, 27−33.
(383) Xiao, J.; Zhai, P.; Wei, Y.; Zhang, X.; Yang, W.; Cui, S.; Jin, C.; Liu, W.; Wang, X.; Jiang, H. In-Situ Formed Protecting Layer from Organic/Inorganic Concrete for Dendrite-Free Lithium Metal Anodes. *Nano Lett.* **2020**, *20*, 3911−3917.
(384) Chen, X.; Zhang, R.; Zhao, R.; Qi, X.; Li, K.; Sun, Q.; Ma, M.; Qie, L.; Huang, Y. A "Dendrite-Eating" Separator for High-Areal-Capacity Lithium-Metal Batteries. *Energy Storage Mater.* **2020**, *31*, 181−186.
(385) Liu, Y.; Wu, Y.; Zheng, J.; Wang, Y.; Ju, Z.; Lu, G.; Sheng, O.; Nai, J.; Liu, T.; Zhang, W.; et al. Silicious Nanowires Enabled Dendrites Suppression and Flame Retardancy for Advanced Lithium Metal Anodes. *Nano Energy* **2021**, *82*, 105723.
(386) Wang, H.; Wang, C.; Matios, E.; Li, W. Critical Role of Ultrathin Graphene Films with Tunable Thickness in Enabling Highly Stable Sodium Metal Anodes. *Nano Lett.* **2017**, *17*, 6808−6815.
(387) Liu, W.; Chen, Z.; Zhang, Z.; Jiang, P.; Chen, Y.; Paek, E.; Wang, Y.; Mitlin, D. Lithium-Activated SnS-Graphene Alternating Nanolayers Enable Dendrite-Free Cycling of Thin Sodium Metal Anodes in Carbonate Electrolyte. *Energy Environ. Sci.* **2021**, *14*, 382−395.
(388) Liu, K.; Zhuo, D.; Lee, H. W.; Liu, W.; Lin, D.; Lu, Y.; Cui, Y. Extending the Life of Lithium-Based Rechargeable Batteries by Reaction of Lithium Dendrites with a Novel Silica Nanoparticle Sandwiched Separator. *Adv. Mater.* **2017**, *29*, 1603987.
(389) Zhang, S. S.; Fan, X.; Wang, C. Preventing Lithium Dendrite-Related Electrical Shorting in Rechargeable Batteries by Coating Separator with a Li-Killing Additive. *J. Mater. Chem. A* **2018**, *6*, 10755−10760.
(390) Yang, H.; Sun, J.; Wang, H.; Liang, J.; Li, H. A Titanium Dioxide Nanoparticle Sandwiched Separator for Na-O2 Batteries with Suppressed Dendrites and Extended Cycle Life. *Chem. Commun.* **2018**, *54*, 4057−4060.
(391) Memarzadeh Lotfabad, E.; Kalisvaart, P.; Cui, K.; Kohandehghan, A.; Kupsta, M.; Olsen, B.; Mitlin, D. ALD TiO2 Coated Silicon Nanowires for Lithium Ion Battery Anodes with Enhanced Cycling Stability and Coulombic Efficiency. *Phys. Chem. Chem. Phys.* **2013**, *15*, 13646−13657.
(392) Li, P.; Xu, T.; Ding, P.; Deng, J.; Zha, C.; Wu, Y.; Wang, Y.; Li, Y. Highly Reversible Na and K Metal Anodes Enabled by Carbon Paper Protection. *Energy Storage Mater.* **2018**, *15*, 8−13.
(393) Yan, C.; Cheng, X. B.; Tian, Y.; Chen, X.; Zhang, X. Q.; Li, W. J.; Huang, J. Q.; Zhang, Q. Dual-Layered Film Protected Lithium Metal Anode to Enable Dendrite-Free Lithium Deposition. *Adv. Mater.* **2018**, *30*, 1707629.
(394) Lee, Y.; Lee, J.; Lee, J.; Kim, K.; Cha, A.; Kang, S.; Wi, T.; Kang, S. J.; Lee, H. W.; Choi, N. S. Fluoroethylene Carbonate-Based Electrolyte with 1 M Sodium Bis(Fluorosulfonyl)Imide Enables High-Performance Sodium Metal Electrodes. *ACS Appl. Mater. Interfaces* **2018**, *10*, 15270−15280.
(395) Zhang, X. Q.; Cheng, X. B.; Chen, X.; Yan, C.; Zhang, Q. Fluoroethylene Carbonate Additives to Render Uniform Li Deposits in Lithium Metal Batteries. *Adv. Funct. Mater.* **2017**, *27*, 1605989.
(396) Liu, Y.; Liu, Q.; Xin, L.; Liu, Y.; Yang, F.; Stach, E. A.; Xie, J. Making Li-Metal Electrodes Rechargeable by Controlling the Dendrite Growth Direction. *Nat. Energy* **2017**, *2*, 1−10.
(397) Lee, H.; Ren, X.; Niu, C.; Yu, L.; Engelhard, M. H.; Cho, I.; Ryou, M. H.; Jin, H. S.; Kim, H. T.; Liu, J.; Xu, W.; Zhang, J. Suppressing Lithium Dendrite Growth by Metallic Coating on a Separator. *Adv. Funct. Mater.* **2017**, *27*, 1704391.
(398) Liu, Y.; Xiong, S.; Wang, J.; Jiao, X.; Li, S.; Zhang, C.; Song, Z.; Song, J. Dendrite-Free Lithium Metal Anode Enabled by Separator Engineering via Uniform Loading of Lithiophilic Nucleation Sites. *Energy Storage Mater.* **2019**, *19*, 24−30.
(399) Wen, K.; Liu, L.; Chen, S.; Zhang, S. A Bidirectional Growth Mechanism for a Stable Lithium Anode by a Platinum Nanolayer Sputtered on a Polypropylene Separator. *RSC Adv.* **2018**, *8*, 13034−13039.
(400) Liu, M.; Deng, N.; Ju, J.; Wang, L.; Wang, G.; Ma, Y.; Kang, W.; Yan, J. Silver Nanoparticle-Doped 3D Porous Carbon Nanofibers as Separator Coating for Stable Lithium Metal Anodes. *ACS Appl. Mater. Interfaces* **2019**, *11*, 17843−17852.
(401) Ma, Y.; Wang, L.; Fu, S.; Luo, R.; Qu, W.; Hu, X.; Chen, R.; Wu, F.; Li, L. In Situ Formation of a Li-Sn Alloy Protected Layer for Inducing Lateral Growth of Dendrites. *J. Mater. Chem. A* **2020**, *8*, 23574−23579.
(402) Hou, Z.; Gao, Y.; Tan, H.; Zhang, B. Realizing High-Power and High-Capacity Zinc/Sodium Metal Anodes Through Interfacial Chemistry Regulation. *Nat. Commun.* **2021**, *12*, 3083.
(403) Ju, Z.; Nai, J.; Wang, Y.; Liu, T.; Zheng, J.; Yuan, H.; Sheng, O.; Jin, C.; Zhang, W.; Jin, Z.; et al. Biomacromolecules Enabled Dendrite-Free Lithium Metal Battery and Its Origin Revealed by Cryo-Electron Microscopy. *Nat. Commun.* **2020**, *11*, 488.
(404) Luo, W.; Zhou, L.; Fu, K.; Yang, Z.; Hu, L. A Thermally Conductive Separator for Stable Li Metal Anodes. *Nano Lett.* **2015**, *15*, 6149−6154.
(405) Kim, P. J. H.; Seo, J.; Fu, K.; Choi, J.; Liu, Z.; Kwon, J.; Hu, L.; Paik, U. Synergistic Protective Effect of a BN-Carbon Separator for Highly Stable Lithium Sulfur Batteries. *NPG Asia Mater.* **2017**, *9*, 375.
(406) Kim, P. J. H.; Pol, V. G. Surface Functionalization of a Conventional Polypropylene Separator with an Aluminum Nitride Layer toward Ultrastable and High-Rate Lithium Metal Anodes. *ACS Appl. Mater. Interfaces* **2019**, *11*, 3917−3924.
(407) Vishnugopi, B. S.; Hao, F.; Verma, A.; Mukherjee, P. P. Double-Edged Effect of Temperature on Lithium Dendrites. *ACS Appl. Mater. Interfaces* **2020**, *12*, 23931−23938.
(408) Yan, K.; Wang, J.; Zhao, S.; Zhou, D.; Sun, B.; Cui, Y.; Wang, G. Temperature-Dependent Nucleation and Growth of Dendrite-Free Lithium Metal Anodes. *Angew. Chem., Int. Ed.* **2019**, *58*, 11364−11490.
(409) Wang, J.; Huang, W.; Pei, A.; Li, Y.; Shi, F.; Yu, X.; Cui, Y. Improving Cyclability of Li Metal Batteries at Elevated Temperatures and Its Origin Revealed by Cryo-Electron Microscopy. *Nat. Energy* **2019**, *4*, 664−670.
(410) Yang, X.; Luo, J.; Sun, X. Towards High-Performance Solid-State Li-S Batteries: from Fundamental Understanding to Engineering Design. *Chem. Soc. Rev.* **2020**, *49*, 2140−2195.
(411) Banerjee, A.; Wang, X.; Fang, C.; Wu, E. A.; Meng, Y. S. Interfaces and Interphases in All-Solid-State Batteries with Inorganic Solid Electrolytes. *Chem. Rev.* **2020**, *120*, 6878−6933.
(412) Krauskopf, T.; Richter, F. H.; Zeier, W. G.; Janek, J. Physicochemical Concepts of the Lithium Metal Anode in Solid-State Batteries. *Chem. Rev.* **2020**, *120*, 7745−7794.
(413) Chen, R.; Li, Q.; Yu, X.; Chen, L.; Li, H. Approaching Practically Accessible Solid-State Batteries: Stability Issues Related to Solid Electrolytes and Interfaces. *Chem. Rev.* **2020**, *120*, 6820−6877.
(414) Wang, M.; Kazyak, E.; Dasgupta, N.; Sakamoto, J. Transitioning solid-state batteries from lab to market: Linking electro-chemo-mechanics with practical considerations. *Joule* **2021**, *5*, 1371−1390.
(415) Zhang, X.; Wang, Q. J.; Harrison, K. L.; Roberts, S. A.; Harris, S. J. Pressure-Driven Interface Evolution in Solid-State Lithium Metal Batteries. *Cell Rep.* **2020**, *1*, 100012.
(416) Wang, M. J.; Choudhury, R.; Sakamoto, J. Characterizing the Li-Solid-Electrolyte Interface Dynamics as a Function of Stack Pressure and Current Density. *Joule* **2019**, *3*, 2165−2178.
(417) Zhao, Y.; Wang, L.; Zhou, Y.; Liang, Z.; Tavajohi, N.; Li, B.; Li, T. Solid Polymer Electrolytes with High Conductivity and Transference Number of Li Ions for Li-Based Rechargeable Batteries. *Adv. Sci.* **2021**, *8*, 2003675.
(418) Zhou, D.; Shanmukaraj, D.; Tkacheva, A.; Armand, M.; Wang, G. Polymer Electrolytes for Lithium-Based Batteries: Advances and Prospects. *Chem.* **2019**, *5*, 2326−2352.
(419) Liu, Y.; Xu, B.; Zhang, W.; Li, L.; Lin, Y.; Nan, C. Composition Modulation and Structure Design of Inorganic-in-Polymer Composite Solid Electrolytes for Advanced Lithium Batteries. *Small* **2020**, *16*, 1902813.

https://doi.org/10.1021/acs.chemrev.1c00838
Chem. Rev. 2022, 122, 8053−8125

(420) Fan, Z.; Ding, B.; Zhang, T.; Lin, Q.; Malgras, V.; Wang, J.; Dou, H.; Zhang, X.; Yamauchi, Y. Solid/Solid Interfacial Architecturing of Solid Polymer Electrolyte-Based All-Solid-State Lithium-Sulfur Batteries by Atomic Layer Deposition. *Small* **2019**, *15*, 1903952.
(421) Ren, Y.; Hortance, N.; McBride, J.; Hatzell, K. Sodium-Sulfur Batteries Enabled by a Protected Inorganic/Organic Hybrid Solid Electrolyte. *ACS Energy Lett.* **2021**, *6*, 345−353.
(422) Tao, X.; Liu, Y.; Liu, W.; Zhou, G.; Zhao, J.; Lin, D.; Zu, C.; Sheng, O.; Zhang, W.; Lee, H. W.; et al. Solid-State Lithium-Sulfur Batteries Operated at 37 °C with Composites of Nanostructured Li7La3Zr2O12/Carbon Foam and Polymer. *Nano Lett.* **2017**, *17*, 2967−2972.
(423) Zhu, P.; Yan, C.; Zhu, J.; Zang, J.; Li, Y.; Jia, H.; Dong, X.; Du, Z.; Zhang, C.; Wu, N.; et al. Flexible Electrolyte-Cathode Bilayer Framework with Stabilized Interface for Room-Temperature All-Solid-State Lithium-Sulfur Batteries. *Energy Storage Mater.* **2019**, *17*, 220−225.
(424) Li, X.; Wang, D.; Wang, H.; Yan, H.; Gong, Z.; Yang, Y. Poly(ethylene oxide)-Li10SnP2S12 Composite Polymer Electrolyte Enables High-Performance All-Solid-State Lithium Sulfur Battery. *ACS Appl. Mater. Interfaces* **2019**, *11*, 22745−22753.
(425) Xu, X.; Li, Y.; Cheng, J.; Hou, G.; Nie, X.; Ai, Q.; Dai, L.; Feng, J.; Ci, L. Composite Solid Electrolyte of Na3PS4-PEO for All-Solid-State SnS2/Na Batteries with Excellent Interfacial Compatibility between Electrolyte and Na Metal. *J. Energy Chem.* **2020**, *41*, 73−78.
(426) Richards, W. D.; Miara, L. J.; Wang, Y.; Kim, J. C.; Ceder, G. Interface Stability in Solid-State Batteries. *Chem. Mater.* **2016**, *28*, 266−273.
(427) Zhu, Y.; He, X.; Mo, Y. Origin of Outstanding Stability in the Lithium Solid Electrolyte Materials: Insights from Thermodynamic Analyses Based on First-Principles Calculations. *ACS Appl. Mater.* **2015**, *7*, 23685−23693.
(428) Lacivita, V.; Wang, Y.; Bo, S. H.; Ceder, G. Ab Initio Investigation of the Stability of Electrolyte/Electrode Interfaces in All-Solid-State Na Batteries. *J. Mater. Chem. A* **2019**, *7*, 8144−8155.
(429) Kamaya, N.; Homma, K.; Yamakawa, Y.; Hirayama, M.; Kanno, R.; Yonemura, M.; Kamiyama, T.; Kato, Y.; Hama, S.; Kawamoto, K.; et al. A Lithium Superionic Conductor. *Nat. Mater.* **2011**, *10*, 682−686.
(430) Fan, L.; Wei, S.; Li, S.; Li, Q.; Lu, Y. Recent Progress of the Solid-State Electrolytes for High-Energy Metal-Based Batteries. *Adv. Energy Mater.* **2018**, *8*, 1702657.
(431) Yue, J.; Han, F.; Fan, X.; Zhu, X.; Ma, Z.; Yang, J.; Wang, C. High-Performance All-Inorganic Solid-State Sodium-Sulfur Battery. *ACS Nano* **2017**, *11*, 4885−4891.
(432) Zhang, Q.; Huang, N.; Huang, Z.; Cai, L.; Wu, J.; Yao, X. CNTs@S Composite as Cathode for All-Solid-State Lithium-Sulfur Batteries with Ultralong Cycle Life. *J. Energy Chem.* **2020**, *40*, 151−155.
(433) Yi, J.; Chen, L.; Liu, Y.; Geng, H.; Fan, L. Z. High Capacity and Superior Cyclic Performances of All-Solid-State Lithium-Sulfur Batteries Enabled by a High-Conductivity Li10SnP2S12 Solid Electrolyte. *ACS Appl. Mater. Interfaces* **2019**, *11*, 36774−36781.
(434) Agostini, M.; Aihara, Y.; Yamada, T.; Scrosati, B.; Hassoun, J. A Lithium-Sulfur Battery Using a Solid, Glass-Type P2S5-Li2S Electrolyte. *Solid State Ion.* **2013**, *244*, 48−51.
(435) Fan, X.; Yue, J.; Han, F.; Chen, J.; Deng, T.; Zhou, X.; Hou, S.; Wang, C. High-Performance All-Solid-State Na-S Battery Enabled by Casting-Annealing Technology. *ACS Nano* **2018**, *12*, 3360−3368.
(436) Lu, Y.; Alonso, J. A.; Yi, Q.; Lu, L.; Wang, Z. L.; Sun, C. A High-Performance Monolithic Solid-State Sodium Battery with Ca2+ Doped Na3Zr2Si2PO12 Electrolyte. *Adv. Energy Mater.* **2019**, *9*, 1901205.
(437) Umeshbabu, E.; Zheng, B.; Zhu, J.; Wang, H.; Li, Y.; Yang, Y. Stable Cycling Lithium-Sulfur Solid Batteries with Enhanced Li/Li10GeP2S12 Solid Electrolyte Interface Stability. *ACS Appl. Mater. Interfaces* **2019**, *11*, 18436−18447.
(438) Wang, L.; Wang, Y.; Xia, Y. A High Performance Lithium-Ion Sulfur Battery based on a Li2S Cathode Using a Dual-Phase Electrolyte. *Energy Environ. Sci.* **2015**, *8*, 1551−1558.
(439) Hao, Y.; Wang, S.; Xu, F.; Liu, Y.; Feng, N.; He, P.; Zhou, H. A Design of Solid-State Li-S Cell with Evaporated Lithium Anode to Eliminate Shuttle Effects. *ACS Appl. Mater. Interfaces* **2017**, *9*, 33735−33739.
(440) Itoh, M.; Inaguma, Y.; Jung, W. H.; Chen, L.; Nakamura, T. High Lithium Ion Conductivity in the Perovskite-Type Compounds Ln12Li12TiO3 (Ln= La, Pr, Nd, Sm). *Solid State Ion.* **1994**, *70*, 203−207.
(441) Arbi, K.; Rojo, J. M.; Sanz, J. Lithium Mobility in Titanium based Nasicon Li1+xTi2-xAlx(PO4)3 and LiTi2-xZrx(PO4)3 Materials Followed by NMR and Impedance Spectroscopy. *J. Eur. Ceram. Soc.* **2007**, *27*, 4215−4218.
(442) Fu, J. Fast Li+ Ion Conducting Glass-Ceramics in the System Li2O-Al2O3-GeO2-P2O5. *Solid State Ion.* **1997**, *104*, 191−194.
(443) Yu, X.; Manthiram, A. Sodium-Sulfur Batteries with a Polymer-Coated NASICON-Type Sodium-Ion Solid Electrolyte. *Matter* **2019**, *1*, 439−451.
(444) Zhang, Z.; Wenzel, S.; Zhu, Y.; Sann, J.; Shen, L.; Yang, J.; Yao, X.; Hu, Y.-S.; Wolverton, C.; Li, H.; et al. Na3Zr2Si2PO12: A Stable Na+-Ion Solid Electrolyte for Solid-State Batteries. *ACS Appl. Energy Mater.* **2020**, *3*, 7427−7437.
(445) Murugan, R.; Thangadurai, V.; Weppner, W. Fast Lithium Ion Conduction in Garnet-Type Li7La3Zr2O12. *Angew. Chem., Int. Ed.* **2007**, *46*, 7778−7781.
(446) Wei, T.; Gong, Y.; Zhao, X.; Huang, K. An All-Ceramic Solid-State Rechargeable Na+-Battery Operated at Intermediate Temperatures. *Adv. Funct. Mater.* **2014**, *24*, 5380−5384.
(447) Seino, Y.; Ota, T.; Takada, K.; Hayashi, A.; Tatsumisago, M. A Sulphide Lithium Super Ion Conductor is Superior to Liquid Ion Conductors for Use in Rechargeable Batteries. *Energy Environ. Sci.* **2014**, *7*, 627−631.
(448) Liu, Z.; Fu, W.; Payzant, E. A.; Yu, X.; Wu, Z.; Dudney, N. J.; Kiggans, J.; Hong, K.; Rondinone, A. J.; Liang, C. Anomalous High Ionic Conductivity of Nanoporous Beta-Li3PS4. *J. Am. Chem. Soc.* **2013**, *135*, 975−978.
(449) Boulineau, S.; Courty, M.; Tarascon, J. M.; Viallet, V. Mechanochemical Synthesis of Li-Argyrodite Li6PS5X (X = Cl, Br, I) as Sulfur-based Solid Electrolytes for All Solid State Batteries Application. *Solid State Ion.* **2012**, *221*, 1−5.
(450) Zhang, Z.; Cao, H.; Yang, M.; Yan, X.; Yu, C.; Liu, D.; Zhang, L. High Performance Room Temperature All-Solid-State Na-SexSy Battery with Na3SbS4-Coated Cathode via Aqueous Solution. *J. Energy Chem.* **2020**, *48*, 250−258.
(451) Wenzel, S.; Leichtweiss, T.; Krüger, D.; Sann, J.; Janek, J. Interphase Formation on Lithium Solid Electrolytes—An in situ Approach to Study Interfacial Reactions by Photoelectron Spectroscopy. *Solid State Ion.* **2015**, *278*, 98−105.
(452) Gao, H.; Xin, S.; Xue, L.; Goodenough, J. B. Stabilizing a High-Energy-Density Rechargeable Sodium Battery with a Solid Electrolyte. *Chem.* **2018**, *4*, 833−844.
(453) Wu, E. A.; Kompella, C. S.; Zhu, Z.; Lee, J. Z.; Lee, S. C.; Chu, I. H.; Nguyen, H.; Ong, S. P.; Banerjee, A.; Meng, Y. S. New Insights into the Interphase between the Na Metal Anode and Sulfide Solid-State Electrolytes: A Joint Experimental and Computational Study. *ACS Appl. Mater. Interfaces* **2018**, *10*, 10076−10086.
(454) Wu, E. A.; Kompella, C. S.; Zhu, Z.; Lee, J. Z.; Lee, S. C.; Chu, I. H.; Nguyen, H.; Ong, S. P.; Banerjee, A.; Meng, Y. S. New Insights into the Interphase between the Na Metal Anode and Sulfide Solid-State Electrolytes: A Joint Experimental and Computational Study. *ACS Appl. Mater. Interfaces* **2018**, *10*, 10076−10086.
(455) Wang, S.; Ding, Y.; Zhou, G.; Yu, G.; Manthiram, A. Durability of the Li1+xTi2-xAlx(PO4)3 Solid Electrolyte in Lithium-Sulfur Batteries. *ACS Energy Lett.* **2016**, *1*, 1080−1085.
(456) Suzuki, K.; Mashimo, N.; Ikeda, Y.; Yokoi, T.; Hirayama, M.; Kanno, R. High Cycle Capability of All-Solid-State Lithium-Sulfur

https://doi.org/10.1021/acs.chemrev.1c00838
Chem. Rev. 2022, 122, 8053−8125

Batteries Using Composite Electrodes by Liquid-Phase and Mechanical Mixing. *ACS Appl. Energy Mater.* **2018**, *1*, 2373−2377.
(457) Wang, S.; Zhang, Y.; Zhang, X.; Liu, T.; Lin, Y. H.; Shen, Y.; Li, L.; Nan, C. W. High-Conductivity Argyrodite Li6PS5Cl Solid Electrolytes Prepared via Optimized Sintering Processes for All-Solid-State Lithium-Sulfur Batteries. *ACS Appl. Mater. Interfaces* **2018**, *10*, 42279−42285.
(458) Xu, S.; McOwen, D. W.; Zhang, L.; Hitz, G. T.; Wang, C.; Ma, Z.; Chen, C.; Luo, W.; Dai, J.; Kuang, Y.; et al. All-in-One Lithium-Sulfur Battery Enabled by a Porous-Dense-Porous Garnet Architecture. *Energy Storage Mater.* **2018**, *15*, 458−464.
(459) Yu, X.; Bi, Z.; Zhao, F.; Manthiram, A. Polysulfide-Shuttle Control in Lithium-Sulfur Batteries with a Chemically/Electrochemically Compatible NaSICON-Type Solid Electrolyte. *Adv. Energy. Mater.* **2016**, *6*, 1601392.
(460) An, T.; Jia, H.; Peng, L.; Xie, J. Material and Interfacial Modification toward a Stable Room-Temperature Solid-State Na-S Battery. *ACS Appl. Mater. Interfaces* **2020**, *12*, 20563−20569.
(461) Tian, Y.; Sun, Y.; Hannah, D. C.; Xiao, Y.; Liu, H.; Chapman, K. W.; Bo, S. H.; Ceder, G. Reactivity-Guided Interface Design in Na Metal Solid-State Batteries. *Joule* **2019**, *3*, 1037−1050.
(462) Zhang, S.; Zhao, Y.; Zhao, F.; Zhang, L.; Wang, C.; Li, X.; Liang, J.; Li, W.; Sun, Q.; Yu, C.; et al. Gradiently Sodiated Alucone as an Interfacial Stabilizing Strategy for Solid-State Na Metal Batteries. *Adv. Funct. Mater.* **2020**, *30*, 2001118.
(463) Wan, H.; Liu, S.; Deng, T.; Xu, J.; Zhang, J.; He, X.; Ji, X.; Yao, X.; Wang, C. Bifunctional Interphase-Enabled Li10GeP2S12 Electrolytes for Lithium-Sulfur Battery. *ACS Energy Lett.* **2021**, *6*, 862−868.
(464) Xu, R. C.; Xia, X. H.; Wang, X. L.; Xia, Y.; Tu, J. P. Tailored Li2S-P2S5 Glass-Ceramic Electrolyte by MoS2-Doping, Possessing High Ionic Conductivity for All-Solid-State Lithium-Sulfur Batteries. *J. Mater. Chem. A* **2017**, *5*, 2829−2834.
(465) Xu, R. C.; Xia, X. H.; Li, S. H.; Zhang, S. Z.; Wang, X. L.; Tu, J. P. All-Solid-State Lithium-Sulfur Batteries based on a Newly Designed Li7P2.9Mn0.1S10.7I0.3 Superionic Conductor. *J. Mater. Chem. A* **2017**, *5*, 6310−6317.
(466) Wan, H.; Cai, L.; Yao, Y.; Weng, W.; Feng, Y.; Mwizerwa, J. P.; Liu, G.; Yu, Y.; Yao, X. Self-Formed Electronic/Ionic Conductive Fe3S4@S@0.9Na3SbS4·0.1NaI Composite for High-Performance Room-Temperature All-Solid-State Sodium-Sulfur Battery. *Small* **2020**, *16*, 2001574.
(467) Samson, A. J.; Hofstetter, K.; Bag, S.; Thangadurai, V. A Bird's-Eye View of Li-stuffed Garnet-Type Li7La3Zr2O12 Ceramic Electrolytes for Advanced All-Solid-State Li Batteries. *Energy Environ. Sci.* **2019**, *12*, 2957−2975.
(468) Wang, C.; Fu, K.; Kammampata, S. P.; McOwen, D. W.; Samson, A. J.; Zhang, L.; Hitz, G. T.; Nolan, A. M.; Wachsman, E. D.; Mo, Y.; et al. Garnet-Type Solid-State Electrolytes: Materials, Interfaces, and Batteries. *Chem. Rev.* **2020**, *120*, 4257−4300.
(469) Xu, L.; Li, J.; Deng, W.; Shuai, H.; Li, S.; Xu, Z.; Li, J.; Hou, H.; Peng, H.; Zou, G.; et al. Garnet Solid Electrolyte for Advanced All-Solid-State Li Batteries. *Adv. Energy Mater.* **2021**, *11*, 2000648.
(470) Bernstein, N.; Johannes, M. D.; Hoang, K. Origin of the Structural Phase Transition in Li7La3Zr2O12. *Phys. Rev. Lett.* **2012**, *109*, 205702.
(471) Han, X.; Gong, Y.; Fu, K. K.; He, X.; Hitz, G. T.; Dai, J.; Pearse, A.; Liu, B.; Wang, H.; Rubloff, G.; et al. Negating Interfacial Impedance in Garnet-based Solid-State Li metal Batteries. *Nat. Mater.* **2017**, *16*, 572−579.
(472) Cheng, L.; Crumlin, E. J.; Chen, W.; Qiao, R.; Hou, H.; Franz Lux, S.; Zorba, V.; Russo, R.; Kostecki, R.; Liu, Z.; et al. The Origin of High Electrolyte-Electrode Interfacial Resistances in Lithium Cells Containing Garnet Type Solid Electrolytes. *Phys. Chem. Chem. Phys.* **2014**, *16*, 18294−18300.
(473) Liu, C.; Rui, K.; Shen, C.; Badding, M. E.; Zhang, G.; Wen, Z. Reversible Ion Exchange and Structural Stability of Garnet-Type Nb-Doped Li7La3Zr2O12 in Water for Applications in Lithium Batteries. *J. Power Sources* **2015**, *282*, 286−293.
(474) Huo, H.; Luo, J.; Thangadurai, V.; Guo, X.; Nan, C. W.; Sun, X. Li2CO3: A Critical Issue for Developing Solid Garnet Batteries. *ACS Energy Lett.* **2020**, *5*, 252−262.
(475) Raj, R.; Wolfenstine, J. Current Limit Diagrams for Dendrite Formation in Solid-State Electrolytes for Li-ion Batteries. *J. Power Sources* **2017**, *343*, 119−126.
(476) Han, F.; Westover, A. S.; Yue, J.; Fan, X.; Wang, F.; Chi, M.; Leonard, D. N.; Dudney, N. J.; Wang, H.; Wang, C. High Electronic Conductivity as the Origin of Lithium Dendrite Formation within Solid Electrolytes. *Nat. Energy* **2019**, *4*, 187−196.
(477) Yu, S.; Siegel, D. J. Grain Boundary Contributions to Li-Ion Transport in the Solid Electrolyte Li7La3Zr2O12 (LLZO). *Chem. Mater.* **2017**, *29*, 9639−9647.
(478) Fu, K.; Gong, Y.; Hitz, G. T.; McOwen, D. W.; Li, Y.; Xu, S.; Wen, Y.; Zhang, L.; Wang, C.; Pastel, G.; et al. Three-Dimensional Bilayer Garnet Solid Electrolyte based High Energy Density Lithium Metal-Sulfur Batteries. *Energy Environ. Sci.* **2017**, *10*, 1568−1575.
(479) Dubey, R.; Sastre, J.; Cancellieri, C.; Okur, F.; Forster, A.; Pompizii, L.; Priebe, A.; Romanyuk, Y. E.; Jeurgens, L. P. H.; Kovalenko, M. V.; et al. Building a Better Li-Garnet Solid Electrolyte/Metallic Li Interface with Antimony. *Adv. Energy Mater.* **2021**, *11*, 2102086.
(480) Wang, C.; Gong, Y.; Liu, B.; Fu, K.; Yao, Y.; Hitz, E.; Li, Y.; Dai, J.; Xu, S.; Luo, W.; et al. Conformal, Nanoscale ZnO Surface Modification of Garnet-Based Solid-State Electrolyte for Lithium Metal Anodes. *Nano Lett.* **2017**, *17*, 565−571.
(481) Xu, H.; Li, Y.; Zhou, A.; Wu, N.; Xin, S.; Li, Z.; Goodenough, J. B. Li3N-Modified Garnet Electrolyte for All-Solid-State Lithium Metal Batteries Operated at 40 degrees C. *Nano Lett.* **2018**, *18*, 7414−7418.
(482) Li, Y.; Chen, X.; Dolocan, A.; Cui, Z.; Xin, S.; Xue, L.; Xu, H.; Park, K.; Goodenough, J. B. Garnet Electrolyte with an Ultralow Interfacial Resistance for Li-Metal Batteries. *J. Am. Chem. Soc.* **2018**, *140*, 6448−6455.
(483) Han, F.; Yue, J.; Fan, X.; Gao, T.; Luo, C.; Ma, Z.; Suo, L.; Wang, C. High-Performance All-Solid-State Lithium-Sulfur Battery Enabled by a Mixed-Conductive Li2S Nanocomposite. *Nano Lett.* **2016**, *16*, 4521−4527.
(484) Lu, X.; Bowden, M. E.; Sprenkle, V. L.; Liu, J. A Low Cost, High Energy Density, and Long Cycle Life Potassium-Sulfur Battery for Grid-Scale Energy Storage. *Adv. Mater.* **2015**, *27*, 5915−5922.
(485) Judez, X.; Zhang, H.; Li, C.; Gonzalez-Marcos, J. A.; Zhou, Z.; Armand, M.; Rodriguez-Martinez, L. M. Lithium Bis(fluorosulfonyl)-imide/Poly(ethylene oxide) Polymer Electrolyte for All Solid-State Li-S Cell. *J. Phys. Chem. Lett.* **2017**, *8*, 1956−1960.
(486) Eshetu, G. G.; Judez, X.; Li, C.; Martinez-Ibanez, M.; Gracia, I.; Bondarchuk, O.; Carrasco, J.; Rodriguez-Martinez, L. M.; Zhang, H.; Armand, M. Ultrahigh Performance All Solid-State Lithium Sulfur Batteries: Salt Anion's Chemistry-Induced Anomalous Synergistic Effect. *J. Am. Chem. Soc.* **2018**, *140*, 9921−9933.
(487) Fang, R.; Xu, B.; Grundish, N. S.; Xia, Y.; Li, Y.; Lu, C.; Liu, Y.; Wu, N.; Goodenough, J. B. Li2 S6-Integrated PEO-Based Polymer Electrolytes for All-Solid-State Lithium-Metal Batteries. *Angew. Chem., Int. Ed.* **2021**, *60*, 17701−17847.
(488) Eshetu, G. G.; Judez, X.; Li, C.; Bondarchuk, O.; Rodriguez-Martinez, L. M.; Zhang, H.; Armand, M. Lithium Azide as an Electrolyte Additive for All-Solid-State Lithium-Sulfur Batteries. *Angew. Chem., Int. Ed. Engl.* **2017**, *56*, 15368−15372.
(489) Wu, N.; Li, Y.; Dolocan, A.; Li, W.; Xu, H.; Xu, B.; Grundish, N. S.; Cui, Z.; Jin, H.; Goodenough, J. B. In Situ Formation of Li3P Layer Enables Fast Li+ Conduction across Li/Solid Polymer Electrolyte Interface. *Adv. Funct. Mater.* **2020**, *30*, 2000831.
(490) Wu, N.; Chien, P. H.; Li, Y.; Dolocan, A.; Xu, H.; Xu, B.; Grundish, N. S.; Jin, H.; Hu, Y. Y.; Goodenough, J. B. Fast Li+ Conduction Mechanism and Interfacial Chemistry of a NASICON/Polymer Composite Electrolyte. *J. Am. Chem. Soc.* **2020**, *142*, 2497−2505.
(491) Jovanović, P.; Mirshekarloo, M. S.; Hill, M. R.; Hollenkamp, A. F.; Majumder, M.; Shaibani, M. Separator Design Variables and

https://doi.org/10.1021/acs.chemrev.1c00838
Chem. Rev. 2022, 122, 8053−8125

Recommended Characterization Methods for Viable Lithium-Sulfur Batteries. *Adv. Mater. Technol.* **2021**, *6*, 2001136.
(492) Li, T.; Bai, X.; Gulzar, U.; Bai, Y. J.; Capiglia, C.; Deng, W.; Zhou, X.; Liu, Z.; Feng, Z.; Proietti Zaccaria, R. A Comprehensive Understanding of Lithium-Sulfur Battery Technology. *Adv. Funct. Mater.* **2019**, *29*, 1901730.
(493) Deng, Y.; Li, J.; Li, T.; Gao, X.; Yuan, C. Life Cycle Assessment of Lithium Sulfur Battery for Electric Vehicles. *J. Power Sources* **2017**, *343*, 284−295.
(494) Rana, M.; Ahad, S. A.; Li, M.; Luo, B.; Wang, L.; Gentle, I.; Knibbe, R. Review on Areal Capacities and Long-term Cycling Performances of Lithium Sulfur Battery at High Sulfur Loading. *Energy Storage Mater.* **2019**, *18*, 289−310.
(495) Nelson, P.; Gallagher, K.; Bloom, I.; Dees, D. *Modeling the Performance and Cost of Lithium-Ion Batteries for Electric-Drive Vehicles*; Argonne National Lab., 2012, No. ANL-12/55. DOI: 10.2172/1209682
(496) Yang, C.; Li, P.; Yu, J.; Zhao, L. D.; Kong, L. Approaching Energy-Dense and Cost-Effective Lithium-Sulfur Batteries: from Materials Chemistry and Price Considerations. *Energy* **2020**, *201*, 117718.
(497) Wang, C. Selenium Minerals and the Recovery of Selenium from Copper Refinery Anode Slimes. *J. South. Afr. Inst. Min. Metall.* **2016**, *116*, 593−600.
(498) Funari, V.; Gomes, H. I.; Coppola, D.; Vitale, G. A.; Dinelli, E.; de Pascale, D.; Rovere, M. Opportunities and Threats of Selenium Supply from Unconventional and Low-Grade Ores: A Critical Review. *Resour. Conserv. Recycl.* **2021**, *170*, 105593.
(499) Li, X.; Liang, J.; Luo, J.; Wang, C.; Li, X.; Sun, Q.; Li, R.; Zhang, L.; Yang, R.; Lu, S.; et al. High-Performance Li-SeSx All-Solid-State Lithium Batteries. *Adv. Mater.* **2019**, *31*, 1808100.
(500) Plaimer, M.; Breitfuß, C.; Sinz, W.; Heindl, S. F.; Ellersdorfer, C.; Steffan, H.; Wilkening, M.; Hennige, V.; Tatschl, R.; Geier, A. Evaluating the Trade-Off Between Mechanical and Electrochemical Performance of Separators for Lithium-Ion Batteries: Methodology and Application. *J. Power Sources* **2016**, *306*, 702−710.
(501) Doyle, M.; Fuller, T. F.; Newman, J. Modeling of Galvanostatic Charge and Discharge of the Lithium/Polymer/Insertion Cell. *J. Electrochem. Soc.* **1993**, *140*, 1526.
(502) Gibson, L. J.; Ashby, M. F. *Cellular Solids: Structure and Properties*; Cambridge University Press, 1999; p 186.
(503) Sun, X. Y.; Xu, G. K.; Li, X.; Feng, X. Q.; Gao, H. Mechanical Properties and Scaling Laws of Nanoporous Gold. *J. Appl. Phys.* **2013**, *113*, 023505.
(504) Yan, S.; Huang, X.; Xiao, X. Measurement of the Through Thickness Compression of a Battery Separator. *J. Power Sources* **2018**, *382*, 13−21.
(505) Halalay, I. C.; Lukitsch, M. J.; Balogh, M. P.; Wong, C. A. Nanoindentation Testing of Separators for Lithium-Ion Batteries. *J. Power Sources* **2013**, *238*, 469−477.
(506) Wang, Y.; Li, Q.; Xing, Y. Porosity Variation of Lithium-Ion Battery Separators Under Uniaxial Tension. *Int. J. Mech. Sci.* **2020**, *174*, 105496.
(507) Yan, S.; Deng, J.; Bae, C.; Kalnaus, S.; Xiao, X. Orthotropic Viscoelastic Modeling of Polymeric Battery Separator. *J. Electrochem. Soc.* **2020**, *167*, 090530.
(508) Chen, K.; Kang, G.; Yu, C.; Lu, F.; Jiang, H. Time-Dependent Uniaxial Ratchetting of Ultrahigh Molecular Weight Polyethylene Polymer: Viscoelastic-Viscoplastic Constitutive Model. *J. Appl. Mech.* **2016**, *83*, 101003.
(509) Chen, J.; Hu, H.; Li, S.; He, Y. Evolution of Mechanical Properties of Polypropylene Separator in Liquid Electrolytes for Lithium-Ion Batteries. *J. Appl. Polym. Sci.* **2018**, *135*, 46441.
(510) Love, C. T. Thermomechanical Analysis and Durability of Commercial Micro-Porous Polymer Li-Ion Battery Separators. *J. Power Sources* **2011**, *196*, 2905−2912.
(511) Dezheng, M.; Peichao, L. Fluid-structure Coupling Effect of Lithium-Ion Battery Separator under Compression. *Energy Storage Science and Technology* **2021**, *10*, 483.
(512) Gor, G. Y.; Cannarella, J.; Prévost, J. H.; Arnold, C. B. A Model for the Behavior of Battery Separators in Compression at Different Strain/Charge Rates. *J. Electrochem. Soc.* **2014**, *161*, F3065.
(513) Cannarella, J.; Liu, X.; Leng, C. Z.; Sinko, P. D.; Gor, G. Y.; Arnold, C. B. Mechanical Properties of a Battery Separator Under Compression and Tension. *J. Electrochem. Soc.* **2014**, *161*, F3117.
(514) Sheidaei, A.; Xiao, X.; Huang, X.; Hitt, J. Mechanical Behavior of a Battery Separator in Electrolyte Solutions. *J. Power Sources* **2011**, *196*, 8728−8734.
(515) Gor, G. Y.; Cannarella, J.; Leng, C. Z.; Vishnyakov, A.; Arnold, C. B. Swelling and Softening of Lithium-Ion Battery Separators in Electrolyte Solvents. *J. Power Sources* **2015**, *294*, 167−172.
(516) Behrou, R. A Thermo-Poro-Viscoelastic Model for the Behavior of Polymeric Porous Separators. *ECS Trans.* **2017**, *80*, 583.
(517) Peabody, C.; Arnold, C. B. The Role of Mechanically Induced Separator Creep in Lithium-Ion Battery Capacity Fade. *J. Power Sources* **2011**, *196*, 8147−8153.
(518) Cannarella, J.; Peabody, C.; Arnold, C. B. Stress-Induced Capacity Fade Due to Separator Creep in Lithium-Ion Cells. *ECS Meeting Abstracts* **2012**, *MA2012-01*, 975.
(519) Shen, X.; Li, C.; Shi, C.; Yang, C.; Deng, L.; Zhang, W.; Peng, L.; Dai, J.; Wu, D.; Zhang, P. Core-Shell Structured Ceramic Nonwoven Separators by Atomic Layer Deposition for Safe Lithium-Ion Batteries. *Appl. Surf. Sci.* **2018**, *441*, 165−173.
(520) Mao, Y.; Sun, W.; Qiao, Y.; Liu, X.; Xu, C.; Fang, L.; Hou, W.; Wang, Z.; Sun, K. A High Strength Hybrid Separator with Fast Ionic Conductor for Dendrite-Free Lithium Metal Batteries. *Chem. Eng. J.* **2021**, *416*, 129119.
(521) Zhu, X.; Jiang, X.; Ai, X.; Yang, H.; Cao, Y. TiO2 Ceramic-Grafted Polyethylene Separators for Enhanced Thermostability and Electrochemical Performance of Lithium-Ion Batteries. *J. Membr. Sci.* **2016**, *504*, 97−103.
(522) Wang, Y.; Wang, Q.; Lan, Y.; Song, Z.; Luo, J.; Wei, X.; Sun, F.; Yue, Z.; Yin, C.; Zhou, L. Aqueous Aluminide Ceramic Coating Polyethylene Separators for Lithium-Ion Batteries. *Solid State Ion.* **2020**, *345*, 115188.
(523) Wu, J.; Zuo, X.; Chen, Q.; Deng, X.; Liang, H.; Zhu, T.; Liu, J.; Li, W.; Nan, J. Functional Composite Polymer Electrolytes with Imidazole Modified SiO2 Nanoparticles for High-Voltage Cathode Lithium Ion Batteries. *Electrochim. Acta* **2019**, *320*, 134567.
(524) Ritchie, R. O. The Conflicts Between Strength and Toughness. *Nat. Mater.* **2011**, *10*, 817−822.
(525) Chen, J.; Sun, T.; Qi, Y.; Li, X. A Coupled Penetration-Tension Method for Evaluating the Reliability of Battery Separators. *ECS Electrochem. Lett.* **2014**, *3*, A41.
(526) Moghim, M. H.; Nahvi Bayani, A.; Eqra, R. Strain-Rate-Dependent Mechanical Properties of Polypropylene Separator for Lithium-Ion Batteries. *Polym. Int.* **2020**, *69*, 545−551.
(527) Ding, L.; Zhang, D.; Wu, T.; Yang, F.; Lan, F.; Cao, Y.; Xiang, M. The Influence of Multiple Stimulations on the Unusual Delamination Phenomenon of a Li-Ion Battery Separator Prepared by a Wet Process. *Ind. Eng. Chem. Res.* **2020**, *59*, 4568−4579.
(528) Chen, Z.; Wang, Y.; Xiong, B.; Zhu, J. *Polymer* **2020**, *203*, 122832.
(529) Barkoula, N. M.; Alcock, B.; Cabrera, N.; Peijs, T. Fatigue Properties of Highly Oriented Polypropylene Tapes and All-Polypropylene Composites. *Polym. Polym. Compos.* **2008**, *16*, 101−113.
(530) Kim, J.; Yoo, K.; Kim, D.; Lee, M.; Yang, W.; Byeon, J. Evaluation of Health and Safety of Mechanically Fatigued Rechargeable Lithium Polymer Batteries for Flexible Electronics Applications. *Microelectron. Reliab.* **2019**, *100*, 113441.
(531) Kim, J. Y.; Kim, J. Y.; Kim, M. K.; Byeon, J. W. Health Monitoring of Mechanically Fatigued Flexible Lithium Ion Battery by Electrochemical Impedance Spectroscopy. *Microelectron. Reliab.* **2020**, *114*, 113818.
(532) Balach, J.; Jaumann, T.; Klose, M.; Oswald, S.; Eckert, J.; Giebeler, L. Functional Mesoporous Carbon-Coated Separator for

Long-Life, High-Energy Lithium-Sulfur Batteries. *Adv. Funct. Mater.* **2015**, *25*, 5285.
(533) Stancovski, V.; Badilescu, S. In Situ Raman Spectroscopic-Electrochemical Studies of Lithium-Ion Battery Materials: A Historical Overview. *J. Appl. Electrochem.* **2014**, *44*, 23−43.
(534) Tripathi, A. M.; Su, W. N.; Hwang, B. J. In Situ Analytical Techniques for Battery Interface Analysis. *Chem. Soc. Rev.* **2018**, *47*, 736−851.
(535) Boebinger, M. G.; Lewis, J. A.; Sandoval, S. E.; McDowell, M. T. Understanding Transformations in Battery Materials Using in Situ and Operando Experiments: Progress and Outlook. *ACS Energy Lett.* **2020**, *5*, 335−345.
(536) Hardwick, L. J.; Hahn, M.; Ruch, P.; Holzapfel, M.; Scheifele, W.; Buqa, H.; Krumeich, F.; Novák, P.; Kötz, R. An in Situ Raman Study of the Intercalation of Supercapacitor-Type Electrolyte into Microcrystalline Graphite. *Electrochim. Acta* **2006**, *52*, 675−680.
(537) Nanda, J.; Yang, G.; Hou, T.; Voylov, D. N.; Li, X.; Ruther, R. E.; Naguib, M.; Persson, K.; Veith, G. M.; Sokolov, A. P. Unraveling the Nanoscale Heterogeneity of Solid Electrolyte Interphase Using Tip-Enhanced Raman Spectroscopy. *Joule* **2019**, *3*, 2001−2019.
(538) Raberg, J. H.; Vatamanu, J.; Harris, S. J.; van Oversteeg, C. H. M.; Ramos, A.; Borodin, O.; Cuk, T. Probing Electric Double-Layer Composition via in Situ Vibrational Spectroscopy and Molecular Simulations. *J. Phys. Chem. Lett.* **2019**, *10*, 3381−3389.
(539) Vivek, J. P.; Berry, N. G.; Zou, J.; Nichols, R. J.; Hardwick, L. J. In Situ Surface-Enhanced Infrared Spectroscopy to Identify Oxygen Reduction Products in Nonaqueous Metal-Oxygen Batteries. *J. Phys. Chem. C* **2017**, *121*, 19657−19667.
(540) Conder, J.; Bouchet, R.; Trabesinger, S.; Marino, C.; Gubler, L.; Villevieille, C. Direct Observation of Lithium Polysulfides in Lithium-Sulfur Batteries Using Operando X-ray Diffraction. *Nat. Energy* **2017**, *2*, 1−7.
(541) Pecher, O.; Carretero-González, J.; Griffith, K. J.; Grey, C. P. Materials' Methods: NMR in Battery Research. *Chem. Mater.* **2017**, *29*, 213−242.
(542) Marker, K.; Xu, C.; Grey, C. P. Operando NMR of NMC811/Graphite Lithium-Ion Batteries: Structure, Dynamics, and Lithium Metal Deposition. *J. Am. Chem. Soc.* **2020**, *142*, 17447−17456.
(543) Wang, H.; Sa, N.; He, M.; Liang, X.; Nazar, L. F.; Balasubramanian, M.; Gallagher, K. G.; Key, B. In Situ NMR Observation of the Temporal Speciation of Lithium Sulfur Batteries during Electrochemical Cycling. *J. Phys. Chem. C* **2017**, *121*, 6011−6017.
(544) Rajagopalan Kannan, D. R.; Terala, P. K.; Moss, P. L.; Weatherspoon, M. H. Analysis of the Separator Thickness and Porosity on the Performance of Lithium-Ion Batteries. *Int. J. Electrochem.* **2018**, *2018*, 1.
(545) Uchic, M. D.; Holzer, L.; Inkson, B. J.; Principe, E. L.; Munroe, P. Three-Dimensional Microstructural Characterization Using Focused Ion Beam Tomography. *MRS Bull.* **2007**, *32*, 408−416.
(546) Hwang, J. Y.; Kim, H. M.; Shin, S.; Sun, Y. K. Designing a High-Performance Lithium Sulfur Batteries Based on Layered Double Hydroxides Carbon Nanotubes Composite Cathode and a Dual-Functional Graphene-Polypropylene-Al2O3 Separator. *Adv. Funct. Mater.* **2018**, *28*, 1704294.
(547) Lagadec, M. F.; Ebner, M.; Zahn, R.; Wood, V. Communication—Technique for Visualization and Quantification of Lithium-Ion Battery Separator Microstructure. *J. Electrochem. Soc.* **2016**, *163*, A992.
(548) Parmenter, C. D.; Nizamudeen, Z. A. Cryo-FIB-Lift-Out: Practically Impossible to Practical Reality. *J. Microsc.* **2021**, *281*, 157−174.
(549) Fujiyoshi, Y. Low Dose Techniques and Cryo-Electron Microscopy. *Methods Mol. Biol.* **2013**, *955*, 103−118.
(550) Liu, L.; Zhang, D.; Zhu, Y.; Han, Y. Bulk and Local Structures of Metal-Organic Frameworks Unravelled by High-Resolution Electron Microscopy. *Commun. Chem.* **2020**, *3*, 1−14.
(551) Lee, J. Z.; Wynn, T. A.; Schroeder, M. A.; Alvarado, J.; Wang, X. F.; Xu, K.; Meng, Y. S. Cryogenic Focused Ion Beam Characterization of Lithium Metal Anodes. *ACS Energy Lett.* **2019**, *4*, 489−493.
(552) Zachman, M. J.; Tu, Z.; Choudhury, S.; Archer, L. A.; Kourkoutis, L. F. Cryo-STEM Mapping of Solid-Liquid Interfaces and Dendrites in Lithium-Metal Batteries. *Nature* **2018**, *560*, 345−349.

https://doi.org/10.1021/acs.chemrev.1c00838
Chem. Rev. 2022, 122, 8053−8125